Shear Behaviour of Lean Duplex Stainless Steel (LDSS) Rectangular Hollow Beams – a Finite Element Study

A thesis submitted for the degree of

Doctor of Philosophy

by

Sonu J.K

Department of Civil Engineering

Indian Institute on Technology Guwahati

Guwahati – 781 039, India

DECLARATION

I, Sonu J.K, declare that the work consists in this thesis titled by "***Shear Behaviour of Lean Duplex Stainless Steel (LDSS) Rectangular Hollow Beams — a Finite Element Study***" submitted here is a partial fulfilment for the requirement for awarding the Degree for **Doctor of Philosophy** and submitted in Indian Institute of Technology Guwahati, India. It is a record of my work carried out in my research in this Institute itself in a period of **July, 2011 to November, 2016** under the supervision of ***Dr. Kongengbam Darunkumar Singh***, Associate Professor, Department of Civil Engineering, Indian Institute of Technology Guwahati, India. I certify that the work which has reported in this thesis is not used for any other degree for me in same Institute or any other institution, and it is not published by any other person. The published works by others which I have consulted are always acknowledged in thesis by exact reference.

Date:

(Mr. Sonu J.K)
Reg. No:11610407

Place: IIT Guwahati

CERTIFICATE

This is to certify that the work embodied in the thesis entitled by "***Shear Behaviour of Lean Duplex Stainless Steel (LDSS) Rectangular Hollow Beams — a Finite Element Study***" being submitted here by Mr**. Sonu J.K** to Indian Institute of Technology Guwahati, India for the award of degree of **Doctor of Philosophy** is a record of authentic research work carried out by the candidate as a research scholar under my supervision and guidance.

The Thesis work, in my opinion is worthy of considering for the award of degree of **Doctor of Philosophy** in accordance with the regulation of the Institute.

(Dr. Konjengbam Darunkumar Singh)
Associate Professor
Department of Civil Engineering
Indian Institute of Technology Guwahati

Date:

Place: IIT Guwahati

to the Lord Almighty

to my dearest parents
Johnkutty and Usha

ABSTRACT

In the recent past, a new breed of stainless steel called Lean Duplex Stainless Steel (LDSS / LDX 2101 / EN 1.4162 / UNS 32101) has been introduced for the construction industry. LDSS offers significant advantages such as better economy (nickel content = ~1.5% i.e. much lower in comparison to austenitic stainless steel), improved strength, high temperature properties, acceptable weldability and fracture toughness properties etc. It is worthwhile to note that LDSS has already been incorporated in EN 1993-1-4 (2006) *via* a recent amendment (A1:2015). In the light of expanding the understanding of the structural performance of LDSS sections or members, an investigation is initiated in this thesis, on the parametric study of LDSS hollow beam (or box girder). Such study, is believed to aid in augmenting the confidence of practising engineers and architects in using LDSS structural elements.

Thus, in this thesis, a systematic investigation of the effect of cross sectional parameters such as flange thickness (t_f), flange width (w_f), and shear span (a) on the shear behaviour *viz*., shear capacity and failure mechanisms, of LDSS rectangular hollow beams (box girders) is presented, using finite element (FE) analysis. On the basis of the understanding gained from the FE analyses, presented herein, appropriateness of the design rules of EN 1993-1-4 (2006/A1:2015) and Direct Strength Method (DSM) are assessed. Based on the comparison, possible modifications to both EN 1993-1-4 (2006/A1:2015) and DSM have been suggested by bifurcating into two span ratios: 1) $a/h_w \leq 1.0$ and 2) $1 < a/h_w \leq 2.0$.

The FE study is then extended to investigate the effect of single circular web perforation in the shear characteristic of LDSS rectangular hollow beams. Primarily, the effect of single perforation size / diameter and locations (along longitudinal, transverse, and diagonals) are assessed with a focus on the shear capacity, deformed shapes (or failure modes) etc. Further, following the method proposed by Hagen, (2005), the proposed modification to EN 1993-1-4 (2006/A1:2015) (mentioned above) for un perforated LDSS hollow beam has been further modified to incorporate the effect of circular perforation, considering two span cases 1) $a/h_w \leq 1.0$ and 2) $1 < a/h_w \leq 2.0$.

Further, the study on perforated LDSS hollow beam has been extended to determine the shear behaviour of stiffened single perforated LDSS rectangular hollow beam, considering various orientations / patterns *viz.*, inclined (*IS*), vertical (*VS*), horizontal (*HS*) and ring (*RS*); and cross-sections i.e. flat, angular and semi-circular. Based on the study, it has been found that inclined stiffener (with flat cross-section) is relatively most effective in enhancing the shear capacity of perforated beams.

ACKNOWLEDGEMENT

The following acknowledgments are an account of the indebtedness I feel towards those given me the guiding light, support and source of inspiration for the completion of this thesis.

First and foremost I would like to express my sincere gratitude to my advisor ***Dr. Konjengbam Darunkumar Singh*** for taken me as a research scholar under his guidance. I am indebted to him for his understanding, wisdom, patience, enthusiasm, and encouragement and for pushing me farther than I thought I could do. He has been supportive since the day I started working on research work in the Institute. Throughout the period of my work, he has supported me not only in my research, but also academically and emotionally through the rough road of finishing this thesis. He gave me the moral support and freedom in my work and thesis writing. He was been a constant source of motivation and treated me as a friend. The extraordinary experience of working with him would be remembered in my life.

I am thankful to Prof. Arbind K. Singh, Dr. Arunasis Chakraboty and Dr. R. Ganesh Narayanan, my Doctoral Committee members, who have contributed valuable suggestions and ideas throughout the project.

I would also like to thank Civil Engineering Department, IIT Guwahati for giving me the opportunity to do my thesis. I wish to express sincere thanks to HODs in this period of my thesis for providing me all the facilities and supports for the completion.

My time in college was made enjoyable due to many friends and groups that became a part of my life. First is my research group friends, Khwairakpam Sachidananda, Longshithung Patton, Narendra Babu and Tekcham Gishan Singh. Second is my close friends, Anoop Balachandran, Jiss Joseph, Sajith S, Piyoosh, Vasudevan Matampu; who have helped me a lot when I passed through emotional situations. I am thankful to all of you for your encouragement and supports for completion of thesis.

A special thanks to my family for their love and encouragement. Words are not enough how to say thanks to my parents, brother and sister for all the sacrifices you have on my behalf and supported me.

I would express my deepest gratitude to all my well wishers.

Last not the least, I express my thanks to Almighty God for his constant guidance and blessings and giving the strength to complete this work.

Sonu J.K

CONTENTS

CHAPTER 5 - STIFFENING EFFECTS ON THE SHEAR BEHAVIOUR OF SINGLE PERFORATED LEAN DUPLEX STAINLESS STEEL (LDSS) RECTANGULAR HOLLOW BEAMS 134-189

LIST OF FIGURES

LIST OF TABLES

NOTATIONS

$\bar{a}_{w}$	slenderness parameter
$\pm_{cr}$	elastic critical buckling stress
μ_{o}	initial imperfection amplitude
£	strain
$\pm^{pl}_{true}$	true plastic stress
$£^{pl}_{true}$	true plastic strain
$\pm_{norm}$	Engineering stress
$£_{norm}$	Engineering strain
$¡_{w}$	shear buckling reduction factor of web
$¡_{f}$	shear buckling reduction factor of flange
a	slenderness
$\bar{a}_{p}$	element slenderness
$\bar{b}$	element width
¬	Poisson’s ratio
°	reduction factor
·	stress or strain ratio
¦	shear area factor
$¥_{M1}$	resistance of members to instability assessed by member checks
$¡_{u, FE}$	shear buckling reduction factor from FE

¡$_{w, mod}$	proposed shear buckling reduction factor for perforated web
¡$_{w,prop}$	proposed shear buckling reduction factor
a	shear span
AC	angular cross-sections
A_f	area of flange
b_c	depth of web on upper side from center of web
b_s	breadth of stiffener
b_t	depth of web on lower side from center of web
c	width or depth of a part of a cross-section
c	width of the tension band
c	reduction factor
d_1	tensile diagonal direction
d_2	compression diagonal direction
DL	Dead Load
d_o	diameter of perforation
D_o	outer diameter of ring stiffener
DSM	Direct Strength method
E	modulus of elasticity
$E_{0.2}$	Tangent modulus of the stress-strain curve at $\sigma_{0.2}$
FC	Flat (or rectangular) cross-sections (stiffener)
FE	Finite Element
F_m	Mean of cross-sectional property
f_{yf}	yield strength of flange
f_{yw}	yield strength of web
HAZ	Heat Affected Zone
HS	Horizontal Stiffener
h_w	height of web
$h_{w,eff}$	effective width of web above neutral axis
$h_{w,eff1}$	effective width of web near to compression flange above neutral

	axis
$h_{w,eff2}$	effective width of web near to neutral axis above neutral axis
$h_{w,non\text{-}eff}$	non-effective width of web between $h_{w,eff1}$ and $h_{w,eff2}$
IS	Inclined Stiffener
K	Ramber-Osgood constant
k_σ	plate buckling co-efficient
k_τ	shear buckling coefficient of web panel
L	length
LDSS	Lean Duplex Stainless Steel
LL	Live Load
l_s	length of stiffener
$M_{c,Rd}$	design resistance for bending about one principal axis of a cross-section
M_{Ed}	design bending moment
$M_{eff,\ Rd}$	design bending resistance of effective cross- section
$M_{f,\ Rd}$	Plastic moment resistance of flange
$M_{f,Rd}$	design plastic moment of resistance of a cross-section consisting of the flanges only
M_m	mean of ratios of mean to nominal material property
$M_{pl,\ Rd}$	design plastic moment of resistance of the cross-section (irrespective of cross-section class)
M_u	ultimate moment capacity
$M_{u,\ FE}$	moment capacity from Finite Element
n	material nonlinearity index
n and $n'_{0.2,1.0}$	stress and strain hardening exponents
$n'_{0.2,1.0}$	Strain hardening exponent
NA	Neutral axis depth
NA_B	Neutral axis depth from bottom
NA_T	Neutral axis depth from top

P_n	Post buckling coefficient
Q_m	Mean of nominal load effect
RF_m	Modified reduction factor
r_i	internal corner radius
R_m	mean of nominal resistance
RS	Ring Stiffener
SC	Semicircular Cross-section
t	thickness
t_f	flange thickness
t_s	stiffener thickness
t_w	web thickness
V	shear load
$V_{prop,\ DSM}$	shear capacity based on proposed DSM
$V_{b,\ Rd}$	ultimate shear buckling resistance
$V_{b,Rd,prop}$	ultimate shear resistance from modified shear buckling reduction factor
$V_{bf,\ Rd}$	contribution of flange in ultimate shear buckling resistance
$V_{bw,\ Rd}$	contribution of web in ultimate shear buckling resistance
$V_{bw,\ Rd,\ mod}$	modified shear capacity of perforated web
$V_{bw,\ Rd,\ solid}$	shear capacity of solid web
V_{cr}	elastic shear buckling capacity
$V_{Ed,\ Rd}$	design shear capacity
V_F	co-efficient of variation of F_m
V_{flange}	shear resistance of flange
V_M	co-efficients of variation of M_m
V_{pb}	post buckling strength
V_{RF}	shear capacity corresponding to onset of rapid-falling curve
VS	Vertical Stiffener
V_u	ultimate shear capacity

$V_{u, FE}$	shear capacity from Finite Element
$V_{u, pp^{=}}$	total shear capacity of perforated beam
$V_{u, RF^{=}}$	drop in shear from ultimate to the onset of rapid-falling curve
V_v	nominal shear capacity
V_y	shear yield capacity of web
w_f	flange width
$w_{f,eff1}$	left half of effective flange width
$w_{f,eff2}$	right half of effective flange width
x	longitudinal direction
y	transverse direction
α	constant
β	reliability index
$\delta_{RF^{=}}$	displacement corresponding to onset of rapid-falling curve
δ_u	mid-span deformation at ultimate capacity
$\delta_{u^{=}}$	mid-span deformation corresponding to ultimate shear
$\varepsilon_{t0.2}$	Total strain at $\sigma_{0.2}$
$\varepsilon_{t1.0}$	Total strain at $\sigma_{1.0}$
λ	slenderness
σ	stress
$\sigma_{0.2}$	Proof stresses corresponding to 0.2% plastic strain
$\sigma_{1.0}$	Proof stresses corresponding to 1.0% plastic strain
σ_u	ultimate tensile strength
σ_y	yield stress
¡ $_{w, mod}$	proposed web buckling reduction factor for perforated web cross-sections
¥ $_{M1}$	shear partial factor
¡ $_{w}$	web buckling reduction factor
¡ $_{w, prop^{=}}$	proposed web buckling reduction factor for unperforated web cross-sections

¥$_{MO}$ = resistance of cross-sections to excessive yielding including local buckling

¦= web contribution factor

CHAPTER 1

INTRODUCTION

1.1 BACKGROUND

For a long time, steel constructions have been akin to the structural uses of carbon steel, essentially due to its numerous advantages such as low cost, easy availability, long experience, established design rules, different strength grades etc. However, a major disadvantage of carbon steel in the construction industry is its relatively low corrosion resistance. On the other hand, stainless steel has significant appealing structural behaviour such as good corrosion resistance, higher strength to weight ratio, low maintenance cost, high ductility, impact resistance, greater durability, fire resistance, recyclability (as a result of residual alloying elements) etc. (Gardner, 2005; Kiymaz, 2005; Zhou and Young, 2005; Gardner *et. al.*, 2006; Ashraf *et. al.*, 2006a) in addition to its aesthetically pleasing good finish. Hence, in the recent past, an increase in the use of stainless steel in the construction industry can be observed, more specifically in exposed architectural applications and where total life economics, durability, improved resistance to aggressive environment etc. are prime deciding criteria. Examples of the application of stainless steel in construction are shown in Figures 1.1-1.5. Using a whole-life costing method, it has been shown that stainless steel offers a very attractive option in relation to comparable carbon steel sections (e.g. Gardner, 2005; Gardner *et. al.*, 2007; Gardner, 2008). In general, austenitic variety of stainless steel is used widely in the construction industry. However, owing to a relatively higher initial cost of austenitic stainless steel i.e. ~ 3-5 times that of the carbon steel, compounded by the need of comparatively specialist knowledge of its behaviour, the utilisation of stainless steel for construction industry remains bounded (e.g. Mann, 1993; Gardner, 2005; Ashraf *et. al.*, 2006a; Theofanous and Gardner, 2010; Saliba and Gardner, 2013a; Estrada *et. al.*, 2007a). One of the primary constituents of stainless steel that prescribes this higher cost is the nickel content (~8-10% by mass for austenitic stainless steel). However, with the advancement of stainless steel metallurgy, it has now become viable to reduce the cost, with the introduction of a new breed of stainless steel called Lean Duplex Stainless Steel, LDSS (LDX 2101 / EN 1.4162 / UNS 32101). LDSS offers significant advantages such as better economy (nickel content = ~1.5% i.e. much lower in comparison to austenitic stainless steel), improved strength, high temperature properties (Gardner *et. al.*, 2010), acceptable weldability (Nilsson *et. al.*, 2008) and fracture toughness properties etc. (e.g. Theofanous and Gardner, 2010, Saliba and Gardner, 2013a). As such, lately, a boost in the research interest on the structural behaviour of LDSS (I-, rectangular, circular sections etc.) has been seen mainly from Gardner, Young and their collaborators (e.g. Theofanous and Gardner, 2010; Saliba and Gardner, 2013; Huang and Young, 2013, 2014a). Studies on LDSS non rectangular columns (e.g. Patton and Singh, 2012), beams (e.g. Huang and Young, 2013), beam-column (e.g. Huang and Young, 2014b), perforated column (e.g. Umbarkar *et. al.*, 2013), etc. have also been reported in the literature. Examples of the application of LDSS structural members in the construction of bridges are shown in Figure 1.6-1.9. It is worthwhile to note that, LDSS has already been incorporated in EN 1993-1-4 (2006) *via* a recent amendment (A1:2015) (i.e. EN 1993-1-4 (2006/A1:2015)), and hence, it is expected to augment visibility of using LDSS structural elements by practising engineers and architects.

In the light of expanding the understanding of the structural performance of LDSS sections or members, an investigation is initiated in this thesis, on the parametric study of hollow LDSS beam (or box girder). Hollow beams have wide range of applications in the construction industry, such as in buildings, bridges, oil refineries etc. Figures 1.10-1.15 presents some application of hollow sections for civil engineering constructions. It is noteworthy to mention that hollow members have structural advantages over open sections due to their closed cross-sectional profile (e.g. improved torsional resistance), in addition to the benefit of aesthetic appearance. However, to the best of author's knowledge limited studies (e.g. Gardner *et. al.*, (2008) reported on the shear behavior of elliptical hollow steel beam) are available on the shear capacity of hollow/closed steel beams, although traditionally, open sections (e.g. I- and channel sections) are primarily used to support shear loads (e.g. Hoglund, 1997; Narayanan *et. al.*, 1989; Luo and Edlund, 1996; Herzog, 1992; Real *et. al.*, 2007; Alinia *et. al.*, 2009; Hassanein, 2011; Pham and Hancock, 2010).

Additionally, under constrained space e.g. shallow floor height or head room, it may become necessary or an option to provide perforation (or opening or cut outs) through beam webs to route building services ducts for water, air conditioning, heating, ventilations, process pipes, electrical and instrumentation cables; to accommodate secondary constructional elements like ceiling systems etc.; for inspection, repair and maintenance work; to improve the strength/weight ratio without significantly affecting the strength and serviceability considerations; and to reduce the stress transfer to beam-column joint (e.g. Hagen *et. al.*, 2009; Feng and Young, 2015; Lagaros *et. al.*, 2008). Some examples of beams with circular / rectangular perforations are shown in Figure 1.16-1.18. Sometimes (multiple or repeated patterns e.g. castellated beams, cellular beams) perforations are also provided for aesthetic reasons and economising materials (e.g. Pellegrino *et. al.*, 2009). Such perforations in the structural beams, can influence the membrane/plate stress redistribution in the webs, and can have adverse effect on the structural performance e.g. elastic stiffness, ultimate load capacity, ultimate load deformation; depending on the location, size and shapes of the perforations (Feng and Young, 2015; Ridley-Ellis, 2000).

Further, in order to enhance or compensate the reduction in the shear/load capacity, several types of stiffeners (e.g. ring, horizontal, transverse, sleeves, doubler plate stiffeners) around the perforations were employed to augment load (shear, compression etc.) capacity of webs/plates perforated with circular / rectangular holes (see e.g. Narayanan and Der Avanessian, 1984b; Pavlovcic *et. al.*, 2007; Cheng and Li, 2012; Keerthan and Mahendran, 2013; Hagen *et. al.*, 2009; Kim *et. al.*, 2015). It may be noted that such studies were mainly reported for open sections e.g. plates, I-sections etc. Figures 1.17 and 1.18 show some examples of the application of stiffeners (e.g. horizontal and vertical stiffeners) around web perforations.

1.2 OBJECTIVES

The research of Gardener and co-workers (e.g. Theophanous and Gardener, 2010; Saliba and Gardner, 2013a) on the structural behaviour of LDSS beam is extended in this thesis. More specifically, the present thesis aims at estimation of shear behaviour of LDSS hollow rectangular beams *viz.*, unperforated, perforated and stiffened perforated beams, considering finite element analyses (FE) approach. Further, the study seek to propose improve design rules/expressions, wherever applicable. The following principal objectives are then identified.

1. To investigate the effect of cross sectional parameters such as flange thickness, flange width, and shear span on the shear behaviour *viz.*, shear capacity and deformed shapes, of LDSS rectangular hollow beams using finite element (FE) analysis.

2. To assess the effect of single circular web perforation in the shear behaviour of LDSS rectangular hollow beams, considering variation in parameters such as perforation size / diameter and location (along longitudinal, transverse, and diagonals) etc.

3. To study the shear behaviour of stiffened single perforated LDSS rectangular hollow beam, considering various orientations / patterns such as vertical, horizontal, diagonal / inclined and ring; and cross-sections i.e. flat, angular and semi-circular.

1.3 THESIS OUTLINE

The content of the thesis is divided into six chapters.

Brief background of the current work is introduced in **Chapter 1**, focussing on the relatively new and promising material 'LDSS', hollow steel sections, perforations on beam webs, and stiffeners around perforations of perforated beam webs.

In **Chapter 2**, literature review pertaining to the present research work is presented. The literature review has been sub-grouped into topics such as steel beams, web opening in steel beams, opening stiffeners, LDSS structural members, and stainless steel design standard (EN 1993-1-4, 2006/A1:2015) and design method (Direct Strength Method or DSM). In addition, literature related to FE modelling of steel members is also presented.

Chapter 3 presents a finite element study on the shear behaviour of LDSS rectangular hollow beam under three point loading. Validation of the FE modelling procedures adopted in this work, along with a parametric investigation on hollow rectangular LDSS tubular beams are shown, considering variation of cross-sectional parameters like flange thickness, web thickness, flange width, and shear span.

Appropriateness of the design rules of EN 1993-1-4 (2006/A1:2015) and Direct Strength Method (DSM) are assessed, for the shear design of LDSS rectangular hollow beams, and new modified design expressions/curves are proposed.

In **Chapter 4**, the earlier FE study (see **Chapter 3**) is extended to investigate the effect of single circular perforation in the shear behavior of LDSS rectangular hollow beams. Primarily, the effect of single perforation size / diameter and locations (along longitudinal, transverse, and diagonals) are assessed with a focus on the shear capacity, deformed shapes (or failure modes) etc.

Additional FE modelling details such as geometry and mesh pattern / refinement for the stiffeners adopted in the study are also presented in **Chapter 5**. The effect of various parameters of the stiffeners e.g. cross-sectional shapes (*FC*, *AC*, and *SC*) and dimensions on the shear behaviour of single circular perforated short span LDSS rectangular hollow beam is investigated.

Chapter 6 presents the main conclusions drawn from the present study on LDSS hollow beams, and possible future work that can be extended.

At the end of the thesis supplementary appendices are included. Design sample of hollow rectangular LDSS beam is shown in **Appendix A**. In **Appendix B**, sample design calculation for perforated LDSS rectangular hollow beam is presented.

Figure 1.1: General view of Stonecutters Bridge (www.worldstainless.org)

Figure 1.2: Cala Galdana Bridge (www.worldstainless.org)

Figure 1.3: Helix Pedestrian bridge (www.e-architect.co.uk)

Figure 1. 4: Walt Disney Concert Hall (http://interactive.wttw.com)

Figure 1. 5: Cloud gate (www.aviewoncities.com)

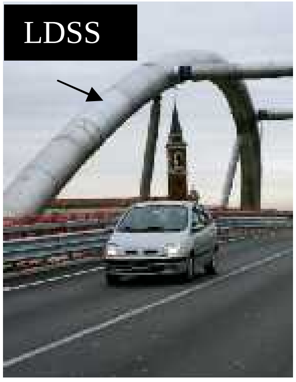

Figure 1. 6: Arco di Malizia Bridge, Siena (www.szs.ch)

Figure 1. 7: Piove di Sacco Bridge, Padua (www.szs.ch)

Figure 1. 8: Celtic Gateway Bridge, Holyhead, Wale

Figure 1. 9: Sant Fruitos Bridge, Spain

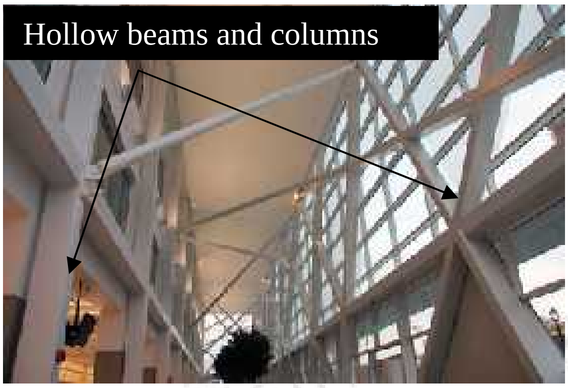

Figure 1.10: Transit Terminal in Wisconsin (www.tboake.com)

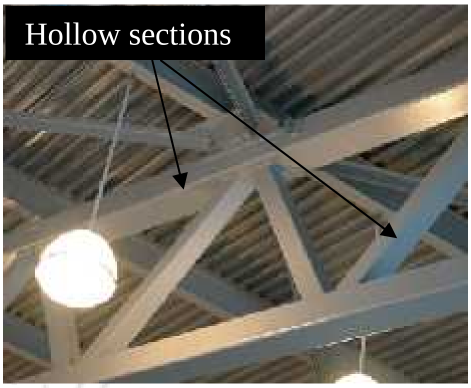

Figure 1.11: Canadian War Museum (www.tboake.com)

Figure 1.12: Illinois River bridge (courtesy. American bridge)

Figure 1.13: Hollow steel beam/steel girder (*theconstructor.org*)

Figure 1.14: Kamal's Bridge in Tualatin, (www.campbellsci.com)

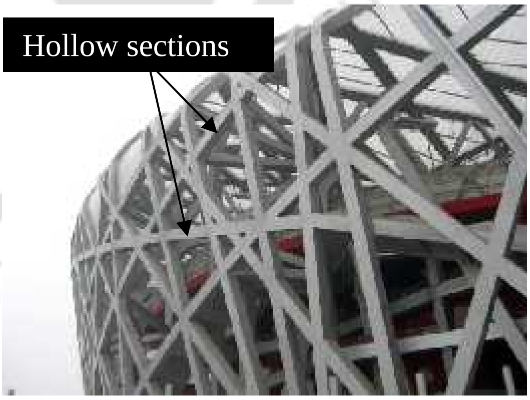

Figure 1.15: Hollow steel structure (Beijing National Stadium, China, www.archilovers.com)

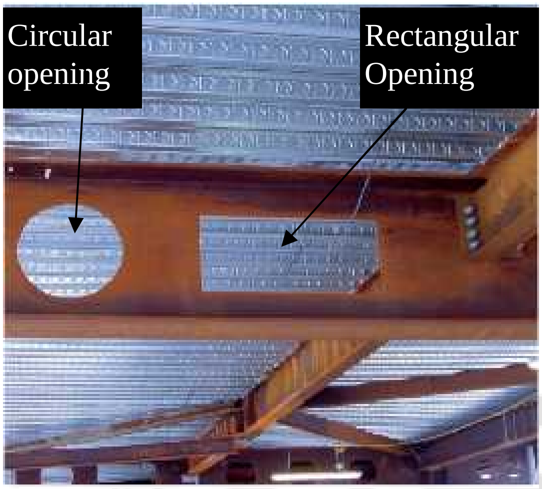

Figure 1.16: Beams with combined circular and rectangular openings (SCI 2011)

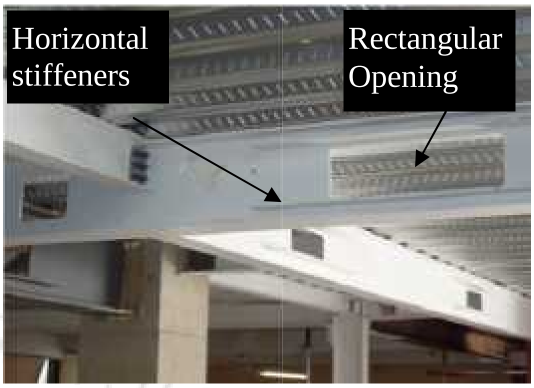

Figure 1.17: Horizontal stiffeners for rectangular opening in webs of steel girder (SCI 2011)

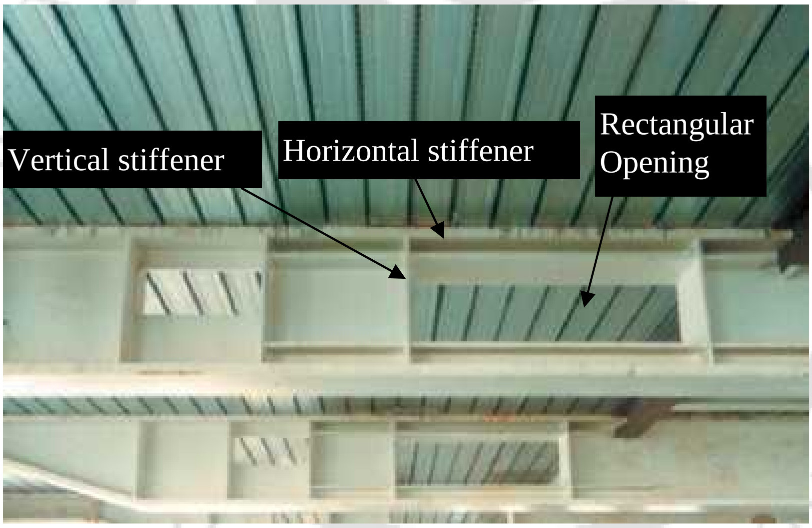

Figure 1.18: Horizontal and vertical stiffeners for rectangular opening in webs of tapered steel girder (SCI 2011)

CHAPTER 2

LITERATURE REVIEW

2.1 INTRODUCTION

A literature review on the previous research on steel beams (of both open and closed sections) with and without perforations (or cut-out or opening) under the action of shear loading is presented in this chapter. In addition, shear studies on perforated steel beams, with stiffeners around the perforation are also mentioned. This is followed by a brief summary on the investigations on Lean Duplex Stainless Steel (LDSS) members and design considerations for shear (e.g. Eurocode, Direct Strength Method, Continuous Strength Method (e.g. Afshan and Gardner, 2013; Theofanous *et. al.*, 2014; Ahmed *et. al.*, 2016). Further, a short review on the state-of-art finite element (FE) modelling of thin walled LDSS members is presented with particular focus on material modeling, geometric imperfections, FE element etc. is highlighted. At the end, a summary of the literature review is presented, underling the necessity of the present direction.

2.2 STEEL BEAMS

In the steel construction industry, uses of both open (e.g. I-, C- Lipped) and closed (e.g. square, circular, rectangular) section beams are found, although traditionally, many were of the open types (e.g. Hoglund, 1997; Lee *et. al.*, 2003; Real and Mirambell, 2005; Alinia *et. al.*, 2009; Hassanein, 2010). In the past decades, with the development and understanding of both hot rolling and cold forming processes, the market availability of closed sections has increased many-fold. These closed or hollow or tubular steel sections are particularly known to provide good torsional rigidity and generally accepted to have better aesthetic appearance in relation to the open sections. In addition, hollow sections can also serve as carriage for electrical wires, service pipes, etc. Hence, a wide spread increase in the use of hollow sections has been observed in buildings, bridges, oil refineries etc. (e.g. D'Aniello *et. al.*, 2014; D'Aniello *et. al.*, 2015; Theofanous *et. al.*, 2009; Theofanous and Gardner, 2010; Huang and Young, 2013; Zheng *et. al.*, 2016; Ma *et. al.*, 2016).

As a result, significant research efforts have been directed towards understanding of the structural behavior of hollow / tubular steel beams, in the literature. For example, numerous studies have been reported on bending behavior steel tubular members with a) circular sections (e.g. Korol, 1979; Reddy, 1979; Gellin, 1979; Rasmussen and Hancock, 1993; Al-Shawi, 2001; Chryssanthopoulos and Low, 2001; Elchalakani *et. al.*, 2002; Jiao and Zhao, 2004; Ayhan *et. al.*, 2012), b) rectangular sections (e.g. Zhao and Hancock, 1992; Pi and Trahair, 1995; Rasmussen, 2000; Mirambell and Real, 2000; Zhou and Young, 2005; Gardner and Nethercot, 2004b; Young and Lui, 2005; Zhou and Young, 2005; Gardner *et. al.*, 2006; Afshan and Gardner, 2013a; Huang and Young, 2013; Zhao *et. al.*, 2015a), c) square sections (e.g. Zhao and Hancock, 1992; Rasmussen and Hancock, 1993; Corona and Vaze, 1996; Rasmussen, 2000; Mirambell and Real, 2000; Gardner and Nethercot, 2004c; Zhou and Young, 2005; Afshan and Gardner, 2013; Huang and Young, 2013; Theofanous and Gardner, 2010) and elliptical cross-section (e.g.

Chan and Gardner, 2008). However, limited investigation(s) have been available in the literature on the shear characteristics of steel tubular members (e.g. Ridley-Ellis, 2000; Gardner *et. al.*, 2008). In the following, i.e. Section 2.3, literature review on steel beams subjected to shear loading is presented. Section 2.3 is further sub-divided into three sub-sections i.e. Sections 2.3.1-2.3.3 dealing with unperforated (or solid), perforated and perforated beams with stiffeners around the perforations, respectively. As mentioned above, since the study on shear behaviour on tubular or hollow steel members is limited, the steel beams (including open-sections) under shear loading is broadly reviewed.

2.3 STEEL BEAMS UNDER SHEAR LOADING

2.3.1 Unperforated beams

As mentioned above, most literature on shear behaviour of steel beams are associated with open sections (e.g. plate girders), e.g. Hoglund, 1997; Lee *et. al.*, 2003; Real *et. al.*, 2007; Alinia *et. al.*, 2009; Gheitasi and Alinia, 2010; Hassanein, 2010; with very limited study on closed sections (e.g. Ridley-Ellis, 2000; Gardner *et. al.*, 2008). Hence, the initial part of the literature on unperfroated beams under shear loading is presented for open sections, followed by studies on closed sections.

Lee and Yoo (1998) carried out a finite element analysis to study the shear behavior of steel plate girders by considering beam parameters such as shear span, web slenderness and flange thickness. It has been shown that shear capacity decreased with increase in web slenderness and shear span, and shear capacity was not much affected by the increase in flange thickness, however the elastic buckling strength increased with increase in flange thickness. New design expressions have been proposed to predict the shear capacity of steel girders.

Lee and Yoo (1999) performed an experimental test to assess the shear behavior of steel plate girders by considering the beam parameters such as flange thickness and shear span, following their earlier work (Lee and Yoo, 1998). It has been noticed that shear capacity increased with increase in flange thickness and shear capacity decreased with increase in shear span. Further, from the study, three types of failure modes have been identified *viz.*, a) flange failure mode (hinge formation at flange and buckling of web occur simultaneously at mid span), b) combined bending and shear failure mode (shear buckling at web and initiation of plastic hinge formation near to mid span of beam) and c) shear failure mode (formation of shear buckling at web and plastic hinge in compression flange at supports). Moreover, a change in the failure mode from flange failure to combined bending and shear failure/shear failure mode with increase in flange thickness, has been observed.

Olsson (2001) studied both experimental and numerical study in shear behavior of stainless steel plate girders by varying the beam geometries such as flange thickness and shear span. It has been found that the shear capacity is not much increased with increase in flange thickness, and shear capacity decreased with increase in shear span. It has been observed that the design curve of EN 1993-1-4 (1996) underestimates the shear capacity of stocky web cross-sections. Hence, new range of slenderness factor and shear buckling factor have been proposed for EN 1993-1-4 (1996), based on their study.

Real *et. al.*, (2007) conducted both experimental and numerical studies on shear behavior of steel plate girders. Three types of structural responses have been observed: a) failure by shear buckling occurring prior to material non-linearity, for slender sections, b) failure by non-linear material effect prior to shear buckling (geometric non-linearity), for intermediate sections and 3) failure by complete yielding of web (pure shear), for stocky sections. It has also been reported that shear capacity increased with decrease in web slenderness for the same flange thickness and decreased with increase in shear span. The shear capacity predicted using EN 1993-1-4 (1996) is conservative in comparison to experimental results.

Estrada *et. al.*, (2007a) conducted both experimental and numerical studies on shear behavior of stainless steel plate girders. Based on the study, it has been shown that shear capacity predictions using design provision for stainless steel, EN 1993-1-4 (1996), which was based on simple post critical method was highly conservative with respect to experimental results. Hence rotated stress field method was employed (following EN 1993-1-5, 1997) for the prediction of shear capacity. However, this method was also found to be conservative.

Estrada *et. al.*, (2007b) extended their earlier research (Estrada *et. al.*, 2007a) by performing a numerical investigation on shear behavior of stainless steel plate girders. Considering the results of the investigation, new design expressions have been proposed based on curve fitting using the lower bound points by bifurcating the spans into two ranges, $a/h_w \leq 1.00$ and $a/h_w > 1.00$ (where a and h_w are the shear span and web height respectively).

Estrada *et. al.* (2008) conducted both experimental and numerical studies on shear behavior of stainless steel plate girders by varying geometrical parameters such as shear span and flange thickness. It has been observed that the shear buckling co-efficient increased with increase in flange thickness up to a certain range (e.g. $t_f/t_w = 7$, where t_f and t_w are the flange and web thicknesses respectively), however, it showed no improvement (i.e. constant) for further increase of flange thickness, and shear buckling co-efficient decreased with increase in shear span. The design rules provided by EN 1993-1-4 (1996) has been found to be conservative as compared to experimental results, hence new design expressions have been proposed based on rotated stress field theory by dividing the range of shear span in to $a/h_w \leq 1.00$ and $a/h_w > 1.00$.

Alinia *et. al.*, (2009) performed a numerical study on shear behavior of steel plate girders by examining the beam parameters such as web slenderness, shear span, flange thickness and flange width. Based on the study, two failure modes have been observed: a) shear failure mode as a result of the formation of plastic hinge in compression flanges at supports (occurred in beams with thicker flanges), and b) bending failure mode caused by the formation of hinge at midspan in compression flange (occurred in beams with lower flange thickness). The predicted shear capacity using EN 1993-1-5 (2003) has been found to underestimate when compared to FE results.

Gheitasi and Alinia (2010) conducted a numerical study on shear behavior of stainless steel plates by varying plate slenderness. It has been observed that plates can be classified as slender, stocky and moderate based on different failure modes *viz.*, shear buckling and shear yielding. It has been found that a) slender plates deformed by elastic shear buckling initiated due to compressive principal stresses occurring in diagonal direction, and tension band has been found to be capable of carrying additional loads, b) stocky plates deformed due to shear yielding prior to plate buckling, and c) moderate plates deformed due to shear buckling and material yielding simultaneously.

Hassaanein and Kharoob (2010) investigated numerically the shear behavior of tubular flange steel plate girders considering parameters such as, shear span and flange depth. It has been observed that shear capacity decreased with increase shear span and increased with increase in flange depth. Further, two key failure modes have been observed: a) formation of plastic hinges at compression flange near to support indicative of shear failure mode, and b) formation of hinge in maximum moment (at midspan) showing bending failure mode. It has also been shown that the predicted shear capacity based on EN 1993-1-5 (2007) is highly conservative with the comparison to FE results. New design expressions have been proposed which showed less scattered predictions of shear capacity.

Hassanein (2010) performed a numerical study on shear behavior of austenitic stainless steel plate girders by considering the beam parameters such as flange width, web slenderness and flange thickness. It has been shown that shear capacity increased with increase in flange width and flange thickness, decreased with increase in web slenderness. Plastic hinges have been found to form in compression flange at supports along with tension band in web, indicating shear failure mode. Comparison of numerical results with shear capacity calculated based on EN 1993-1-4 (2006) suggest that EN 1993-1-4 (2006) has been found to be more conservative. Hence, a new design expression to compute shear capacity has been put forward.

Hassanein (2011) conducted a numerical study on shear behavior of LDSS steel plate girders considering variation in flange thickness and flange width. It has been observed that beams with higher flange thickness failed by shear (formation of hinge on flanges at support), while beams with lower flange thickness failed by bending (formation of hinge at midspan). Moreover, it has also been shown that shear capacity, deformation capacity and ductility increased with increase in flange thickness and flange width. It has been shown that the predicted shear capacity using EN 1993-1-4 (2006) is lesser conservative than EN 1993-1-5 (2007) when compared to FE results. Further, based on the FE results, new design expressions have been proposed.

Safar (2013) investigated shear behavior of steel plate girders by considering the geometric parameters included web slenderness, shear span and flange thickness. It has been shown that shear capacity decreased with increase in web slenderness and shear span, increased with increase in flange thickness. Further, it has been shown that shear capacity predictions based on AISC (2005) is observed to be highly conservative in comparison to FE results; thus new shear capacity expressions have been proposed.

Saliba and Gardner (2013a) conducted both experimental and numerical studies on shear behavior of LDSS steel plate girders by examining web slenderness, flange thickness and shear span. It has been found that shear capacity increased with decrease in web slenderness and increase in flange thickness; and shear capacity decreased with increase in shear span. Based on the study, three failures modes have been observed: a) shear, b) bending, and c) combined shear and bending modes. These failure modes observations have been found to co-relate well with those suggested by shear-moment interaction diagram (EN 1993-1-4 (2006). It has also been found that predictions made by EN 1993-1-4 (2006) is applicable for LDSS members.

Saliba *et. al.*, (2014) compared the experimental data from Saliba and Gardner (2013a), Estrada *et. al.*, (2007a), Real *et. al.*, (2007) and Olsson (2001) with those predicted by EN 1993-1-4 (2006) and EN 1993-1-5 (2006); and found that predictions made by EN 1993-1-4 (2006) is conservative as compared to EN 1993-1-5 (2006). Hence, new design expressions have been proposed to predict the shear capacity. These designs curves are now incorporated in the latest amendment to EN 1993-1-4 (2006) i.e. EN 1993-1-4, 2006/A1:2015.

Kwon and Ryu (2016) performed experimental and numerical studies on shear behavior of steel plate girders. Based on the study, new DSM expressions have been proposed to predict the shear capacity. It has been found that the new DSM expressions resulted in improving the reliability of shear capacity predictions as compared to those of EN 1993-1-5 (2006).

Gardner *et. al.*, (2008) conducted both experimental and numerical studies on elliptical hollow sections (i.e. closed section) subjected to three point bending load by varying section slenderness and shear span. It has been shown that shear capacity decreased with increase in section slenderness and shear span. It has been observed that the slenderness limit of hollow cylinders taken from EN 1993-1-6 (2007) is conservative and can be safely applied to elliptical hollow sections.

2.3.2 Perforated beams

Perforations can be provided as an option in beams when the floor head room is restricted and it becomes necessary to accommodate services like pipe line for water, electricity, air conditioning, access for inspection and maintenance. Sometimes perforations are also provided in beams for aesthetic reasons and optimizing strength/weight ratio (Hoglund, 1971; Shanmugam, 1997). Applications of such perforated beams (especially the webs) can be found at large span industrial structures, oil refineries, offshore structures, highway bridges etc. (e.g. Sharkley and Brown, 1996; Shanmugam *et. al.*, 2002; Liu and Chung, 2003). Past studies indicate that providing perforations can significantly (depending the perforation size, shape and location) reduce the original unperforated capacity (e.g. Uenoya and Redwood, 1977; Maiorana *et. al.*, 2009). Brief literature review of perforated plates, open and closed section steel beams under shear loading are presented in the following paragraphs.

Hoglund (1971) conducted an experimental study to determine the shear behavior of circular perforated steel plate girders by varying opening size and web slenderness. It has been reported that shear capacity decreased with increase in opening size and web slenderness. The variation of shear capacity of the perforated beam was found to be directly proportional to percentage of opening size with respect to the web height.

Narayanan and Rockey (1981) conducted an experimental study to assess shear behavior of steel plate girders with centrally located circular web perforations by varying opening size and flange thickness. It has been reported that shear capacity decreased with increase in opening size and increased with increase in flange thickness.

Narayanan and Der-Avanessian (1984a) conducted an experimental study in shear behavior of steel plate girders with circular web perforations by considering different opening sizes and opening location at corner of compression diagonal. It has been shown that shear capacity decreased with increase in opening size. In addition, it has also been observed that the reduction in shear capacity is lesser for opening location at compression diagonal compared to opening at center of the web.

Narayanan and Der-Avanessian (1984b) performed an analytical study to investigate shear behavior of central circular perforations in steel plates by varying the opening size, variation of location of opening along tension and compression diagonals. It has been shown that critical shear stress coefficient decreased with increase in opening size, increased for opening location moving along compression diagonal from the center of plate towards corner, and decreased for opening location along tension band away from the center of plate.

Roberts and Azizian (1984) carried out an analytical study on shear behavior of plates with circular perforations located at center of plate. It has been observed that shear buckling load decreased with increase in opening size and decreased with increase in web slenderness.

Ridley-Ellis (2000) conducted experimental and numerical studies to estimate shear behavior of perforated rectangular hollow beams by varying the dimension of circular web perforation. It has been shown that shear capacity and ductility decreased with increase in the size of web opening. Further, design expressions have been put forward to compute the shear capacity of perforated beams.

Shanmugam *et. al.,* (2002) performed a numerical study on analyze the shear behavior of steel plate girders with centrally located circular perforation by varying the flange and web thicknesses. It has been observed that shear capacity is slightly decreased with increase in web slenderness, however the increase in flange thickness is found to have little influence.

Paik (2007) conducted a numerical study in shear strength of circular perforated steel plates by varying the perforation size, plate slenderness and aspect ratio of plate. It has been observed that shear strength decreased with increase in opening size, decreased with increase in aspect ratio of plate and shear strength is not much affected by the increase in web slenderness.

Pellegrino *et. al.* (2009) conducted a numerical study on shear strength of circular perforated plates, considering variation in opening sizes and opening locations, and plate slenderness. It has been shown that shear buckling coefficient decreased with increase in opening size and it is not much affected by the change in opening locations. Also, it has been reported that critical shear stress decreased with increase in plate slenderness.

Hagen *et. al.*, (2009) conducted a numerical study on shear behavior of perforated cantilever steel plate girders by varying perforation sizes and web slenderness. It has been observed that shear capacity decreased with increase in opening size and increase in web slenderness for particular opening size. Design procedures based on EC 1993-1-5 (2006) have been proposed to estimate shear capacity of perforated steel plate girders by approximating the reduction in capacity to be directly proportional to percentage of opening size with respect to web height.

Hassanein (2014) performed a numerical study on the effects of square perforations in steel plate girders by varying perforation sizes, web thickness and flange thickness. It has been found that shear capacity decreased with increase in opening size and web slenderness, and increased with increase in flange thickness. Further, the failure mode of the perforated beam has been reported to be consisting of shear buckling deformation in the web along with the formation of plastic hinge near the supports at compression flange. Based on the numerical study, design expressions have been proposed to determine the shear capacity of perforated sections.

El-Khoriby *et. al.*, (2016) conducted a numerical study on shear behavior of hollow flange steel plate girders with square perforation on the web, by considering varied perforation size, location of perforation (along tension and compression diagonal) and web slenderness. It has been shown that shear capacity decreased with increase in opening size. Further, it has also been seen that reduction in shear capacity is lesser for opening located at corners of compression band compared to opening located along tension diagonal band; and shear capacity decreased with increase in web slenderness.

2.3.3 Stiffened perforated beams

As mentioned in the previous section i.e. Section 2.3.2, from the literature review (e.g. Narayanan and Der-Avanessian, 1984b; Ridley-Ellis, 2000; Hagen *et. al.*, 2009), it has been seen that, perforation (e.g. in the webs) can cause reduction in the shear capacity of steel beams or plates. The amount of reduction in the shear capacity is seen to depend on various parameters such as perforation size, shape, location etc. In the literature, in order to enhance the shear capacity or compensate the reduction in shear capacity due to such perforations, studies on using various stiffeners (e.g. horizontal, vertical, inclined stiffeners etc.; see Figures 1.17-1.18) around the perforations, have been reported. Literature on stiffened perforated beams / plates under the action of shear loading are shown in the following paragraphs.

Narayanan and Der-Avanessian (1984b) conducted an analytical study on the effect of ring stiffeners for circular openings in steel plate subjected to shear loading, by varying stiffener thickness and width. It has been shown that critical shear stress coefficient increased with increase in stiffener thickness; and flattened after a certain limit with further increase of stiffener thickness. It is also observed that critical shear stress coefficient increased with increase in stiffener width.

Hagen *et. al.*, (2009) conducted a numerical study on shear behaviour of circular perforated cantilever steel plate girders stiffened with ring stiffener. It has been observed that ring stiffened perforated beams were able to attain the shear capacity of unperforated beams for smaller openings; for the larger perforations, the shear capacity improved considerably.

Cheng and Li (2012) performed a numerical study on the shear behavior of perforated steel plates, stiffened (the perforation) with various types of stiffeners such as ring and straight stiffeners. Effects of variation in the orientation of straight stiffeners e.g. horizontal , vertical, inclined have also been reported. It is shown that buckling behavior of stiffened plate is similar to perforated plate. It has been found that elastic buckling stress is effectively increased by inclined stiffeners located along compression diagonal, whereas inclined stiffener located along compression diagonal and ring stiffener are seen to be effective stiffeners to increase the elasto-plastic ultimate strength.

Hamoodi and Gabar (2013) carried out both experimental and numerical studies on shear behavior of ring stiffened circular perforated steel plate girders by considering thickness and width of stiffener as parameters. It has been shown that shear capacity increased with increase in thickness and width. However, the increased shear capacity (with increase in cross sectional area of the stiffener) has been found to be lower than that of the unperforated steel plate girders.

Keerthan and Mahendran (2013) conducted both experimental and numerical studies on shear behavior of perforated LiteSteel beams stiffened with transverse and sleeve stiffeners. It has been shown that shear capacity is not significantly changed from unstiffened perforated beam by increasing the thickness of transverse and sleeve stiffeners.

2.4. DESIGN CONSIDERATIONS OF STAINLESS STEEL BEAMS UNDER SHEAR LOADING

Shear design of stainless steel beams can be realized through various national design codal provisions such as EN 1993-1-4 (2006), SEI/ASCE-8 (2002), AS/NZS 4673 (2001) etc. In addition, the design methods such as Direct Strength Method (e.g. Schafer, 2008) and Continuous Strength Method (e.g. Gardener and Nethercot, 2004a; Saliba, 2012) have also been demonstrated in the literature. Further, as most studies on shear behaviour of plated structures are generally assessed with respect to European design standards (i.e. EN 1993-1-4, 2006), the review is presented herein is related only to EN 1993-1-4.

a) Shear design via EN 1993 Part 1-4

EN 1993 Part 1-4 (1996) was the first European code dealing with design procedures for stainless steel structures. The design approach used for the calculation of shear strength of stainless steel beam was Simple Post-Critical method developed by Dubas (1980), based on Hoglund's (1971, 1973) Rotated Stress Field theory. The tests results available at that time of formulation were from the work of Carvalho *et. al.* (1990). However, the predicted ultimate shear capacity using Simple Post-Critical method was found to be extremely conservative. The reason is attributed to the fact that post critical method based on Rotated stress field theory did not consider the contribution of flanges in shear resistance of cross-section. Olsson (2001) conducted experiments in stainless steel plate girders and proposed new design expressions based on Hoglund's Rotated stress field theory, which took the contribution of flange and web in total shear capacity, but avoided the type of end posts, i.e. rigid and non-rigid posts. The shear capacity prediction using this method was observed to be more accurate than Simple Post-Critical method in EN 1993-1-4 (1996). This method was adopted in the version, EN 1993-1-4 (2006), which is harmonized to EN 1993-1-5 (2006) with modifications in the design expressions (Estrada *et. al.*, 2007a; Saliba *et. al.*, 2014).

As mentioned previously, on comparison of the experimental results (see Saliba and Gardner, 2013a; Estrada *et. al.*, 2007a; Real *et. al.*, 2007; Olsson, 2001) with those predicted by EN 1993-1-4 (2006) and EN 1993-1-5 (2006), it has been observed that both the codal predictions are found to be much conservative. Thus, further improvement in the design expressions have been proposed by Saliba *et. al.*, (2014). The new design expressions form the basis of the recent amendment to EN 1993-1-4 (2006) i.e. EN 1993-1-4 (2006/A1:2015), for stainless steel. The key difference in the new amendment (EN 1993-1-4, 2006/A1:2015) for the shear capacity curve, is the splitting of slenderness factor ($\bar{\lambda}_w$) regimes into three regions ($\bar{\lambda}_w \le \frac{0.65}{\eta}$, $\frac{0.65}{\eta} < \bar{\lambda}_w \le 0.65$, $\bar{\lambda}_w \ge 0.65$), where η is the shear area factor, instead of the usual two regimes as depicted in EN 1993-1-4 (2006). The rationale behind the increased number of divisions to primarily to smoothen up the design curve in intermediate range ($\frac{0.65}{\eta} < \bar{\lambda}_w \le 0.65$), where the design curve is inconsistent for $\bar{\lambda}_w > 0.50$ in EN 1993-1-4 (2006) (Saliba *et. al.*, 2014).

b) Direct Strength Method (DSM)

Direct strength method was put forward by Schafer and Pekoz (1998) and can be related to the work of Hancock *et. al* (1994), with several improvements being made by Schafer (2005, 2008). DSM has been extended to the studies of cold formed steel column (Landesmann and Camotim, 2013), open sections (Camotim *et. al.*, 2008) and build-up sections (Georgieva *et. al.*, 2012). This method is incorporated in the annexes of design codes of cold formed steel members by NAS in AISI-S100-07 (2007) and Australian/New Zealand Cold formed steel structures standard AS/NZS 4600 (2005) specifications. The expression of this method is an explicit function of gross cross-sectional properties, elastic critical buckling stresses for all relevant stability modes and yield strength (Theofanous and Gardner, 2011). The advantages of DSM are its simplicity of design rules (no effective width is required), no interactions are required, gross cross-sectional areas are used for calculation of load capacity, incorporated the buckling behavior of whole cross-section, effectively taking account of complex cross-sectional shapes, provide ultimate strength based on yield stress (Kwon, 2014). However, DSM shows uneconomical for stocky sections due to conservative nature. Earlier, the application of DSM was to find the nominal axial strength of columns and flexural strengths of beams. DSM is also employed in stainless steel members subjected to compression (Becque *et. al.* 2008) and aluminum flexural members (Zhu and Young, 2009). This method has been extended to study the shear characteristics of LiteSteel beams (Keerthan and Mahendran, 2011), longitudinally stiffened web channels (Pham and Hancock, 2015) and longitudinally web stiffeners (Pham *et. al.*, 2014). Recently, DSM has been employed to investigate steel plate girders subjected to shear loading (Kwon and Ryu, 2016).

c) Continuous Strength Method (CSM)

Continuous Strength method (CSM) is a newly introduced approach to calculate the sectional capacity, employing a continuous measure between cross-section slenderness and deformation capacity (Su *et. al.*, 2012). This method is proposed by Gardner and Nethercot (2004a). CSM has been found to be suitable for cold formed hollow as well as open cross-section beams and columns (Bock *et. al.*, 2015a; Liew and Gardner, 2015), stainless steel continuous beams (Theofanous *et. al.*, 2014), aluminium columns (Ashraf and Young, 2011) and shear behavior of LDSS welded sections (Saliba, 2012). Saliba (2012) proposed a CSM method for the shear design of LDSS steel plate girders, by harmonizing the new CSM expressions to the original CSM for steel members under compression and bending. The proposed CSM expression has been found to provide good predictions of shear capacity for stocky sections. Further, it has been mentioned that the proposed CSM method is still under the process for improvement.

2.5 LEAN DUPLEX STAINLESS STEEL (LDSS) MEMBERS

Due to several impressive advantages of Lean Duplex Stainless Steel (LDSS) as mentioned in Section 1.1 (in Chapter 1), in the recent past, several publications related to LDSS members have been reported, e.g. non rectangular columns (e.g. Patton and Singh, 2012), beams (e.g. Huang and Young, 2013), beam-column (e.g. Huang and Young, 2014b), perforated column (e.g. Umbarkar *et al.*, 2013) etc. However, it may be mentioned that studies on LDSS beams are limited. Bending behaviour of LDSS square (Theofanous and Gardner, 2010), rectangular (Huang and Young, 2013) beams and steel girders (Hassanein and Silvestre, 2013; Saliba and Gardner, 2013b) beams have been reported. Shear performance of LDSS I-beams have been studied by Hassanein (2011) and Saliba and Gardner (2013a). The effect of perforation on LDSS C-section beams has been investigated by Lawson *et. al.*, (2015).

2.6 FINITE ELEMENT MODELLING OF THIN-WALLED LDSS MEMBERS

Numerical techniques such as Finite Element Analysis (FE Analysis) has been employed as a standard analysis tool to understand various non-linear behaviour of structural elements or members, and it is widely used by researchers and engineers to model metallic thin walled structures (e.g. Hassanein, 2011, Alinia *et. al.*, 2011, Saliba and Gardner, 2013b). When properly validated or calibrated against experimental results, FE analysis can be used to generate reliable large number of results, thereby facilitating parametric study that encompasses a wide range of variables (which may be difficult to be covered experimentally). Thus, FE analysis can serve as a relatively cheaper and efficient solution technique. Further, properly calibrated FE models may be used to extract indebt understanding of the variation of key parameters like stresses, strains etc. influencing structural behaviour such as failure mechanism (Ashraf *et. al.*, 2006b, Ellobody *et. al.*, 2014). Accuracy and reliability of FE modelling of thin-walled LDSS structures, can be influenced by several factors such as material modeling, element types, meshing, boundary conditions, loading, imperfection types, residual stress etc., and are presented briefly in the following sections.

2.6.1 LDSS Material modeling

An accurate representation of non-linear material model plays a vital role in the analysis of steel structures. In this attempt several models have been proposed for different types of steels, as early as 1930s (e.g. Holmquist and Nadai, 1939; Ramberg-Osgood, 1943; Hill, 1944). Since then, a number of researchers (e.g.

Mirambell and Real, 2000; Rassmussen, 2003; Gardner and Ashraf, 2006) have proposed various material models for stainless steels, essentially with Ramberg-Osgood (RO) model as the basis. Stainless steel exhibits non-linear stress-strain behaviour and is characterized by low proportionality stress, without well defined yield stress and extensive-strain hardening. Holimquist and Nadai (1939) developed a polynomial equation for material behavior beyond proportional limit for stainless steel, iron and brass metal tubes. Ramberg-Osgood (1943) proposed a model (R-O model) for aluminum alloys, later on it was found out that R-O model is suitable for stainless steel and other metals (Equation 2.1).

$$\varepsilon = \frac{\sigma}{E_o} + K\left(\frac{\sigma}{\sigma_{0.2}}\right)^n \tag{2.1}$$

where, ε, σ, $\sigma_{0.2}$, and E_o, are strain, stress, proof stress (corresponding to 0.2% plastic strain), initial Young's modulus of elasticity respectively. K and n are material non-linear constants / indices to be determined from experiments. RO model is found to provide good predictions up to $\sigma_{0.2}$, but showed to overestimate beyond $\sigma_{0.2}$. Hence, in order to model the stress beyond $\sigma_{0.2}$, an expression has been proposed considering ultimate stress (σ_u) and strain (ε_u) (Mirambell and Real, 2000; Rasmussen, 2003) for the complete stress-strain curve for stainless steel alloys (see Equation 2.2).

$$\varepsilon = \frac{(\sigma - \sigma_{0.2})}{E_{0.2}} + \varepsilon_u \times \left(\frac{\sigma - \sigma_{0.2}}{\sigma_u - \sigma_{0.2}}\right)^m + \varepsilon_{t0.2} \tag{2.2}$$

where, $E_{0.2}$ and m are the tangent stiffness at $\sigma_{0.2}$, and strain hardening exponent respectively. $E_{0.2}$ and m are given in Equations 2.3 and 2.4.

$$E_{0.2} = \frac{\sigma_{0.2} E_s}{\sigma_{0.2} + 0.002 n E_s} \tag{2.3}$$

$$m = 1 + 3.5\frac{\sigma_{0.2}}{\sigma_u} \tag{2.4}$$

The ultimate tensile stress (σ_u) and ultimate strain (ε_u) are expressed in term of $\sigma_{0.2}$, E_0 and n (see Equations 2.5 and 2.6),

$$\frac{\pm_{0.2}}{\pm_{u}} = \frac{0.2+185\left(\frac{\pm_{0.2}}{E_s}\right)}{1-0.0375(n-5)} \qquad (2.5)$$

$$£_{u} = 1-\frac{\pm_{0.2}}{\pm_{u}} \qquad (2.6)$$

It may be noted that the guideline material model for stainless steel in EN 1993-1-4 (2006/A1:2015) follows from the work of Rasmussen (2003).

Gardner and Nethercot (2001) observed that as necking is absent during compression (unlike in tension specimen), the expression of Equation 2.2 may not be applicable for compression stress-strain models, due to the involvement of ultimate stress and ultimate strain terms. Thus, it has been put forward by Gardner (2002) that instead of ultimate values of stress and strain, 1% proof stress, $\sigma_{1.0}$ and corresponding strain, $\varepsilon_{t1.0}$ be considered. Based on this proposal, Gardner and Ashraf (2006) suggested a new model for stresses greater than $\sigma_{0.2}$ as shown in Equation 2.7.

$$£ = \left(\frac{\pm-\pm_{0.2}}{E_{0.2}}\right)+\left(£_{t1.0}-£_{t0.2}-\frac{\pm_{1.0}-\pm_{0.2}}{E_{0.2}}\right)\times\left(\frac{\pm-\pm_{0.2}}{\pm_{1.0}-\pm_{0.2}}\right)^{n'_{0.2,1.0}}+£_{t0.2} \qquad (2.7)$$

where $\varepsilon_{t1.0}$, $\varepsilon_{0.2}$ and $n'_{0.2,0.1}$ are the total strains at $\sigma_{1.0}$ and $\sigma_{0.2}$ and strain hardening index respectively. It has been reported that material model given by Equation 2.7 provides reasonably accurate predictions of stress-strain curve for both compression and tension testing (Ashraf *et al.*, 2006b). Gardner and Ashraf (2006) model is widely used for modelling stainless steel members, including that of LDSS, and is reported to provide reasonably accurate agreement with those of experiments.

2.6.2 Element type

In the literature, shell FE elements are generally used for modelling thin walled metallic structures, where the thickness is relatively smaller than other dimensions and variation of stress is negligible in the thickness direction. In many of the studies available in the literature for modelling thin walled steel members, a general purpose FE element named S4R, available in Abaqus (2009) is generally employed (e.g. Theofanous and Gardner, 2010; Zhou and Long, 2016; Theofanous *et. al.*, 2009; Ruiz-Teran and Gardner, 2008). S4R elements are general purpose four noded reduced integration elements have six degrees of freedom per node, i.e., three rotations and three translations. It has been shown by Theofanous & Gardner (2009), Huang & Young (2014a), Hassanein (2010), and Saliba & Gardner (2013b) etc. that FE models with S4R elements can accurately predict the experimental results for compression, bending and shear tests. In most studies (e.g. Ellobody, *et. al.*, 2014; Patton and Singh, 2012) an element aspect ratio of 1 is suggested. Eigen value analysis is generally adopted to arrive at an optimum mesh size or density (e.g. Theofanous *et. al.*, 2009; Huang and Young, 2013; Zhao *et. al.*, 2015a; 2015b; Saliba and Gardner, 2013a). Similar procedure has been followed for refining mesh around perforation by Ridley-Ellis (2000), Hagen (2005), Pellegrino *et. al.*, (2009).

2.6.3 Initial imperfections

Geometric imperfections (local and/or flexural) are undulations of actual members and can occur during manufacturing, transportation, handling of material and fabrication of specimens etc. Presence of imperfections can significantly influence load carrying capacity, deformed shapes and post ultimate behaviour. Two types of initial imperfections can occur *viz.*, local and global imperfections. Local imperfections are the deformation formed perpendicular to the surface and can be found in inner and outer surface of plates. Global imperfections on the other hand, deformation occur globally due to whole member deformation along the length of member in any direction (e.g. bowing, warping and twisting). In FE modelling, initial imperfections are generally seeded based on the lowest eigen mode (which is considered as critical mode) from elastic eigen value buckling analysis. This approach has been employed for steel members subjected to compression (Ellobody & Young, 2005; Patton and Singh, 2012), bending (Theofanous and Gardner, 2010) or shear (Saliba and Gardner, 2013a; Hassainen, 2011). The imperfection amplitude for metallic structure can be obtained from direct experimental measurements of specimens or *via* models suggested by Dawson and Walker (1972) or its modifications (Gardner, 2002; Gardner and Nethercot, 2004b; Cruise and Gardner, 2006; Bock *et. al.*, 2015; Ashraf *et. al.*, 2006a). Dawson and Walker (1972) model is given below:

$$\mu_o / t = 0.023\left(\frac{\pm_{0.2}}{\pm_{cr}}\right) \tag{2.8}$$

where σ_{cr} is the elastic critical buckling stress determined from the buckling analysis and t is the thickness. This empirical has been arrived at based on experimental measurements. In other studies (especially for open sections), simpler relation for imperfection magnitude such as L/1000 (Hassanein and Kharoob, 2012), h_w/100, h_w/500 & h_w/100000 (Hassanein, 2011) and L/1000 (Hassanein and Kharoob, 2010) have been used, where, h_w and L are the web height and length of the member respectively. Dawson and Walker's model (Equation 2.8) has been employed in the investigations of both open (Saliba and Gardner, 2013a, 2013b) and hollow / closed (Theofanous and Gardner, 2009, 2010) LDSS members.

2.6.4 Residual Stress

Residual stresses are induced in structural member before loading due to deformation by cold forming and temperature differences as a result of welding and cutting. Internal stresses and bending moment (that are in equilibrium in the specimen itself) can result from residual stress formation. The effect of residual stress is reported to have less significant influence in structural behavior in the studies of welded LDSS steel girders under bending (Saliba and Gardner, 2013a; Hassanein and Silvestre, 2013; Hassanein and Kharoob, 2010; Huang and Young, 2012) and shear loading (Saliba and Gardner, 2013a, 2013b) and hence, are generally neglected in FE studies (e.g. Saliba and Gardner, 2013a; Huang and Young, 2012, 2014 etc.).

2.7 SUMMARY

A review on the literature related to the effect of shear loading on steel beams with or without perforations or cutouts under shear loading is presented in this chapter. Literature on stiffener effects on perforated steel webs / plates is also presented. Previous work on LDSS members is shown briefly. Design considerations for shear (e.g. Eurocode, Direct Strength Method, Continuous Strength Method) are mentioned. Pertinent details for FE modelling of thin-walled steel members are described. From the literature review the following conclusions can be drawn:

1) Shear behaviour of steel beams have been widely studied experimentally as well as numerically, considering various parameters like shear span, web slenderness, flange thickness etc. It is found that very limited studies have been reported to assess the shear behavior of closed section beams. Further, most of the reported studies in shear behaviour focused on carbon steel beams.

2) Several literature have been published on the effect of perforation on the shear characteristics of steel beams, mostly on open sections like plate girders, plates etc., although such studies on hollow section beam has been very limited. Key parameters included in the study are found to be opening types, size, locations etc.

3) Investigations on the effects of stiffeners on shear capacity of perforated steel I beams, plate girders and plates have been reported, using various stiffeners e.g. horizontal, vertical, inclined stiffeners etc. Again, such studies have not been reported for closed steel sections.

4) Various studies on shear capacity of steel beams have been compared with international codes such as EN 1993 Part 1-4. Recent amendment to EN 1993 Part 1-4 (i.e. 2006/A1:2015) has included the shear design of LDSS stainless steel members. Further, attempts to use design methods such as Direct Strength Method (DSM) and Continuous Strength Method (CSM) for the shear design of beams have also been reported, although apparently only a single study has been available for the CSM.

5) Due to several impressive advantages of Lean Duplex Stainless Steel (LDSS), there is a growing interest on LDSS sections for compression, bending and shear. However, so far no report has been found on the shear study of hollow LDSS beam.

6) Details of relevant FE modelling techniques for modelling thin-walled steel members have been discussed with particular focus on the material modelling aspects of LDSS. The FE modelling procedures presented are known to provide accurate predictions of experimental results.

CHAPTER 3

SHEAR BEHAVIOR OF LEAN DUPLEX STAINLESS STEEL (LDSS) RECTANGULAR HOLLOW BEAMS

3.1 INTRODUCTION

With the enhanced development of numerical procedures such as finite element (FE) method it has now become increasingly cost- and time-effective to use FE to analyse the structural performance of metal structures, when convincingly validated (with the use of suitable inputs such as material constitutive models, element types, solution algorithm, boundary conditions etc.) against reliable experimental results. Experimental investigations can be affected by several factors such as loading frame capacity, loading actuator specifications, trained technical staff, data acquisition and measuring instruments, costs, time etc., and hence it becomes unrealistic and impossible to generate substantial wide band of test data, covering entire spectrum of possible material as well as member shape and size variations. Hence, in the literature, a large amount of FE studies have been attempted to bridge the research gaps, expand the data domain, and fill-in the data shortage (e.g. Ellobody *et al.*, 2014). Further, a key advantage of FE modelling is its inherent capability to extract desired stresses, strains, deformations at any location, which otherwise would be difficult to obtained through traditional instrumentation. In this regard, it may be worthwhile to mention that only a very limited experimental investigations have been reported in the literature about the structural behaviour of LDSS members, mostly from the research works of Gardner and co-workers (Saliba and Gardner, 2013a; Theofanous and Gardner, 2010, etc.); and Young and co-workers (Huang and Young, 2013a; Islam and Young, 2014, etc.). Hence, in this chapter, an attempt has been made to study the structural response (deformed shapes and ultimate shear capacity (V_u)) of hollow rectangular (LDSS) tubular beam under three point loading, *via* FE modelling. The FE modelling has been realised through the use of widely used and accepted commercial FE software ABAQUS, after having the modelling approach validated against nearly comparable published experimental data. The present study is then expected to generate more data on the shear characteristic of LDSS rectangular hollow beam, which is expected to be useful for both research community and design engineers. Various parameters considered for the analysis such as flange thickness, flange width, web thickness and shear spans. The observed results have been compared with available stainless steel design code, European specification (EN 1993-1-4, 2006/A1:2015) Direct Strength Method (DSM), to assess their applicability to rectangular LDSS tubular beam.

3.2 FINITE ELEMENT MODELLING

3.2.1 General

FE modelling approach followed in this paper is similar to those widely published in the literature (e.g. Theofanous and Gardner, 2009; Patton and Singh, 2012; Hassanein and Silvestre 2013; Huang and Young, 2013), and known to provide reasonably accurate results. Essentially well proven shell FE elements were used to model the plate elements of the rectangular hollow sections, using the commercial FE software, Abaqus (2009). Before proceeding with the parametric study, the FE modelling approach is validated by comparing with a representative experimental data on LDSS hollow beam from Theofanous and Gardner (2010). The key steps involved in the FE modelling are briefly explained in the subsequent sub-sections.

3.2.2 Geometry and boundary conditions

The cross-sectional geometry of the beam is rectangular in shape as shown in Figure 3. 1 (a) where h_w, t_w, w_f, t_f and a are height of web, web thickness, flange width, flange thickness and shear span respectively. Note that h_w and w_f are the internal and outer dimensions respectively of the beam. The in-plane deformation of the beam is constrained at both ends and mid-span *via* kinematic coupling (Theofanous *et. al.*, 2009; Theofanous and Gardner, 2010) available in Abaqus. Loading and support conditions are applied through the three reference points (RP1, RP2 and RP3) which are coupled to the cross-sectional nodes, at mid-span and ends respectively as shown in Figure 3.1(b). Displacement is applied through RP2 to transfer uniformly to the flanges and webs of the coupled cross-section. Constraining kinematically of the nodes at the mid-span section (i.e. at the section where the external displacement is applied) and end supports have been artificially done to avoid local buckling due to the externally applied displacement and support reactions, and thus ensuring rigid post conditions, both at the mid-span and end supports. In order to get constant shear along the span of the beam (shear span is half the beam length, i.e. a = L/2), beam is simply supported at both the ends (one end is hinge and other is roller supported), and using displacement control, point displacement is applied statically at the mid-span of the beam as shown in Figure 3.1 (c).

3.2.3 Finite element mesh

The reduced integration four noded general purpose curved shell element (S4R) with six degrees of freedom per node (three displacements and three rotational degrees of freedoms per node) as recommended by various researchers for similar type studies conducted in thin walled structures (Saliba and Gardner, 2013a; Alinia *et al.*, 2009; Patton and Singh 2012) are adopted in this study to discretize the models, as shown in Figure 3.1(b). Aspect ratios of element are kept at ~1.0 for the entire FE specimens. Based on mesh convergence study (through linear elastic eigen-value buckling analyses), typical global mesh size of ~18–25 mm has been arrived at for optimum acceptable result (see e.g. Figure 3.1(b)).

3.2.4 Local geometric imperfection

Geometrical imperfections arising during fabrication, production, transportation etc. are the undulations on geometry compared to perfect ones; it exists in actual structures and affects the structural performance. Mostly two types of imperfections are present in structures; they are local and global geometric imperfections. In the present study, only local imperfections are incorporated in the analysis by considering the lowest eigen mode from linear elastic eigen-value buckling analysis (e.g. Theofanous and Gardner, 2010; Saliba and Gardner, 2013a). Hence, a linear elastic eigen-value analyses using subspace iteration method (Abaqus, 2009) was firstly invoked to extract the lowest eigen mode shape. The imperfection amplitude provided by Dawson and Walker (1972) model (Equation 2.8) which has been employed by Gardner and Nethercot (2004c) for stainless steel, is applied to the lowest eigen mode to perturb the actual geometry of the beam for subsequent non-linear analyses.

3.2.5 Material modeling

The material properties (Tables 3.1a and 3.1b) for the LDSS material used in the present study is based on the experimental study conducted on LDSS hollow beams by Theofanous and Gardner (2010). As per EN 10088-4 (2009), an ultimate tensile strength ranging from 700–900 MPa and a minimum 0.2% proof stress ($\sigma_{0.2}$) of 530 MPa can be associated with LDSS Grade EN 1.4162. A modified two stage (Equations 2.1 and 2.7) compound Ramberg-Osgood (1943) proposed by Gardner and Ashraf (2006) for stainless steel material has been adopted for the non-linear stress-strain curve used in the present FE analyses. Equation 2.1 represents the Ramberg-Osgood (1943) model for $\sigma \leq \sigma_{0.2}$ ($\sigma_{0.2}$ is the 0.2% proof stress) and is reported in the literature to provide good accord with stress strain curve obtained from experiments for steel up to $\sigma_{0.2}$. For strains exceeding $\varepsilon_{t0.2}$ (total strains at $\sigma_{0.2}$), Ramberg-Osgood model is known to give higher values of stress values as compared to that of experimental data, and hence a modified version has been suggested by Gardner and Ashraf (2006) (see Equation 2.7). The two-stage model by Gardner and Ashraf (2006) was initially developed for compression elements where the necking phenomenon is not evident as in tensile specimens. Using the full expression (both Equations 2.1 and 2.7) for stress-strain behavior it has been shown by Gardner and Ashraf (2006) that their model could provide reasonably good comparison for stainless steel in both compression and tension loading cases. In the Abaqus model, the two stage non-linear stress strain model given by Equations 2.1 and 2.7 are approximated by a piecewise-linear stress-strain curve, taken due care to insert enough points where the curvature is sharper. The values of E_o for both compression (above neutral axis) and tensile (below neutral axis) parts are given in Table 3.1 (from Theofanous and Gardner, 2010). Poisson's ratio was taken as 0.3. Figure 3.2 shows the schematic stress-strain diagram of LDSS of grade EN 1.4162 used to input in the FE model after the conversion of engineering stress-strain to true plastic stress ($\pm^{pl}_{true}$)-strain ($£^{pl}_{true}$) using the Equations 3.1 and 3.2.

$$\pm_{true} = \pm_{norm}\left(1 + \pounds_{norm}\right) \tag{3.1}$$

$$\pounds_{true}^{pl} = \ln\left(1 + \pounds_{norm}\right) - \frac{\pm_{true}}{E_0} \tag{3.2}$$

where $\pm_{norm}$ and $\pounds_{norm}$ are engineering stress and strain respectively.

The conversion of the nominal static stress-strain curve to true stress and true strain curve was considered necessary as the post-buckling analysis involves significant inelastic strains (e.g. Theofanous and Gardner, 2009; Patton and Singh, 2012). Further, modified RIKS method (Riks, 1979) available in Abaqus (2009) has been used for the non-linear analysis to obtain structural behaviors such as full shear and mid-span deflection response of the beam accurately.

3.2.6 Validation of finite element model

To establish confidence (and hence validation) in the FE modeling approach, a representative experimental test performed on a square hollow LDSS beam from the work of Theofanous and Gardner (2010) has been considered as the benchmark for comparison with the FE result. This particular experimental data has been used to compare, considering the similarities in cross-section and loading conditions, with those of the present research work. Both the flat material properties and beam dimensions of the beam (SHS-60 × 60 × 3-B2) are shown in Tables 3.1 and 3.2 respectively. The beam was cold-formed and hence difference in properties between flat and corner (internal corner radius, r_i = 3.1 mm) regions such as residual stresses, as a result of inelastic deformation during cold forming is expected. However, it has been noted by Theofanous and Gardner (2010) that residual stresses may not be explicitly modeled as the material properties obtained through experimental testing has inbuilt residual stress effect. In addition to the above mentioned material model for flat plates, the tensile corner properties (Table 3.1c) are assigned to the corner regions and extended to flat region for a length of two times the thickness of plate to incorporate the expected strength enhancement in corner regions by cold rolling (Gardner and Nethercot, 2004c; Ashraf *et al.*, 2006b; Theofanous and Gardner, 2010). Local geometric imperfection as described in Section 2.6 was seeded considering the lowest eigen buckling mode shape. Figure 3.3 shows the comparison of FE and experimental mid-span moment vs. rotation. It can be seen from Figure 3.3 that the result from the present FE analysis agrees very well (ultimate moment capacity, M_u and rotation at M_u i.e. $^{-}_{u}$ are also well predicted) with the experimental observation from Theofanous and Gardner (2010), thus establishing a good degree of confidence in the present FE modeling approach. Please note that this validation against SHS (square hollow section) failing by local buckling is due to lack of test results on RHS (rectangular hollow section) where shear buckling is the prevailing failure mode. However, it may be noted that similar kind of shell FE modeling approach was also adopted by Saliba and Gardner (2013a), and Hassanein (2011) for the shear response of LDSS plate girders (i.e. open section), and found to predict accurately the experimental test results. Hence, in the present parametric analyses that followed, such similar well proven shell FE modeling approach, and widely accepted in the literature for modeling thin-walled structures is then adopted. Additional validations are provided in the Appendix C.

3.2.7 Parametric study

In order to investigate the shear behavior of rectangular hollow LDSS beams, effects of key cross sectional parameters *viz.*, flange thickness (t_f), flange width (w_f), web thickness (t_w) and shear span (a) have been considered. The ranges of various parameters considered in this study are: t_f = 4–150 mm, t_w = 2–30 mm; w_f = 150–400 mm and a = 600–1200 mm. Height of the web (h_w) is fixed at 600 mm, so that a/h_w is in the range of 1–2. In all, about 125 FE models have been analysed. In the parametric study, the corners at the junction of flange and web are assumed to be at right angles i.e. no corner radii has been considered as in the FE validation (Section

2.6). This is essentially because, it is assumed that the rectangular LDSS hollow beam having different thickness of web and flange plates would be formed by welding similar to the case of I-sections studied by Saliba and Gardner (2013a). Again, in the absence of experimental data, the modifications in the material properties near the heat affected zone (HAZ) due to possible welding process is neglected, and hence, it is further assumed that same material properties exist both at the corners and the flat parts. It may also be noted that the effect of considering with and without residual stresses in the modelling of welded LDSS I-sections in the structural behaviour was found to be insignificant (Saliba and Gardner, 2013a & 2013b). The same material properties determined by Theofanous and Gardner (2010) (Table 3.1) and used in the validation of FE modelling (Section 2.6) are considered to model both the compression and tension parts. As mentioned before, non-linear FE analyses were performed after the models were seeded with local geometrical imperfections (Equation 2.8). The results of the FE analyses are presented in the form of shear capacity and deformed / failure shapes. In addition, comparisons of the FE results with those predicted by EN 1993-1-4 (2006/A1:2015) and Direct Strength Method (DSM) are presented. Further, proposed modified curves to EN 1993-1-4 (2006/A1:2015) and Direct Strength Method (DSM) are suggested in the end.

3.3 RESULTS AND DISCUSSIONS

3.3.1 Effect of flange to web thickness ratio (t_f/t_w)

Typical plots showing the effect of flange thickness (t_f) and web thickness (t_w) are shown in the form of variation of shear (V and V/V_y; where $V_y = (f_y/\sqrt{3})(2t_w h_w)$ is the yield shear capacity of the section by considering only the webs; f_y = yield stress) with mid-span deformation (¢) (Figures 3.4 and 3.6 respectively), whereas von-Mises stress contours are shown in Figures 3.5 and 3.7 respectively. In Figure

3.4a, the variation of V with ¢ is shown for t_f/t_w = 2–5, keeping web thickness, flange width and shear span constant (i.e. t_w = 4 mm, w_f = 200 mm and a = 600 mm). From Figure 3.4a, it can be seen that the value of ultimate shear (V_u) or shear capacity increased by ~24% for 150% increase in t_f (8–20 mm) or t_f/t_w (2–5). Similar behavior has also been reported in the case of I-section steel girders by Lee and Yoo (1998), Estrada *et. al.*, (2008), Alinia *et. al.*, (2009), Hassanein and Kharoob (2010), Hassanein (2010), Hassanein (2011), Safar (2013), Saliba and Gardner (2013a) etc. Further, an increase in the deformation capacity (δ_u, mid-span deformation at V_u) and ductility can be seen for increasing t_f/t_w. It can be observed that the increase in t_f changes the behaviour of V-δ curve, i.e., in the case of lower flange thickness (t_f/t_w = 2) the curve is relatively sharper around ultimate shear (V_u) whereas as t_f/t_w increases, the shear curve become increasingly flatter, a plateau type can be clearly seen for t_f/t_w = 5. A normalised plot (with respect to V_y) of the shear variation is plotted again in Figure 3.4b. A value of $V_u/V_y < 1$, shows the sections have failed or locally buckled before reaching the yield shear capacity of the web (V_y), whilst in the case of $V_u/V_y > 1$, the sections have yielded prior to reaching V_u. Figure 3.5 shows von-Mises stress contour plot of two selected typical cases: 1) t_f/t_w = 2 (or t_f = 8 mm), and 2) t_f/t_w = 5 (or t_f = 20 mm), at δ_u (i.e. at V_u) and 2.5 δ_u (i.e. post ultimate shear capacity). It may be noted that the average 0.2% yield stress ($\sigma_{0.2}$) is ~733 MPa considering both compression and tensile values (Table 3.1). The increase of stress beyond the yield stress can be associated to strain hardening. It can be readily seen that, for the slender/thinner flange (t_f/t_w = 2), initiation of local buckling (at the yielded region located around mid of each of the shear span) at the compression flange and web can be seen at $V_{u,}$; and at 2.5 δ_u, the local buckling (this behaviour agrees to observations of Gheitasi and Alinia, 2010) is significantly enhanced (Figures 3.5a, b), suggesting of a 'combined shear and bending failure' mode (more discussions of the possible failure mechanisms are presented in Section 3.3.4). In contrast, for the stockier/thicker flange section i.e. t_f/t_w = 5 (or t_f = 20 mm), there is an apparent absence of local buckling at the compression flange, although buckling is initiated for the web at V_u (Figures 3.5c and 3.5d). Rather, plastic hinge type deformation is seen for the stockier flange, one each at the shear span and away from the mid-span i.e. towards the supports (Figures 3.5c and 3.5d), which is an indication of the anchorage of the tension band. On increasing the flange thickness, it is also seen that the size of the diagonally highly stressed or yielded region (an indication of tension band size (e.g. Lee and Yoo, 1998)) is enhanced (and more uniform), for the same thickness of web. This may be related to the improved anchorage of the tension band for the stockier flange. Such type of failure mode as shown in Figures 3.5c and 3.5d, is suggestive of a 'shear dominant failure' mode. The plateauing effect on the shear variation plot (see Figure 3.4) for the stockier flange may be because of the enhanced flange stiffness (thus improving compression plate stability and anchorage of the webs on to the flanges) which results in improved load distribution in the web and delayed web buckling (thus increasing the participation of the web in the shear resistance). At both the ultimate and post ultimate shear, the zone of yielded region on the compression flange for the slender flange section, is found to be non-uniform and relatively larger as compared to that of stockier flange section. This may be because the transfer / interaction of stress between the flange and the web (to maintain compatibility at the flange-web junction), is limited due to increased mismatch between flange and web thicknesses (and hence stiffness mismatch), for stockier flange section; on the other hand, such stress interaction / transfer is made relatively easier for comparable or lesser flange thickness. As such, the marked non-uniformity in the stress distribution (i.e. relatively broader near the flange-web junction and lesser at the flange centerline) for the compression flange of relatively slender flange section (in Figure 3.5a), may be due to the corner junctions getting the maximum effect for the stress interaction. However, for the slender flange section, at the post ultimate shear i.e. at 2.5 δ_u (Figure 3.5b), as the webs buckled (indicated by sharper drop in the shear at post ultimate; see Figure 3.4), mid-span deflection increases, leading towards stress relaxation caused by elastic unloading, in the webs (region of highly stressed zone is now reduced), and in the compression flange. Further, as increase in out-of-plane buckling takes place in the webs, the corner junction also participates in the buckling of flange; further at higher mid-span deformation, more redistribution of stress takes place at the compression flange, thus increasing the region of yielded zone in the compression flange. In the case of stockier flange section, at post ultimate shear i.e. 2.5 δ_u (Figure 3.5d), unlike the slender flange section, due to the delayed buckling (or plateau effect; see Figure 3.4) as discussed above, a decrease in the yielded diagonal zone in the web is not visible. It thus can be seen that, increasing flange thickness (keeping the same web thickness) can enhance both the ultimate shear capacity and ductility.

The effect of web thickness (t_w), keeping t_f constant (t_f = 12 mm) is shown in Figures 3.6 and 3.7, for a = 600 mm and w_f = 200 mm. Variation of V and V/V_y with δ are shown in Figs 3.6a and 3.6b respectively, for t_w = 2-10 mm (or t_f/t_w = 1.2 – 6). From Figure 3.6a, it can be observed that as t_w is increased by ~400% (2-10 mm), V_u is increased by ~506%, along with an increase in sharpness of the shear-deformation curve around V_u. Similar observation has been reported in I-section steel girders by Real *et. al.*, (2007). But there is no significant change in the location of δ_u, with increasing t_w. This may be related to the increase in shear capacity associated with stockier webs (or decreasing t_f/t_w, for constant t_f). Hence, a plateau type behavior is expected for t_w = 2 mm as compared to t_w = 10 mm, as discussed in the previous paragraph (see Figures 3.4 and 3.5). From Figure 3.6b, it can be seen that V_u/V_y approaches 1.0 for stockier web (t_w = 8 mm), suggesting that for higher values of t_w (t_f/t_w = 1.5 in this case), prediction considering shear yielding of web, gives reasonably accurate result for the estimation of shear capacity (i.e. V_y = ~V_u). But for the largest value of t_w (= 10 mm), a drop in V_u/V_y is seen, in comparison to that of the immediate lower value of t_w (= 8 mm), indicating that increasing t_w beyond a threshold value (8 mm in this case), keeping the same t_f/t_w ratio, is not likely to improve the shear capacity, as much when compared to sub-threshold t_w

values (see Figure 3.6a).This phenomenon may hint the change in the failure mechanism e.g. from shear dominated to bending dominated mechanism. For slender (or sub-threshold) web sections, as mostly local web buckling dominates (along with the formation of diagonal tension band) the failure mechanism, the value of V_u/V_y is lesser than 1.0. Comparison of the von-Mises stress contour plots for t_w = 2 mm (or t_f/t_w = 6) and t_w = 10 mm (or t_f/t_w = 1.2) at δ_u and 2.5 δ_u is shown in Figure 3.7. It can be seen that for the stockier t_w, at δ_u, the yielded region extends vertically around the mid-span (right through the compression flange, without little sign of flange buckling), along with an initiation of a spread along the diagonal direction, thus the formation of tension band type failure is not apparent, rather net section (through vertical zone yielding) yielding dominates (Figure 3.7c), resulting in the drop of V_u/V_y due to change in the failure mechanism, as mentioned above. This type of relatively stockier section with low t_f/t_w, can lead to 'bending dominated failure' due to the formation of mid-span hinge. In the post-ultimate (Figure 3.7d), a spread of yielded region can be seen in the form of inverted pyramid type in the web, and local buckling at the yielded region can now be seen on the compression flange, near the loaded mid-span, indicating further the absence of tension band type of failure for stockier webs. On other hand, for slender web i.e. t_w = 2 mm (or t_f/t_w = 6), evidently formation of diagonal tension band along with the initiation web buckling can be seen at V_u (Figure 3.7a). Again, similar to the discussion corresponding to Figure 3.5c (in the above paragraph), stockier flange assisted in anchoring (the yielded zone in the compression flange has been moved towards the support) the tension band (see Figure 3.7a). Due to the larger thickness of the flange (t_f/t_w = 6), compression flange developed improved resistance to local bucking, with the appearance of plastic hinge type of failure pattern in the post ultimate shear (Figure 3.7b). Thus the failure pattern for the stockier flange suggests of a 'shear dominated failure' mode similar to that shown in Figures 3.5c and 3.5d.

Variation of V_u with h_w/t_w (a/h_w = 1.0; w_f = 200 mm) has been shown in Figure 3.8 for t_f/t_w = 2–5. The web slenderness (h_w/t_w) has been varied from 20–300 (corresponding to t_w = 30–2mm). The ranges of t_f considered at h_w/t_w = 300 mm, corresponds to 4 – 10 mm, whereas at h_w/t_w = 20 the range of t_f is 60–150 mm. It can be seen that V_u drops asymptotically with increasing h_w/t_w; the decrease in V_u being sharp till h_w/t_w = 75, beyond which the drop is very mild. The behaviour of decrease in shear capacity with increase in web slenderness also agrees to the findings in the case of I-section steel girders by Lee and Yoo (1998), Alinia *et. al.*, (2009), Hassaanein and Kharoob (2010), Hassanein (2010), Hassanein (2011), Safar (2013), Saliba and Gardner (2013a) etc. Also it is observed that variation of t_f/t_w have little effect on V_u for $h_w/t_w \geq$ ~75, whereas for stockier web section e.g. $h_w/t_w <$ ~75, an increasing rise in V_u can be seen with increasing t_f/t_w. Numerically, V_u increases by ~63%, 50%, 18%, 16%, 24% and 57% for h_w/t_w = 20, 30, 60, 75, 150, 300 respectively, when t_f/t_w is increased by 150%. It is interesting to note that % increase in V_u increases on both sides of t_f/t_w = 75 (or t_w = 8 mm), indicating that the effect of t_f is more pronounce both for lower and higher (i.e. towards left and right extremes of h_w/t_w) values of t_w, whilst the effect is relatively less for intermediate values, keeping t_f/t_w constant. This may be because, in relation to Figure 3.9, two prominent failure mechanisms can be identified: 1) Web Buckling Dominated Failure (WBDF) mechanism (e.g. $h_w/t_w \geq$ ~75) and 2) Web Yielding Dominated Failure (WYDF) mechanism (e.g. $h_w/t_w <$ ~75). In both the cases increasing t_f can influence: 1) making the section stockier thereby enhancing the shear load capacity for the web yielding dominated failure region (e.g. $h_w/t_w \geq$ ~75), and 2) increasing the anchorage capacity of the tension band, leading to improved shear load capacity.

In order to compare V_u with the shear yield capacity of the web V_y, plot of the variation of V_u/V_y with h_w/t_w are shown in Figures 3.9 and 3.10 for two spans, a/h_w = 1.0, and 2.0, respectively, for t_f/t_w = 2–5. For the shorter span, two regions can be identified, corresponding to the failure mechanism mentioned above: 1) WYDF region for $V_u/V_y \geq 1.0$, and 2) WBDF region for $V_u/V_y < 1.0$. It is seen that for the shorter span ($a/h_w = 1.0$), data points for $h_w/t_w <$ ~75, lie in the WYDF region, whereas they lie in the WBDF region for $h_w/t_w \geq$ ~75. Thus, at the first instance, data points located in the WYDF region (e.g. inset figures A and B of Figure 3.9) can correspond to shear dominated mechanism (note the complete yielding of the web in the inset Figures A and B of Figure 3.9, characteristic of shear dominated failure mechanism; similar pattern has also been reported in plates subjected to shear loading by Gheitasi and Alinia, 2010), whilst it can be associated with shear dominated (note the shear web buckling along with the formation of yielded region in the compression flange near the support, characteristic of shear dominated mechanism) or combined shear and bending mechanisms (note the shear web buckling and formation of yielded region in the compression flange towards the mid-span) in the WBDF region (e.g. inset figures C and D of Figure 3.9 respectively).

As the shear span gets longer (e.g. $a/h_w = 2.0$), for most data points, $V_u/V_y < 1.0$, e.g. values of V_u/V_y are completely below the value of 1.0 for all the values of h_w/t_w considered. A closer look into the von-Mises stress distribution at V_u shows that for data points that corresponds to $t_f/t_w = 2$ and 3 and $h_w/t_w <$ ~75 (i.e. relatively stockier sections), mode of failure is apparently not of the shear buckling type as expected when $V_u/V_y < 1.0$, rather the failure mode is of the bending dominated type (whole cross-section around the mid-span is yielded, see inset figure B of Figure 3.10). However, shear buckling of the web still dominated for slender webs with relatively stockier flange (inset figure C of Figure 3.10).This may be because as the span gets longer and the section gets relatively stockier, shear buckling of the web is resisted, which results in a yielded zone that is confined to a relatively smaller zone around the mid-span, with significant area of the web being stressed below yield at ultimate shear (see inset figure B of Figure 3.10), and hence a reduced shear capacity is obtained. Thus, at higher values of h_w/t_w, the failure mechanism is either shear dominated or combined shear and bending (e.g. inset figures C and D of Figure 3.10 respectively) for data points which corresponds to $V_u/V_y < 1.0$. Further, as can be seen from Figure 3.10, region classifications into WYDF and WBDF regions is strictly not possible for relatively longer shear span e.g. bending dominated failure can occur even if $V_u/V_y < 1.0$ (see inset figure B of Figure 3.10). Although, for data points located in the $V_u/V_y > 1.0$ region is expected to be shear dominated (e.g. in the inset figure A of Figure 3.10, almost all of the web is yielded, characteristic of a shear dominated failure mode) mechanism.

3.3.2 Effect of shear span to web height ratio (a/h_w)

The effect of shear span is presented in the plot of V/V_y vs δ in Figures 3.11a and 3.11b, for both stocky and slender web thicknesses i.e. for t_w = 30 mm and t_w = 2 mm respectively, keeping $t_f/t_w = 5$ (w_f = 200 mm). Shear span has been varied from a/h_w = 1–2. It can be seen that the shear capacity (V_u) of the beam decreases with increasing span, the decrement being ~32% and 36%, for t_w = 30 mm and t_w = 2 mm respectively. The observed effect of shear span agrees with the observation made on I-section steel girders by Lee and Yoo (1999), Lee and Yoo (1998), Gardner *et. al.*, (2008), Real *et. al.*, (2007), Estrada *et. al.*, (2008), Alinia *et. al.*, (2009), Safar (2013), Saliba and Gardner (2013a) etc. For the stockier web section (Figure 3.11a), $V_u/V_y \geq 1$, whereas it is $V_u/V_y < 1$ for the slender web section, consistent with the increased shear buckling resistance contribution from both the stockier (t_w = 30 mm, t_f = 150 mm) web and flange parts. The increase of V_u above V_y is again attributable mainly from the contribution of stockier flange (i.e. increased resistance to buckling of the compression flange and resistance to tensile stress for the tension flange; improving the overall resistance) together with the material strain hardening effect (see e.g. inset figure A of Figures 3.9 and 3.10). In the case of slender web, the increase of V_u (or V_u/V_y) with decreasing shear span may be related to the improved distributing of the stress in both the web and flange (see inset figures C and D of Figure 3.9 in comparison to those of Figure 3.10), enabling better participation of the web and flange in resisting shear (corresponding size of the tension band appears to be relatively larger for the shorter span case).

Similarly, for stockier sections also, shorter span promotes better distribution of stress with most area of flange and web being stressed at least to the yield (inset figures A and B in Figure 3.9), whereas in the longer span (inset figures A and B in Figure 3.10), yielded region is confined only to the web or around the mid-span in the web, with only a small portion (near the mid-span) of the compression flange being yielded. It is also noted that an improved ductility can be seen in the case of stockier sections i.e. the values of V have not dropped (Figure 3.11a) even after undergoing a mid-span deflection of ~70 mm for all the spans considered, whereas post peak decrement in V can be seen for δ > ~50 mm, for the slender web sections (Figure 3.11b). The increase in deformation capacity (or ductility) for stockier section, can be explained from the observation that most or all of the webs have undergone or surpassed yielding, without little sign of buckling at peak shear, allowing relatively large mid-span deformation (> ~70 mm) before post-peak shear drop at a later stage (the drop is not shown in Figure 3.11a, as the FE analyses were stopped to save run time). For, slender sections (Figure 3.11b), the deformation capacity is found to increase with increasing span. This may be because of the weaker anchorage offered (inset figure C in Figure 3.10) by the flange on the tension band, due to increase in span, whilst the anchorage in the flange is clearly visible for shorter span (see inset figure C in Figure 3.9).

Figures 3.12a and 3.12b show the von-Mises stress contour for stocky (t_w = 30 mm, t_f = 150 mm) and slender (t_w = 2 mm, t_f = 10 mm) web sections respectively at peak and post peak shear (for w_f = 200 mm and a/h_w = 2). The increase in shear capacity of the stocky section is evident with more areas of web being stressed beyond yield (Figure 3.12a), unlike for the slender web section, where shear buckling of web has occurred (Figure 3.12b). Effect of span is plotted as a variation of V_u/V_y with h_w/t_w

in Figure 3.13 (for t_w/t_f = 5, w_f = 200 mm). A near equally spaced parallel decrease in V_u/V_y (indication of nearly linear drop) can be seen when a/h_w is increased from 1 to 2. An average decrease of ~34% is observed in V_u/V_y, for 100% increase in a/h_w (= 1–2).

3.3.3 Effect of flange width to web height ratio (w_f/h_w)

Variation of V_u/V_y with δ, for stocky (t_w = 30 mm, t_f = 150 mm) and slender (t_w = 2 mm, t_f = 10 mm; a/h_w = 2) sections are shown respectively in Figure 3.14a and 3.14b, for w_f/h_w ranging from 0.25–0.67 i.e. w_f = 150–400 mm. Typical von-Mises stress contours, for both stocky and slender sections for w_f = 150 and 400 mm are shown in Figures 3.15a-d respectively, at V_u. It can be seen from Figure 3.14a that, there is a significant increase in V_u/V_y (~61%) with ~166% in w_f (from w_f = 150 mm), for the stocky section, whereas the increase is much lesser ~9% for the same amount of increase in w_f for slender sections (Figure 3.14b). Similar behavior has been noticed in the case of I-section steel girders by Alinia *et. al.*, (2009), Hassanein (2010), Hassaanein and Kharoob (2010), Hassanein (2011) etc. In the slender sections, deformation capacity is found to increase by ~90%, for the 166% in w_f (such effects are not shown for stocky section due to the termination FE analyses), as shown in Figure 3.14b. For w_f = 400 mm (i.e. wider flange), it is seen that the whole of web and a major portion of the stockier compression flange (t_f = 150 mm) around the mid span has yielded, indicating more load carrying capacity (Figure 3.15b), whereas the yielded region is for a relatively smaller region around the mid-span (Figure 3.15a), indicative of lower load capacity as shown in Figure 3.14a. This may be because, as the flange gets wider, more area of both top and bottom flanges gets available to resist the load, resulting in better distribution of the stresses (i.e. more web area is mobilised to resist load). From Figures 3.15c and 3.15d, for the case of slender web section, there appears to be not much contribution (the stress in compression flange is much lower than yield stress) of the flange in resisting the load, although apparently, the width of the diagonal tension band is relatively larger (and hence improved load capacity) for the wider flange beam (Figure 3.15d). However, in the wider flange beam, contribution from the tension flange in supporting the load, due to enhanced tension (i.e. bottom) flange sectional area is also the likely reason for the small increase in load capacity. The decrease in deformation capacity (Figure 3.14b) for smaller flange width beam, in the case of slender web beams, may also be related to the reduced flange cross sectional area, e.g. reduction in tension flange cross sectional area, may help in earlier post ultimate drop in shear. Variation in V_u/V_y with h_w/t_w for various values of w_f/h_w = 0.25–0.67, for t_f/t_w = 5 and h_w/t_w = 20-300, is plotted in Figure 3.16. It can be seen from Figure 3.16, that, the rate of increase gets relatively higher, in a nearly linear fashion, as the section gets stockier (h_w/t_w < ~75), in comparison to slender sections ($h_w/t_w \geq$ ~75), where the average increase is ~10% (increase being nearly constant). Higher rate of increase in stockier section may again be related to the contribution from both the flange and webs in supporting the load (see e.g. Figure 3.15a and 3.15b), as discussed above, such load carrying mechanism is primarily absent for slender sections, where shear web buckling with little contribution from the flange in resisting the load, being the mechanism.

3.3.4 Failure mechanisms

Observing the von-Mises stress distribution (superimposed on deformed shapes) both at ultimate (i.e. at δ_u) and post ultimate load (e.g. 3 δ_u) of the FE models, along with the identification of their location on the moment and shear interaction curve (EN 1993-1-4 (2006/A1:2015)), three main failure mechanisms have been identified: a) shear dominant failure, b) bending dominant failure, and c) combined bending and shear failure mechanisms. It may be noted that, similar type of failure mechanisms have also been identified in the case of open sections (e.g. Alinia *et al.*, 2009; Saliba and Gardner, 2013a; Hassenien, 2011).

a) Shear dominant failure

For a typical shear dominant failure mechanism, it is seen that there is an appearance of shear buckling deformation failure type in the webs (Figure 3.17a) at V_u, resulting in an evident presence of diagonal tension band, which anchors at the flange (or near the support). At the post-ultimate shear, plastic hinge type yielded region near to the support, where anchorage of the tension band takes place, can be observed (Figure 3.17b). Such type shear dominant failure are observed in stockier flange sections (e.g. $t_f/t_w \geq 3$ for $a/h_w = 1.0$), when the web is relatively slender ($h_w/t_w \geq 75$). This observation is in accord with the failure mode observed in I-section steel girders subjected to shear loading by Lee and Yoo (1999), Alinia *et. al.*, (2009), Hassanein and Kharoob (2010), Hassanein (2010), Saliba and Gardner (2013a). In the longer span (a/h_w = ~2.0), shear dominant failure can take place when the flange thickness is sufficiently stocky as compared to that of web (e.g. t_f/t_w = 5) where the stockier flange provides sufficient anchorage to the tension band (as a result of shear buckling) of the web (in the case of slender web, e.g. $h_w/t_w \geq 75$), whereas on the other hand, for stockier webs ($h_w/t_w < 75$) both the increase in thicknesses of web and flange, helped in mobilizing most areas of webs in sustaining shear. Typical example shown in Figure 3.17 corresponds to a FE model with w_f = 200 mm, t_f = 10 mm, t_w = 2 mm; a/h_w = 2 (referred to with the nomenclature W600FW200TF10WT2).

In Figure 3.18, moment-shear interaction curve i.e. $V/V_{b,\ Rd}$ vs $M/M_{c,Rd}$, as per EN 1993-1-4 (2006/A1:2015) is plotted, where $V_{b,\ Rd}$ (Equation 3.3-3.12) is the total shear resistance of the section i.e. including the shear resistance of flange ($V_{bf,\ Rd}$) and shear resistance of web ($V_{bw,\ Rd}$), $M_{f,\ Rd}$ is the flange bending resistance and $M_{eff,\ Rd}$ and $M_{c,Rd}$ are the bending resistance of effective cross-section (in the case of Class 4 section) and cross section respectively. V and M are the applied shear and bending moment.

$$V_{b,Rd} = V_{bw,Rd} + V_{bf,Rd} \le \frac{\eta f_{yw} h_w t_w}{\sqrt{3}\gamma_{M1}} \tag{3.3}$$

where, f_{yw}, η, and γ_{M1} are the web yield strength, web contribution factor and shear partial factor respectively. The values of η and γ_{M1} are taken as 1.2 and 1.0 respectively (Saliba and Gardner, 2013a). The contribution of the web ($V_{bw,Rd}$) is defined as:

$$V_{bw,Rd} = \frac{\chi_w f_{yw} h_w t}{\sqrt{3}\gamma_{M1}} \tag{3.4}$$

where, the web buckling reduction factor (χ_w) taken as, ,

$$\chi_w = \eta \qquad \text{for } \bar{\lambda}_w \le \frac{0.65}{\eta} \tag{3.5}$$

$$= \frac{0.65}{\bar{\lambda}_w} \qquad \text{for } \frac{0.65}{\eta} < \bar{\lambda}_w \le 0.65 \tag{3.6}$$

$$= \frac{1.56}{0.91 + \bar{\lambda}_w} \qquad \text{for } \bar{\lambda}_w \ge 0.65 \tag{3.7}$$

Here, web slenderness parameter for webs stiffened (or coupled) at supports and mid-span ($\bar{\lambda}_w$) is defined as,

$$\bar{\lambda}_\tau = \frac{\bar{b}/t}{37.4\varepsilon\sqrt{k_\tau}} \tag{3.8}$$

where, k_τ is the shear buckling coefficient given by,

$$k_\tau = 5.34 + 4.00\left(\frac{h_w}{a}\right)^2 \qquad \text{for } a/h_w \ge 1.0 \tag{3.9}$$

$$= 4.00 + 5.34\left(\frac{h_w}{a}\right)^2 \qquad \text{for } a/h_w < 1.0 \tag{3.10}$$

The contribution from the flange ($V_{bf,Rd}$) is defined as,

$$V_{bf,Rd} = \frac{b_f t_f^2 f_{yf}}{c\text{¥}_{M1}} \left(1 - \left(\frac{M_{Ed}}{M_{f,Rd}} \right)^2 \right) \tag{3.11}$$

where, M_{Ed} is the bending design moment, and c is width of the tension band given by

$$c = a\left(0.17 + \frac{3.5 b_f t_f^2 f_{yf}}{t_w h_w^2 f_{yw}}\right) \quad \text{and} \quad \frac{c}{a} \le 0.65 \tag{3.12}$$

Here, f_{yf} is the yield stress in the flange. In this study, both f_{yf} and f_{yw} are taken as equal to $\pm_{0.2}$ of the compression part (see Table 3.1), hence f_{yf}/f_{yw} =1.0 in Equation 3.12.

Interaction of bending and shear (i.e. consisting of combined bending and shear) conditions for I or box girder should satisfy (provided, design shear force is equal to or greater than 50% of the plastic shear resistance or $\eta_3 \ge 0.5$):

$$\eta_1 + \left(1 - \frac{M_{f,Rd}}{M_{pl,Rd}}\right)(2\eta_3 - 1)^2 \le 1.0 \tag{3.13}$$

where,

$$\eta_1 = M_{Ed} / M_{pl,Rd} \tag{3.14}$$

$$\eta_3 = V_{Ed} / V_{bw,Rd} \tag{3.15}$$

Here, $M_{pl,\ Rd}$ is the design plastic moment resistance of the section consisting of effective area of the flanges and web (Gardner and Nethercot, 2011). In constructing the interaction diagram, all partial factors of safety are taken to be unity. $M_{f,Rd}$ is calculated as the product of yield strength, the effective area of the flange with the distance from the neutral axis.

On the moment-shear interaction figure (Figure 3.18), the FE values for the example model (W600FW200TF10WT2) is marked, using the coordinates ($V_u/V_{b,Rd}$, $M_u/M_{c,\ Rd}$), where V_u, and M_u corresponds to the ultimate shear and moment computed from FE analysis. It is seen that, the value of $V_{u,\ FE}/V_{b,\ Rd}$ is relatively much higher as compared to $M_u/M_{c,\ Rd}$ ($V_u/V_{b,\ Rd}$ / $M_u/M_{c,\ Rd}$ = ~3.18), indicating the failure mode of the beam is shear dominated (EN 1993-1-4, 2006/A1:2015). This is consistent with the failure mode observation (Figure 3.17).

b) Bending dominant failure

In the bending dominant failure mode, the yielding is confined to a narrow region around the mid-span, wherein at V_u, evidence of compression and tensile yielding initiation (around the mid-span) can be observed at the top and bottom flange respectively. It is possible to accompany such failure with the presence of local buckling around the mid-span for slender webs (h_w/t_w = 300), or absence of local buckling of the web for stockier webs (e.g. h_w/t_w = 20). At the post ultimate shear, development of full plastic hinge type can be seen at the midspan associated with stress relaxation on other parts of the beam i.e. towards the supports (the failure mode agrees to failure mode observed in I-section steel girders by Alinia *et. al.*, (2009), Hassaanein and Kharoob (2010), Saliba and Gardner (2013a)). Figure 3.19 shows typical bending dominant failure mode for W600WF200FT12WT8 (a/h_w = 2) specimen. Bending dominant failure is found to occur mostly on the longer span beam (a/h_w = 2), and when the flange thickness is smaller (e.g. t_f/t_w = 2). Smaller flange thickness allows both the compression and tension flange around the mid-span to yield earlier (see e.g. inset figure D of Figure 3.10), and this helps in the bending of the beam around the mid-span. Similar observation can also be made for shorter span (a/h_w = 1), especially for slender web (h_w/t_w = 300) with lower t_f/t_w (e.g. t_f/t_w = 2). FE data point for W600WF200FT12WT8 (a/h_w = 2) specimen is located on the interaction moment-shear interaction diagram in Figure 3.20. For this beam, a relatively high value of $M_{u,\ FE}/M_{c,\ Rd}$ as compared to $V_u/V_{b,\ Rd}$ ($M_u/M_{c,\ Rd}$ / $V_u/V_{b,\ Rd}$ = ~ 1.60) is seen, indicative of bending dominant failure mode.

c) Combined shear and bending failure

When both shear and bending failure modes (see Sections 3.3.4a and b) interact and both are present, a mixed type of failure termed as combined shear and bending failure mode can occur. Typical example of combined shear and bending failure modes are shown for specimen, W600WF200FT8WT4 (a/h_w = 1), in Figure 3.21. In Figure 3.21, the presence of shear web buckling in webs and yielding (due to bending) on both the compression and tension flange is seen at ultimate shear (Figure 3.21a). Deformation around the mid-span (with a relaxation of stress at the mid-span due to stress redistribution) with the formation of yielded region close to the mid-span at post ultimate load (i.e. at 3 δ_u) suggest of a combined shear and bending failure mode (similar failure mode has also been reported in the study in I-sections by Gardner and Saliba (2013a)). The location of the FE data corresponding for the specimen shown in Figure 3.21, in the moment-shear interaction diagram is shown in Figure 3.22, wherein it lies in the transition area ($M_u/M_{c,\ Rd}$ / $V_u/V_{b,\ Rd}$ = ~0.66) of shear and moment in interaction curve.

It can be seen from the previous discussion that, although the interaction curves are similar in nature for all the specimens, a unique interaction curve needs to be explicitly defined based on the values of $V_{bw,Rd}$ / $V_{b,Rd}$ and $M_{f,Rd}$/ $M_{c,Rd}$, for each specimen. Thus, it is not possible to device a single curve or diagram on which all the specimens can be compared and probe for their failure mechanisms. Hence, a similar method for comparison reported by Saliba *et al.*, (2014) has been followed in this work. In this method, three normalised moment-shear (*M*-*V*) i.e. $V/V_{b,Rd}$ and $M/M_{c,Rd}$ interaction curves are drawn (Figure 3.23) based on the average, minimum and maximum of the two ratios i.e. $V_{bw,Rd}$ / $V_{b,Rd}$ and $M_{f,Rd}$/ $M_{c,Rd}$, considering all the FE results of ~125 models. The results of FE analyses for which the ratio of shear force to bending i.e. $V_{u,FE}/M_{u,FE} > V_{bw,Rd}/M_{f,Rd}$, indicating shear dominant failure mode are then plotted on the M-V diagram. The data points corresponding to bending or combined bending and shear dominant failure modes (i.e. $V_{u,FE}/M_{u,FE} \leq$

$V_{bw,Rd}/M_{f,Rd}$) are omitted for brevity in Figure 3.23. Further, as the focus of the current work is mainly on studying the shear behavior, only shear dominant FE results are considered for comparison with EN 1993-1-4 (2006/A1:2015) (EN 1993-1-4) and Direct Strength Method (DSM) in the subsequent sections.

3.4 COMPARISON OF FE RESULTS WITH EN 1993-1-4 (2006/A1:2015)

In order to assess the applicability of the shear resistant model provided in EN 1993-1-4 (2006/A1:2015) (EN 1993-1-4) to the present study on LDSS beams, comparisons on the variation of ¡_w (shear buckling reduction factor for web buckling) with $\bar{\text{a}}_w$ (web slenderness) is shown in Figure 3.24. It may be mentioned that EN 1993-1-4 (2006/A1:2015) shear design approach takes into consideration of the contribution of both the web (¡_w) and flange (¡_f) to the shear resistance and ignores the effect of rigid end post. EN 1993-1-4 (2006/A1:2015)'s method is based on Höglund's (1971, 1973, 1997) rotated stress field method, adopting simple post-critical assumption (e.g. Saliba and Gardner, 2013a). Expressions for calculating ¡_w and $\bar{\text{a}}_w$ are Equations 3.5-3.10, based on EN 1993-1-4 (2006/A1:2015). FE ¡_w values are calculated as $(V_u – V_{bf,\ Rd}) / V_y$, i.e. flange shear capacity ($V_{bf,\ Rd}$, see Equation 3.11) has been deducted from the FE ultimate shear capacity (V_u). Two separate comparisons are made between FE and EN 1993-1-4 (2006/A1:2015): 1) for $a/h_w \leq 1.0$, and 2) $1 < a/h_w \leq 2.0$, in similar lines done for stainless steel plate girders by Estrada *et al.*, (2008). A higher value of $\bar{\text{a}}_w$ represents slender webs and a lower value of ¡_w show lesser contribution of the web in the shear resistance. In Figure 3.24, only those FE models which have shown shear dominant failure mechanism (see Section 3.3.4) i.e. data points satisfying $(M_u/M_{c,\ Rd}) / (V_u/V_{b,\ Rd}) >$ 1.0 are considered for comparison with EN 1993-1-4 (2006/A1:2015). For the comparison, web panel range (a/h_w) from 0.83–2.0 have been considered. From Figure 3.24, it is observed that for the lower web panel ratio (i.e. $a/h_w \leq 1.0$), FE predicted higher values of χ_w in comparison to that of EN 1993-1-4 (2006/A1:2015), indicating a conservative codal prediction. The mean and coefficient of variation (COV) of the ratio of FE to codal predictions i.e. $V_u / V_{EN\ 1993\text{-}1\text{-}4}$ are found to be 1.47 and 0.19. In the case of higher web panel ratio ($1< a/h_w \leq 2.0$), FE values are also above those of EN 1993-1-4 (2006/A1:2015) (but relatively closer to the FE values as compared to the case of $a/h_w \leq 1.0$, see Figure 3.24b), with the mean and COV of $V_u / V_{EN\ 1993\text{-}1\text{-}4}$ being 1.36 and 0.19 respectively. Thus it is seen that as the FE values are on the higher side as compared to the $V_{EN\ 1993\text{-}1\text{-}4}$, predictions, suggesting that EN 1993-1-4 (2006/A1:2015) stainless steel shear resistance design model can be conservatively applied for LDSS hollow rectangular beams. However, in this chapter, based on the FE analyses, an improved optimal design expression is suggested to provide safe and economical sections, similar to that of EN 1993-1-4 (2006/A1:2015). The new modified shear buckling reduction factor ($\chi_{w(EN\text{-}proposed)}$) expressions (obtained through non-linear regression analysis using least square method, considering the lower bound FE values for 1) for $a/h_w \leq 1.0$, and 2) $1< a/h_w \leq 2.0$, are provided in Table 3.3. It can be seen from Table 3.3 that the value of η (=1.2) is maintained same as that given by EN 1993-1-4 (2006/A1:2015) for $\bar{\lambda}_w \leq 0.65/\eta$. The mean and COV (Tables 3.5 & 3.6) for the proposed modification are found to be: 1) 1.19 and 0.14 for $a/h_w \leq 1.0$, and 2) 1.18 and 0.16 for $1< a/h_w \leq 2.0$, respectively, suggesting an improvement in both mean and COV as compared to EN 1993-1-4 (2006/A1:2015).

3.5 COMPARISON OF FE RESULTS WITH DIRECT STRENGTH METHOD (DSM)

Direct Strength Method (DSM) is an alternative method to the traditional 'effective width method', proposed by Schafer and Pekoz (1998) for the design of cold formed steel members considering local, global and distortional buckling. DSM procedure is now currently integrated into the North American Specification (NAS, 2001, 2007) and Australian/ New Zealand Standard (AS/NZS, 2001). The details of DSM procedure are provided in the Appendix 1 of NAS (2007). In DSM, rather than considering the slenderness ratio of the most slender constituent plate elements, slenderness of the full cross-section is utilised in estimating the load capacity. Hence, DSM does not require calculation of the effective width, instead the elastic buckling load in local, global and distortional modes are required to be determined, to compute the ultimate capacities of cold formed steel members. Thus, DSM provides simplistic design procedures offering an attractive solution to design engineers, and can reasonably take into consideration of complex cross sectional shapes (e.g. Pham *et al.*, 2014; Keerthan *et al.*, 2015). The elastic buckling loads (necessary in DSM, and explained later) can be obtained through finite strip (e.g. CUFSM (2012), THIN-WALL (2006) or finite element softwares (e.g. Abaqus, 2009). Till date, significant development have been made on the application of DSM for members subjected to compression and bending, formal application to members subjected to shear is apparently lacking, although recently, Pham *et al.*, (2014) and Keerathan and Mahendran (2011, 2015a, 2015b) reported of the successful application of DSM on sections with longitudinal stiffeners, and lipped channel, hollow flange etc., respectively, subjected to shear. It is also noted that, application of DSM for LDSS members subjected to compression and bending have been reported by Young and co-workers (e.g. Huang and Young, 2013, 2014a). Hence, in this section, an attempt has been made to develop DSM design rules based on the FE results. At first, comparison of the FE results with those predicted by DSM design expression without considering the effect of post-critical strength enhancement (developed through recasting of the original DSM expressions in terms of nominal shear loads, especially shear yield capacity (V_y) of the web has been brought in) (e.g. Pham *et al.*, 2014; Keerthan and Mahendran, 2015a, 2015b). The DSM design rules for shear (without considering post-buckling strength) (Equations 3.16-3.18). But as the development of diagonal tension field action is evident in the present FE analyses, corresponding to shear failure dominant specimens, it is desirable to extend the original DSM for shear (mentioned above), to take into consideration of the post-buckling strength, as suggested by Keerthan and Mahendran (2015a, 2015b). Hence, in this work, based on non-linear regression analysis (least square method) using lower bound values of the FE results, a further improvement has been proposed i.e. modifications to Keerthan and Mahendran (2015a), to include the effect of post-buckling strength (Equations 3.19-3.21).

a) *DSM design rules (without post-buckling strength)*

$$\frac{V_v}{V_y} = 1 \qquad a \le 0.815 \tag{3.16}$$

$$\frac{V_v}{V_y} = \frac{1}{a} \qquad 0.815 < a \le 1.23 \tag{3.17}$$

$$\frac{V_v}{V_y} = \frac{1}{a^2} \qquad a > 1.23 \tag{3.18}$$

Here, V_y (shear yield capacity of the web based on average shear yield stress of 0.6 f_y) = 0.6 $h_w t_w f_y$; $a = \sqrt{V_y / V_{cr}}$, where V_{cr} elastic shear buckling capacity (obtained through FE analysis).

a) *Proposed DSM design rules (with post-buckling strength)*

$$\frac{V_v}{V_y} = 1 \qquad a \le 0.815 \tag{3.19}$$

$$\frac{V_v}{V_y} = \frac{0.815}{a} + P_n\left[1 - \frac{0.815}{a}\right] \qquad 0.815 < a \le 1.23 \tag{3.20}$$

$$\frac{V_v}{V_v} = \frac{1}{a^2} + P_n\left[1 - \frac{1}{a^2}\right] \qquad a > 1.23 \tag{3.21}$$

Here, P_n is the post buckling coefficient and is found to be 0.50 and 0.33 for $a/h_w \leq$ 1.0 and 1< $a/hw \leq$ 2.0, respectively. The corresponding values for LiteSteel beam with RHFB (Rectangular Hollow Flange Beam) and I-section beams, have been reported to be 0.25 (Keerthan and Mahendran, 2011, 2015a). In Equations 3.19-3.21, the values of V_v/V_y for $\lambda \leq 0.815$, $0.815 < \lambda \leq 1.213$, $\lambda > 1.213$ correspond to shear yielding, inelastic buckling and elastic buckling respectively. The proposed design expressions of DSM are given in Table 3.4. Comparisons of the DSM (without post-buckling), proposed design rules for I-section by Keerthan and Mahendran (2015a, 2015b) (with post-buckling) and proposed DSM (with post-buckling) design rules are presented in Figures 3.25a and 3.25b, for $a/h_w \leq 1.0$ and 1< $a/hw \leq 2.0$, respectively, in non-dimensional format, as a variation of V_v/V_y vs λ. The mean and COV (Tables 3.5 & 3.6) for the proposed DSM design rule value of V_v/V_y in comparison to that of FE, are found to be 1.20, 0.17 and 1.21, 0.16 respectively for $a/h_w \leq 1.0$ and $1 < a/h_w \leq 2.0$, indicating an improved performance. Further, from Figure 3.25, it can be observed that significant post buckling strength can be observed, for relatively slender webs (h_w/t_w) consistent with those reported by Keerthan and Mahendran (2015a, 2015b).

3.6 RELIABILITY ANALYSIS

The applicability of EN 1993-1-4 (2006/A1:2015) and proposed design modifications for EN 1993-1-4 (2006/A1:2015) and DSM for the prediction of shear capacity of LDSS rectangular hollow beam have been assessed through reliability analysis. In the reliability analysis, the method proposed in the commentary (Equation C-2) of ASCE 8-02 (2002) for cold formed steel structures has been considered. A resistance factor (ϕ_o) value of 0.85 suggested by ASCE 8-02 (2002) for the web under shear buckling for flexural members is taken in the calculation of reliability index (β). In accordance to ASCE 8-02 (2002), a load combination of 1.2DL +1.6 LL (DL = dead load; LL = live load), along with statistical parameters M_m, F_m, V_M and V_F (i.e. mean, coefficients of variation (COV) of material and fabrication, respectively) with values of 1.10, 1.0, 0.10 and 0.05, respectively, are considered (See Section 1.5.4 of ASCE 8-02 (2002). The ratio of nominal resistance to load effect (i.e. R_m/Q_m) are taken from Equation C-15 ASCE 8-02 (2002). As per ASCE 8-02 (2002), a target reliability index (β_o) value of 3 has been adopted. From the reliability analyses, for the proposed design modifications, the values of β are calculated to be 3.39 and 3.21, respectively, indicating that the proposed design modifications are reliable (i.e. $\beta > 3.0$), for LDSS hollow beams.

3.7 CONCLUSIONS

The shear behavior of LDSS (lean duplex stainless steel) rectangular hollow beams have been investigated in this chapter, through a parametric study, using the commercial finite element software, Abaqus. Effects of key cross sectional parameters *viz.*, flange thickness (t_f), flange width (w_f), web thickness (t_w) and shear span (a) have been studied in the FE study, keeping the height of the web (h_w) constant. The conclusions drawn from the FE investigations are presented below:

1) An asymptotic drop in shear capacity (V_u) has been observed with increasing values of web slenderness (h_w/t_w), the decrease in V_u being relatively steeper till $h_w/t_w < 75$. The variation of t_f/t_w is found to have little effect on V_u for $h_w/t_w \geq \sim 75$, whereas for stockier web sections e.g. $h_w/t_w < \sim 75$, an increasing rise in V_u can be seen with increasing t_f/t_w. Further, in general, it is observed that increasing flange thickness for the same web thickness, can enhance both the ultimate shear capacity and ductility.

2) The % increase in V_u increases on both sides of $h_w/t_w = 75$, indicating that the effect of t_f is more pronounce both for lower and higher values of t_w (i.e. towards left and right extremes of h_w/t_w), whilst the effect is relatively less for intermediate values, on keeping t_f/t_w constant.

3) The shear capacity (V_u) of the beam is seen to decrease with increasing shear span for both the stocky and slender web sections.

4) The effect of increasing flange width (w_f) is found to be significant for stockier sections as compared to the slender sections. The increase in V_u/V_y is found to be ~61% with ~166% increase in w_f (from w_f = 150 mm), for the stocky section, whereas the increase is much lesser (~9%) for the slender web sections, for the same amount of increase in w_f.

5) Three failure mechanisms have been identified *viz*., 1) shear dominant, 2) bending dominant, and 3) combined shear and bending, in consistent to the observation made on LDSS plate girders in the literature.

6) In general, both EN 1993-1-4 (2006/A1:2015) and DSM are found to be applicable for the shear design of LDSS rectangular hollow beams (although their predictions are conservative), in comparison to the FE results presented herein. Hence, a possible modifications to both EN 1993-1-4 (2006/A1:2015) and DSM have been suggested by bifurcating two span ratios: 1) $a/h_w \leq 1.0$ and 2) $1 < a/h_w \leq 2.0$.

Table 3.1: LDSS material properties (Theofanous and Gardner, 2010)

SHS 60 × 60 × 3 – B2 specimen					
a) Tension flat material properties					
E_o (MPa)	$\sigma_{0.2}$ (MPa)	$\sigma_{1.0}$ (MPa)	σ_u (MPa)	Compound R-O coefficients	
				n	$n'_{0.2,0.1}$
209797	755	819	839	6.0	4.3
b) Compression flat material properties					
206430	711	845	-	5.0	2.7
c) Tensile corner material properties					
212400	885	1024	1026	6.3	4.0

Table 3.2: Beam dimensions (Theofanous and Gardner, 2010) for FE validation

Specimen	L (mm)	B (mm)	D (mm)	t (mm)	r_i (mm)	w_o
SHS	1100	60	60	3.10	2.3	Eq.

L = Length, B = Width, H = Depth, t = thickness, r_i = internal corner radius, w_0 = local geometric imperfection

Table 3.3: EN 1993-1-4 (2006/A1:2015) design expressions to evaluate the web buckling co-efficient (χ_w)

Web panel ratio	$\bar{a}_w$	χ_w	$\chi_{w,\,prop}$
$a/h_w \leq 1.0$	$\bar{a}_w \leq \frac{0.65}{¦}$	¦	¦
	$\frac{0.65}{¦} < \bar{a}_w \leq 0.65$	$\frac{0.65}{\bar{a}_w}$	$\frac{0.69}{\bar{a}_w}$
	$\bar{a}_w \geq 0.65$	$\frac{1.56}{0.91+\bar{a}_w}$	$\frac{2.42}{1.53+\bar{a}_w}$
$1 < a/h_w \leq 2.0$	$\bar{a}_w \leq \frac{0.65}{¦}$	¦	¦

	$\frac{0.65}{\vert} < \bar{a}_w \leq 0.65$	$\frac{0.65}{\bar{a}_w}$	$\frac{0.675}{\bar{a}_w}$
	$\bar{a}_w \geq 0.65$	$\frac{1.56}{0.91+\bar{a}_w}$	$\frac{2.03}{1.27+\bar{a}_w}$

Table 3.4: Proposed design expressions of Direct Strength Method (DSM) V_v/V_y

Web panel ratio	$\bar{a}_w$	$V_v/V_{y(DSM\text{-}proposed)}$
$a/h_w \leq 1.0$	$\lambda_w \leq 0.815$	1.0
	$0.815 < \lambda_w \leq 1.23$	$\frac{1}{a^2}+0.50\left[1-\left(\frac{1}{a^2}\right)\right]$
	$\lambda_w > 1.23$	$\frac{0.815}{a}+0.50\left[1-\left(\frac{0.815}{a}\right)\right]$
$1< a/h_w \leq 2.0$	$\lambda_w \leq 0.815$	1.0
	$0.815 < \lambda_w \leq 1.23$	$\frac{0.815}{a}+0.33\left[1-\left(\frac{0.815}{a}\right)\right]$
	$\lambda_w > 1.23$	$\frac{1}{a^2}+0.33\left[1-\left(\frac{1}{a^2}\right)\right]$

Table 3.5: Comparison of FE results with predictions of EN 1993 1-4 (2006/A1:2015) and Direct Strength Method (DSM) for shear span of $a/h_w \leq 1.0$

Section (a/h_w)	V_u (kN)	$V_{EN,\,1993\text{-}1\text{-}4}$ (kN)	$V_{EN\text{-}\,proposed}$ (kN)	$V_{prop,\,DSM}$ (kN)	$V_u/V_{EN,\,1993\text{-}1\text{-}4}$	$V_u/V_{EN,\,prop}$	$V_{u,FE}/V_{prop,DSM}$
W600WF200FT4WT2 (1.00)	435	283	358	544	1.54	1.22	0.80
W600WF200FT8WT4 (1.00)	1402	1022	1196	1284	1.37	1.17	1.09
W600WF200FT6WT2 (1.00)	592	316	390	546	1.88	1.52	1.08
W600WF200FT12WT4 (1.00)	1540	1088	1262	1300	1.42	1.22	1.19
W600WF200FT24WT8 (1.00)	4042	3406	3657	3791	1.19	1.11	1.07
W600WF200FT30WT10 (1.00)	5750	4805	5030	5119	1.20	1.14	1.12
W600WF200FT8WT2 (1.00)	650	338	412	547	1.92	1.58	1.19
W600WF200FT16WT4 (1.00)	1638	1149	1323	1309	1.43	1.24	1.25
W600WF200FT32WT8 (1.00)	4220	3550	3801	3830	1.19	1.11	1.10
W600WF200FT40WT10 (1.00)	6084	4990	5215	5119	1.22	1.17	1.19
W600WF200FT10WT2 (1.00)	683	360	434	547	1.90	1.57	1.25
W600WF200FT20WT4 (1.00)	1742	1201	1375	1315	1.45	1.27	1.32
W600WF200FT40WT8 (1.00)	4498	3656	3907	3863	1.23	1.15	1.16
W600WF200FT50WT10 (1.00)	6258	5120	5345	5119	1.22	1.17	1.22
W600WF200FT100WT20 (1.00)	17254	15136	14062	10238	1.14	1.23	1.69
W600WF200FT150WT30 (1.00)	30000	25191	23579	15358	1.19	1.27	2.05
W600WF200FT6.25WT2.5 (1.00)	764	430	531	705	1.78	1.44	1.08
W600WF200FT9WT2.5 (1.00)	850	461	562	707	1.84	1.51	1.20
W600WF200FT10.5WT3 (1.00)	1074	628	756	885	1.71	1.42	1.21
W600WF200FT12.25WT3.5 (1.00)	1326	816	968	1083	1.62	1.37	1.22
W600WF200FT15WT5 (1.00)	2083	1414	1624	1805	1.47	1.28	1.15
W600WF200FT12WT6 (1.00)	2471	2029	2265	2411	1.22	1.09	1.02
W600WF200FT18WT6 (1.00)	2663	2140	2375	2461	1.24	1.12	1.08
W600WF200FT18WT6 (1.00)	3269	2742	2991	3117	1.19	1.09	1.05
W600WF200FT21WT7 (1.00)	2828	2013	2249	2486	1.40	1.26	1.14
W600WF200FT24WT6 (1.00)	3475	2550	2799	3150	1.36	1.24	1.10
W600WF200FT28WT7 (1.00)	730	357	432	548	2.04	1.69	1.33
W600WF200FT12WT2 (1.00)	1540	1081	1255	1299	1.43	1.23	1.19
W600WF200FT12WT4 (1.00)	2471	2019	2254	2413	1.22	1.10	1.02

W600WF200FT15WT2 (1.00)	792	384	459	549	2.06	1.73	1.44
W600WF200FT15WT4 (1.00)	1612	1002	1176	1306	1.61	1.37	1.23
W600WF200FT15WT6 (1.00)	3075	2072	2308	2448	1.48	1.33	1.26
W700WF200FT60WT10 (0.86)	7595	5610	5903	5972	1.35	1.29	1.27
Mean					1.47	1.19	1.20
COV					0.19	0.14	0.17

Table 3.6: Comparison of FE results with predictions of EN 1993 1-4 (2006/A1:2015) and Direct Strength Method (DSM) for shear span of 1< a/h_w ≤ 2.0

Section (a/h_w)	V_u (kN)	$V_{EN,\,1993}$ (kN)	$V_{EN,\,proposed}$ (kN)	$V_{prop,\,DSM}$ (kN)	$V_u/V_{EN,\,1993}$	$V_u/V_{EN,\,proposed}$	$V_{u,FE}/V_{prop,DSM}$
W600WF200FT8WT2 (2.00)	424	265	294	369	1.60	1.44	1.16
W600WF200FT16WT4 (2.00)	1161	926	991	935	1.25	1.17	1.24
W600WF200FT10WT2 (2.00)	445	276	305	370	1.61	1.46	1.20
W600WF200FT20WT4 (2.00)	1214	942	1007	942	1.29	1.21	1.29
W600WF200FT40WT8 (2.00)	3431	3000	3063	3338	1.14	1.12	1.03
W600WF200FT50WT10 (2.00)	5013	4251	4269	4811	1.18	1.17	1.04
W600WF200FT150WT30 (2.00)	20396	20349	18737	15358	1.00	1.09	1.33
W600WF200FT6.25WT2.5 (2.00)	483	378	417	479	1.28	1.16	1.01
W600WF200FT9WT2.5 (2.00)	559	367	406	483	1.52	1.38	1.16
W600WF200FT10.5WT3 (2.00)	717	503	551	612	1.43	1.30	1.17
W600WF200FT12.25WT3.5 (2.00)	910	719	777	758	1.27	1.17	1.20
W600WF200FT24WT6 (2.00)	2036	1837	1915	1885	1.11	1.06	1.08
W600WF200FT28WT7 (2.00)	2638	2364	2437	2569	1.12	1.08	1.03
W600WF200FT10WT2 (1.30)	600	293	323	377	2.05	1.86	1.59
W600WF200FT20WT4 (1.30)	1517	964	1028	998	1.57	1.48	1.52
W600WF200FT40WT8 (1.30)	4033	3341	3383	3546	1.21	1.19	1.14
W600WF200FT50WT10 (1.30)	5715	4704	4690	5119	1.21	1.22	1.12
W600WF200FT150WT30 (1.30)	26150	23469	21857	15358	1.11	1.20	1.70
W600WF200FT10WT2 (1.60)	517	271	300	374	1.91	1.72	1.38
W600WF200FT20WT4 (1.60)	1329	1009	1073	967	1.32	1.24	1.38
W600WF200FT40WT8 (1.60)	3747	3153	3207	3438	1.19	1.17	1.09
W600WF200FT50WT10 (1.60)	5359	4456	4460	4970	1.20	1.20	1.08
W600WF200FT150WT30 (1.60)	23549	22394	20782	15358	1.05	1.13	1.53
W600WF200FT10WT2 (2.00)	464	265	294	371	1.75	1.58	1.25

W600WF200FT20WT4 (2.00)	1241	973	1038	947	1.28	1.20	1.31
W600WF200FT40WT8 (2.00)	3522	3061	3124	3369	1.15	1.13	1.05
W600WF200FT50WT10 (2.00)	5197	4411	4428	4860	1.18	1.17	1.07
W600WF200FT10WT2 (2.00)	469	273	302	371	1.71	1.55	1.26
W600WF200FT20WT4 (2.00)	1278	962	1027	950	1.33	1.24	1.35
W600WF200FT40WT8 (2.00)	3600	3194	3257	3382	1.13	1.11	1.06
W600WF200FT50WT10 (2.00)	5276	4618	4635	4860	1.14	1.14	1.09
W600WF200FT100WT20 (2.00)	16293	14772	14131	10238	1.10	1.15	1.59
W600WF200FT150WT30 (2.00)	28123	25191	23579	15358	1.12	1.19	1.83
W600WF200FT10WT2 (2.00)	437	269	298	370	1.62	1.47	1.18
W600WF200FT20WT4 (2.00)	1160	936	1001	934	1.24	1.16	1.24
W600WF200FT12WT2 (2.00)	458	269	298	371	1.70	1.54	1.24
W600WF200FT12WT4 (2.00)	1081	892	956	922	1.21	1.13	1.17
W600WF200FT15WT2 (2.00)	493	283	312	371	1.74	1.58	1.33
W600WF200FT15WT4 (2.00)	1122	913	978	927	1.23	1.15	1.21
Mean					1.36	1.18	1.21
COV					0.19	0.16	0.16

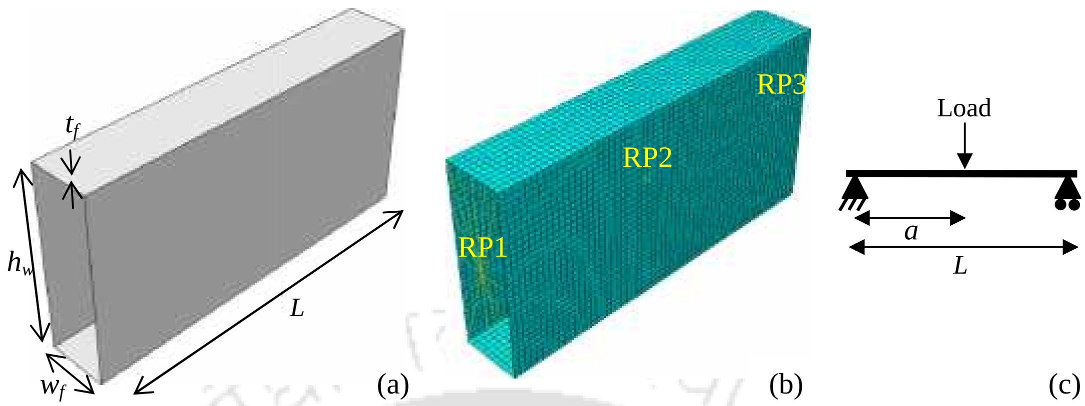

Figure 3.1: (a) Schematic diagram of FE LDSS hollow beam (b) FE mesh (RP1, RP2 and RP3 are reference points (c) boundary condition.

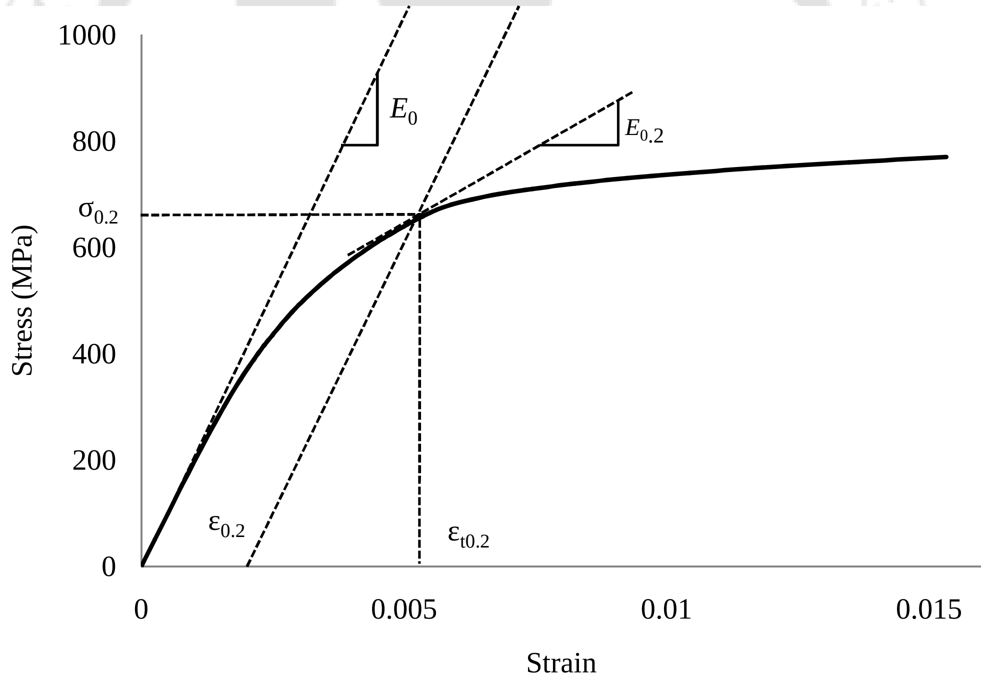

Figure 3.2: Schematic diagram of stress-strain curve of LDSS material Grade EN 1.4162 (Gardner & Ashraf, 2006).

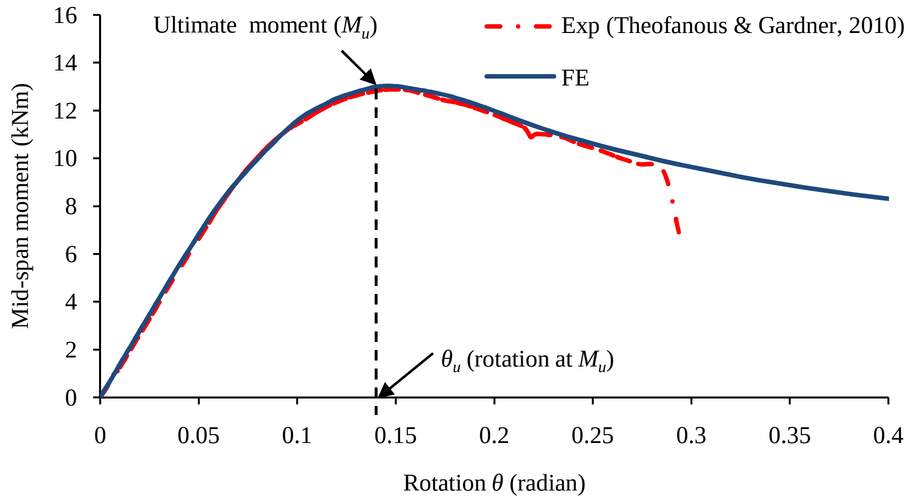

Figure 3.3: Variation of mid-span moment vs rotation (SHS-60 × 60 × 3-B2).

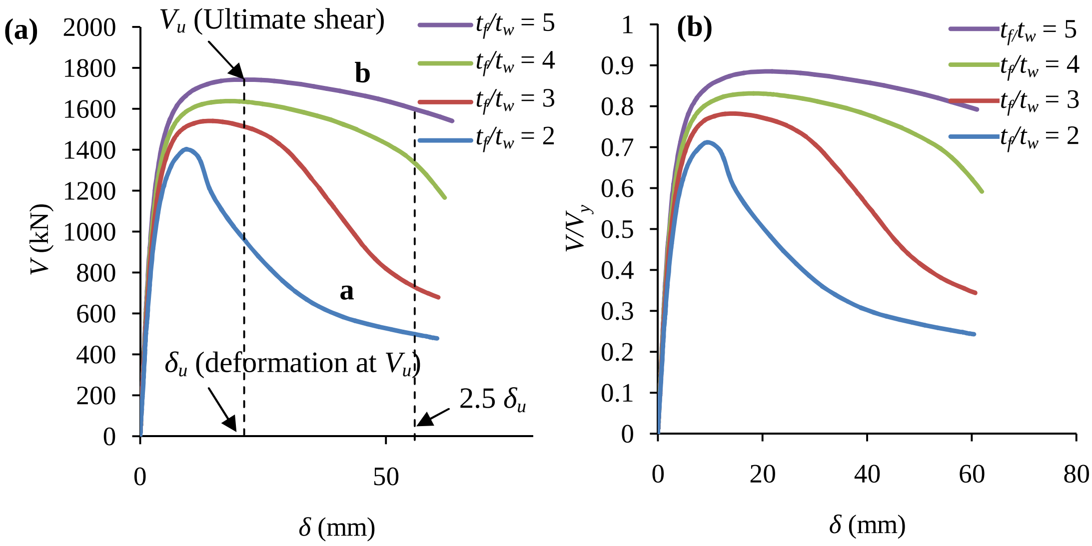

Figure 3.4: Variation of a) V vs δ and b) V/V_y vs δ (t_w = 4 mm and a = 600 mm, w_f = 200 mm).

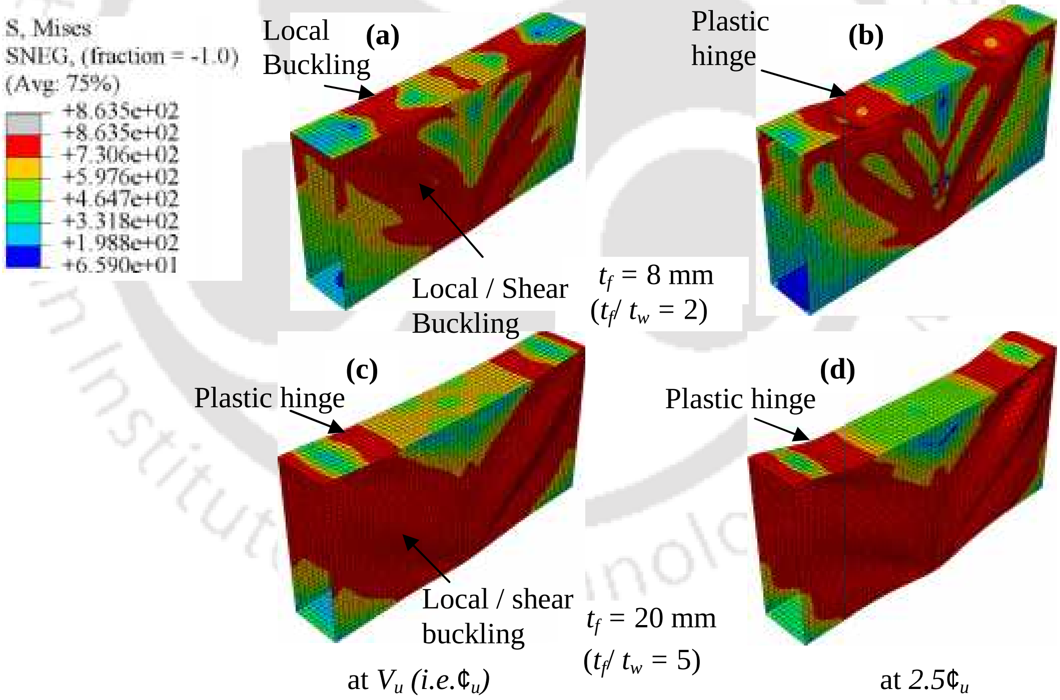

Figure 3.5: Von-mises stress contour at δ_u (corresponding to P_u) and 2.5 δ_u for i) t_f = 8 mm (a, b) and ii) t_f = 20 mm (c, d) (t_w = 4 mm, h_w = 600 mm, w_f = 200 mm and a = 600 mm).

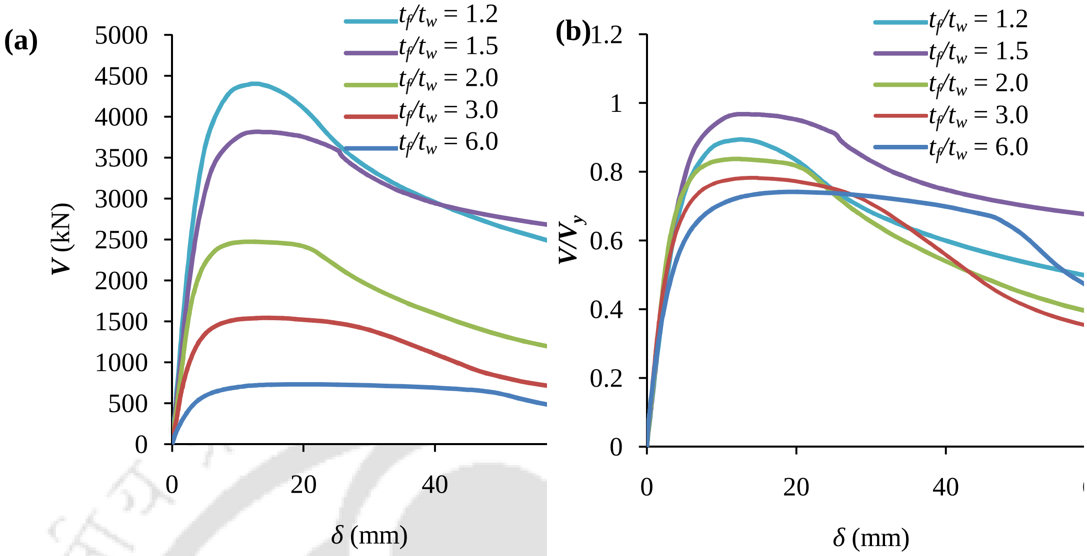

Figure 3.6: Variation of a) V vs δ b) V/Vy vs δ (t_f = 12 mm, w_f = 200 mm and a = 600 mm).

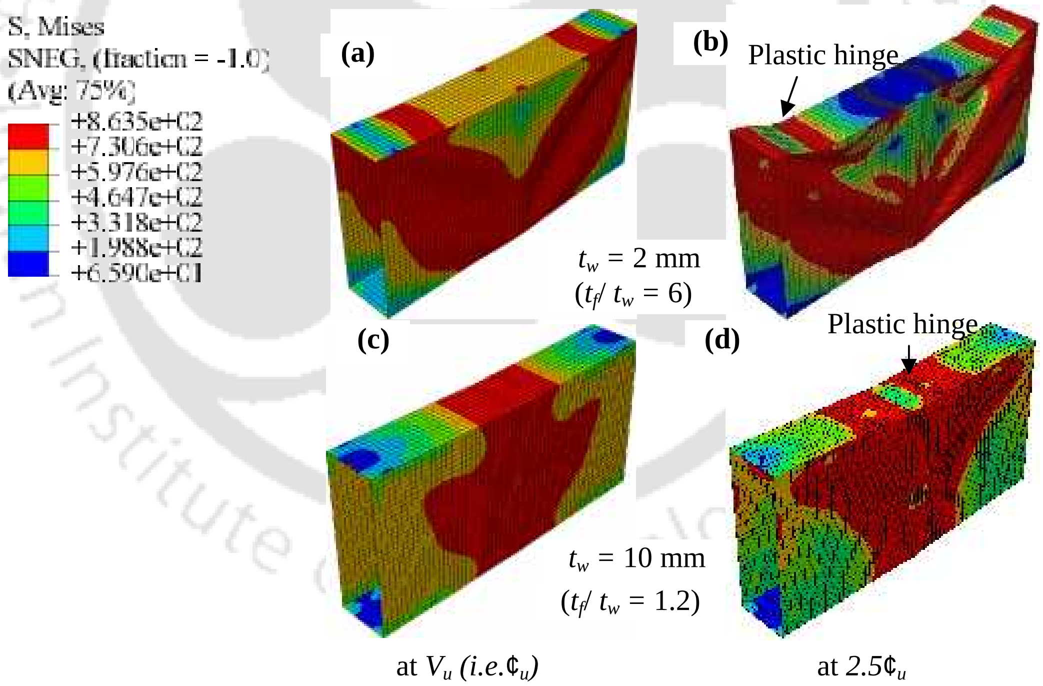

Figure 3.7: Von-mises stress contour at δ_u (corresponding to P_u) and 2.5 δ_u for i) t_w = 2 mm (a, b) and ii) t_w = 10 mm (c, d) (t_f = 12 mm, w_f = 200 mm and a = 600 mm).

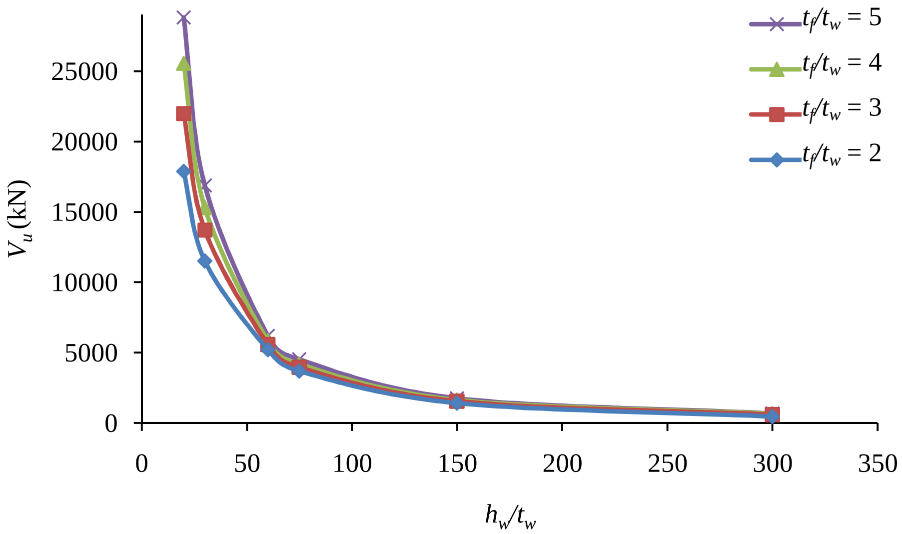

Figure 3.8: Variation of V_u vs h_w/t_w (a/h_w = 1.0; w_f = 200 mm).

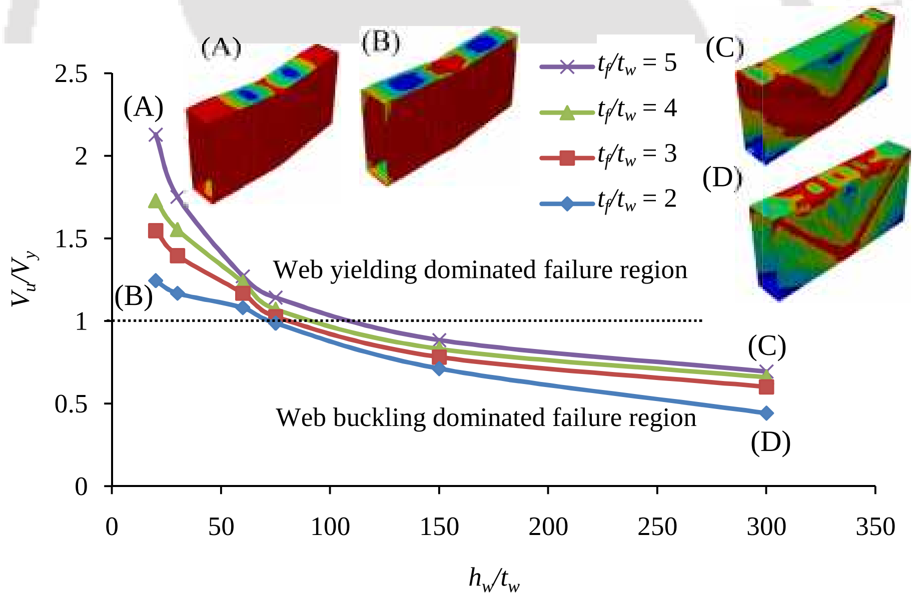

Figure 3.9: Variation of V_u/V_y vs h_w/t_w (a/h_w = 1.0, w_f = 200 mm). Von-Mises stress contours are plotted at δ_u (corresponding to V_u at insite).

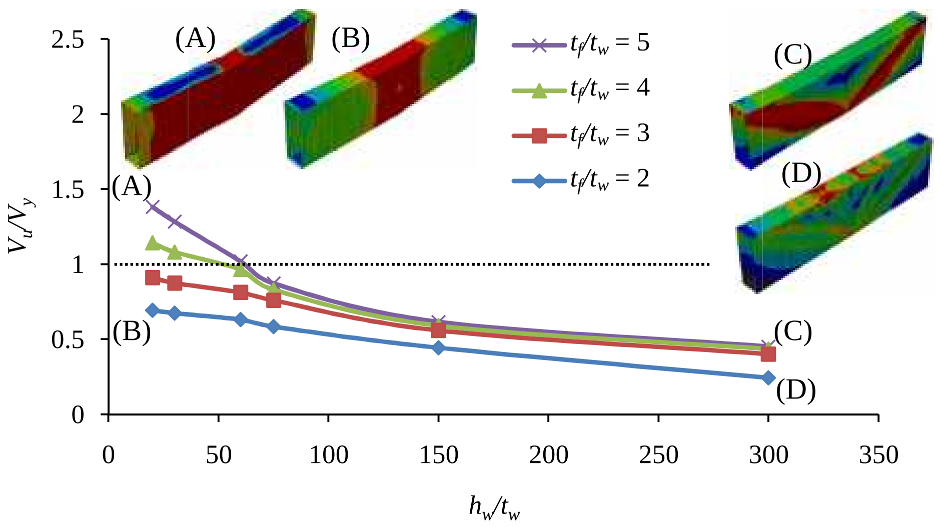

Figure 3.10: Variation of V_u/V_y vs h_w/t_w (a/h_w = 2.0, w_f = 200 mm). Von-Mises stress contours are plotted at δ_u (corresponding to V_u at insite).

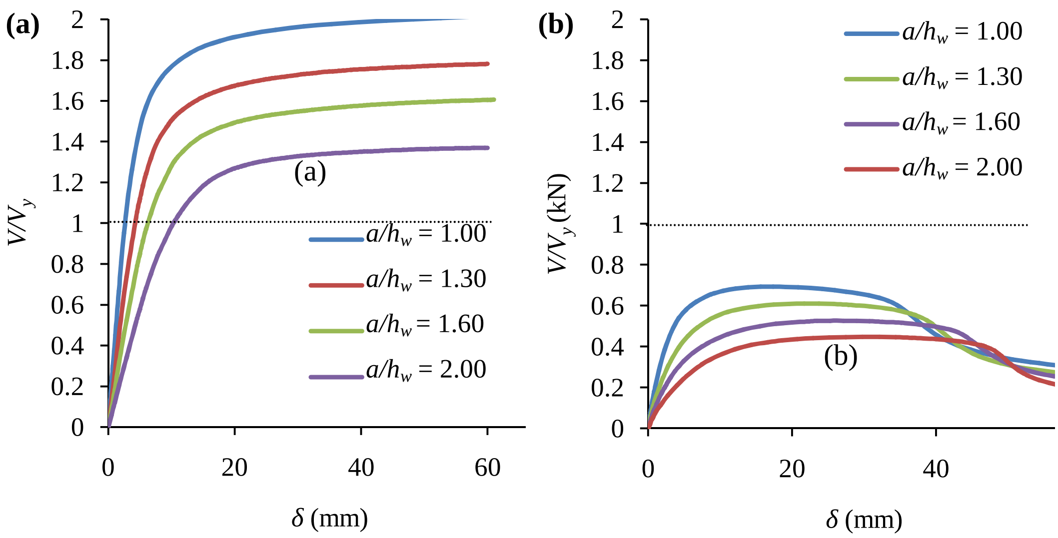

Figure 3.11: Variation of V/V_y vs δ: a) t_w = 30 mm (t_f = 150 mm) and b) t_w = 2 mm (t_f = 10 mm) (t_w/t_f = 5; w_f = 200 mm).

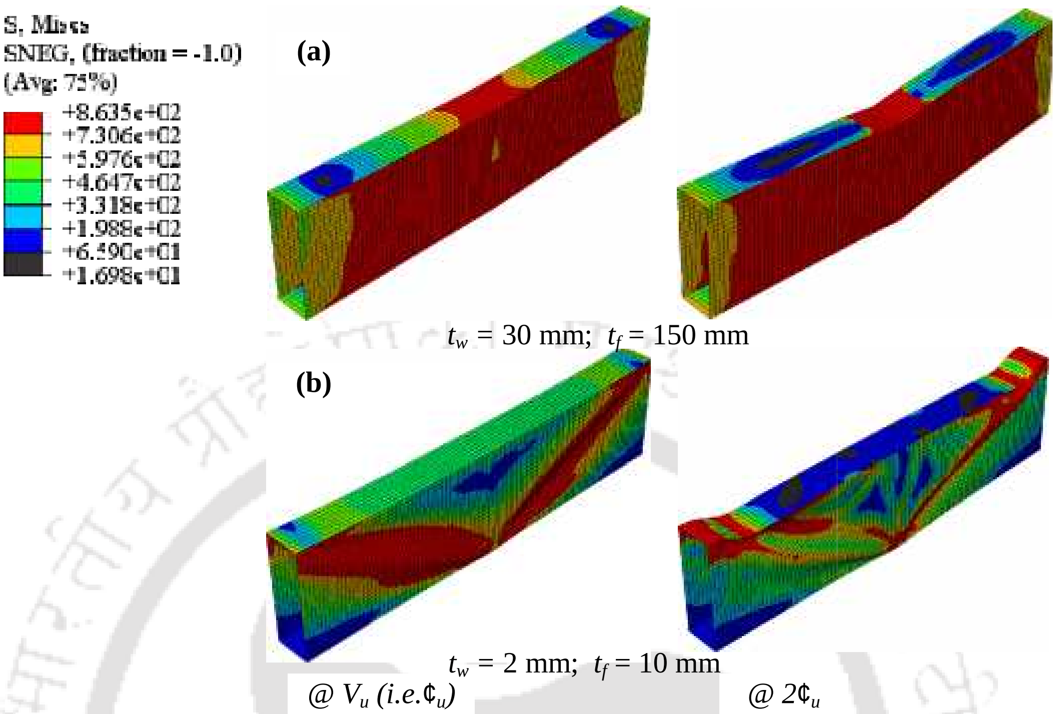

Figure 3.12: Von-mises stress contour at δ_u (corresponding to P_u) and 2.0 δ_u for i) t_w = 30 mm (a) and ii) t_w = 2 mm (b) (t_f/t_w = 5 mm, w_f = 200 mm, and a/h_w = 2).

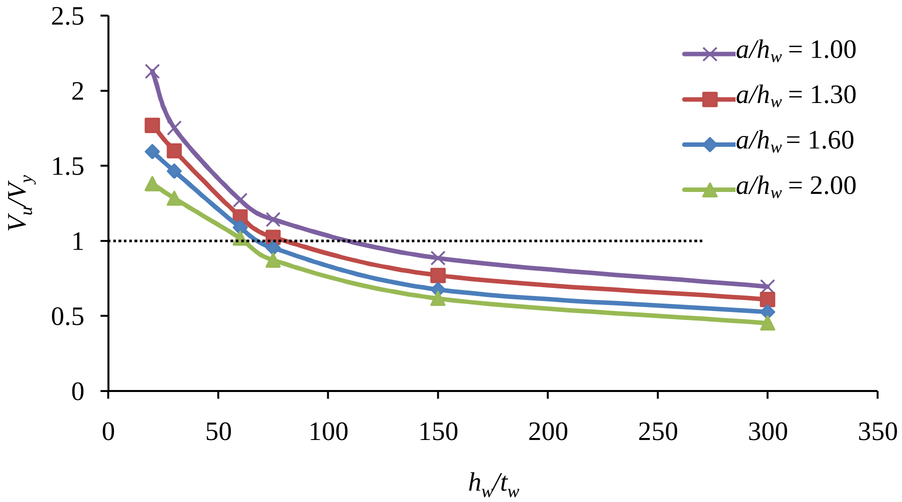

(b)

Figure 3.13: Variation of V/V_y vs h_w/t_w for a/h_w = 1.00 – 2.00 (t_w/t_f = 5, w_f = 200 mm).

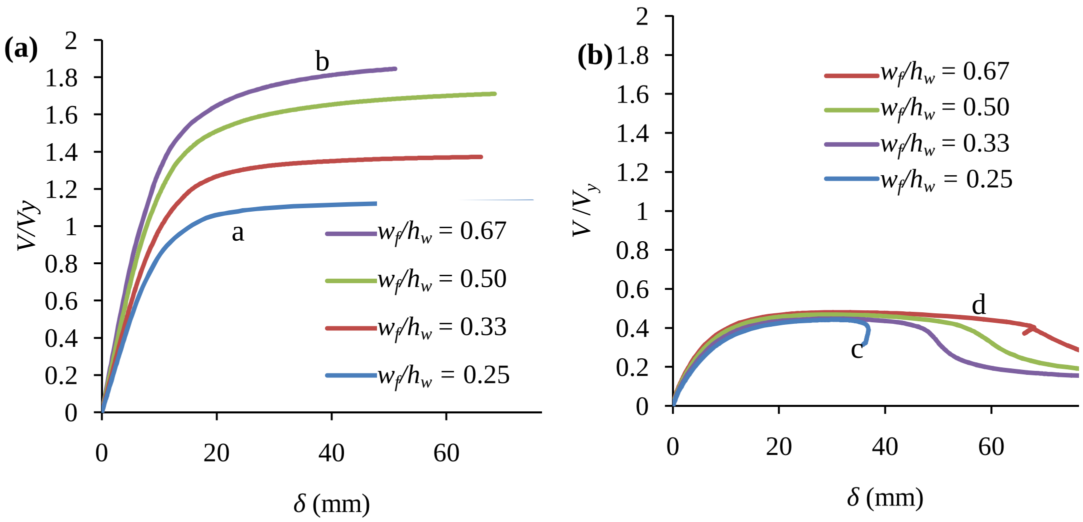

Figure 3.14: Variation of V/V_y vs δ: a) h_w/t_w = 20 (t_f = 150 mm), b) h_w/t_w = 300 (t_f = 10 mm) for shear span of a/h_w = 2.

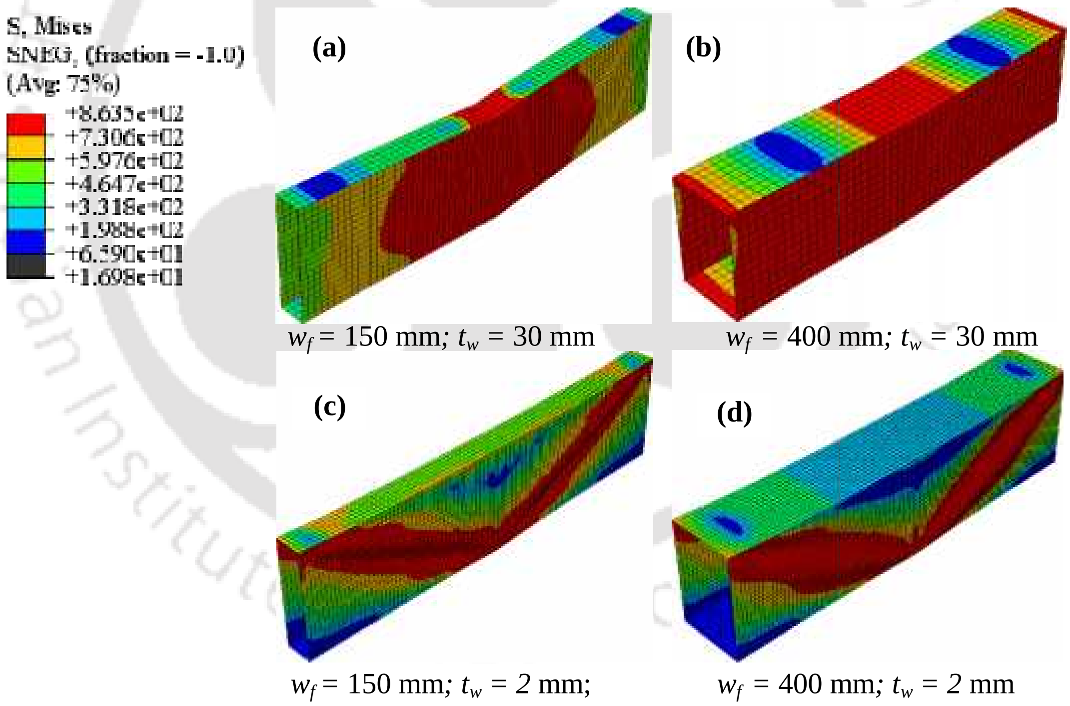

Figure 3.15: Von-mises stress contour at (i.e. δ_u): a) w_f = 150 mm, b) w_f = 400 mm(t_w = 30 mm; t_f = 150 mm); c) w_f = 150 mm, d) w_f = 400 mm (t_w = 2 mm; t_f = 10 mm); (t_f/t_w = 5, a/h_w = 2).

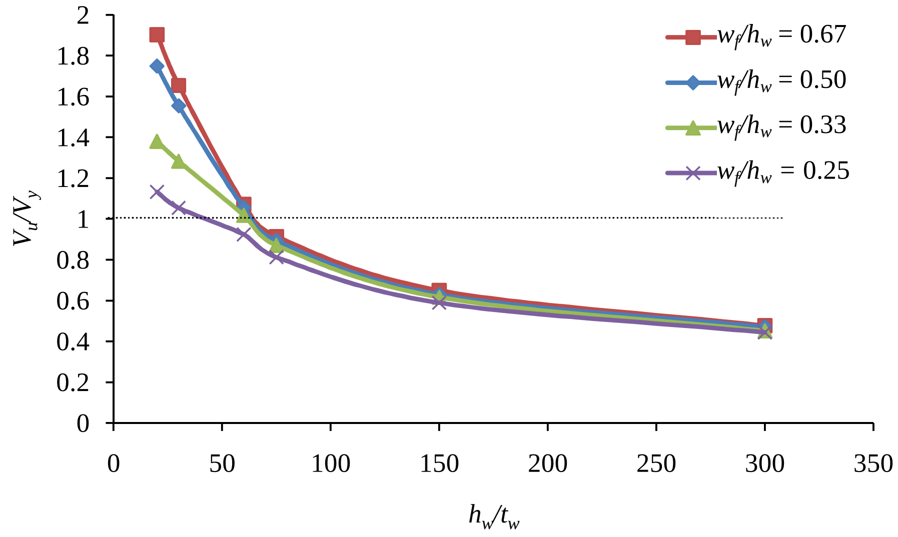

Figure 3.16: Variation of V/V_y vs h_w/t_w for variation of flange width (t_w/t_f = 5; w_f = 200 mm).

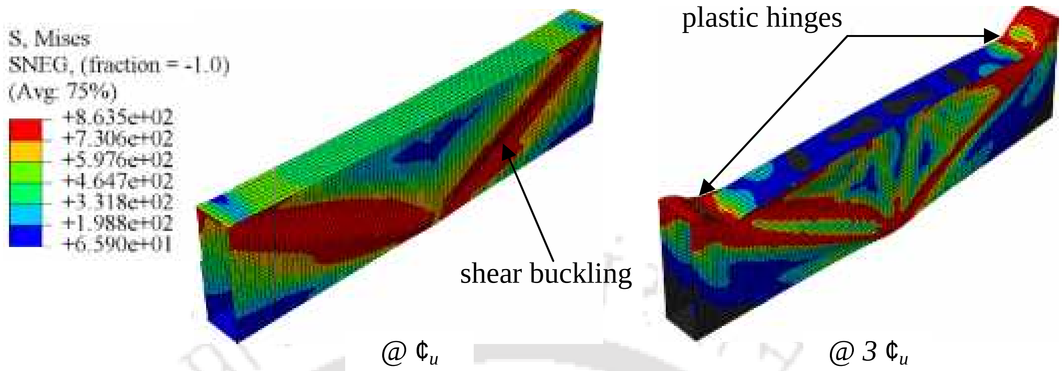

Figure 3.17: Typical shear dominant failure mode at δ_u and 3 δ_u (w_f = 200 mm, t_f = 10 mm, t_w = 2 mm; a/h_w = 2).

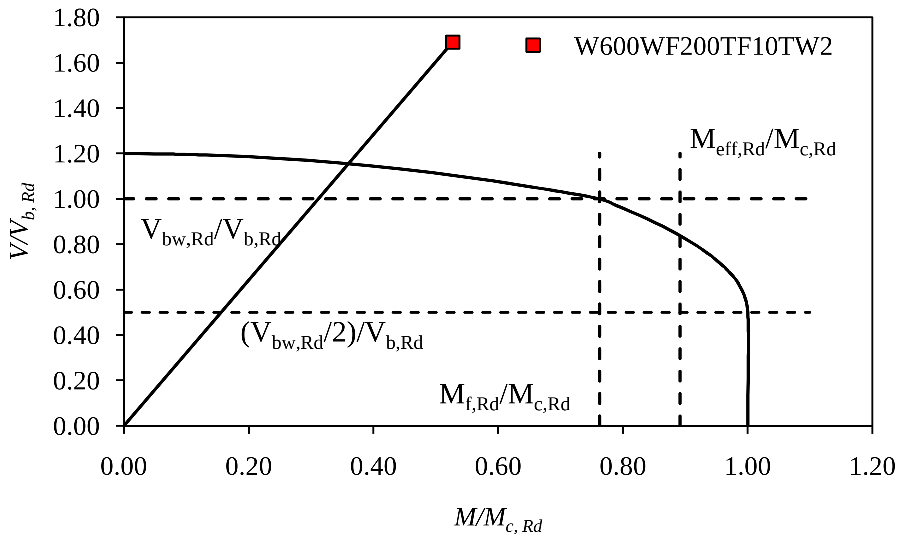

Figure 3.18: Moment and shear interaction curve (EN 1993-1-4, 2006) showing location of typical shear dominant failure (w_f = 200 mm, t_f = 10 mm, t_w = 2 mm; a = 1200 mm).

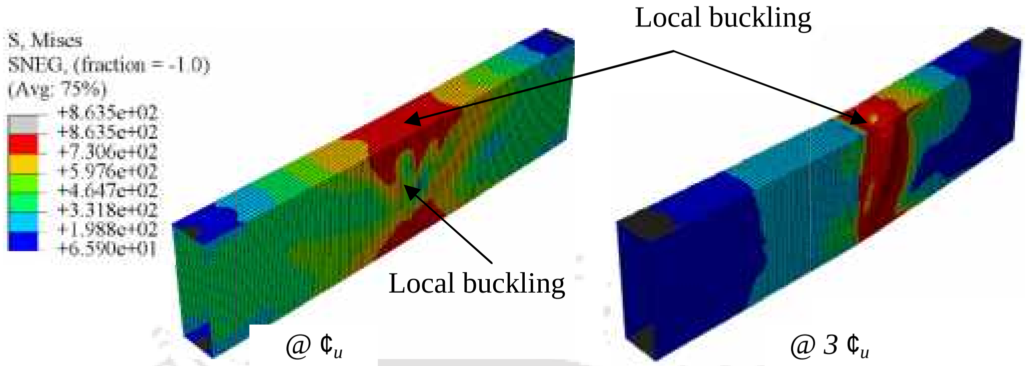

Figure 3.19: Typical bending dominant failure mode at δ_u and 3 δ_u (w_f = 200 mm, t_f = 12 mm, t_w = 8 mm; a = 1200 mm).

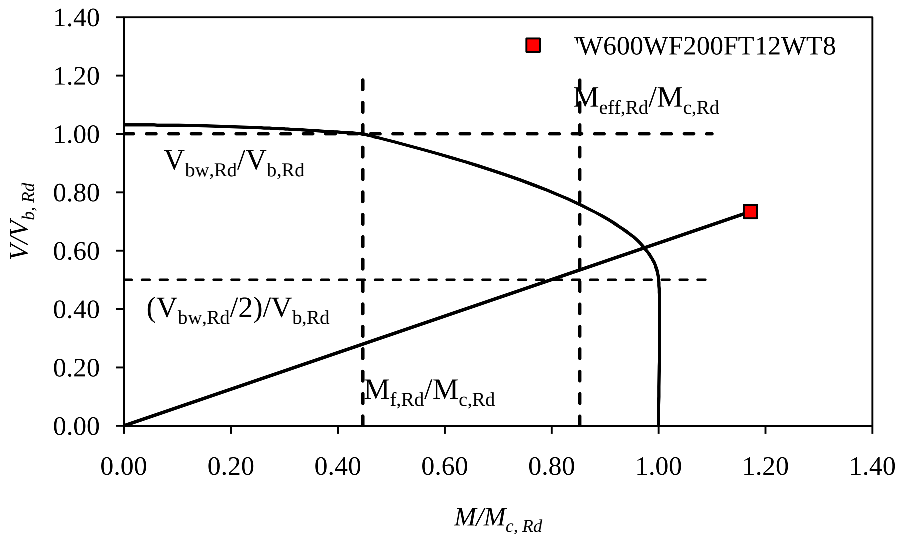

Figure 3.20: Bending and shear interaction curve (EN 1993-1-4, 2006) showing location of typical bending (w_f = 200 mm, t_f = 12 mm, t_w = 8 mm; a = 1200 mm).

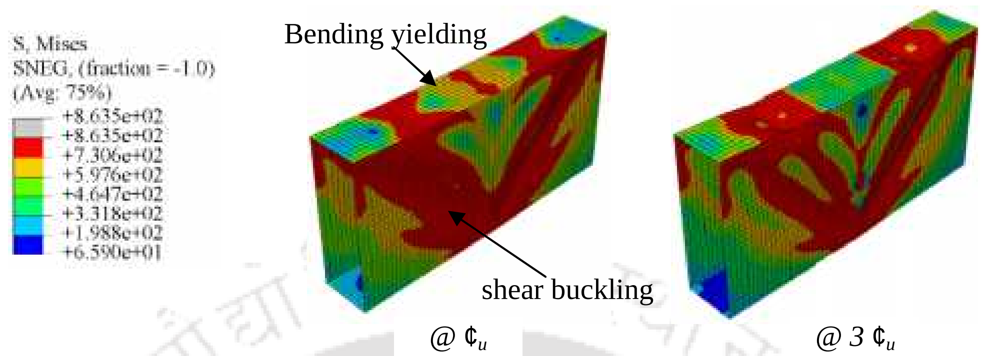

Figure 3.21: Typical combined shear and bending failure mode at δ_u and 3 δ_u (w_f = 200 mm, t_f = 12 mm, t_w = 6 mm; a = 600 mm).

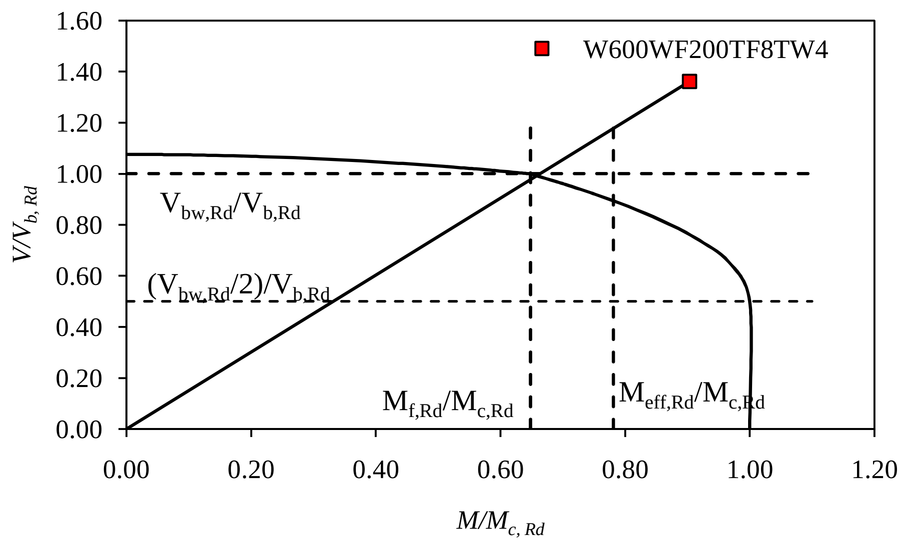

Figure 3.22: Bending and shear interaction curve (EN 1993-1-4, 2006) showing location of typical combined shear and bending failure (w_f = 200 mm, t_f = 8 mm, t_w = 4 mm; a = 600 mm).

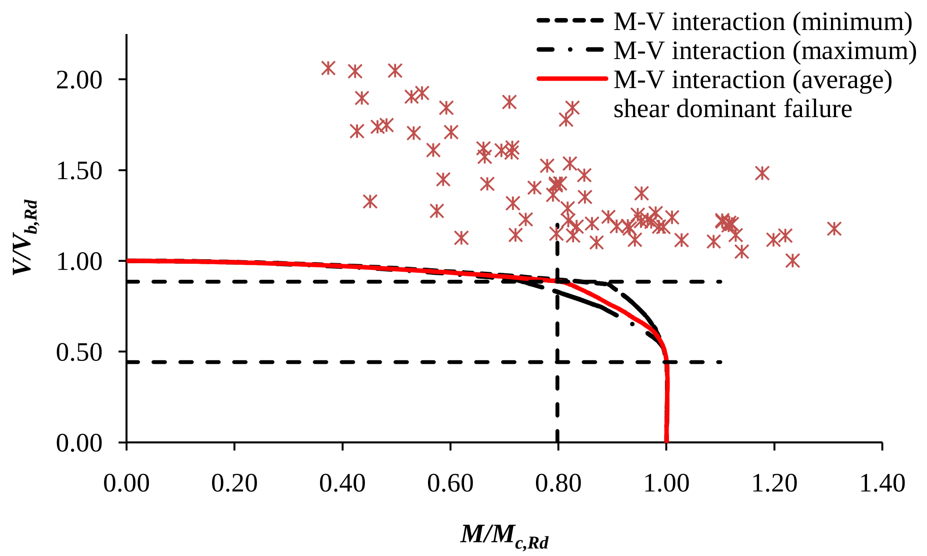

Figure 3.23: Comparison of FE results with moment-shear interaction curve from EN 1993-1-4 (2006/A1:2015).

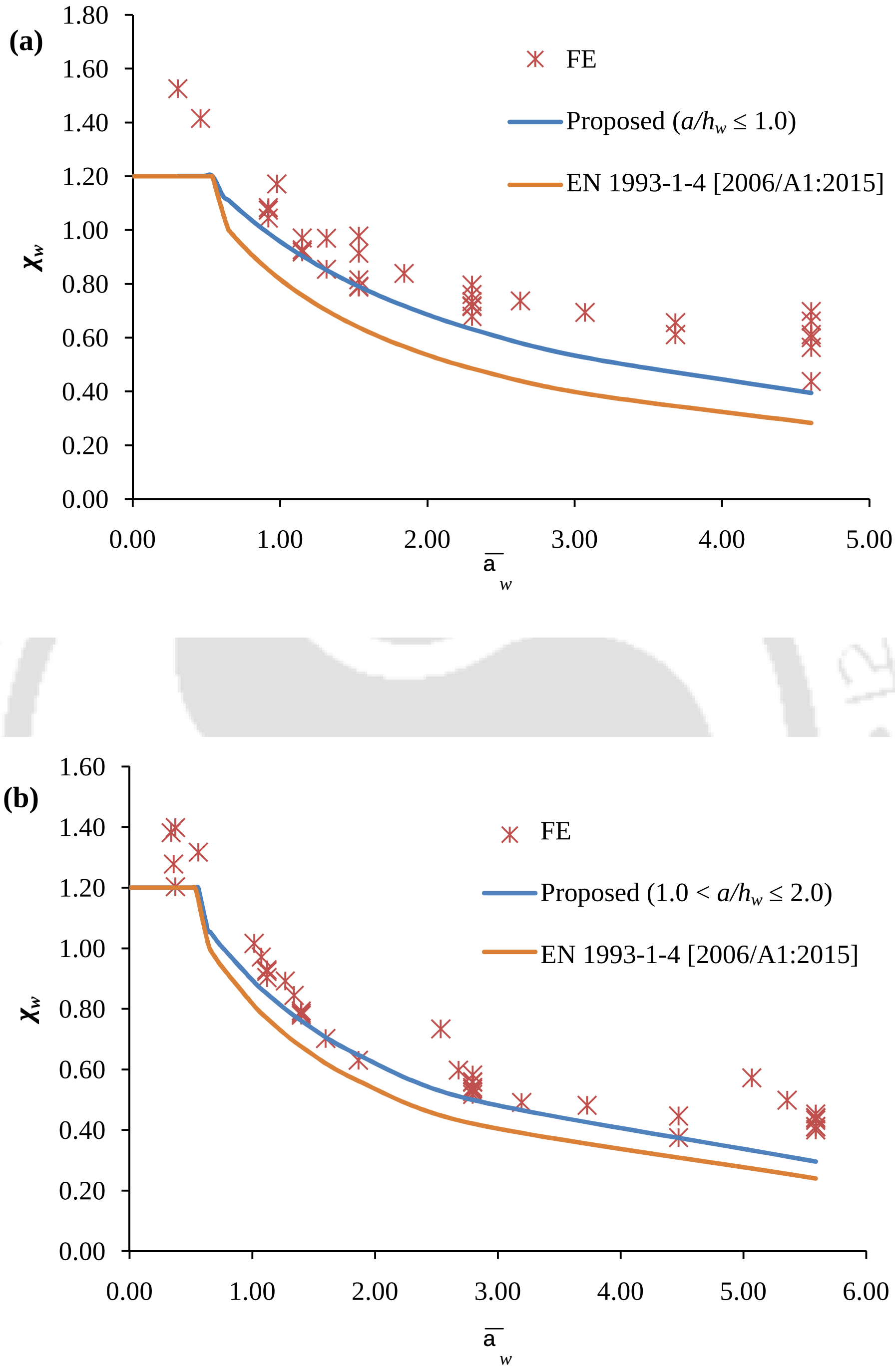

Figure 3.24: Comparison of FE and with EN 1993-1-4 (2006/A1:2015) shear design curve: a) $a/h_w \leq 1.0$ and b) $1 < a/h_w \leq 2.0$.

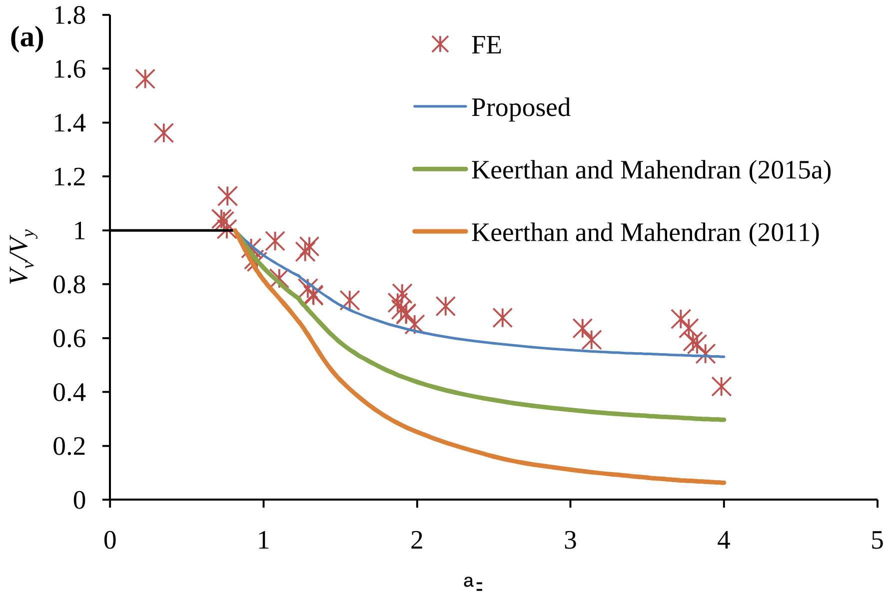

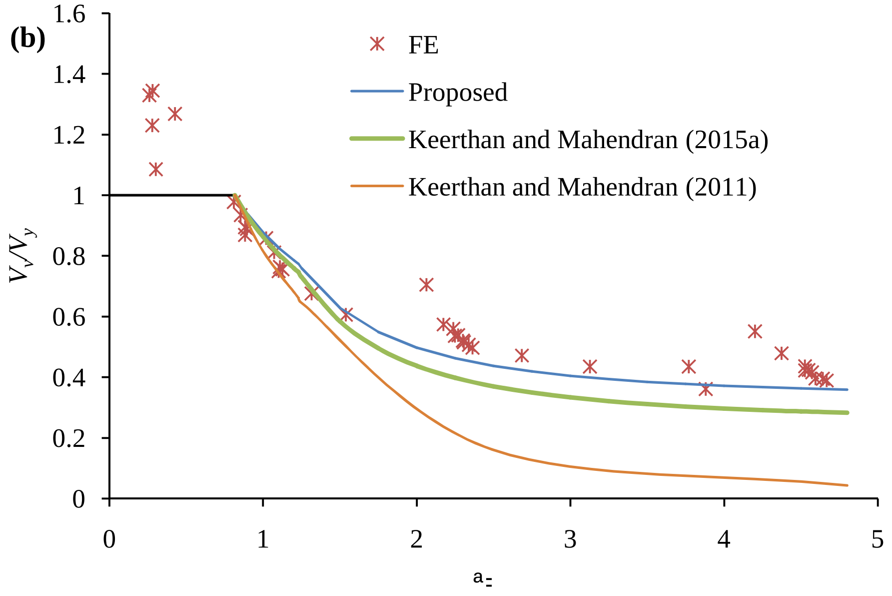

Fig. 3.25: Comparison of FE and with DSM shear design curve: a) $a/h_w \leq 1.0$ and b) $1< a/h_w \leq 2.0$.

CHAPTER 4

SHEAR BEHAVIOR OF SINGLE PERFORATED LEAN DUPLEX STAINLESS STEEL (LDSS) RECTANGULAR HOLLOW BEAMS

4.1 INTRODUCTION

As mentioned in the literature review (Chapter 2), under constrained space e.g. floor height or head room, it may become necessary or an option to provide perforation (or opening or cut outs) through beam webs to route building services ducts for electricity, water, air conditioning, heating, ventilations, process pipes, electrical and instrumentation cables; to accommodate secondary constructional elements like ceiling systems etc.; for inspection, repair and maintenance work; to improve the strength/weight ratio without significantly affecting the strength and serviceability considerations; and to reduce the stress transfer to beam-column joint (e.g. Hagen *et al.*, 2009; Feng and Young, 2015; Lagaros *et al.*, 2008). In addition, sometimes (multiple or repeated patterns e.g. castellated beams, cellular beams) perforations are provided for aesthetic reasons and economising materials (e.g. Pellegrino *et al.*, 2009). Earlier studies (see e.g. Uenoya and Redwood, 1977; Narayanan and Der-

Avanessian, 1984b; Shakerly and Brown, 1996; Liu and Chung, 2003; Brown and Yettram, 1986; Narayanan *et al.*, 1989; Hassanein, 2014; Tsavdaridis and D'Mello, 2011, 2012) have considered several perforated shapes *viz.*, circular, square, rectangular, on web perforated 'open' (e.g. I, C - sections) beams and observed a decrease in load capacity when compared to un-perforated (or solid) beams. Such perforations in the structural beams, can influence the membrane/plate stress redistribution in the webs, and can have adverse effect on the structural performance e.g. elastic stiffness, ultimate load capacity, ultimate load deformation; depending on the location, size and shapes of the perforations (Feng and Young, 2015; Ridley-Ellis, 2000; Shanmugam *et.al.*, 2002; Liu and Chung, 2003; Hagen and Larsen, 2009; Hassanein, 2014). As mentioned earlier (Section 2.3), to the best of author's knowledge, Ridley-Ellis (2000) was the first to report shear load capacity of rectangular hollow section (RHS) made of carbon steel, perforated at mid height of the beam web, through limited (i.e. d_o/h_w = 0.66 and 0.83, a/h_w = 3.5 and 4.37, h_w/t_w = 25, t_f/t_w = 1.0, where d_o = perforation diameter) experimental and FE studies. Hence, in this chapter, the earlier FE study (see Chapter 3) is extended to assess the effect of single circular perforation in the shear characteristic of LDSS rectangular hollow beams, in a systematic manner, considering a wide range of cross sectional parameters e.g. flange thickness, flange width, web thickness, shear span etc., again noting that the study is being performed on a relatively promising duplex steel (i.e. LDSS). Primarily, the effect of single perforation size / diameter and location (along longitudinal, transverse, and diagonals) are assessed with a focus on the shear load capacity (V_u/V_y), deformed shapes (or failure modes) etc. The effects of the perforation are presented parametrically in relation to web slenderness (h_w/t_w) and flange to web thickness ratio (t_f/t_w). The FE results are then compared with the currently adopted stainless steel European design code (EN 1993-1-4, 2006/A1:2015). Further, based on the current FE study, new design expressions for shear buckling factor are suggested. The suitability of the new design expressions are presented in the form of mean and COV.

4.2 NUMERICAL (FE) MODELLING

4.2.1 General

Similar FE modelling approach presented in the previous chapter (see Section 3.2) is again used to model the perforated LDSS rectangular hollow beams. The two-stage constitutive material model proposed by Gardner and Ashraf (2006) as mentioned in Section 3.2.5 has been used again to model the LDSS material. Local imperfection amplitude suggested by Gardner and Nethercot (2004c) for stainless steel is seeded using the mode shape given by lowest eigen mode, to idealise the geometric imperfection of the beam (details are given in Section 3.2.4).

4.2.2 Geometry and boundary conditions

A schematic representation of the beam geometry (cross section and elevation) along with the support and loading boundary conditions are shown in Figure 4.1(a & b). A single circular perforation of diameter d_o, located on one web of the left shear span is considered as marked in Figure 4.2a. Three sets of coordinate axes *viz.*, x-, y-axes (origin at lower left corner), d_1-axis (origin at top left corner), and d_2-axis (origin at top right corner) are used to define the location of the perforation centre (Figure 4.1b). The x-, y-, d_1- and d_2- axes are used for the longitudinal, transverse, tensile diagonal (subjected to tensile plate/membrane stress) and compression diagonal (subjected to compression plate/membrane stress) respectively. In the present study, only single side perforation has been attempted, hence the beam is not symmetric owing to the presence of the perforation. It may be mentioned that the study reported by Ridley-Ellis (2000), showed that the shear strength of doubly perforated (on opposite sides for web for a mid-height located perforations) are of ~67 and ~87% of comparable singly perforated rectangular hollow beam (for d_o/h_w = 82.5–66% respectively). A minimum clear distance of ~30 mm is maintained for perforations from the beam edges, so as to have reasonable FE elements around the perforation (discussed in the next sub-section 4.2.3), to avoid the results being influenced too closed edge boundary conditions, and possibly it is very unlikely to have such perforations very near to the edge, in real life applications.

4.2.3 Finite element mesh

Typical FE mesh of the perforated beam is shown in Figure 4.2b (d_o/h_w = 0.50; a/h_w = 1.0). Except for the region surrounding the perforation, similar global square mesh size (~18–25 mm) arrived through mesh convergence study for unperforated beam (see Section 3.2.3) are again used to model the geometry of the beam. In order to capture the local stress near the perforation edge, a widely reported fan-type mesh (see e.g. Ridley-Ellis, 2000; Hagen *et.al.*, 2009; Hagen, 2005; Liu and Chung, 2003; Paik, 2007; Pellegrino *et.al.*, 2009; Bowmick, 2014) pattern adjoining the circular perforation has been adopted. The fan-type mesh around the perforation is confined to a square of sides ~1.7d_o – 4d_o (achieved through 'partitioning' in Abaqus, 2009), thus resulting in 56 and 112 S4R elements around the circumference of the smallest and largest perforations respectively. It may be noted that the type of mesh arrangement adopted (i.e. global square elements in the periphery of the perforation) for the present study, the number of elements along the edge of the perforation is equal to those of elements located at the edge of the square region surrounding the fan-type mesh. Inside the partitioned square region, the number of elements radiating from perforation edge is in the range ~8–10. A uniform mesh size was seeded along the radial direction inside the partitioned square region. Studies using biased mesh (with mesh size getting finer towards the perforation edge) did not significantly alter the results, hence only uniform radial meshing was adopted. The total number of S4R elements adopted are in the range ~6500–7000 for short span beams (a/h_w = 1.0) and ~13800–14200 for long span beams (a/h_w =

2.0). The aforementioned mesh configuration are found to be optimum and sufficiently fine enough, and are arrived at after performing mesh convergence study through linear elastic eigen-value buckling analysis.

4.2.4 Parametric study

Shear behavior of the perforated LDSS hollow rectangular beams have been assessed considering the following ranges of key cross-sectional parameters: t_w = 2–30 mm, t_f = 6–150 mm; a = 600–1200 mm. The values of h_w and w_f have been fixed at 600 mm and 150–300 mm. These parameters result in the values of h_w/t_w = 20–300, a/h_w = 1 (short span) and 2 (long span), t_f/t_w = 3–5. It may be mentioned here that, as the current focus is to study the effect of perforation in the web, the parameter matrix is mostly limited to t_f/t_w = 5 (i.e thicker flange with respect to web), with more attention given to web slenderness (i.e. h_w/t_w). This is to cut-down the number of analyses, further, as discussed in Chapter 3 (see Figures 3.9 and 3.10), the variation of V_u/V_y with h_w/t_w has been observed to have increasing trend (depicted by nearly parallel shift of the V_u/V_y curve) with increasing values of t_f/t_w. Hence, it is expected that understanding the structural behaviour corresponding to t_f/t_w = 5, would provide reasonably good insight, which can be scaled for other values of t_f/t_w e.g. t_f/t_w = 4, 3 and 2. Three sizes of perforation are considered *viz.*, d_o=60, 180 and 300 mm, giving raise to d_o/h_w = 0.1, 0.3 and 0.5. The location of the perforation (i.e. the centre of the perforation) were varied from x/h_w = 0.2–0.8, y/h_w = 0.2–0.8, d_1/h_w = 0.2–1.2, d_2/h_w = 0.2–1.8, for longitudinal, transverse, tensile diagonal and compression diagonal respectively. It may be noted that for larger perforations, there the range of location variation would be reduced. In all, a total of 170 FE analyses have been investigated, with due focus on the load – transverse deformation at mid-span (V/δ), ultimate load (V_u), deformed shape (in the form of von-Mises contour plot over deformed shapes). In order to quantify the effect of perforation, results from perforated beam studies have been compared with those of corresponding unperforated (or solid), where d_o/h_w = 0.0 (d_o = perforation of zero size). First the typical failure modes and shear variations with perforation size (d_o/h_w) and locations (x/h_w, y/h_w, d_1/h_w and d_2/h_w) are presented, followed by shear capacity curves (V_u/V_y vs h_w/t_w) for centrally located perforations. Lastly, in order to compare the present FE results with the predictions from the Euro code (EN 1993-1-4, 2006/A1:2015), selected results which exhibit shear-dominant failure modes (see Section 3.3.4) are presented in the form of shear buckling capacity (χ_w) variation with non-dimensional slenderness ratio ($\bar{a}_w$), for two sizes of perforations (d_o/h_w = 0.1 and 0.5). Based on the FE study, proposed design curves are presented finally.

4.3 RESULTS AND DISCUSSION

Von-Mises contour plot and variation of σ_{vm}/σ_y ($\sigma_y = \sigma_{0.2}$) at ultimate shear (V_u) with normalised distance i.e. distance/h_w, where σ_{vm} is the von-Mises stress, are shown in Figures 4.3 and 4.4 for both short (a/h_w = 1.0) and long span (a/h_w = 2.0) 'unperforated' beams respectively, (t_f/t_w = 5, h_w/t_w = 300). Variation of $\sigma_{vm}/\ \sigma_y$ is plotted along the x-, y-, d_1, and d_2 axes (indicated in Figures 4.3b and 4.4b). The contour of $\sigma_{vm}/\ \sigma_y \geq 1$ (red colour), is seen to be located along the diagonal direction and this diagonal contour is indicative of the tension band. The size of this highly stressed tension band measured along x- (i.e. c_h) and y- (i.e. c_v); and d_2- (i.e. c_d) axes are found to be ~ 200, 176 and 367 mm respectively, for the short span, whilst they are ~ 360, 115 and 380 mm respectively, for the longer span. These values of c_h are found to be slight higher than those tension band width predicted by EN 1993-1-5 (2006) i.e. ~ 25% and 12.5% higher for the short and long spans respectively. From Figures 4.3b and 4.4b, it can be seen that there is little variation in the value of σ_{vm}/σ_y along d_1 axis, with σ_{vm}/σ_y = ~1.2. This is expected because, the diagonal tension band is highly stressed (the exceedance of σ_{vm} over σ_y is due to strain hardening) throughout its length. Whereas in the other axes, a drop in the stress profile can be observed at locations away from the tension band. The initial drop in σ_{vm}/σ_y along d_2 axis (around d_2/h_w = ~0.12 and 0.35–0.44 for a/h_w = 1 and 2 respectively) near the loaded region may be related to the localised buckling. The distribution of stress is likely to be influenced by the location and size of the perforation on the web, leading to a change in the value of V_u for the perforated beams. The effect of perforation on V_u is presented in the following sub-sections, as a function of the perforation size and their locations along various axes mentioned above.

4.3.1 Variation of perforation size (d_o)

The effect of perforation size (d_o) for both the short (a/h_w = 1) and long (a/h_w = 2) spans are presented in Figures 4.5, and 4.6, and 4.7 and 4.8, respectively. Figure 4.5 shows variation of V/V_y (i.e. shear load normalised with shear yield capacity of solid webs) with δ (mid-span deofrmation) and von-Mises contour plot for centrally located perforation corresponding to d_o/h_w = 0.0, 0.1, 0.3 and 0.5 for the short span (x/h_w = 0.5, y/h_w = 0.5; t_f/t_w =5; h_w/t_w = 300). It can be observed from Figure 4.5a that the overall behaviour (consisting of rising curve, post-ultimate falling-plateau and post-ultimate rapid-falling curve) of V/V_y, is maintained for all the perforated beams, similar to that of the unperforated beam. Such type of behaviour is typical for higher value of t_f/t_w with lower values of t_w (t_f/t_w = 5 and t_w = 2 mm in this case), as also discussed in Section 3.3.1. Further, it is seen that V/V_y < 1.0, suggesting that buckling of webs preceded the net web section is yielded, a situation associated with slender webs. From Figure 4.5a, it can be seen that the ultimate shear capacity (V_u/V_y) is found to decrease with increasing the perforation size; with the highest shear capacity associated with the unperforated/solid beam. In the first instance this is consistent with the removal of the web (i.e. perforated area) material, thereby reducing the shear capacity. However, it can be seen that the onset of rapid-falling curve (marked M2, L2 corresponding to d_o/h_w = 0.1 and 0.5 respectively) is getting delayed (or occurring at a later value of δ) with increasing perforation size (see for example Shanmugam *et al.*, 2002) e.g. the value of δ_{RF} (mid-span displacement corresponding to onset of rapid-falling curve; see Figure 4.5a) increased by ~46% for 400% increase (d_o/h_w = 0.1–0.5) in perforation size. In contrast, the mid-span deformation corresponding to ultimate shear (δ_u) remains nearly the same for the perforated beams, although it is lesser than that of solid beam by ~47%. For the perforation parameters considered, the drop in shear (V_{uRF}) from ultimate to the onset of rapid-falling curve i.e. V_{uRF}/V_y (= V_u/V_y – V_{RF}/V_y) are respectively ~19% and 21% for perforation sizes of d_o/h_w = 0.1 and 0.5. These values are slightly higher than that of the unperforated beam case, where it is obtained as ~ 13%. The comparison of the von-Mises contour plot for two perforated beams corresponding to d_o/h_w = 0.1 and 0.5 with that of unperforated beam is shown in Figures 4.5b. It can be seen that with perforation, the stress distribution in the diagonal tension band is altered. At the ultimate shear (V_u), a discontinuity in von-Mises stress contour, corresponding to the highly stressed tension band (coloured red, σ_{vm}/σ_y > 1.0) is introduced due to perforation (see M1, L1 as compared to S1 in Figure 4.5b), with the area of the discontinued highly stressed tension band visibly reduced (see L1) for the largest perforation considered. In the case of solid beam, as perforation is absent, the distribution on either shear span is symmetric both at ultimate (see S1) and post-ultimate deformations (see S2 and S3). However, due to the presence of perforation on one shear span (left side), the stress distribution is no longer symmetric on either side of the mid-span (see M1-M3; L1-L3 as compared to S1-S3). For perforated beams, at V_u, it can be seen that, the width of the highly stressed tension band on the un-perforated web (i.e. on the right side shear span) is getting reduced, with signs of distressing on the top flange of the un-perforated side as compared to that of the perforated side. This may be because of reduction in the shear resistance of the perforated web panel, thereby forming a mechanism in which the proportion of load resisted by the top flange located near the left support is enhanced. This led to the initiation of yielding of the top flange near the support and the bottom flange at the mid-span resulting in plastic-hinge type deformations near the support (see e.g. M2 and L2 in Figure 4.5b). As the plastic hinge formation is initiated at top and bottom flanges on the perforated span, redistribution and relaxation of stress can be observed on the unperforated span side (see M2 and L2 in Figure 4.5b). This plastic hinge formations on the top and bottom flanges where the diagonal tension band anchored is primarily associated with the onset of rapid-falling curve (M2, L2 in Figure 4.5a), leading to a significant loss of load resistance with enhanced lateral web deformation (see the corrugated buckling along the diagonal tension band) of the web. After the onset of the rapid-falling curve, it can be seen that the stress in the unperforated span is very much relaxed/relieved, while the highly stressed region (or the diagonal tension band) is now concentrated along the diagonal tension band, top-flange near the support, and bottom flange near the midspan, of the perforated span. The increase in δ_{RF} with perforation size (mentioned above) may now be related to the presence of relatively lesser web material (a quantity which decreases with increasing the perforation size) in the tension band, to transfer the tensile stress on to the top and bottom flanges, through anchorage, whereby, a relatively higher mid-span deformation (till δ_{RF}) is required to initiate yielding on the flanges. In the case of unperforated beam, the relatively higher value of δ_{RF} (comparable to that of perforated beam with perforation size, d_o/h_w = 0.5) is essentially due to both the spans resisting the shear load, hence requiring the beam to undergo larger transverse deformation, before activating the yielding of flanges on both the spans. Figure 4.6 presents variation of V_u/V_y with d_o/h_w, for slender (h_w/t_w = 300 i.e. t_w = 2 mm) and stocky(h_w/t_w = 20 i.e., t_w = 30 mm) webs. The variations are shown for two flange thicknesses (t_f/t_w = 5 and 3) i.e. t_f = 10 and 6 mm; and 150 and 90 mm, corresponding to t_w = 2 mm and 30 mm, respectively. It can be observed from Figure 4.6a that, there is a nearly linear decrease in the value of V_u/V_y of ~ 25% and 23% with 500% (i.e. d_o/h_w = 0.0–0.50) increase in perforation size, for t_f/t_w = 5 and 3, respectively (h_w/t_w = 300). The current finding i.e. near linear drop of shear capacity with increasing perforation sizes, also agrees with those reported studies in the literature e.g. FE studies on plates (Rockey *et al.*, 1967; Rockey *et al.*, 1981; Roberts and Azizian, 1984; Narayanan and Der-Avanessian, 1984b; Paik, 2007), plate girders (Narayanan and Der-Avanessian, 1986; Shanmugan *et al.*, 2002; Hagen *et al.*, 2009; Hassanein, 2014); experimental study on plate girders (Narayanan and Rockey, 1981). The reduction in shear capacity reported for a/h_w = 1 and for 50% (d_o/h_w = 0.5) perforation size are ~ 38%, 50%, 46%, 40%, 23-51%, 48-50%, 54%, 41-54%, by Narayanan and Rockey (1981), Roberts and Azizian (1984), Narayanan and Der-Avanessian (1984b), Narayanan and Der-Avanessian (1986), Shanmugan *et al.*, 2002, Paik (2007), Hassanein (2014) respectively. Most of these values is ~ twice the values observed in Figure 4.6a (~21-23%), and may be seen as near agreeable, given the consideration that the present analyses are focussed on perforations provided in one web only. It is seen from Figure 4.6b, that the decreases are ~ 8% and 10% for h_w/t_w = 30 (i.e. stockier web), when t_f/t_w = 5 and 3 are considered respectively. It thus suggests that perforation has relatively higher shear reducing effect for slender webs. This observation is in accord with the results of Paik (2007), Roberts and Azizian (1984), Narayanan and Rockey (1981), Hagen *et al.*, (2009), Narayanan and Der-Avanessian (1986), Hassanein (2014), Shanmugan *et al.*, (2002). This may be because, as the webs gets slender, shear web buckling with a well defined tension band would be the main failure mode of the web, thereby any removal of material in the tension zone (note that perforation is located in the center and hence, well within the tension band area), is likely to have more effect on shear capacity reduction. In Figure 4.5b, the average width of the yielded diagonal tension band for unperforated web is ~ 360 mm (c_d; see Figure 4.3a), which is nearly equal to the diameter of the largest perforation ($d_{o,largest}$ = 300 mm) considered. On the other hand, when web is stockyenough e.g. h_w/t_w = 20 (or t_w = 30 mm as in the present case), web yielding is likely to prevail (see Fig 3.9) rather than the shear web buckling failure mode; hence the total web area (which is yielded) participates in the resistance of load, and perforation forms a small fraction of area reduction.

For example, in Figure 4.6b, it can be observed that for the stocky web (t_w = 30 mm), at ultimate shear, the web is almost fully yielded in the unperforated beam, and this situation remains nearly the same even after perforation, whereas the stress around the perforation is significantly modified and appears that the yielded web area is reduced, so as to reduce the shear capacity; for both the thicknesses of flange (t_f/t_w = 5 and 3) analysed. The drop in shear capacity with decrease in t_f/t_w for perforated beams is again consistent with the similar behaviour observed for the case unperforated beams (see Figure 3.9). The observed effect of flange thickness (or t_f/t_w) in reducing the shear capacity has also been reported by Narayanan and Rockey (1981), Shanmugan *et al.*, (2002), Hassanein (2014), Narayanan and Der-Avanessian (1986). Similar observations have also been made for longer shear span ratio i.e. a/h_w = 2, and are presented in Figures 4.7 and 4.8. A near linear reduction in shear capacity is seen for both the slender and stocky webs. For 500% increase in perforation size the reduction in V_u/V_y is ~25% for slender web (t_w = 2mm or h_w/t_w = 300), for both the flange thickness considered (t_f/t_w = 4 and 5) (see Figure 4.8a). However the reduction appears to be a milder in the case of thicker web (h_w/t_w = 20 or t_w = 30mm), e.g. a drop of ~ 2.7% and 1.7% can be observed in shear capacity for t_f/t_w = 5 and 4 respectively. This observation is consistent with the difference in shear capacity observed for the unperforated case (see Figure 3.10). Furthermore, as seen in Figure 4.6, and mentioned above, for the longer span also, the relatively lesser effect of perforation for the thicker web is consistent with observation in Figure 4.8 where even such large perforation such as d_o/h_w =0.5 did not significantly alter the yielded web region. Whilst a decrease of ~ 15-39% in shear capacity can be seen in the present case for d_o/h_w = 0.50 for an increase of shear span (a/h_w) from 1 to 2 (see Figures 4.6 and 4.8), a marginal or no significant change in the critical shear stress coefficient is seen for perforated plates, when a/h_w is increased from 1 to 1.5 (Narayanan and Der-Avanessian, 1984b). It may be mentioned that Narayanan and Der-Avanessian (1984b) reported an increase of ~23% in shear buckling coefficient of 'unperforated' plate when a/h_w is increased from 1.0 to 1.5, hence the findings of perforated plate (mentioned above) appears to contradict. On the other hand, for perforated plates subjected to 'edge' shear loading, it is shown that the shear capacity increases with increasing a/h_w (Paik, 2007). This may be related to the increase in edge loading area (along the two span edges) with increasing span.

4.3.2 Variation of location

4.3.2.1 Longitudinal direction (*x*-axis)

In Figure 4.9, typical variation of V_u/V_y with δ and von-Mises contour plots corresponding to ultimate shear and onset of rapid-falling curve, for three perforation locations *viz.*, x/h_w = 0.20, 0.50 and 0.80, along longitudinal axis, keeping the transverse location of the perforation at mid height of the beam i.e. y/h_w = 0.5 (a/h_w = 1), is shown. The plots in Figure 4.9b corresponds to a perforation size, d_o/h_w = 0.10. A value of x/h_w = 0.50 corresponds to perforation located at the center of the web, while x/h_w = 0.20 and 0.80, to the left and right of the web center, respectively. From Figure 4.9a, it can be seen that perforation located at the center of the web (x/h_w = 0.5) predicted the lowest value (~3%) of V_u/V_y, whilst the perforations located on the left and right of the web center predicted higher values. Further, the values of V_u/V_y for perforation located at x/h_w = 0.2 and x/h_w = 0.8 are found to be similar, and these values are observed to be close to that of the unperforated beam. It is also observed that in spite of the prediction of similar ultimate shear capacities between unperforated and perforated beams (especially for the smaller perforations which are located at regions away from the web center e.g. for x/h_w = 0.2 and x/h_w = 0.8), a much delayed occurrence of the onset of rapid-falling curve resulted for the unperforated case i.e. δ_{RF} is increased by ~40% for the unperforated beam. It can also be seen that perforations corresponding to x/h_w = 0.2 and 0.8 predicted similar values of δ_u and δ_{RF} (consistent with similar predicted values of V_u/V_y), however, they showed ~65% higher in δ_u, as compared to that of x/h_w = 0.5 case. Notwithstanding the difference in δ_u, it is found that irrespective of the longitudinal location, δ_{RF} appears to be similar. From Figure 4.9b, it can be seen that at the ultimate shear capacity, the region of highly stressed diagonal tension region remains mostly unaffected by the presence of perforation at x/h_w = 0.2 and x/h_w = 0.8, although the stress distribution is disturbed by the presence of the perforation at x/h_w = 0.5 (see L1, C1, R1 of Figure 4.9b). It can be seen from L1 and R1 (Figure 4.9b) that the off-center perforations are located at the edge of the highly stressed region, suggesting that their effect on the shear capacity would be similar to that of the unperforated beam as discussed above (see Figure 4.9a). Again, as the perforation size is small (d_o/h_w = 0.1), it appears that, at δ_{RF} (see L2, C2, and R2 of Figure 4.9b), the area of highly stressed diagonal tension zone appears to be similar; and hence the activation of the yielding top and bottom flanges (at zones where the diagonal tension band is anchored), at similar mid-span deformation.

Variation of the V_u/V_y with perforation location (x/h_w) along the longitudinal or x-direction is shown in Figure 4.10, for 400% increase in perforation size from d_o/h_w = 0.1 (t_f/t_w=5, h_w/t_w=300, a/h_w = 1). A horizontal line is also plotted corresponding to unperforated case (d_o/h_w = 0.0) for comparison. It can be observed from Figure 4.10 that, maximum decrease in the value of V_u/V_y is obtained for perforations located in the highly stressed diagonal tension band, with the maximum reduction notably occurring for x/h_w = 0.5 for all the perforations considered. For the smallest perforation size considered, as the perforations are moved away from the span-center (or x/h_w = 0.5), either towards the support (x/h_w < 0.5) i.e. to the left, or towards the midspan i.e. towards the right, the reduction in shear capacity gradually reduces and reaches the value of V_u/V_y corresponding to that of unperforated case at x/h_w = 0.2 or x/h_w = 0.80. With larger perforations e.g. d_o = 180 and 300 mm (or d_o/h_w = 0.3 and 0.5), there appears to be have insignificant change in the values of V_u/V_y for the perforations located over a region of 0.30 ≤ x/h_w ≤ 0.70 (i.e. ~50% of the middle shear span). This may be because, as the perforation size gets larger (e.g.

$d_o/h_w \geq 0.30$), significant changes in the reduction of tension band area (as a result of perforation location), may not be expected when the perforation is moved away for very short distance, from the center of the web or tension band (i.e. $x/h_w = 0.5$). For example, when the perforation size of 180 mm and 300 mm are moved by a distance equal to ~60 mm on either side of the span center (or $\Delta x/h_w = 0.10$), it corresponds to $0.3d_o$ and $0.2d_o$ respectively, and they are likely to be still within the major zone of influence of the tension band, hence predicted similar values of shear capacity with that of $x/h_w = 0.50$. In general, the reduction in shear capacity appears to follow a near linear trend with increasing perforation size i.e. ~20% reduction in V_u/V_y for 400% increase in perforation size (from $d_o/h_w = 0.1$), for perforations located along the longitudinal directions passing through the mid web height (y/h_w=0.5). In particular, it can also be seen that the drop in shear capacity with the $d_o/h_w = 0.5$ perforation size located at the mid span is found ~24.6% as compared to that of unperforated case.

Figure 4.11 shows the variation of V_y/V_u with δ and von-Mises contour plot for longer span beam i.e. $a/h_w = 2.0$, for three longitudinal location of perforation i.e. $x/h_w = 0.2$, 1.0 and 1.8 ($t_f/t_w = 5$, $y/h_w = 0.5$). From Figure 4.11a, it can be seen that, the value of V_u/V_y for perforations located at $x/h_w = 0.2$ and 1.8 are found to be similar (for the beam parameters considered), but higher than that corresponding to $x/h_w = 1.0$ by ~2%. This may be because, when the perforation is at $x/h_w = 0.20$ & 1.8, it appears to be considerably away so as not to significantly influence the diagonal tension band (see L1 of Figure 4.9b). The perforation located at $x/h_w = 1.0$ have interaction with the diagonal tension band, thus bringing the reduction value of V_u/V_y, although the distribution of the highly stressed diagonal tension band is not similar (see L1 and R1 to C1 in Figure 4.11b).

Variation of V_u/V_y with x/h_w are plotted for $a/h_w = 2.0$, for perforation size ranging from $d_o/h_w = 0.1$–0.5 in Figure 4.12 ($t_f/t_w = 5$, $y/h_w = 0.5$). As mentioned before, for the smallest perforation size considered i.e. $d_o/h_w = 0.1$, there appears to be no significant change in the value of V_u/V_y value with longitudinal variation of perforation locations, and V_u/V_y value is found to be ~0.43, which is ~4% lesser than that of the unperforated case. This may be because, of the lower shear capacity associated with larger span as compared to short span (Fig. 4.10), in addition to the small perforation (d_o/h_w = 0.1) size considered. However, as observed in the case of short span beam (see Figure 4.10), a near linear decreasing value of V_u/V_y (~20%) is seen for increasing perforation size (~400% from d_o/h_w = 0.10), for perforation located at $0.60 \leq x/h_w \leq 1.20$ (i.e. ~50% of the middle shear span). However, unlike the case of short span beam (i.e. a/h_w = 1.0; see Figure 4.10), the unperforated shear strength is not recovered for the smallest perforation (d_o/h_w = 0.1) even when the perforation is close to the support or the mid-span of the beam (say x/h_w = 0.20 or 1.8). As in the case of short span beam (see Figure 4.10), a slight increase in the value of shear capacity, for perforations located away from the major influence of the diagonal tension band i.e. towards the left and right ends of the shear span i.e. x/h_w =0.2, and 0.8. Similar to that of the short span beam, for the long span beam also, the reduction in shear capacity corresponding to mid shear span located perforation of size d_o/h_w = 0.5, is found to be ~24.4%, when compared to the unperforated case.

4.3.2.2 Transverse direction (*y*-axis)

Variation in the location of perforation along the transverse direction (*y*-axis) along the mid shear span (i.e. x/h_w = 0.5) is presented for perforation located at y/h_w = 0.2, 0.5 and 0.8 (d_o/h_w = 0.1, t_f/t_w = 5) in the form of V/V_y vs δ plot and corresponding key von-Mises contour plots in Figure 4.13. As expected, for the perforation located at the mid of highly stressed diagonal tension band, the value of V_u/V_y and δ_u are found to be the lowest (although the difference in the values of V_u/V_y is not significant ~3%) as compared to that corresponding to perforations located on top and bottom (~1.5%) of it i.e. towards the top and bottom flanges and away from the tension band (note the location of the perforation at the edge of the highly stressed diagonal zone in B1 and T1 in Figure 4.13b). From Figure 4.13a, it can be observed that the values of V_u/V_y and δ_u (also V_{RF} and δ_{RF}) are closed and this agrees with the similarity in stress distribution as shown in Figure 4.13b (B1, B2 and T1 and T2).

Figure 4.14 shows the variation of V_u/V_y with y/h_w (y/h_w = 0.5; t_f/t_w = 5, h_w/t_w = 300, a/h_w = 1), for three perforation sizes i.e. d_o/h_w = 0.1, 0.3 an 0.5. It can be seen that no significant variation in V_u/V_y can be seen for 0.30 ≤ x/h_w ≤ 0.6 (i.e. ~60% middle web height), however, a near linear reduction (~20%) in shear capacity can be observed for 400% increase in perforation size (from d_o/h_w = 0.1). A slight increase in the shear capacity as perforations are moved away from the significance influence of the tension band i.e towards the top and bottom flanges i.e. y/h_w = 0.2, and 0.8 is also observed, similar to that of the variation of perforation in longitudinal direction (see Figure 4.10). When the smallest perforation (d_o/h_w = 0.1) is located close to flanges (i.e. y/h_w = 0.2 or 0.8) i.e. away from the mid height of the web, the reduction in shear capacity is found to be ~ 1.4% that of the unperforated case.

The effect of transverse variation in perforation location for the long span (a/h_w = 2.0) is presented in Figure 4.15, (d_o/h_w = 0.1, x/h_w = 1.0; t_f/t_w = 5, h_w/t_w = 300) in the form of V/V_y vs δ and von-Mises contour plots. Again, like the case of short span beams (see Figure 4.13), no significant change in the V_u/V_y values can be seen for the three locations of perforation considered (y/h_w = 0.2, 0.5, 0.8), for the small perforation size (d_o/h_w = 0.1). Variation of V_u/V_y with y/h_w for increasing perforation size is shown in Figure 4.16. Again, similar to that of short span case (a/h_w =1), there appears to have insignificant or little influence of the transverse variation of perforation location on the shear capacity, for all the perforation sizes considered. And similar near linear trend in the reduction of the shear capacity can be observed for increasing perforation size for 0.40 ≤ y/h_w ≤ 0.60. It can also be seen that the reduction in shear capacity for the smallest perforation size (i.e. d_o/h_w = 0.10), is ~

4.4% (note that it is ~1.4% for the short span, see Figure 4.14) as compared to that of unperforated beam shear strength, when the perforation is located close to the flanges (or away from the diagonal tension band), as in the case of transverse variation for short span beams (see Figures 4.14 & 4.12).

4.3.2.3 Tensile diagonal direction (d_1-axis)

The effect of variation in the location of perforation of size d_o/h_w = 0.1 along the tensile diagonal direction (i.e. along d_1-axis at d_1/h_w = 0.2, 1.0, and 1.4) is presented in Figure 4.17, in the form of V_u/V_y variation with δ and corresponding von-Mises contour plots at V_u for short span beam (a/h_w = 1.0). From Figure 4.17, it can be observed that for the values of d_1/h_w considered, there appears to be no significant change in the value of V_u/V_y, δ_u and δ_{RF} (see Figure 4.17a). This results also agrees with the relatively nominal or little variation of critical shear stress coefficient (as compared to perforations located along the compression diagonal) reported by Narayanan and Der-Avanessian (1984b) in their shear studies on perforated plate with circular perforations (d_o/h_w = 0.33; a/h_w = 1.0). From the von-Mises stress contour plot at V_u (B1, C1 and T1 in Figure 4.17b), it can be seen that distribution of the highly stressed band is seen to be similar for beams corresponding to perforations located at d_1/h_w = 0.2 and d_1/h_w = 1.4, although slightly different in distribution pattern with that corresponding to d_1/h_w = 1.0. However, the average area of the highly stressed region at V_u, appears to be not too different, resulting in similar values of V_u/V_y. Figure 4.18, variation of V_u/V_y with d_1/h_w are presented for perforation sizes, d_o/h_w = 0.1, 0.3 & 0.5. It can be observed that, there appears to be not significant effect of the perforation location (along d_1-axis) on the shear capacity, for all the perforation sizes considered. At first, this may be related to the size of the diagonal highly stressed tension band being nearly uniform, with almost constant stress level all along the diagonal for the unperforated case (see Figure 4.3). Hence any perforation located along the tensile diagonal is likely to have similar kind of effect on the shear capacity, as long as the perforation size remains unchanged, although a change in the pattern of the stress distribution may be observed as a result of the inclusion of perforation in the web.

Figure 4.19 shows the effect of perforation location along the tensile diagonal for the long span (a/h_w = 2.0) beam (t_f/t_w =5, h_w/t_w = 300; d_o/h_w = 0.1) in the form of V_u/V_y variation with δ and von-Mises contour plots at V_u. Like the case of short span beam (discussed above), no significant effect on V_u/V_y, δ_u and δ_{RF} can be observed when the perforation of size d_o/h_w = 0.1 is moved along the tensile diagonal. In Figure 4.19b, it can be seen that at V_u, the area of highly stressed diagonal tensile band appears to be similar, indicative of the same shear capacity (see B1, C1 and T1). In Figure 4.20, variation of V_u/V_y with d_1/h_w is presented for various sizes of the perforations i.e. d_o/h_w = 0.1, 0.3 and 0.5. Although the values of V_u/V_y are lower as compared to the short span beam (see Figure 4.18), similar pattern in the variation of V_u/V_y can again be seen for the long span case i.e. V_u/V_y values remain nearly unaffected for different locations of the perforations along the tensile diagonal. As stated for the case of short span, this behaviour may again be related to the case of unperforated beam (see Figure 4.4) where nearly uniform diagonal tensile band is seen with almost constant value of stress, and hence a similar structural response is expected when perforation are made along the tensile diagonal.

4.3.2.4 Compression diagonal direction (d_2-axis)

The effect of perforation location along the compression diagonal i.e. d_2-axis is presented in Figures 4.21, for d_o/h_w = 0.1, in the form V_u/V_y vs δ and von-Mises contour plots at V_u, and post-V_u deformations, for short span beam (a/h_w = 1.0, t_f/t_w =5, h_w/t_w = 300), considering d_2/h_w = 0.2, 0.7 and 1.0 perforation locations. From Figure 4.21 it can be seen that perforations corresponding to d_2/h_w = 0.2 and 1.0

gave similar values of V_u/V_y, δ_u and δ_{RF} (see Figure 4.21a), also the value of V_u/V_y is found to be similar to that of unperforated case. This may be because, the perforation size (d_o/h_w) is small are located outside the influence of the highly stressed diagonal tension band (see B1 and T1 in Figure 4.21b). However, it can be noticed that post-V_u behaviour (e.g. δ_{RF}) is much shorter for the perforated beam as compared to that of unperforated beam (Figure 4.21a). As discussed before, this is essentially due to the presence of perforation which allowed enhanced web buckling (leading to more transverse deformation of the beam) on the perforated beam span, thereby initiating the formation of yielded zones where tension band is anchored. However, as the perforation corresponding to d_2/h_w = 0.7 is seen to affect the distribution of the highly stressed diagonal tension band, resulting in the reduction (~2.9 %) of the shear capacity as compared to those of d_2/h_w = 0.2 and 1.0. Variation of V_u/V_y with d_2/h_w are plotted in Figure 4.22 for d_o/h_w = 0.1, 0.3 and 0.5. It can be seen that the reduction in V_u/V_y is seen to be larger for central region i.e. ~0.50 ≤ d_2/h_w ≤ 1.0, whereas the reduction gets smaller on either side of the central region. This behaviour may be related to the von-Mises stress distribution along d_2 axis, for unperforated beam as shown in Figure 4.3b, where maximum von-Mises stress is located in the central region (corresponding to the highly stressed diagonal tension band). Any perforation along this central region is likely to have the lowest, yet similar values of reduction in shear capacity within the tension band. Outside this central region, a reduced reduction is expected with perforation. Similar behaviour i.e. drop in critical shear stress coefficient when the location of the circular perforation is changed along the compression diagonal, towards the mid-diagonal (or web center), has been reported by Narayanan and Der-Avanessian (1984) in their shear studies on perforated plate (d_o/h_w = 0.33; a/h_w = 1.0). Tests performed on plate girders with circular openings by Narayanan and Der-Avanessian (1984a) suggested that perforations located close to corners (thus making d_2/h_w smaller) in the compression diagonal could provide higher shear capacity; in accord with the present finding.

Figure 4.23 presents the effect of perforation (d_o/h_w = 0.1) location along the compression diagonal (d_2-axis) for long span beam (a/h_w = 2.0; t_f/t_w =5, h_w/t_w = 300). Variation of V_u/V_y with δ and von-Mises contour plot at V_u and post-V_u are plotted in Figure 4.23a and 4.23b respectively, for d_2/h_w = 0.2, 1.1 and 1.8. Similar to the case of short span beam (mentioned above), both perforations (d_2/h_w = 0.2 and 1.8) located much outside the zone of influence of the highly stressed diagonal tension band, showed similar/identical values of V_u/V_y (~0.44). In Figure 4.24, variation in V_u/V_y with d_2/h_w for various perforation sizes are plotted. It can be observed that perforations located in the central region ~1.0 ≤ d_2/h_w ≤ 1.5, corresponding to the highly stressed diagonal tension band, the reduction in V_u/V_y is nearly same and decreases on either side of this central region. The size of this region may be related to the size of the highly stressed region (σ_{vm}/σ_y > 1.0) as depicted in Figure 4.4b for the unperforated case. As expected, the values of V_u/V_y for the long span are seen to be lower than those of short span beam (see Figure 4.22). It is also noticed that, in general, beams with perforations in the compression diagonal appears to have slightly higher shear capacity as compared to perforations located in the tension diagonal (see Figures 4.18, 4.22, 4.20, 4.24). This effect is relatively more visible in the case of long span i.e. for a/h_w = 2.0. Similar observation has also been reported by El-Khoriby *et al.*, (2016) based on their study on tubular flange plate girders with square web perforations.

4.3.3 Variation of V_u/V_y with h_w/t_w

The effect of web slenderness (h_w/t_w) on the shear capacity is presented in Figures 4.25 and 4.26 for short (a/h_w = 1.0) and long (a/h_w = 2.0) spans respectively, for centrally (x/h_w = y/h_w = 0.5) located two perforation sizes i.e. d_o/h_w = 0.1 and 0.5 (t_f/t_w = 5). For comparison the corresponding results for unperforated beams are also plotted, as benchmark curve. A decrease in the shear capacity (V_u/V_y) with increasing values of web slenderness (h_w/t_w) can be seen for both the perforated short and long span beams, similar to that of unperforated beams. Similar observations have been reported in circular perforated plates subjected to shear loading by Robert and Azizian (1984), in circular perforated I-section steel girders by Hagen *et. al.*, (2009) and Shanmugam *et. al.*, (2002), and in square perforated tubular flange I-section steel girders by Hassanein (2014). In general, for the case of slender webs with $h_w/t_w \geq \sim 75$, there appears to be a near parallel decrease in the values of V_u/V_y, for 400% increase in perforation size (from $d_o/h_w = 0.1$), for both the short and long span beams. The parallel drop also indicates that, the percentage reduction decreases with decreasing in h_w/t_w ratios, in other words, the effect of perforation in the reduction of shear capacity is felt most when the web become slender.

For example, the reduction in shear capacity as compared to that of unperforated beams, considering $d_o/h_w = 0.5$ are ~ 19.2% and 24.6% for $h_w/t_w = 75$ and 300 respectively, for the short span beam, and for the long span, the reduction are ~ 19.5% and 26.6% respectively for $h_w/t_w = 75$ and 300, for the same value of $d_o/h_w = 0.5$. For stockier webs e.g. $h_w/t_w < \sim 75$, it can be seen that the difference between V_u/V_y values for both the perforation sizes diminished and when the web is sufficiently stocky e.g. $h_w/t_w = 20$, no significant difference in the shear capacity can be observed, for both the short and long span beams. This may be because, sufficiently stockier webs (e.g. $h_w/t_w < \sim 75$) promotes web yielding without showing signs of lateral web buckling at V_u, and hence the full net section of the web is utilised in resisting the load. This is evidently seen in inset figures A, B and C of Figures 4.25 and 4.26, where almost complete webs are yielded at V_u. Whereas for slender webs e.g. $h_w/t_w = 300$, as discussed previously, the distribution of the highly stressed diagonal tension band is affected by the presence of perforation (see Figure D, E and F in Figures 4.25 and 4.26). Observing the failure modes (through visual inspection of the stress contour and deformed shapes) and analysis of the moment-shear interaction following the procedure described in Section in 3.3.4, it is found that the failure modes have not been significantly influenced by the presence of the perforation, for the parameters considered. For example, a) in the case of short span beams, shear dominated failure occurred for both sizes of perforations considered, similar to that of the unperforated beams, for the ranges of h_w/t_w considered, and b) at low values of h_w/t_w (say h_w/t_w = 20), bending dominated failure, whilst shear dominated failure occurred in higher h_w/t_w ratios (say h_w/t_w = 300), again similar to that of unperforated beams.

4.4 MODIFIED EN 1993-1-4 (2006) DESIGN EXPRESSIONS FOR PERFORATED BEAMS

EN 1993-1-4 (2006/A1:2015) is not very specific to the design aspects of perforated webs, hence it is exactly not possible to compare the present FE results with EN 1993-1-4 (2006/A1:2015). Further, as discussed in Section 3.4 (see also Figure 3.24 and Table 3.3), the expressions of shear buckling factor (χ_w) provided by EN 1993-1-4 (2006/A1:2015) are found to be very conservative for unperforated beams. Hence, modified design expressions proposed for unperforated LDSS beams (see Table 3.3), have been used as benchmark curve for comparison with the FE results of perforated beams as shown in Figure 4.27 in terms of variation of χ_w (shear buckling factor) with $\bar{a}_w$ (web slenderness). The FE results in Figure 4.27 corresponds to centrally located perforations of two different sizes i.e. d_o/h_w = 0.1 and 0.5. It may be noted that for the comparison purpose and development of design expressions (discussed later), only results of shear failure dominated results have been considered (through inspection of the moment-shear interaction diagram as described in Section 3.3.4), to enable comparison with EN 1993-1-4 (2006/A1:2015). As in the design curves reported by Real *et al*., (2007a) for unperforated I-section steel girders (and similar to the modified design expressions regimes as shown in Figure 3.24), the variation of χ_w with $\bar{a}_w$ are plotted for two span conditions *viz*., 1) $a/h_w \leq 1.0$ (Figure 4.27a) and 2) $1 < a/h_w \leq 2.0$ (Figure 4.27b). The FE results in Figure 4.27a corresponds to a/h_w = 1.0, which can be considered as lower bound (i.e. conservative) values for $a/h_w \leq 1.0$. However, the FE results in Figure 4.27b are for span values of $a/h_w = 1.3$, 1.6 and 2 (i.e. $1 < a/h_w \leq 2.0$). The values of a/h_w were so chosen to depict a distributed $\bar{a}_w$ values. The modified or proposed curves for unperforated LDSS are marked as $\chi_{w,\ prop}$ in Figure 4.27. From Figure 4.27, there appears to be a near parallel drop in the FE χ_w values corresponding to $d_o/h_w = 0.5$ as compared to those of $d_o/h_w = 0.1$, at least for $\bar{a}_w \geq 1.0$. Hagen *et al.*, (2006) proposed a reduction factor, RF = $[1–d_o/h_w]$ for $\chi_{w,}$ for centrally located circular perforation in webs. The same reduction factor was also checked for square perforations by Hassanein (2014) found to give good agreement with FE results. In this work, a modified reduction factor, $RF_m = [1– (1/2)\ d_o/h_w]$ has been considered, with the factor (1/2) being introduced, as the perforation is provided only in one web of the hollow LDSS beam. Hence, the proposed value of χ_w for perforated web (or $\chi_{w,\ mod}$) = RF_m ($\chi_{w,\ prop}$) = $[1– (1/2)\ d_o/h_w]$ ($\chi_{w,\ prop}$) (see Table 4.1 for the expressions of $\chi_{w,\ mod}$). It can be seen from Figure 4.27 that the FE results of χ_w compare well with those obtained from the modified expressions of $\chi_{w,\ prop}$. Based on $\chi_{w,\ mod}$, the total shear capacity of the section ($V_{u,\ pp}$) i.e. considering the contributions of both flanges and webs are estimated using Equations 3.3–3.12. In Tables 4.2 and 4.3, comparison of the FE and predicted total shear capacity results are shown for 1) $a/h_w \leq 1.0$ and 2) $1 < a/h_w \leq 2.0$, respectively. In the nomenclature of the section e.g. p60tw2tf10wf200a600, p60, tw2, tf10, wf200 and a600 denote perforation of size 60 mm, web thickness of 2 mm, flange thickness of 10 mm, flange width of 200 mm and span length of 600 mm respectively. Observing the $V_{u,FE}/V_{u,\ pp}$ values, it can be seen that proposed expressions of shear buckling factors ($\chi_{w,\ mod}$, see Table 4.2) are able to reasonably predict the FE results; mean and COV values for 1) $a/h_w \leq 1.0$ (Figure 4.27a) and 2) $1 < a/h_w \leq 2.0$ (Figure 4.27b), are found to be 1.20 and 0.13, and 1.11 and 0.12 respectively. It may be noted that, for $\bar{a}_w \leq 0.65/\eta$, the FE values of χ_w are much higher (specially for $a/h_w = 1.0$, owing to strain hardening) as compared to the adopted $[1– (1/2)\ d_o/h_w]\eta$, hence it has a bearing on the comparison i.e. mean and COV values are increased.

4.5 CONCLUSIONS

Shear behavior of the circular perforated LDSS hollow rectangular beams have been assessed in this chapter, by considering a wide range of cross sectional parameters e.g. flange thickness, flange width, web thickness, shear span etc. Primarily, the effect of single circular perforation size / diameter and location (along longitudinal, transverse, and diagonals) are estimated with a focus on the shear load capacity, deformed shapes (or failure modes) etc.

1) A nearly linear decrease in the value of shear capacity (V_u/V_y) of ~ 23-25% for 500% (i.e. d_o/h_w = 0.0–0.50) increase in perforation size can be seen with slender (h_w/t_w = 300) webs, for short span (a/h_w = 1.0), whereas, the decreases are ~ 8-10% for stockier (h_w/t_w = 20) webs. It thus suggests that perforation has relatively higher shear reducing effect for slender webs. In the case of long span (a/h_w = 2.0) the reduction appears to be a milder (~1.7-2.7%) in the case of stockier webs.

2) Shear capacity is observed to increase with increasing flange thickness (or t_f/t_w) for perforated beams, consistent with the similar behaviour observed for the case unperforated beams.

3) When perforation location is changed along longitudinal and transverse directions, not very significant difference in shear capacity is seen, although maximum reduction in shear capacity appears to occur corresponding to perforations located in the highly stressed diagonal tension band. For the smallest (d_o/h_w = 0.10) perforation size considered, as the perforations are moved away from the span - towards the supports, the reduction in shear capacity gradually reduces and reaches the value corresponding to that of unperforated beam. However, unlike the case of short span beam (i.e. a/h_w =

1.0), for the longer span (i.e. $a/h_w = 2.0$) beam the unperforated shear strength is not recovered for the smallest perforation.

4) It is observed that, there appears to be not significant variation on the shear capacity, when the location is changed along tension diagonal. Whereas, for the change in perforation location along compression direction, the reduction in shear capacity is seen to be relatively larger for the central diagonal region i.e. $\sim 0.50 \leq d_2/h_w \leq 1.0$, whereas the reduction gets smaller on either side of the central region.

5) A decrease in the shear capacity with increasing values of web slenderness (h_w/t_w) is observed for perforated beams, similar to that of unperforated beams. In general, for the case of slender webs with $h_w/t_w \geq \sim 75$, there appears to be a near parallel decrease in the values of shear capacity, for 400% increase in perforation size (from $d_o/h_w = 0.1$). The effect of perforation in the reduction of shear capacity is felt most when the web becomes slender. For stockier webs e.g. $h_w/t_w < \sim 75$, it can be seen that the shear capacity values seems not to get affected by perforation when the web is sufficiently stocky, e.g. $h_w/t_w = 20$.

6) Based on the FE results, shear buckling factor expressions have been proposed for perforated beams considering two span regimes ($a/h_w \leq 1.0$ and $1 < a/h_w \leq 2.0$), modifying EN 1993. It can be seen that proposed expressions of shear buckling factors are able to reasonably predict the FE results; mean and COV values for 1) $a/h_w \leq 1.0$ and 2) $1 < a/h_w \leq 2.0$, are found to be 1.20 and 0.13, and 1.11 and 0.12 respectively.

Table 4.1: EN 1993-1-4 (2006/A1:2015) design expressions to evaluate the web buckling co-efficient (χ_w)

Web panel ratio	$\bar{\lambda}_w$	$\chi_{w,\,mod}$
$a/h_w \le 1.0$	$\bar{\lambda}_w \le \frac{0.65}{\eta}$	$\left(1-\frac{1}{2}\frac{d_o}{h_w}\right)\eta$
	$\frac{0.65}{\eta} < \bar{\lambda}_w \le 0.65$	$\left(1-\frac{1}{2}\frac{d_o}{h_w}\right)\frac{0.69}{\bar{\lambda}_w}$
	$\bar{\lambda}_w \ge 0.65$	$\left(1-\frac{1}{2}\frac{d_o}{h_w}\right)\frac{2.42}{1.53+\bar{\lambda}_w}$
$1 < a/h_w \le 2.0$	$\bar{\lambda}_w \le \frac{0.65}{\eta}$	$\left(1-\frac{1}{2}\frac{d_o}{h_w}\right)\eta$
	$\frac{0.65}{\eta} < \bar{\lambda}_w \le 0.65$	$\left(1-\frac{1}{2}\frac{d_o}{h_w}\right)\frac{0.675}{\bar{\lambda}_w}$
	$\bar{\lambda}_w \ge 0.65$	$\left(1-\frac{1}{2}\frac{d_o}{h_w}\right)\frac{2.03}{1.27+\bar{\lambda}_w}$

Table 4.2: Comparison between FE and proposed model results for $a/h_w \leq 1.00$, h_w = 600 mm

Sections	$V_{u,FE}$ (kN)	$V_{u,pp}$ (kN)	$V_{u,FE}/V_{u,pp}$
p60wt2ft10fw200a600	654	450	1.45
p180wt2ft10fw200a600	582	411	1.41
p300wt2ft10fw200a600	514	372	1.38
p60wt2ft6fw200a600	573	406	1.41
p60wt4ft12fw200a600	1475	1313	1.12
p60wt8ft24fw200a600	3890	3802	1.02
p60wt10ft30fw200a600	5499	5229	1.05
p60wt20ft60fw200a600	13486	13100	1.03
p60wt30ft90fw200a600	21545	20651	1.04
p300wt2ft6fw200a600	456	328	1.39
p300wt4ft12fw200a600	1176	1064	1.11
p300wt8ft24fw200a600	3187	3091	1.03
p300wt10ft30fw200a600	4433	4235	1.05
p300wt20ft60fw200a600	11622	10736	1.08
p300wt30ft90fw200a600	19549	17104	1.14
p60wt4ft20fw200a600	1655	1426	1.16
p60wt8ft40fw200a600	4420	4052	1.09
p60wt10ft50fw200a600	6118	5544	1.10
p60wt20ft100fw200a600	16217	14545	1.11
p60wt30ft150fw200a600	27296	24305	1.12
p300wt4ft20fw200a600	511	372	1.37
p300wt8ft40fw200a600	1349	1177	1.15
p300wt10ft50fw200a600	3631	3341	1.09
p300wt20ft100fw200a600	5140	4571	1.12
p300wt30ft150fw200a600	15027	12181	1.23
p60wt2ft10fw200a600	653	442	1.48
p180wt2ft10fw200a600	581	404	1.44
p300wt2ft10fw200a600	513	365	1.41
p60wt2ft6fw200a600	573	398	1.44
p180wt2ft6fw200a600	511	359	1.42
p300wt2ft6fw200a600	455	321	1.42
p60wt30ft90fw200a600	21545	20408	1.06
p180wt30ft90fw200a600	20640	18635	1.11
p300wt30ft90fw200a600	19549	16862	1.16
p60wt30ft150fw200a600	28420	24305	1.17

p180wt30ft150fw200a600	27324	22531	1.21
p300wt30ft150fw200a600	26352	20758	1.27
p60wt2ft4fw200a600	426	378	1.13
p60wt8ft24fw200a600	3960	3590	1.10
p60wt10ft30fw200a600	5635	4925	1.14
p60wt6ft12fw200a600	2397	2288	1.05
p60wt7ft21fw200a600	3204	2948	1.09
p60wt20ft100fw200a600	16908	12888	1.31
p60wt30ft150fw200a600	27600	19463	1.42
p300wt2ft4fw200a600	326	301	1.08
p300wt8ft24fw200a600	2990	2879	1.04
p300wt10ft30fw200a600	4198	3952	1.06
p300wt6ft12fw200a600	1853	1821	1.02
p300wt7ft21fw200a600	2419	2361	1.02
p300wt20ft100fw200a600	13802	10524	1.31
p300wt30ft150fw200a600	25200	15916	1.58
Mean			1.20
COV			0.13

In name p60wt2ft10fw400a1200, variables indicate perforation size (d_o) = 60 mm, web thickness (t_w) = 2 mm, flange thickness (t_f) = 10 mm, flange width (w_f) = 400 mm, shear span (a) = 600 mm.

Table 4.3: Comparison between FE and proposed model results for $1.0 < a/h_w \leq 2.00$, h_w = 600 mm

Sections	$V_{u, FE}$ (kN)	$V_{u, pp}$ (kN)	$V_{u,FE}/V_{u, pp}$
p60wt2ft10fw200a1200	422	365	1.16
p180wt2ft10fw200a1200	377	284	1.33
p300wt2ft10fw200a1200	331	255	1.30
p60wt2ft8fw200a1200	422	302	1.40
p60wt4ft16fw200a1200	1094	1025	1.07
p60wt8ft32fw200a1200	3206	3153	1.02
p60wt10ft40fw200a1200	4636	4418	1.05
p60wt20ft80fw200a1200	10541	12594	0.84
p60wt30ft120fw200a1200	16697	19233	0.87
p300wt2ft8fw200a1200	314	243	1.29
p300wt4ft16fw200a1200	874	828	1.06
p300wt8ft32fw200a1200	2660	2553	1.04
p300wt10ft40fw200a1200	3814	3580	1.07
p300wt20ft80fw200a1200	10397	10214	1.02
p300wt30ft120fw200a1200	16498	15687	1.05
p180wt2ft10fw200a1200	1142	1062	1.08
p300wt2ft10fw200a1200	3206	3252	0.99
p60wt2ft6fw200a1200	4932	4549	1.08
p180wt2ft6fw200a1200	12530	12961	0.97
p300wt2ft6fw200a1200	20197	20576	0.98
p60wt30ft90fw200a1200	329	255	1.29
p180wt30ft90fw200a1200	921	865	1.06
p300wt30ft90fw200a1200	2797	2652	1.05
p60wt30ft150fw200a1200	4022	3711	1.08
p180wt30ft150fw200a1200	12021	10581	1.14
p300wt30ft150fw200a1200	19723	17029	1.16
p60wt2ft10fw200a1200	421	314	1.34
p180wt2ft10fw200a1200	376	284	1.32
p300wt2ft10fw200a1200	330	255	1.29
p60wt2ft8fw200a1200	421	302	1.40
p180wt2ft8fw200a1200	364	273	1.34
p300wt2ft8fw200a1200	313	243	1.29
p60wt30ft120fw200a1200	16697	19233	0.87
p180wt30ft120fw200a1200	16659	17460	0.95
p300wt30ft120fw200a1200	16498	15687	1.05

p60wt30ft150fw200a1200	20197	20576	0.98
p180wt30ft150fw200a1200	20067	18802	1.07
p300wt30ft150fw200a1200	19723	17029	1.16
p60wt2.5ft6.25fw200a1200	482	425	1.14
p60wt6ft24fw200a1200	2015	1946	1.04
p60wt7ft28fw200a1200	2637	2452	1.08
p60wt8ft40fw200a1200	3564	3379	1.05
p60wt10ft50fw200a1200	5222	4806	1.09
p60wt4ft12fw200a1200	1097	999	1.10
p60wt30ft150fw200a1200	20192	19463	1.04
p300wt2ft4fw200a1200	371	338	1.10
p300wt8ft24fw200a1200	1587	1563	1.02
p300wt10ft30fw200a1200	2057	1963	1.05
p300wt6ft12fw200a1200	2844	2779	1.02
p300wt7ft21fw200a1200	4326	3969	1.09
p300wt20ft100fw200a1200	856	802	1.07
p300wt30ft150fw200a1200	19580	15916	1.23
Mean			1.11
COV			0.12

In name p60wt2ft10fw400a1200, variables indicate perforation size (d_o) = 60 mm, web thickness (t_w) = 2 mm, flange thickness (t_f) = 10 mm, flange width (w_f) = 400 mm, shear span (a) = 1200 mm.

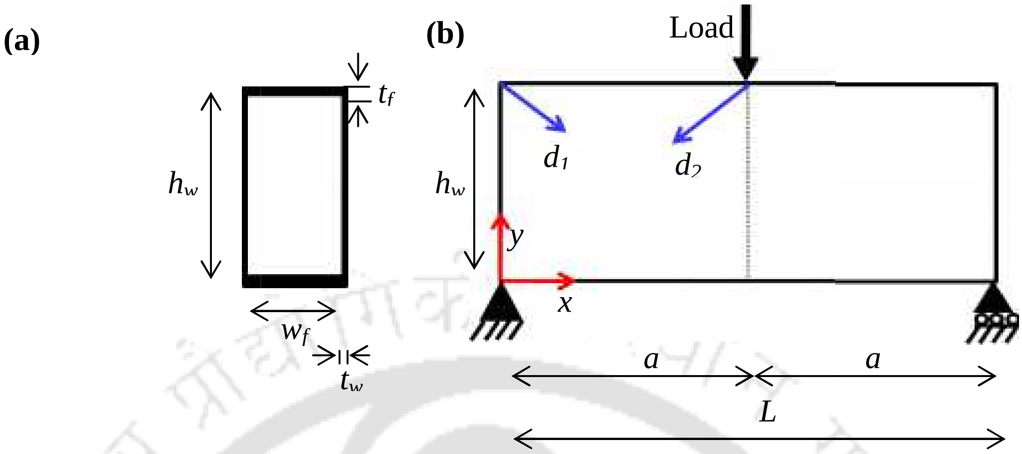

Figure 4.1: (a) Geometry, (b) boundary conditions.

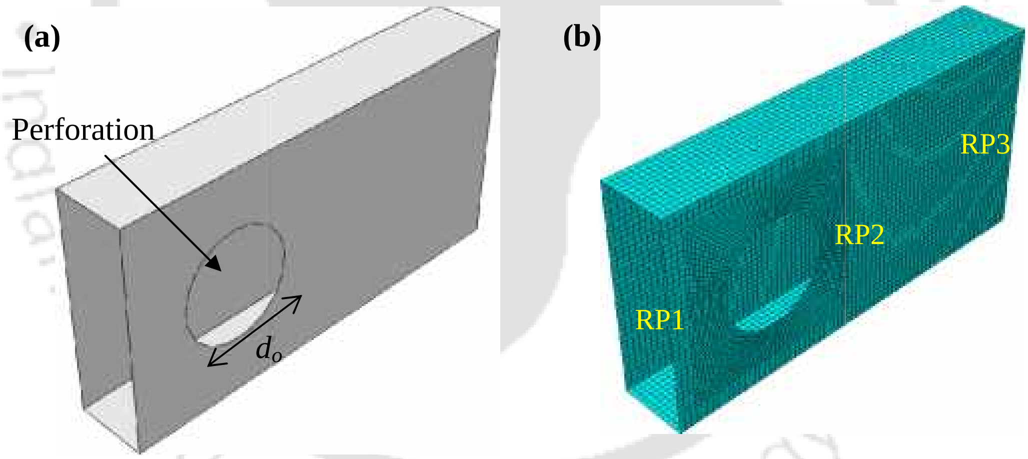

Figure 4.2: (a) circular perforation, (b) FE mesh of perforated beam.

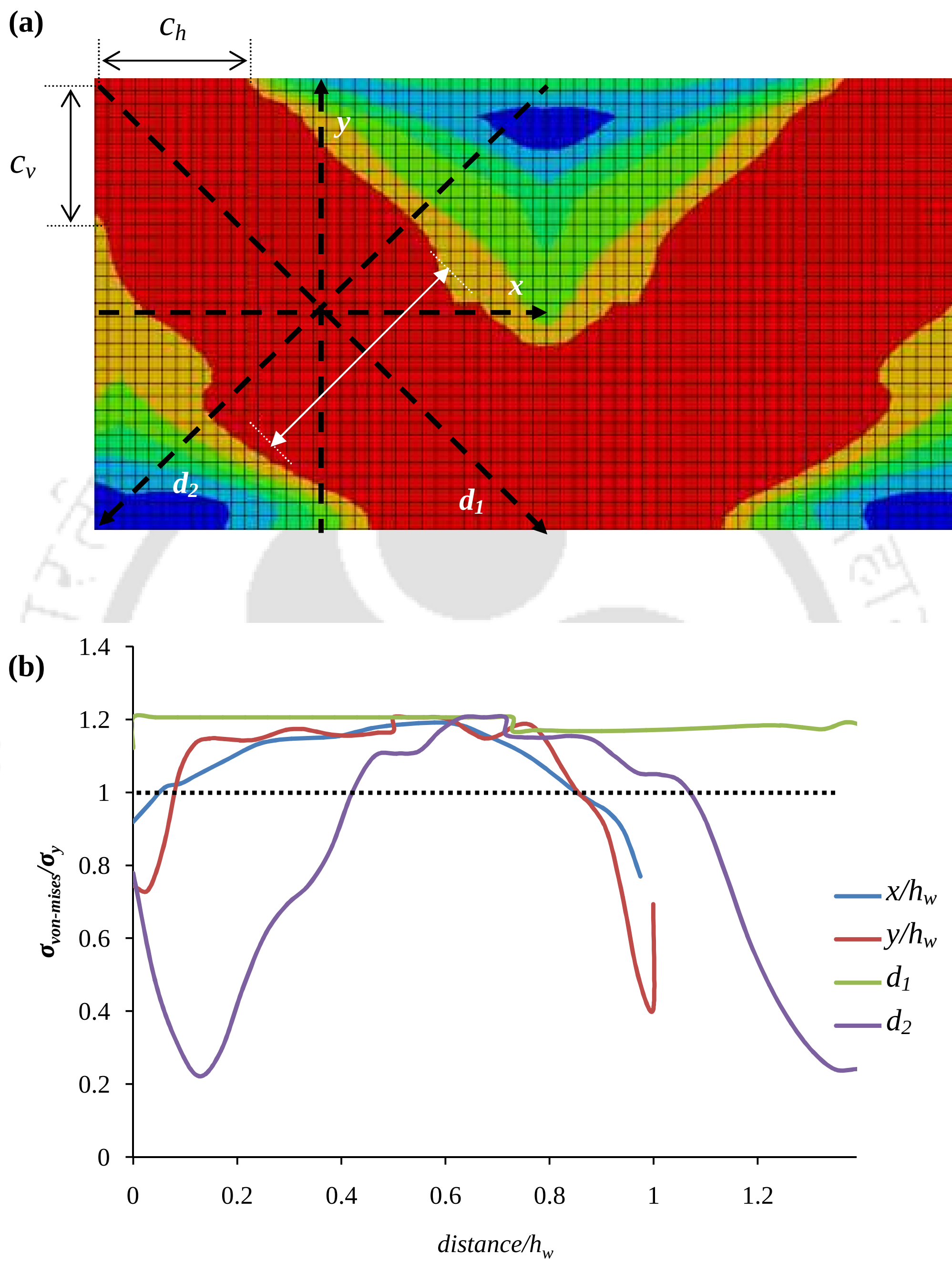

Figure 4.3: a) von-Mises stress contour, b) variation of σ_{vm}/σ_y vs distance/h_w, for unperforated beam (a/h_w = 1.0, t_f/t_w =5, h_w/t_w = 300) at V_u.

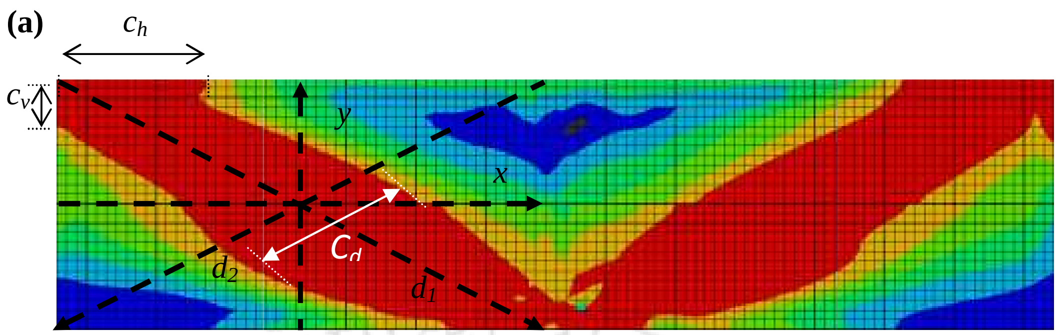

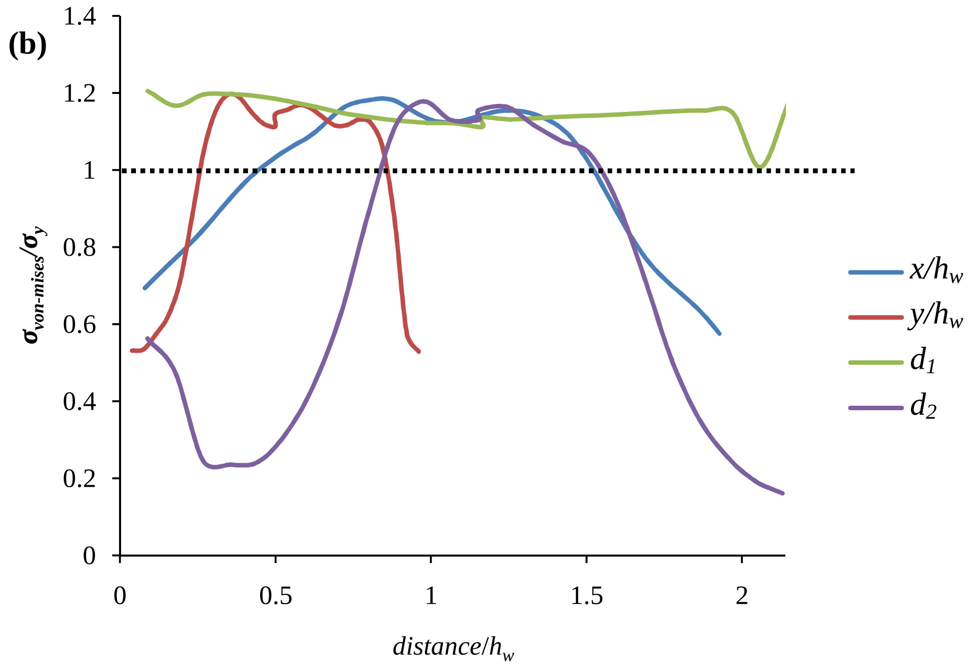

Figure 4.4: a) von-Mises stress contour, b) variation of σ_{vm}/σ_y vs distance/h_w, for unperforated beam (a/h_w = 2.0, t_f/t_w = 5, h_w/t_w = 300) at V_u.

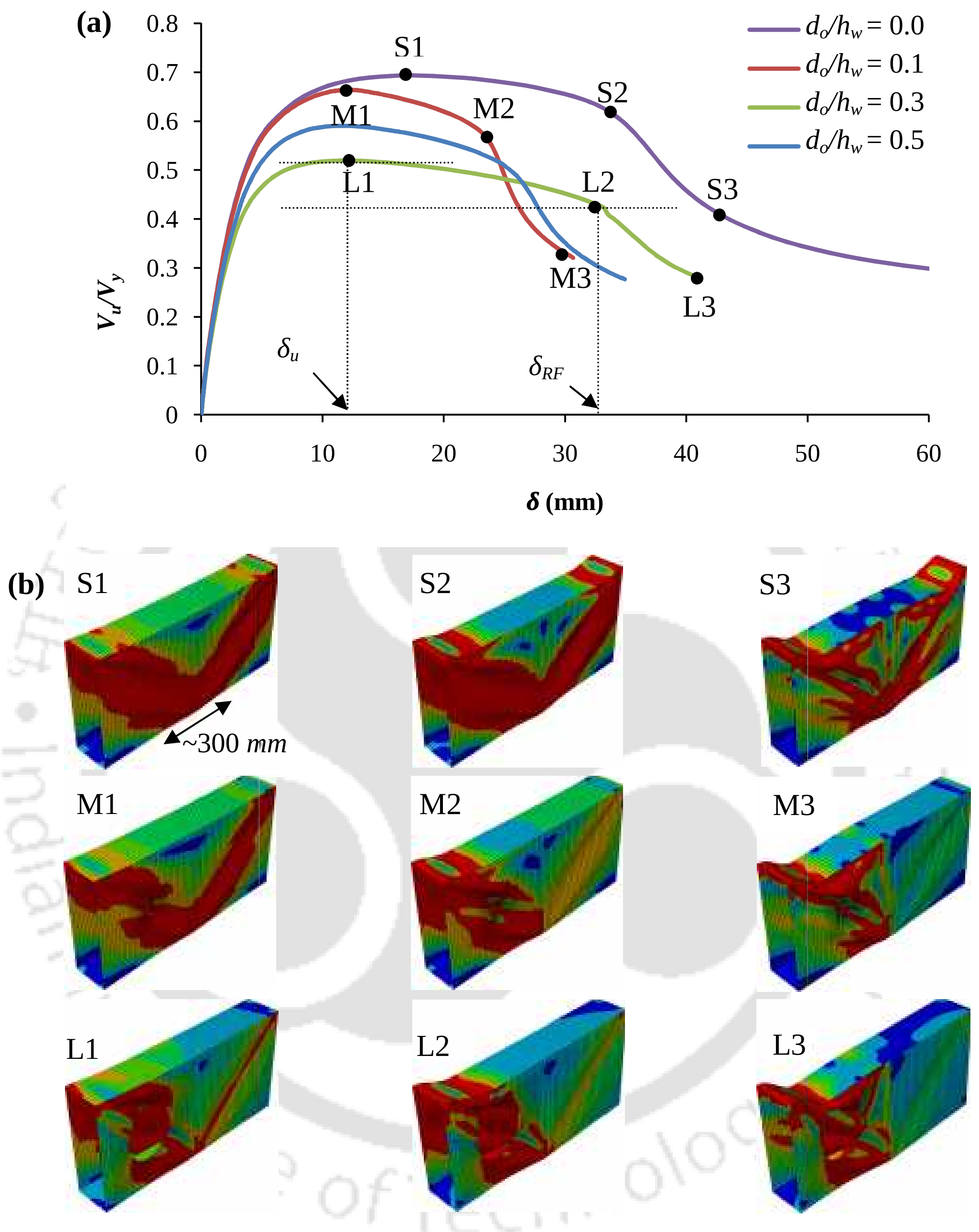

Figure 4.5: a) Variation of V_u/V_y vs δ, and b) von-Mises stress contour for d_o/h_w = 0.0 (S1, S2, S3), d_o/h_w = 0.1 (M1, M2, M3), d_o/h_w = 0.5 (L1, L2, L3) (x/h_w = 0.5, y/h_w = 0.5; a/h_w = 1.0, t_f/t_w = 5).

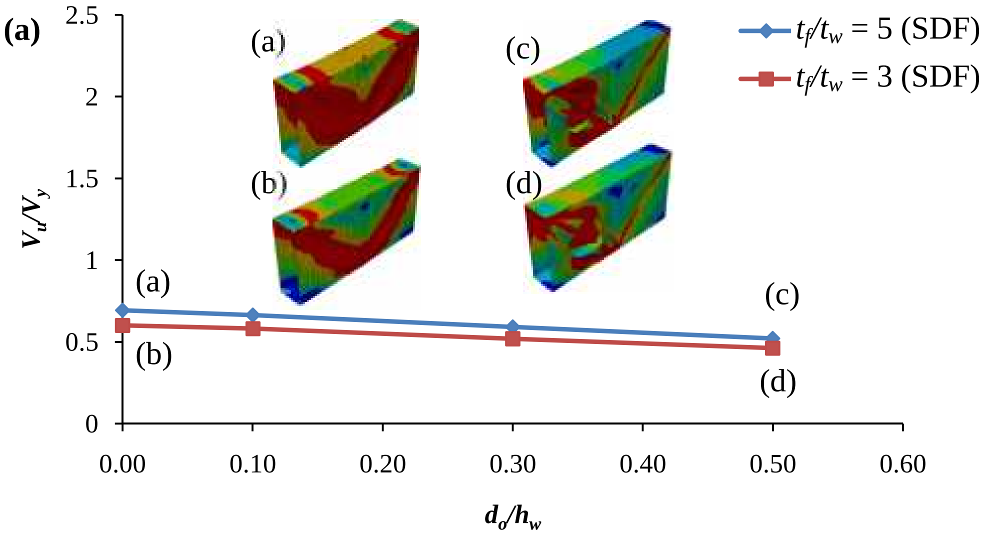

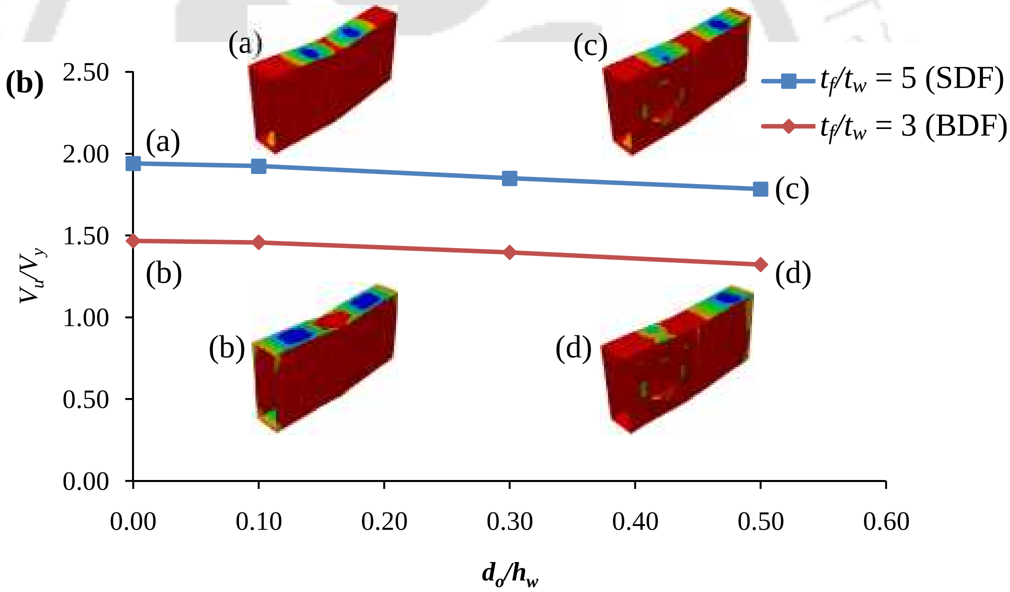

Figure 4.6: Variation of V_u/V_y vs d_o/h_w: (a) h_w/t_w = 300 and b) h_w/t_w = 20 (x/h_w = 0.5, y/h_w = 0.5; a/h_w = 1.0, t_f/t_w = 3 & 5).

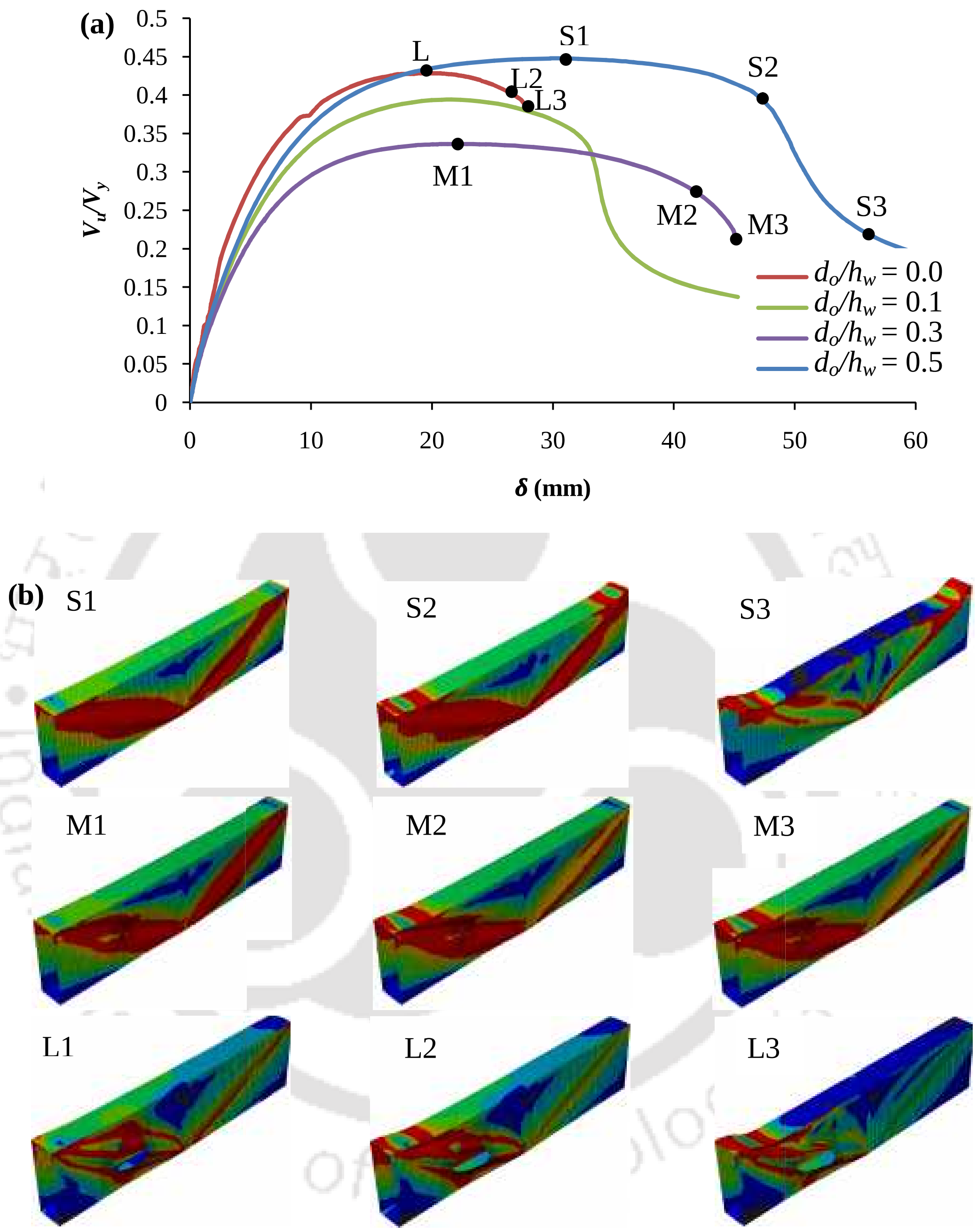

Figure 4.7: a) Variation of V_u/V_y vs δ, and b) von-Mises stress contour for d_o/h_w = 0.0 (S1, S2, S3), d_o/h_w = 0.1 (M1, M2, M3), d_o/h_w = 0.5 (L1, L2, L3), (x/h_w = 1.0, y/h_w = 0.5; a/h_w = 2.0, t_f/t_w = 5).

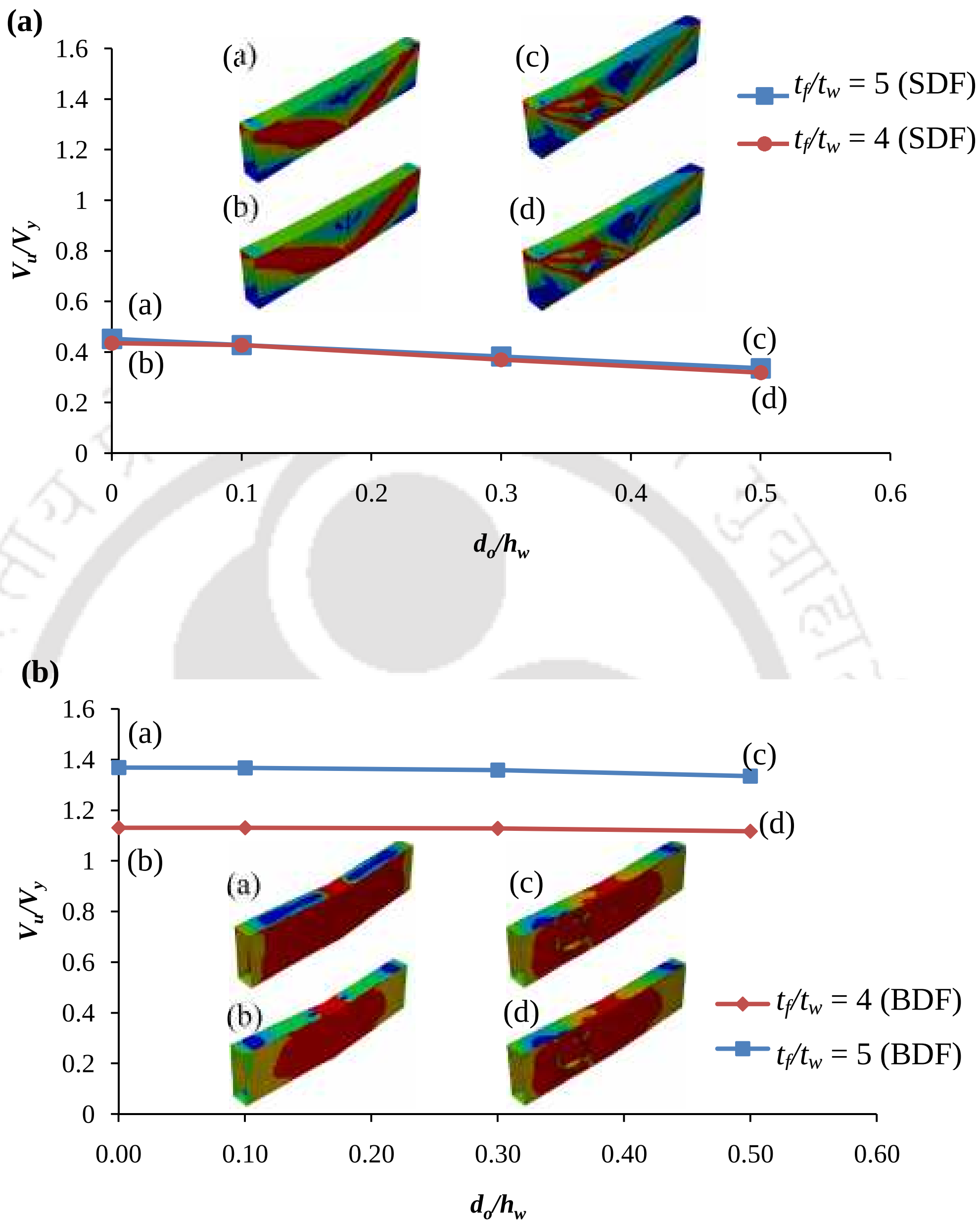

Figure 4.8: Variation of V_u/V_y vs d_o/h_w: (a) h_w/t_w = 300 and b) h_w/t_w = 20 (x/h_w = 1.0, y/h_w = 0.5; a/h_w = 2.0, t_f/t_w = 4 & 5)

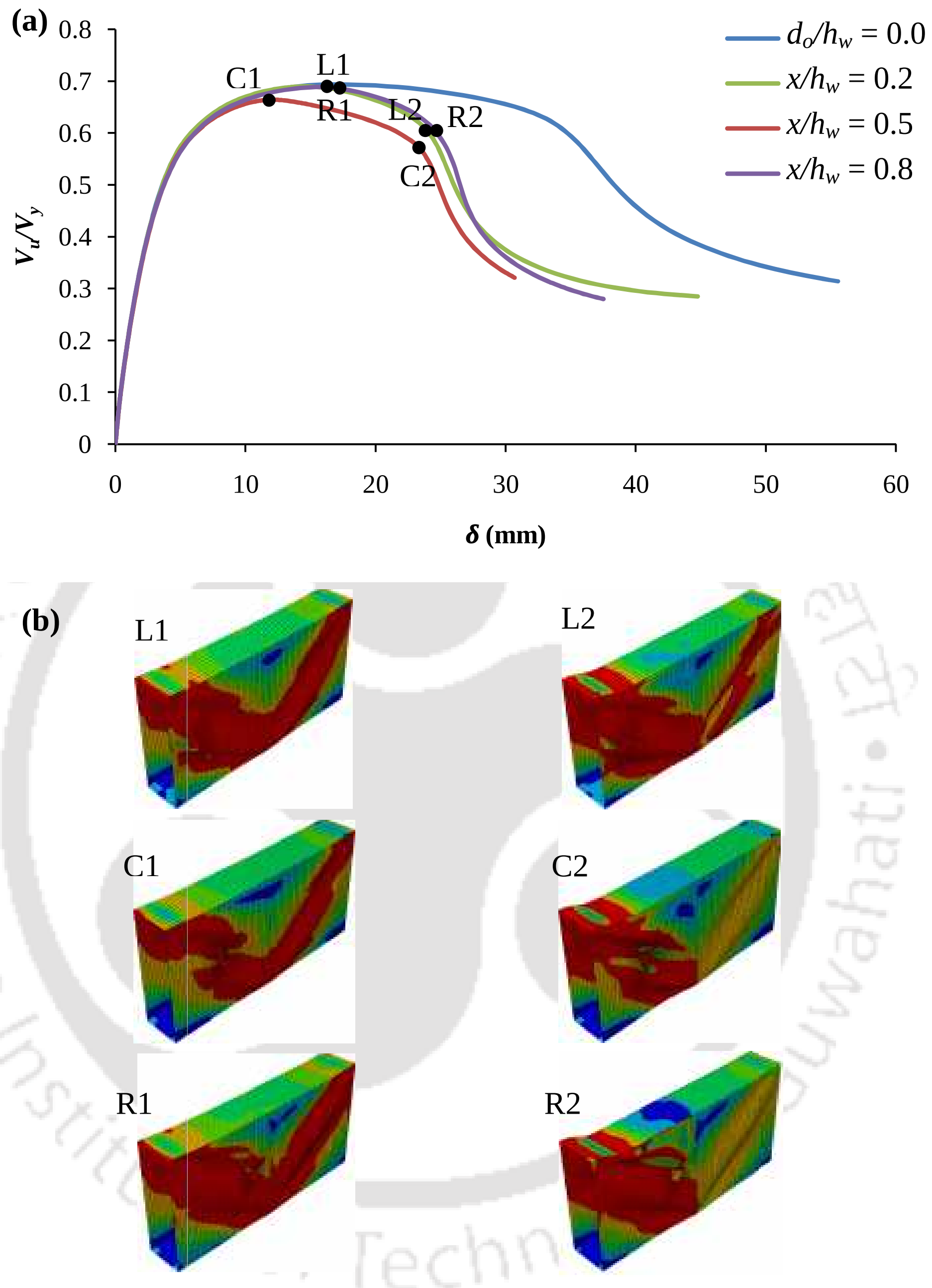

Figure 4.9: a) Variation of V_u/V_y vs δ, and b) von-Mises stress contour for x/h_w = 0.2 (L1, L2), x/h_w = 0.5 (C1, C2), x/h_w = 0.8 (R1, R2) (d_o/h_w = 0.1, y/h_w = 0.5; a/h_w = 1.0, t_f/t_w = 5, h_w/t_w = 300; d_o/h_w = 0.1).

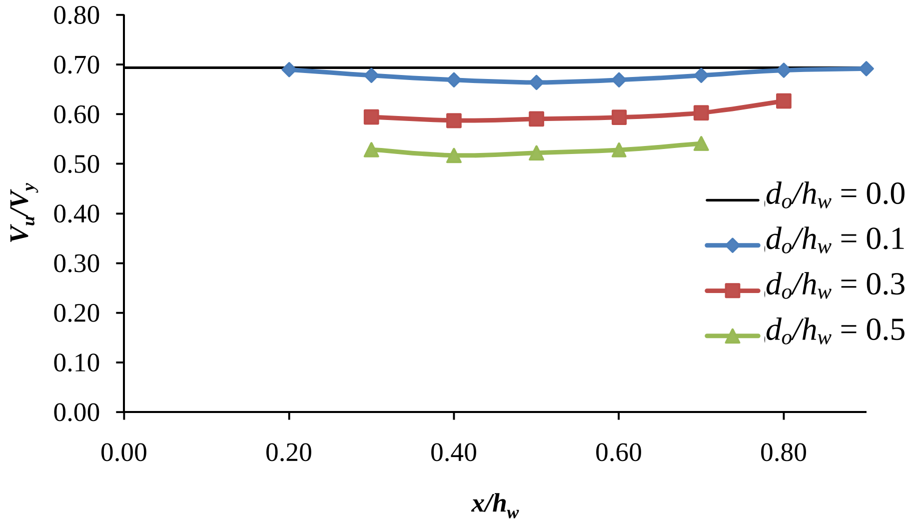

Figure 4.10: Variation of V_u/V_y vs x/h_w (y/h_w = 0.5, t_f/t_w = 5, h_w/t_w = 300, a/h_w = 1).

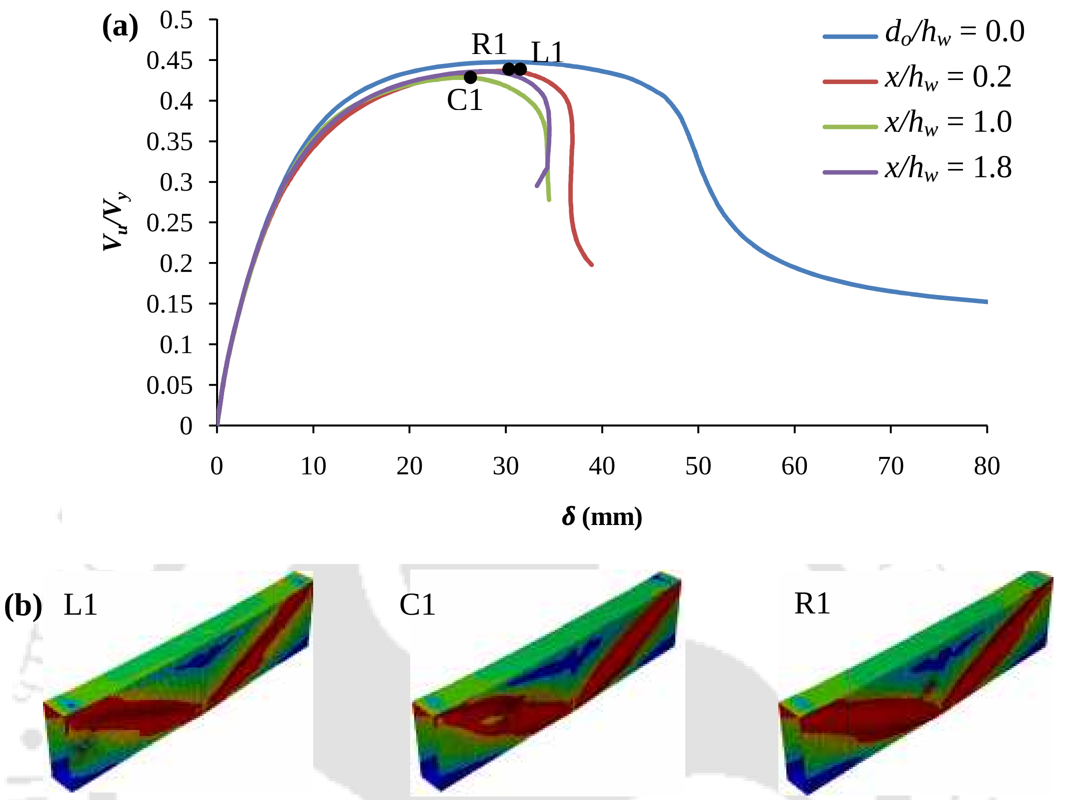

Figure 4.11: a) Variation of V_u/V_y vs δ, and b) von-Mises stress contour for x/h_w = 0.2 (L1), x/h_w = 1.0 (C1), x/h_w = 1.8 (R1) (d_o/h_w = 0.1, y/h_w = 0.5; a/h_w = 2.0, t_f/t_w =5, h_w/t_w = 300).

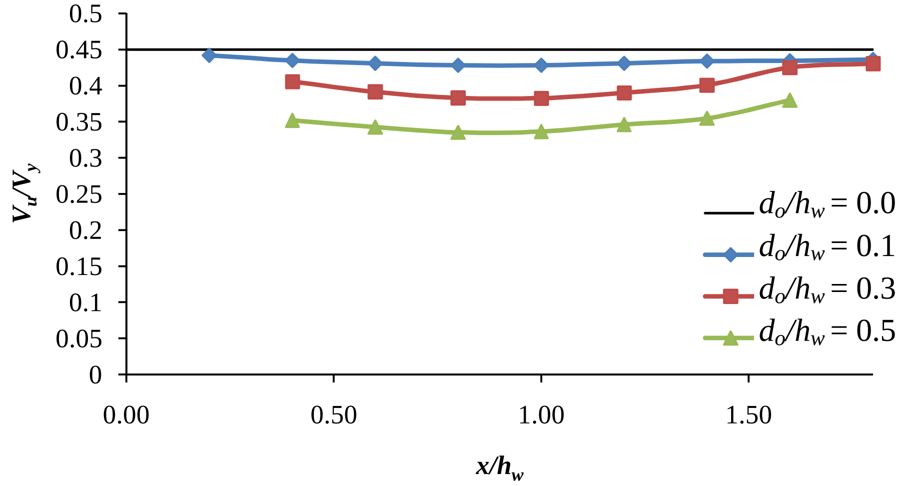

Figure 4.12: Variation of V_u/V_y vs x/h_w (y/h_w = 0.5, t_f/t_w = 5, h_w/t_w = 300, a/h_w = 2).

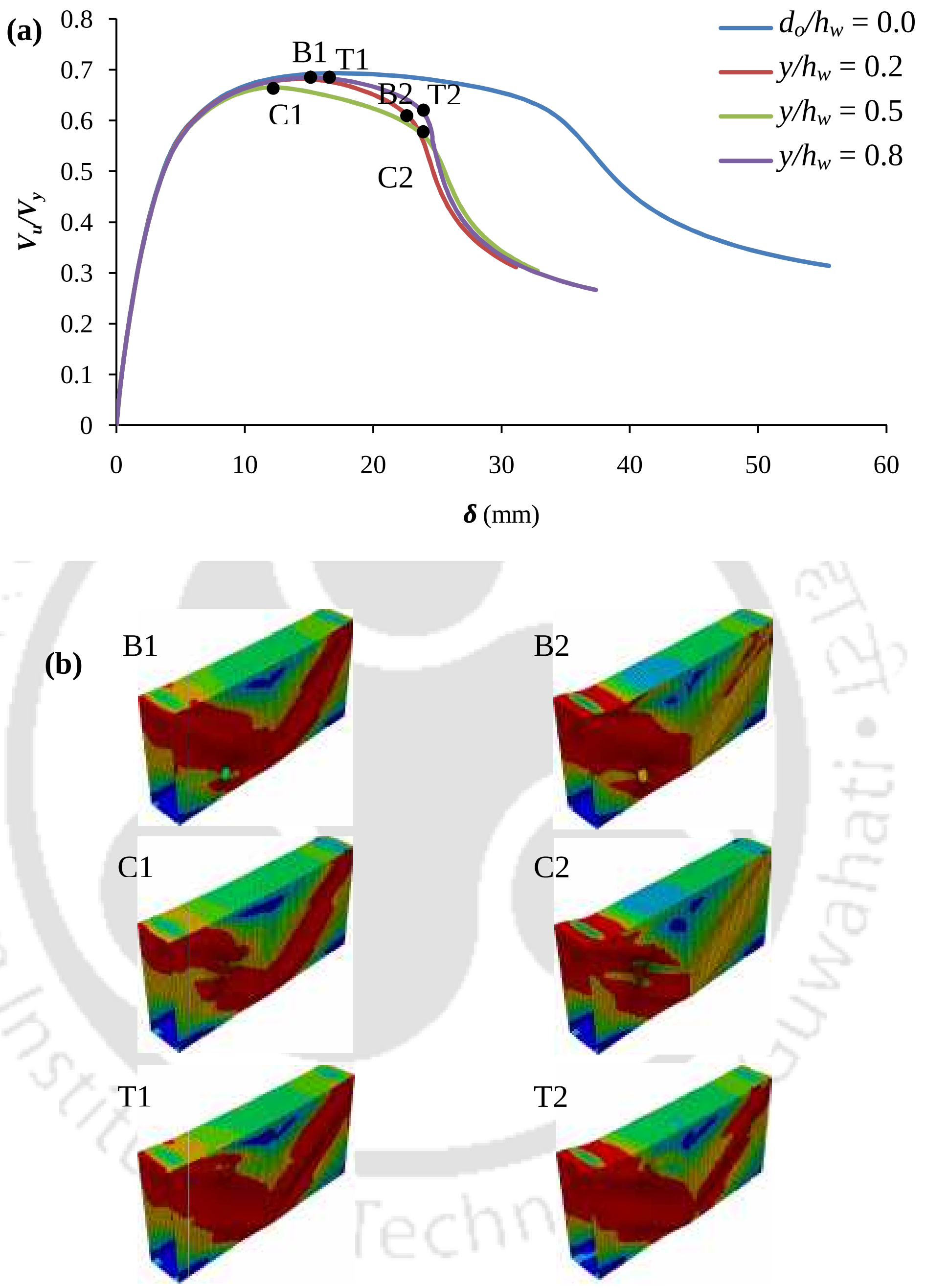

Figure 4.13: a) Variation of V_u/V_y vs δ, and b) von-Mises stress contour for y/h_w = 0.2 (B1, B2), y/h_w = 0.5 (C1, C2), y/h_w = 0.8 (T1, T2) (d_o/h_w = 0.1, x/h_w = 0.5; a/h_w = 1.0, t_f/t_w = 5, h_w/t_w = 300).

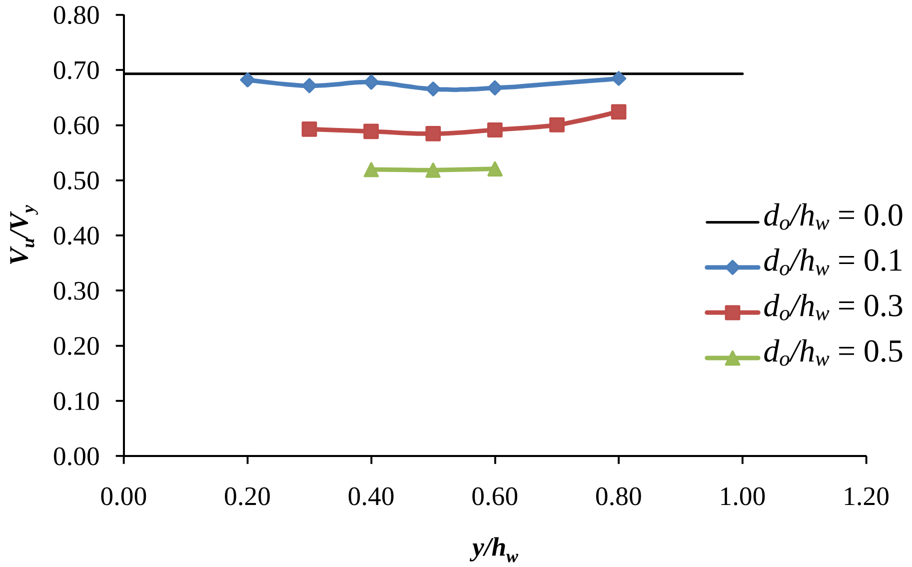

Figure 4.14: Variation of V_u/V_y vs y/h_w (y/h_w = 0.5; t_f/t_w = 5, h_w/t_w = 300, a/h_w = 1).

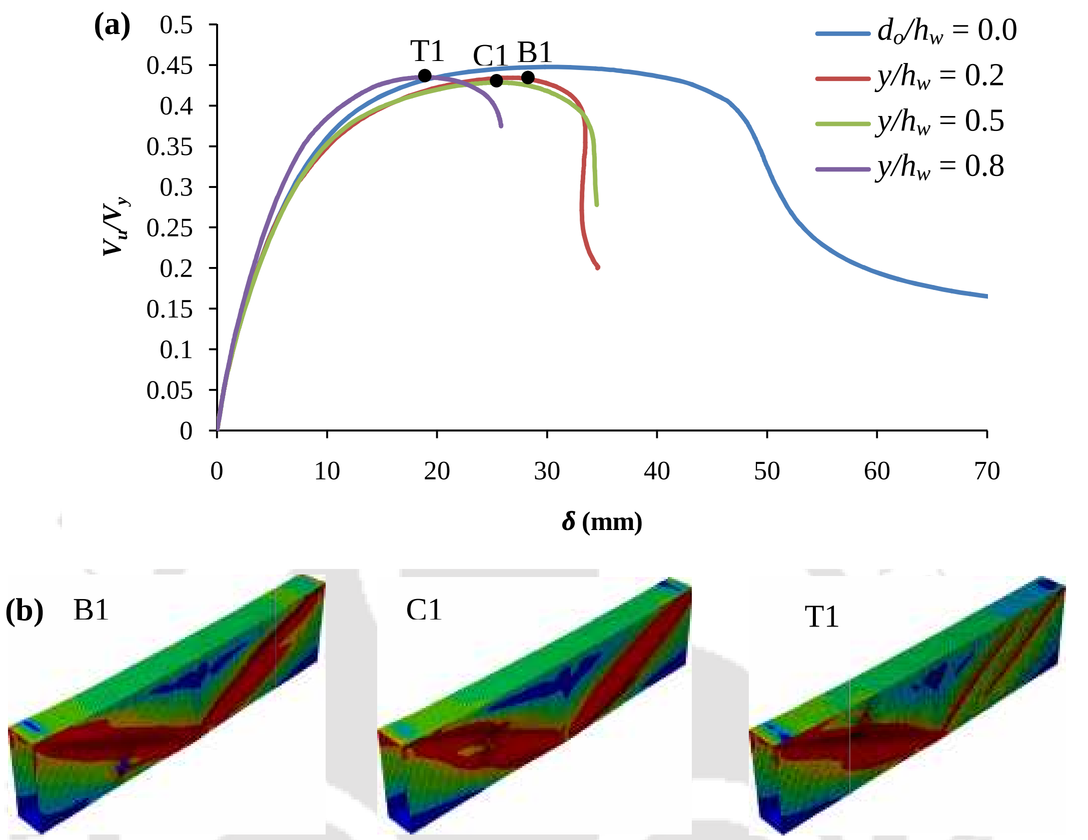

Figure 4.15: a) Variation of V_u/V_y vs δ, and b) von-Mises stress contour for y/h_w = 0.2 (B1), y/h_w = 0.5 (C1), y/h_w = 0.8 (T1) (d_o/h_w = 0.1, x/h_w = 1.0; a/h_w = 2.0, t_f/t_w = 5, h_w/t_w = 300).

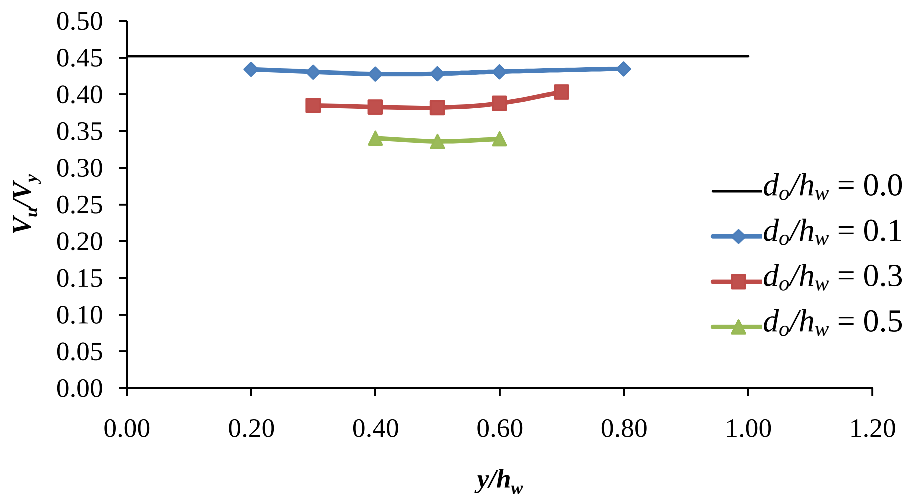

Figure 4.16: Variation of V_u/V_y vs y/h_w (x/h_w = 1.0; t_f/t_w = 5, h_w/t_w = 300, a/h_w = 2.0).

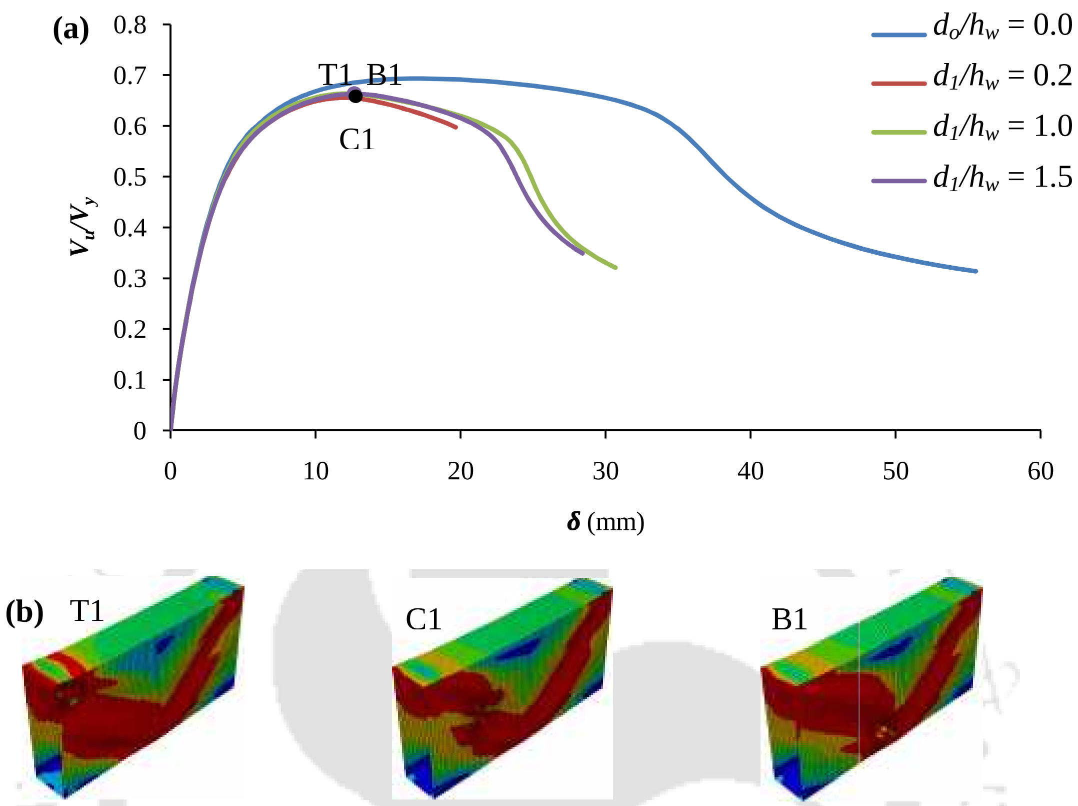

Figure 4.17: a) Variation of V_u/V_y vs δ, and b) von-Mises stress contour for d_1/h_w = 0.2 (T1), d_1/h_w = 1.0, (C1), d_1/h_w = 1.4, (B1), (d_o/h_w = 0.1, a/h_w = 1.0; t_f/t_w = 5, h_w/t_w = 300).

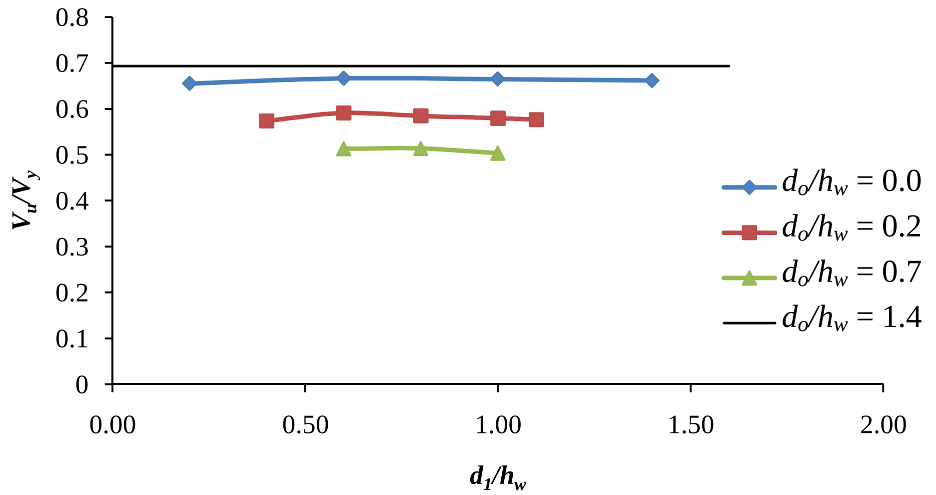

Figure 4.18: Variation of V_u/V_y vs d_1/h_w (t_f/t_w = 5, h_w/t_w = 300 a/h_w = 1.0).

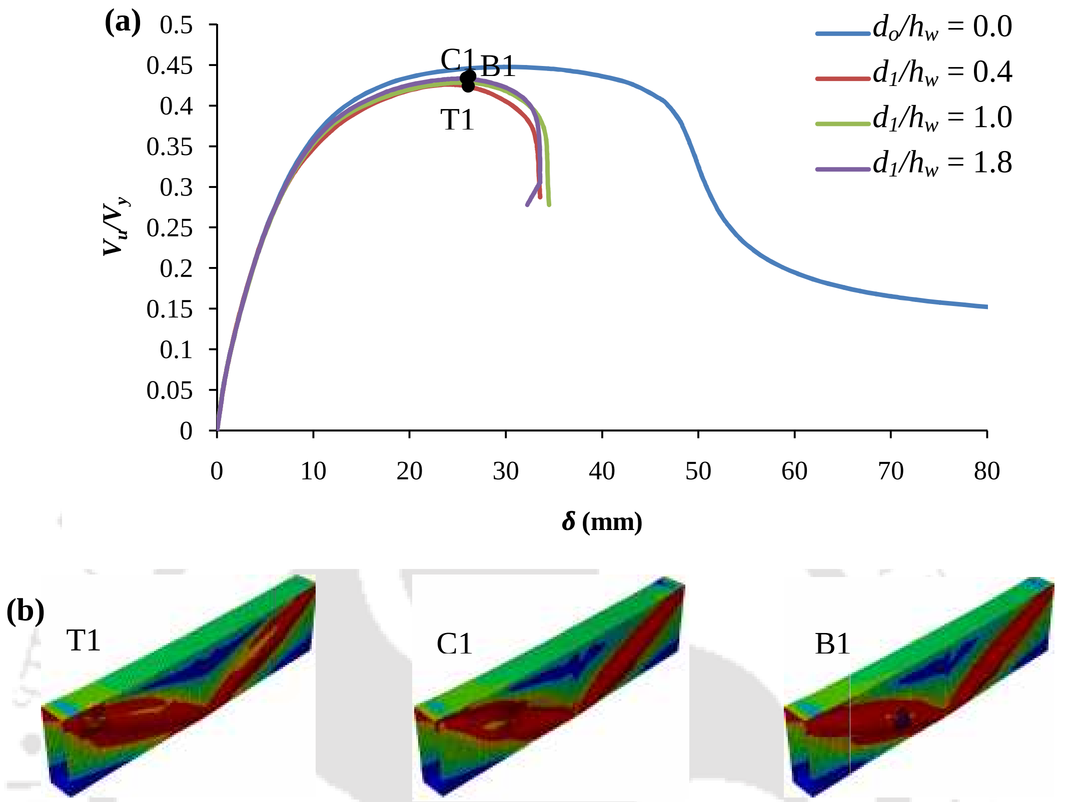

Figure 4.19: a) Variation of V_u/V_y vs δ, and b) von-Mises stress contour for d_1/h_w = 0.4 (T1), d_1/h_w = 1.1 (C1), d_1/h_w = 1.2 (B1) (d_o/h_w = 0.1; a/h_w = 2.0, t_f/t_w = 5, h_w/t_w = 300).

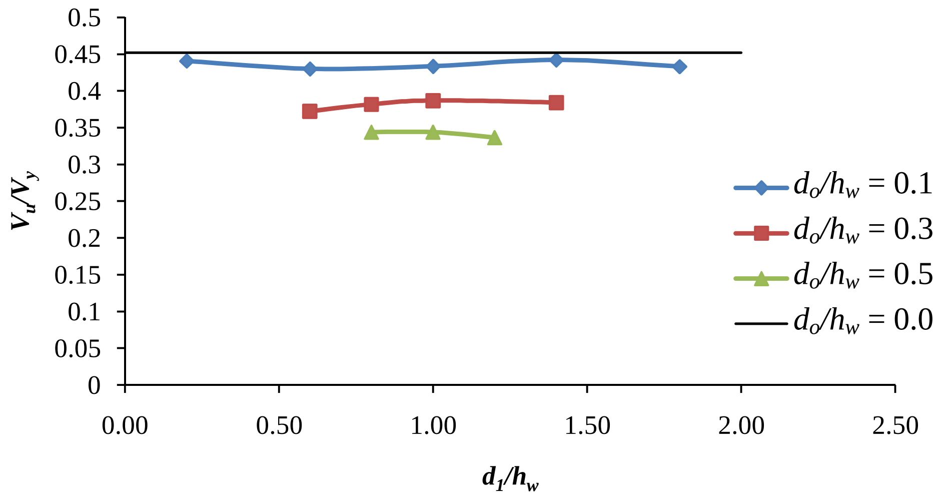

Figure 4.20: Variation of V_u/V_y vs d_1/h_w (t_f/t_w = 5, h_w/t_w = 300, a/h_w = 2.0)

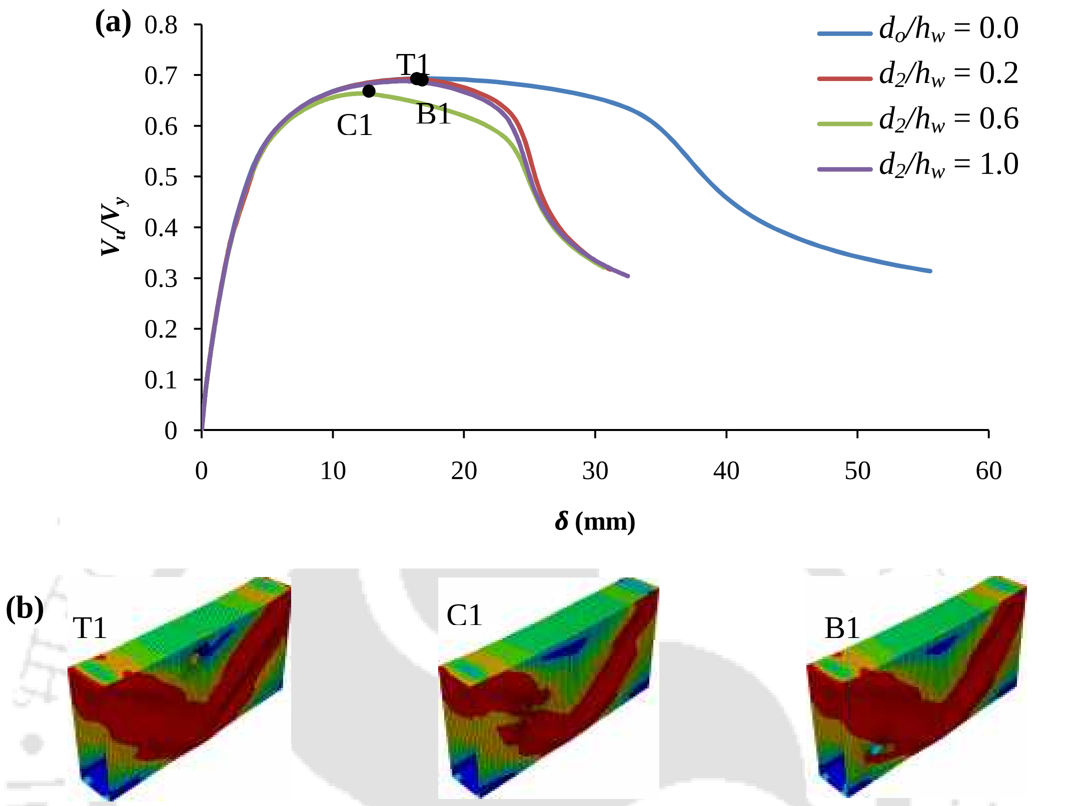

Figure 4.21: a) Variation of V_u/V_y vs δ, and b) von-Mises stress contour for d_2/h_w = 0.2 (T1), d_2/h_w = 0.6 (C1), d_2/h_w = 0.8 (B1) (d_o/h_w = 0.1; a/h_w = 1.0, t_f/t_w = 5, h_w/t_w = 300).

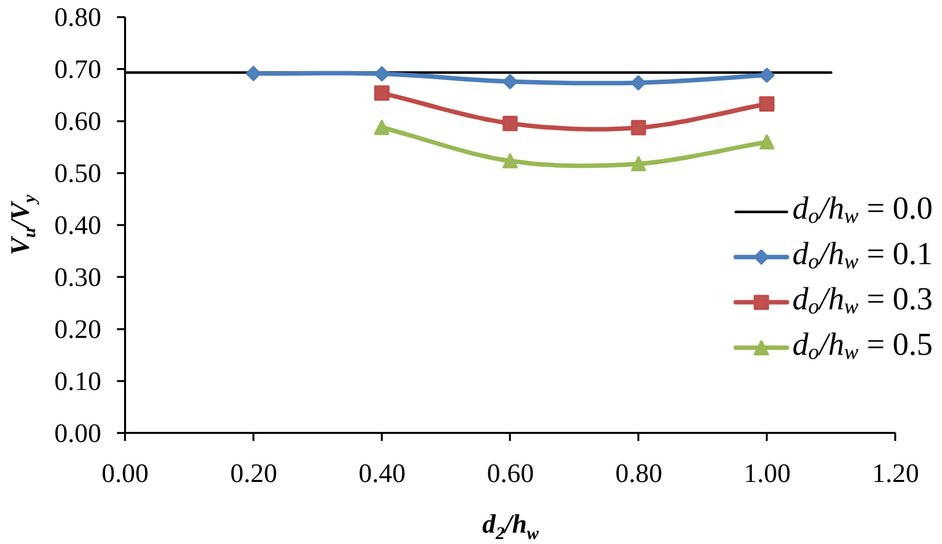

Figure 4.22: Variation of V_u/V_y vs d_2/h_w (a/h_w = 1.0, t_f/t_w = 5, h_w/t_w = 300).

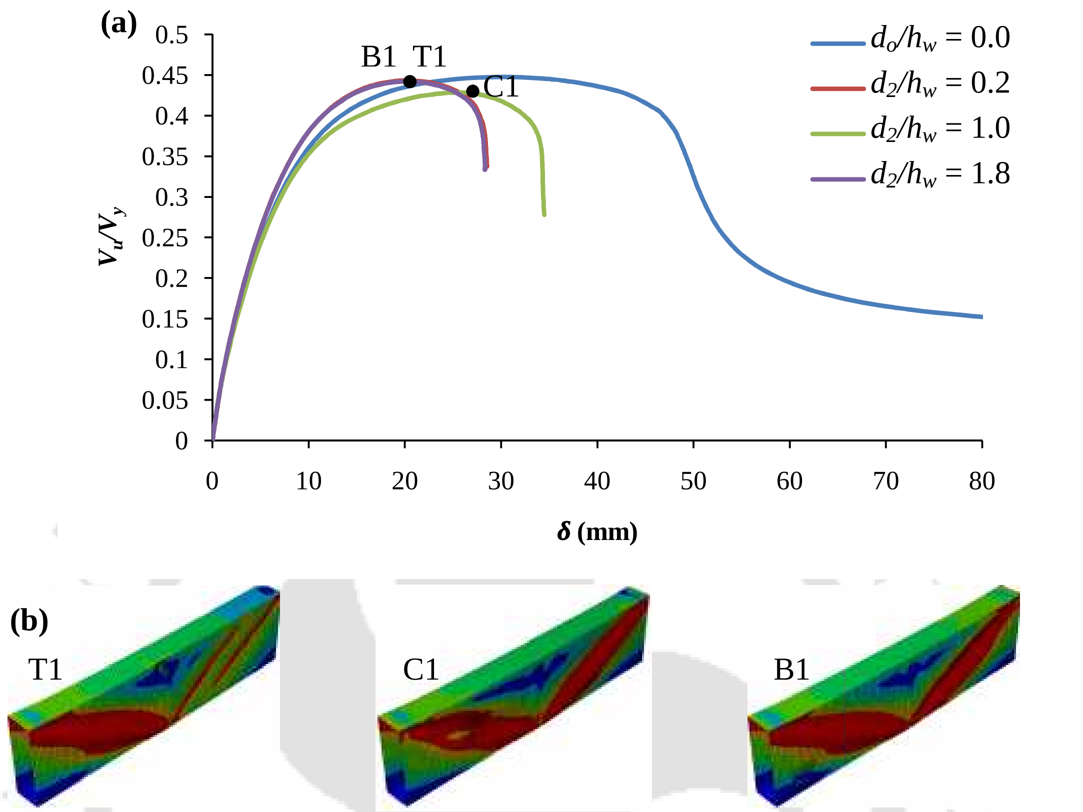

Figure 4.23: a) Variation of V_u/V_y vs δ, and b) von-Mises stress contour for d_2/h_w = 0.2 (T1), d_2/h_w = 1.0 (C1), d_2/h_w = 1.8 (B1), (d_o/h_w = 0.1; a/h_w = 2.0, t_f/t_w = 5, h_w/t_w = 300).

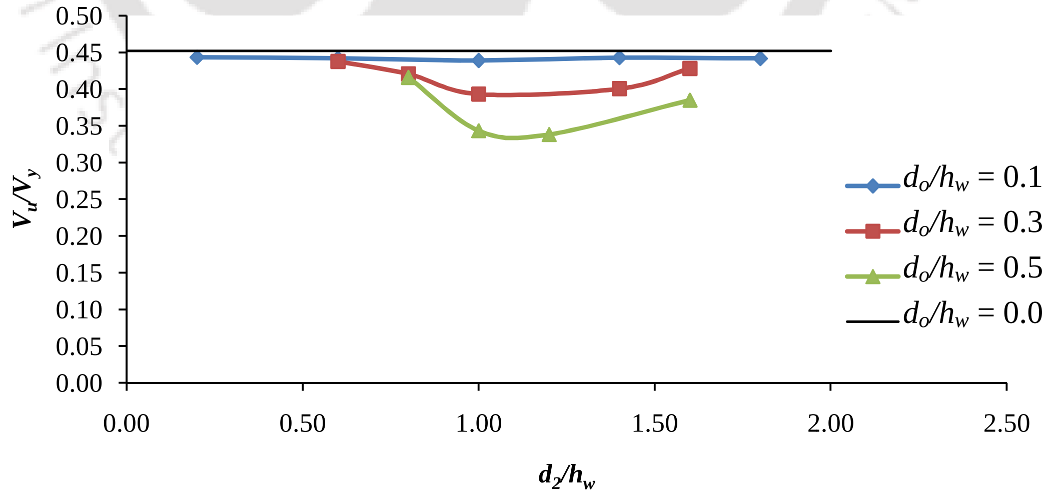

Figure 4.24: Variation of V_u/V_y vs d_2/h_w (a/h_w = 2.0, t_f/t_w = 5, h_w/t_w = 300)

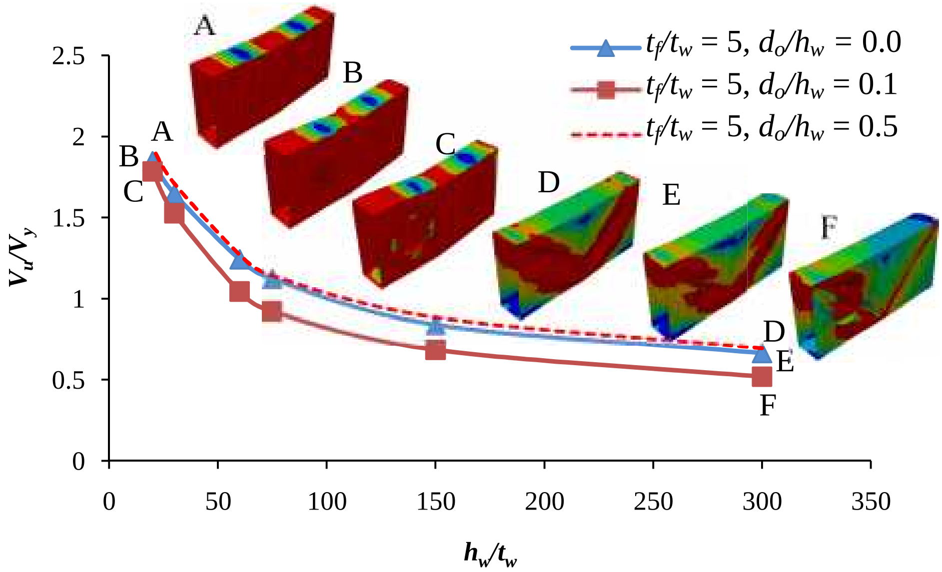

Figure 4.25: Variation of V_u/V_y vs h_w/t_w for d_o/h_w = 0.1 and 0.5 (t_f/t_w = 5, a/h_w = 1)

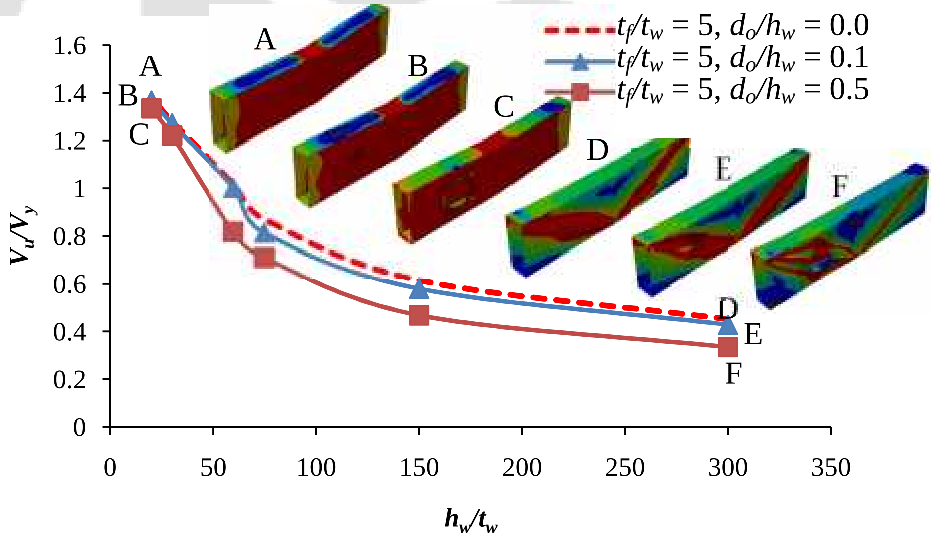

Figure 4.26: Variation of V_u/V_y vs h_w/t_w for d_o/h_w = 0.1 and 0.5 (x/h_w = 1.0; y/h_w = 0.5, t_f/t_w = 5, a/h_w = 2.0)

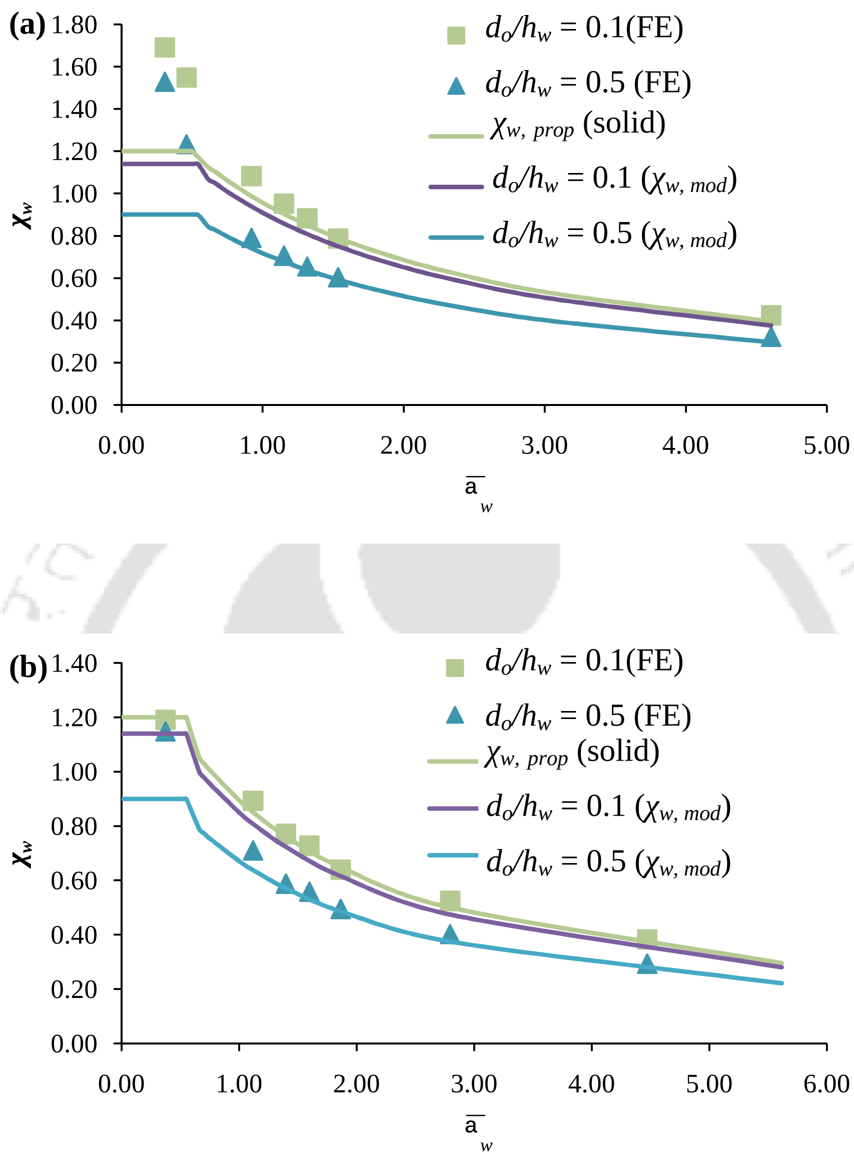

Figure 4.27: Comparison of FE results of circular opening sizes with proposed EN 1993-1-4 (2006/A1:2015) curve for d_o/h_w = 0.1 & 0.5 of 1) $a/h_w \leq 1.0$ and 2) $1.0 < a/h_w \leq 2.0$.

CHAPTER 5

STIFFENING EFFECTS ON THE SHEAR BEHAVIOR OF SINGLE PERFORATED LEAN DUPLEX STAINLESS STEEL (LDSS) RECTANGULAR HOLLOW BEAMS

5.1 INTRODUCTION

In the previous chapter i.e. Chapter 4, the effect of perforation parameters i.e. size and location (along longitudinal, transverse and diagonals) on the shear capacity and deformation behaviour of single perforated LDSS rectangular hollow beams. In general, a reduction in the shear capacity (V_u/V_y) was observed when single perforation was introduced in the web panel even for a relatively small perforation size i.e. d_o/h_w = 0.10. It then becomes pertinent to study if such reduction in shear capacity can at least be compensated through reinforcements such as stiffener attachment around the perforation. As discussed in the literature review (Chapter 2), several types of stiffeners (e.g. ring, horizontal, transverse, sleeves, doubler plate stiffeners) were employed to augment load (shear, compression etc.) capacity of open webs/plate perforated with circular / rectangular holes (see e.g. Narayanan and Der-Avanessian, 1984b; Keerthan and Mahendran, 2013; Hamoodi and Gabar, 2013; Hagen *et. al.*, 2009; Kim *et. al.*, 2015). It may be noted that such studies were mainly on open sections e.g. plates, I-sections etc. Types of stiffeners used in members subjected to shear loading are, doubling plate (Keerthan and Mahendran, 2013; Kim *et.al.*, 2015); ring (Keerthan and Mahendran, 2013; Hamoodi and Gabar, 2013, Narayanan and Der-Avanessian, 1984b; Kim *et.al.*, 2015); vertical and horizontal, inclined (Cheng and Li, 2012) stiffeners. In this study, such studies are extended to assess the shear behaviour of stiffened single perforated LDSS rectangular hollow beam (i.e. closed section), using FE analysis approach considering various orientations / patterns such as vertical, horizontal, diagonal / inclined and ring; and cross-sections i.e. flat, angular and semi-circular. More specifically, the effect of variation in cross-sectional dimensions (or slenderness) e.g. width (b_s), thickness (t_s) and length (l_s) of the stiffener for the abovementioned stiffener patterns are investigated. The results of the FE analyses are presented in the form of variations in shear capacity (V_u/V_y) with respect to normalised parameters like l_s/d_o, b_s/h_w (for various values of t_s/t_w), mid-span deformation (δ), deformation shapes etc.

5.2. NUMERICAL (FE) MODELLING

5.2.1 General

The FE modelling procedure (e.g. meshing, boundary conditions, imperfection seeding, material modelling etc.) followed in this chapter is similar to those described in Sections 3.2 and 4.2 for unperforated and perforated LDSS rectangular beams respectively, and hence, are not repeated in this chapter. The key additional difference is the incorporation of FE models for the various types of stiffeners mentioned above. Geometry and FE mesh used for the stiffeners are presented in the following subsections.

5.2.2 Geometry

Figure 5.1 shows the schematic representation for a typical geometry, FE mesh and boundary conditions considered. The various fixed cross-sectional parameters were h_w = 600 mm, a = 600 mm, w_f = 200 mm, t_f = 10 mm, t_w = 2 mm, such that a/h_w = 1.0 and t_f/t_w = 5. A centrally located perforation with moderately large diameter, d_o = 300 mm (d_o/h_w = 0.5) was chosen as the benchmark perforated beam upon which the effect of stiffener is studied. It may be noted that the reduction maximum in the shear capacity for the case of d_o/h_w = 0.5 was seen to be about 26% as compared to the unperforated case (see Figure 4.5), whilst it was lesser for smaller perforation sizes (d_o/h_w < 0.5). Further, it was also seen that for the small perforation size (d_o/h_w = 0.1) considered, for the various perforation locations tested (transverse, longitudinal and diagonals), no significant variation in the shear capacity could be seen, although centrally located perforation (i.e. $x/h_w = y/h_w$ = 0.5; see Chapter 4), apparently gave the highest reduction in shear capacity, suggesting that central location is the critical location. Four types of stiffener patterns *viz.*, inclined (*IS*), vertical (*VS*), horizontal (*HS*) and ring (*RS*) were considered (see Figure 5.2). For *IS*, *VS* and *HS*, two parallel stiffeners of equal length located at opposite sides of perforation were considered. Stiffener with flat (or rectangular) cross-sections (*FC*) were considered for all the stiffener patterns i.e. *IS*, *VS*, *HS* and *RS*, initially; whereas angular (*AC*; 90^{o} between equal legs) and semicircular (*SC*) cross-sections were considered for the inclined orientation (*IS*), to assess cross-sectional shape effect (see Figure 5.3).

The values of length (l_s), breadth (b_s) and thickness (t_s) of the stiffeners adopted in the FE analyses ranged from 300–515 mm (or l_s/d_o = 1.00–1.75, where d_o = diameter of opening, $D_o = d_o + 2 \times 10$ mm, D_o is diameter of ring stiffener), 24–72 mm (or b_s/h_w = 0.04–0.12) and 2–14 mm (or t_s/t_w = 1–7). A 10 mm clearance (s/t_w = 5, where s is the distance between edge of opening to stiffener edge) of the stiffeners from the edge of the perforation has been maintained, such that the stiffeners are separated by an additional 20 mm (i.e. 2 × 10 mm) in addition to the perforation size (or perforation diameter, d_o). The clearance was assumed to avoid the stiffener being too close to the perforation edge so that welding can be done at ease (e.g. Hagen (2005) assumed s/t_w = ~ 0.6-1.2 i.e., 10-20 mm; Cheng and Zhao (2010) have taken the s/t_w = 0.5). The inclined stiffeners (*IS*) were provided perpendicular to the diagonal of the perforated web (resulting in perpendicular to the tension band, as seen in Chapter 4); in the case (i.e. a/h_w = 1), it is at 45^o to the longitudinal axis of the beam. In order to compare the effectiveness of the three cross sections (*FC*, *AC* and *SC*) of the stiffeners, in the inclined mode, the material consumption (or cross-sectional area) was kept same. To realise this, the legs of the *AC* section are made equal to half of the *FC* breadth (i.e. b_s/2); and the circumference of the *SC* section was taken to be equal to b_s (the diameter of the *SC* section, D_s was taken as the variable; D_s = 15–46 mm in this study). Further, the maximum length of stiffener (l_s) was chosen so that the outer dimensions of the stiffeners were limited to the inner edge of the flanges.

5.2.3 Finite element mesh

Typical FE mesh for perforated beam with inclined stiffeners (*IS*) with flat cross section (*FC*) is shown in Figure 5.1c. Except for the additional FE mesh for the stiffeners, the rest of the meshing pattern follows those discussed in Section 4.2.3. Stiffeners were also meshed with similar elements i.e. S4R elements (with aspect ratio ~1), except that relatively finer meshes (or smaller elements) were adopted, since the stiffener geometry is smaller in comparison to the main beam. A minimum of 10 S4R elements were adopted along the breadth of the stiffener in order to capture the interaction of stresses between the perforated web and stiffeners, based on mesh convergence study. The stiffeners were modelled separately using a uniform mesh and then tied to the perforated web through ‘tie’ option available in Abaqus (2009). This makes it possible to mesh both the web and stiffener, without much concern on the node location compatibility at the junction. The total number of elements in a stiffener ranges from 50–200, depending on their geometry.

5.2.4 Parametric study

In the parametric study, the effect of various parameters of the stiffeners e.g. cross-sectional shapes (*FC*, *AC*, and *SC*) and dimensions (l_s, b_s, t_s) on the shear characteristic of single circular perforated short span (a/h_w = 1) LDSS rectangular hollow beam was investigated, for the range of parameters mentioned in Section 5.2.2. The results are presented in the form of i) variation of shear with mid-span transverse deformation (V/V_y vs δ), von-Mises stress contours, and variation of shear capacity (V_u/V_y).

5.3 RESULTS AND DISCUSSION

First, the effect of the stiffener pattern i.e., *IS*, *VS*, *HS* and *RS* on the shear behavior *viz*., shear capacity and deformed shapes are presented in terms of variation in stiffener lengths (l_s) and breadth (b_s) in Sections 5.3.1–5.3.4. This is followed by a comparison of the effect of cross-sectional shapes viz., *FC*, *AC* and *SC* on the shear capacity keeping the same material cross-sectional area and length (Section 5.3.5). The results for perforated (without stiffeners) and unperforated beams (shown in the previous chapter i.e. Chapter 4) are also presented for comparison.

5.3.1 Inclined stiffener (*IS*)

5.3.1.1 Effect of stiffener length (l_s)

Variation of V/V_y with δ (along with von-Mises contour plots) for b_w = 24 mm (or b_w/h_w = 0.04) are shown in Figures 5.4 and 5.5 for thin (t_s = 2 mm or t_s/t_w = 1) and thick (t_s = 14 mm or t_s/t_w = 7) stiffeners respectively. In Figures 5.4a and 5.5a, the results are presented for l_s = 300–525 mm (or l_s/d_o = 1.00–1.75 i.e. 75% increase in l_s from 300 mm). It can be seen from Figure 5.4a, there is no significant change in both the shear capacity (V_u/V_y or V_{RF}/V_y) or the shape of the V/V_y vs δ profile, for the thin stiffeners considered. An increase of about 2% in V_u/V_y can be observed when l_s is increased by 75%. The enhancement in V_u/V_y for the stiffened beam in comparison to the perforated beam is about ~1.5–3.6%. Figure 5.4b, shows the von-Mises contour plot at V_u, V_{RF} and post V_{RF} shear values, for unperforated (S1, S2, S3), perforated (P1, P2 and P3) , and stiffened beams (inset L1, L2 and L3 for l_s/d_o = 1; inset H1, H2 and H3 for l_s/d_o = 1.75). It can be seen that there is little variation in von-Mises stress contour plot and deformed shapes for l_s/d_o = 1.00 and 1.75 (see L1, L2, L3 and H1, H2, H3). This may be related to the relatively thin section (t_s/t_w = 1) considered. It is also seen that due to the presence of stiffeners, the local corrugated (accompanied by both inward and outward buckling) buckling of perforation edges (mostly along the tension band; see inset figure P1 in Figure 5.4b) is now changed to outward local buckling, at V_u. The outward local buckling of the stiffened web (inset L1 and H1 figures in Figure 5.5b), may be related to the weaker cross-sectional slenderness (owing to thinner section). Very similar post-V_u failure modes (i.e. formation of plastic hinge in the compression flange, stress distribution pattern in the vicinity of the perforation) are also seen for both the short and long values of l_s; this observation also agrees with the similar values of δ_{RF} as seen in Figure 5.4a.

The effect of thick stiffener (t_s/t_w = 7; or t_s = 14 mm) is shown in Figure 5.5. (l_s/d_o = 1.00–1.75, b_w/h_w = 0.04). From Figure 5.5a, a significant enhancement in the shear capacity of the stiffened beam can be seen when the value of l_s/d_o is increased from 1.00–1.75 (i.e. as the stiffener gets thicker). The increase in V_u/V_y is ~2.8, 6, and 21% for l_s/d_o = 1.25, 1.5 and 1.75 respectively, in comparison to l_s/d_o = 1.0. For, the smallest length considered i.e. l_s/d_o =1, the value of V_u/V_y is found to be higher by ~9% compared to the perforated case. When l_s/d_o = 1.75, the unperforated shear capacity is nearly recovered. It may be noted that the value of δ_{RF} for the longest stiffener length considered (i.e. l_s/d_o = 1.75) is about ~25% shorter as compared to that corresponding to l_s/d_o = 1.0 i.e. the onset of rapid-falling curve occurs much earlier when the thickness of the stiffener is sufficiently large enough. Von-Mises contour plot corresponding to l_s/d_o = 1.0 and 1.75 are shown in Figure 5.5b. It can be observed that due to the presence of the thick stiffeners, highly stressed von-Mises stress near the perforation is relatively distributed over a larger area, at V_u (see inset figures L1 and H1 in Figure 5.5b). Again, corrugated local buckling at the perforated edge of the unstiffened web, is prevented due to the stiffening effect. But unlike in the case with thin stiffeners, the outward buckling of the stiffened web is visibly reduced (see L1 and H1 in Figure 5.5b), when thick stiffeners are used. It may be noted that for the longest stiffener (i.e. l_s/d_o = 1.75), the formation of plastic hinge at the compression flange is now shifted towards the unperforated side (see H2), unlike the case for shorter stiffener (see L1 and L2). This may be because, due to the thick elongated stiffener, significant improvement in the load capacity of the perforated span may have achieved. The effect of l_s on the shear capacity is plotted in the form of V_u/V_y vs l_s/d_o, for thickness, t_s/t_w = 1–7 (or t_s = 2–14 mm) in Figure 5.6. Shear capacity increased with increase in stiffener thickness (t_s/t_w = 1 to 7) in a non linear trend. It can be seen that, for higher thicknesses e.g. $t_s/t_w \geq 3$, the rate of increase in V_u/V_y increases with increasing l_s/d_o, thus suggesting that the role of stiffener thickness in enhancing the shear capacity becomes more effective at longer length (l_s). For the longest and thickest stiffener (l_s/d_o = 1.75 & t_s/t_w = 7), the stiffened perforated beam has already achieved the shear capacity of unperforated beam.

5.3.1.2 Effect of stiffener breadth (b_s)

The effect of stiffener breadth (b_s) is presented in the form of variation of V/V_y with δ, von-Mises contour plots, and V_u/V_y with b_w/h_w, for two cases *viz.*, short (l_s/d_o = 1) and long (l_s/d_o = 1.75) stiffeners in Figures 5.7–5.9 and 5.10–5.12 respectively. Variation of V_u/V_y with δ and von-Mises contour plots are shown for thin (t_s/t_w = 1) and thick (t_s/t_w = 7) for short stiffener (l_s/d_o = 1) in Figures 5.7 and 5.8 respectively, for b_s ranging from 24–60 mm (or b_s/h_w = 0.04–0.10). Moreover, it can be seen from Figures 5.7 and 5.8 that it is not able to regain the unperforated shear capacity even after an increase of 150% in b_s from 24 mm. For both the thin and thick stiffeners, the enhancement in V_u/V_y is ~8.8% as compared to the unstiffened beam. It is also seen that the von-Mises stress distribution in the stiffened perforated web is not noticeably changed for the change in b_s (see L1, H1 in Figures 5.7 and 5.8). Figure 5.9 shows the variation of V_u/V_y with b_s/h_w for t_s/t_w = 1–7. It can be seen that, there is no significant change in the value of V_u/V_y for b_s/b_w ranging from 0.04–0.10, for the thicknesses considered, suggesting that there is not much benefit in increasing the cross-sectional dimension (in terms of b_s and t_s) for short stiffeners (l_s/d_o = 1.0). In the case of long stiffeners (l_s/d_o = 1.75), an improved enhancement in V_u/V_y can be seen even for thin stiffeners; an increase of ~19% in V_u/V_y as compared to non stiffened case, can be observed for b_s/h_w = 0.10 (or b_s = 60 mm). Whereas for thick stiffeners (t_s/t_w = 7), almost full strength of the unperforated beam could be achieved at lower b_s (= 0.04). A comparision of the von-Mises contour plots between thin (Figure 5.10b) and thick (Figure 5.11b) stiffeners for longer stiffeners shows that due to sufficiently improved shear capacity has resulted in the occurrence of plastic hinge formation at the compression flange being shifted towards the unperforated span (L2 and H2 in Figure 5.11b), with stress relaxation in the stiffened webs. Variation of V_u/V_y with b_s/h_w for long stiffeners (l_s/d_o = 1.75) is shown in Figure 5.12, for t_s/t_w = 1–7. It can be seen that, uperforated shear capacity has been achieved at b_s/h_w = 0.04, 0.06, 0.08 for t_s/t_w = 7, 5 and 3 respectively, whereas it could not be attained for the thin stiffener (t_s/t_w = 1). This indicates that increase of b_s has relatively more enhancement effect for thicker stiffeners (e.g. t_s/t_w $\geq$ 3) in stiffener length l_s/d_o = 1.75.

5.3.2 Vertical stiffener (*VS*)

5.3.2.1 Effect of stiffener length (l_s)

The effect of vertical stiffener lengths on the shear capacity is presented in Figures 5.13–5.15. Figures 5.13 and 5.14 show V/V_y *vs* δ and von-Mises contour plots for thin and thick stiffeners respectively, for l_s/d_o = 1.00–1.75 (b_s/h_w = 0.04). Unlike in the case of inclined stiffeners as discussed above, there appears to have no significant effect (or enhancement) on V_u/V_y due to the presence of either thin or thick vertical stiffeners, for $l_s/d_o \leq 1.5$ (the V/V_y vs δ profile is almost similar to that of perforated beams), however a slight increase (~ 4%) in V_u/V_y can be observed when l_s/d_o is increased to 1.75. Observing the von-Mises stress contour plots at V_u/V_y, it can be seen that the stress distribution more or less remains similar to that of unstiffened beam. The local buckling of the perforation edge along the diagonal tension band appears to remain unaffected by the presence of vertical stiffeners, and most of the highly stress region is now confined within the region bounded by the vertical stiffeners (atleast for the longest stiffener i.e. l_s/d_o = 1.75) (see L1 and H1 in Figures 5.13b and 5.14b). Variation of V_u/V_y with l_s/d_o is shown for t_s/t_w = 1–7 in Figure 5.15. Again, there appears to have no significant improvement in V_u/V_y for both the variation in length (l_s/d_o = 1.00–1.75) and thicknesses (t_s/t_w = 1–7), indicating that length effect does not make any enhancement in shear capacity.

5.3.2.2 Effect of stiffener breadth (b_s)

The effect of vertical stiffener width (b_s) for short and long stiffeners are presented in Figures 5.16–5.18 and 5.19–5.21 respectively. For each of the short and long stiffeners, the results of both thin and thick stiffeners are also presented. For the short stiffener, variation of V/V_y with δ along with von-Mises contour plots is shown in Figures 5.16 and 5.17 respectively for thin and thick stiffeners. From Figure 5.16

and 5.17, it can be observed that there is almost no improvement in the shear capacity of the perforated beam, even after the b_s is increased from 24–60 mm (or b_s/h_w = 0.04–0.10), for both the thin and thick stiffeners. The local buckling near the perforation edge appears to remain unaffected by the presence of the short (both thin and thick) stiffeners. The distribution of the highly stressed region along the diagonal tension band remains more or less unaltered (see L1 and H1 in Figures 5.16b and 5.17b). Figure 5.18 shows the variation of V_u/V_y with b_s/h_w, for the short stiffener, for thickness ranging from t_s/t_w = 1–7. Clearly, no improvement in V_u/V_y can be seen for the range of b_s and t_w considered, suggesting that short vertical stiffeners do not have any measureable effect on the shear capacity of the perforated beam. Again, this may be related to the inability of the vertical stiffeners to arrest local buckling around the perforation edge. The effect of b_s for long stiffener are presented in Figures 5.19 and 5.20 respectively for thin and thick stiffeners. A slight improvement (~5%) in V_u/V_y can be seen for both the thin and thick stiffeners, although there is no apparent change in V_u/V_y for the range of b_s/h_w (0.04–0.10) considered. Again, it is seen that at V_u, most of the highly stressed region in the vicinity of the perforation is now confined between the vertical stiffeners (see L1, H1 in Figures 5.19 and 5.20). Unlike the case of short stiffeners, the increase in shear capacity may be attributed to the enhanced restriction imposed by the elongated (spans the web height i.e. l_s/d_o = 1.75) on the local buckling in the vicinity of the stiffeners and near the perforation edge. It may be seen that such restriction of local buckling associated with the long stiffeners is relatively low (see 5.16b, 5.17b and 5.19b, 5.20b). Figure 5.21 shows the variation of V_u/V_y with b_s/b_w for t_s/t_w = 1–7. It can be seen that there is no significant change in V_u/V_y for b_s/h_w = 0.04–0.10, for all the thickness considered, although in an average increase in V_u/V_y due to the presence of stiffeners is ~5%. This suggests the beneficial effect of providing vertical stiffeners is little.

5.3.3 Horizontal stiffener (*HS*)

5.3.3.1 Effect of stiffener length (l_s)

The length effect (l_s) for thin and thick horizontal stiffeners are presented in Figures 5.22 and 5.23 respectively, in the form of V_u/V_y vs δ and von-Mises contour plots, for l_s/d_o = 1.00–1.75 (b_s/h_w = 0.04). From Figures 5.22 and 5.23 it can be seen that, for the case with thin stiffeners, there is no significant improvement in V_u/V_y, whereas an enhancement of ~ 5% could be obtained with thick stiffeners. However there is little variation in V_u/V_y for the range of stiffener length considered i.e. l_s/d_o = 1.00–1.75. From Figure 5.22b, it can be seen that the thin horizontal stiffeners are not able to arrest the local buckling occurring in the vicinity of the perforation, even after l_s/d_o is increased up to 1.75. Whereas for thick horizontal stiffeners, it appears that some resistance has been offered to the local buckling around the perforation, especially for the case of l_s/d_o = 1.75 (see H1 in Figure 5.23). Variation of V_u/V_y with l_s/d_o for t_s/t_w = 1–7 is shown in Fig. 5.24. For the range of l_s/d_o = 1.00–1.75, it is seen that there is no significant variation in V_u/V_y for the range of t_s/t_w considered. For the highest thickness considered, an average enhancement of ~5% for V_u/V_y could be obtained. Thus, there appears to have little beneficial effect of horizontal stiffeners for the range of t_s and l_s considered.

5.3.3.2 Effect of stiffener breadth (b_s)

The effect of horizontal stiffener breadth (b_s) for short and long stiffeners are presented in Figures 5.25–5.26 and 5.28–5.29 respectively. The results are also presented for thin and thick stiffeners. It can be seen that in the case of short stiffener length, there is no significant increase in V_u/V_y for the case of thin stiffeners (Figure 5.25), however, an increase of ~7% in average could be obtained for the case of thick stiffeners (Figure 5.26), with little variation in V_u/V_y for b_w/h_w =

0.04–1.0. Thus suggest that the effect of b_s increases at higher thickness, and this is consistent with the increase in stiffener cross-sectional stiffness. From Figures 5.25b and 5.26b (inset L1 and H1), it can be seen that at V_u, it appears that increase in b_s, did not significantly improve the buckling resistance of the perforated web, with the stress distribution more or less unchanged. Variation of V_u/V_y with b_s/h_w for the short length stiffener is presented in Figure 5.27, for t_s/t_w = 1–7. Again, no significant change in V_u/V_y can be seen for b_s/h_w = 0.04–0.10, for the range of thicknesses considered. For the case of long stiffeners, an improved V_u/V_y is seen with both thin (Figure 5.28) and thick (Figure 5.29) stiffeners with increasing b_s/h_w, with no substantial variation in V_u/V_y when b_s/h_w is varied from 0.04–0.10. The increase in V_u/V_y is in the range ~2.5–5%, and 5.5–8% for the thin and thick stiffeners respectively. From Figures 5.28b and 5.29b, again, it is seen that no substantial resistance being offered by the long horizontal stiffeners in preventing local web buckling in the vicinity of the perforation, although the resistance appears to have improved for the thick stiffeners (L1, H1 in Figures 5.28b and 5.29b). Again, the effect of b_s/h_w on V_u/V_y, appears to be minimal, for the variation in t_s/t_w from 1–7 (the plot appears nearly horizontal in Figure 5.30). Thus, again, it appears horizontal stiffeners are also not very effective in enhancing V_u/V_y for the perforated beams.

5.3.4 Ring stiffener (*RS*)

5.3.4.1 Effect of stiffener breadth (b_s)

Figures 5.31 and 5.32 shows the effect of stiffener breadth (b_s) for ring stiffeners provided around the perforation, for thin and thick stiffeners respectively, in the form of V_u/V_y vs δ and von-Mises contour plots. For the thin stiffeners, the increase in V_u/V_y, when b_s/h_w is increased from 0.04–0.10 is ~2% in an average, whereas for thick stiffener, the increase is in the range ~9–15%, for the same increase in b_s/h_w.

This may be because, the thin stiffeners are apparently not able to resist substantially, the local web buckling around the perforation (L1 and H1 in Figure 5.31b). However, with the thick stiffener, an enhanced resistance to web buckling is visible (Fig 5.32b). In Figure 5.32b, it can be seen that at V_u, the circular shape of the ring is not distorted, especially for b_s/h_w = 0.10, an indication that web buckling is resisted. In Figure 5.33, variation of V_u/V_y with b_s/h_w is shown, for t_s/t_w = 1–7. It can be seen from figure 5.33 that, V_u/V_y increases with increasing b_s/h_w and t_s/t_w, although the highest increase is ~15% corresponding to b_s/h_w = 0.1 and t_s/t_w = 7. The rate of increase in V_u/V_y (with respect to the unstiffened beam) appears to be slightly higher for larger values of b_s/h_w. This may be related to the increase in cross-sectional stiffness due to increase in cross-sectional area of the stiffeners.

5.3.5 Comparison of flat (*FC*), angular (*AC*) and semi-cricular (*SC*) inclined stiffeners

From the previous discussions on inclined, vertical and horizontal stiffeners (see Sections 5.3.1–5.3.3), it was observed that, amongst the three types of flat stiffeners, inclined flat stiffeners were able to achieve the full unperforated beam strength: 1) for the shortest stiffener width i.e. b_s/h_w = 0.04, the unperforated shear capacity was reached for the thickest stiffener (t_s/t_w = 7) and longest stiffener length (l_s/d_o) provided, and 2) for the longest stiffener length i.e. l_s/d_o = 1.75, the unperforated shear capacity was reached at t_s/t_w = 7, 5, 3 for b_s/h_w = 0.04, 0.06 and 0.08 respectively (see Figures 5.6 and 5.12). Hence in this section, the results of variation in cross-sectional shape of the stiffener i.e. flat (*FC*), angular (*AC*) and semi-circular (*SC*) sections, for inclined stiffeners are presented considering the same cross-sectional area for material consumption, to check their efficiency.

5.3.5.1 Flat (*FC*) vs angular (*AC*) cross sections

Typical dimensions for the comparison between angular and flat sections are: l_s/d_o = 1.5 and t_s/t_w = 1 and 5, for all the cross-sections considered (see Figure 5.4). Figures 5.34 and 5.35 shows the effect of b_s/h_w for thin (t_s/t_w = 1) and thick (t_s/t_w = 5) angular stiffeners. It can be seen from Figures 5.34 and 5.35 that V_u/V_y is found to increase with increasing b_s/h_w; an increase of 200% in b_s/h_w (from b_s/h_w = 0.04), resulted an increase in V_u/V_y of ~17% and ~32% from the unstiffened shear capacity, for the thin (t_s/t_w = 1) and thick (t_s/t_w = 5) stiffener section respectively. Typical von-Mises contour plots are also shown for b_s/h_w = 0.04 and 0.12 at V_u and post-V_u (at $3\delta_u$) in Figure 5.34b and 5.35b corresponding to thin and thick stiffeners respectively. At V_u, it can be seen that for thin sections (L1 and H1 in Figure 5.34b) and for b_s/h_w = 0.04 for the thick section (L1 in Figure 5.35b), the angular stiffeners are not able to resist the local web buckling in the vicinity of the perforations; the stiffeners are also seen to buckle which at later post-V_u stage (L2 and H2 in Figure 5.34b; and L2 in Figure 5.35b). However, for the wider breadth i.e. b_s/h_w = 0.12, thick section appears to have provided sufficient stiffness to prevent local buckling around the perforations (H1 in Figure 5.35b). In the post-V_u, such enhancement of V_u, resulted in shifting of the plastic hinge formation of the compression flange towards the unperforated span side (H2 in Figure 5.35b). This strengthening of the perforated web along with the non-formation of the plastic hinge on the compression flange on the stiffened side with subsequent formation of the compression flange plastic hinge on the unperforated span side, may have resulted in the reduction of δRF in Figure 5.35a. Similar such observations have also been made in the case of flat stiffeners (see Figure 5.5a). Comparison of the effect of angular and flat inclined stiffeners is shown in Figure 5.36 in the form of variation of V_u/V_y with b_s/h_w, for both thin and thick sections. It can be seen that angular stiffeners predicted lesser V_u/V_y for $b_s/h_w \leq 0.08$ and 0.10 for thin and thick sections, beyond which both the sections resulted in similar shear capacity values. This may be because, for the same value of b_s/h_w, the stiffness of the angular section may be relatively less in comparison to that of the comparable flat section, as the each legs of the angular section would of $(b_s/2)/h_w$ and further, they are oriented at an angle of 45^o with respect to the web surface.

5.3.5.2 Flat (*FC*) vs semi-circular (*SC*) cross sections

Figures 5.37 and 5.38 presents the effect of inclined stiffeners with semi-circular cross-sections, for thin (t_s/t_w = 1) and thick (t_s/t_w = 5) respectively. Again, similar to the case for angular cross-section (mentioned in the previous section), the semicircular circumferential length has been fixed at b_s, with l_s/d_o = 1.5, so that it has the same material cross-sectional area as that of flat section with breadth, b_s. This results in the outer diameter of the semicircular section in the range of 15–46 mm, corresponding to b_s/h_w = 0.04–0.12. It can be seen from Figure 5.37a that V_u/V_y increases with increasing b_s/h_w; the increase being ~19% with b_s/h_w = 0.12, when compared to the unstiffened case. For the thick section (t_s/t_w = 5), the unperfroated shear capacity has been achieved with b_s/h_w = 0.10–0.12. Similar to the case of flat and angular section as discussed above, both thin stiffener and thick section with lower b_s/h_w (e.g b_s/h_w = 0.04), the semicircular stiffener appears not to be effective in resisting the web buckling, rather, local buckling can be observed around the mid-length of the semicircular stiffener (along with the web). Again, for thicker sections (t_s/t_w = 5) and higher width (b_w/h_w = 0.12), it can be seen that at V_u, the semicircular stiffener is able to resist the local web buckling, and allows for better stress distribution in both the web and stiffeners (see H1 in Figure 5.38b). The comparison between flat and semicircular stiffeners are shown in figure 5.39, as a plot of V_u/V_y vs b_s/h_w, for t_s/t_w = 1 and 5 (l_s/d_o = 1.50). It can be seen from Figure 5.39 that, for the thick stiffeners, semicircular section showed lower values of V_u/V_y for $b_s/h_w \leq 0.10$, and for $b_s/h_w > 0.10$, both semicircular and flat section is able to provide the unperforated strength. On the other hand, for the thin sections, semicircular sections showed a slightly higher value of V_u/V_y as compared to that of flat sections, for b_s/h_w > 0.08. This may be related to the enhanced stiffness associated with the semicircular section as compared to flat sections, for higher values of b_s/h_w (e.g. 0.08).

Comparison of angular and semicircular section for both thick and thin stiffeners is presented in Figure 5.40. It can be observed that the variation of V_u/V_y with b_s/h_w due to angular and semicircular (keeping the same material consumption), for both thick and thin sections are very similar. V_u/V_y is found to increase with increasing b_s/h_w till ~0.1 and plateaus for b_s/h_w > 0.10, indicating that for the stiffeners dimensions analyses, both the stiffeners behaved similarly. Hence both may be used with equal efficiency for enhancing the shear capacity of perforated beam, although a thicker section with longer b_s/h_w is desirable.

5.4 CONCLUSIONS

FE studies on shear behavior of stiffened single perforated LDSS rectangular hollow beam have been investigated considering various stiffener parameters *viz.*, stiffener orientations / patterns such as inclined / diagonal, vertical, horizontal and ring; and stiffener cross-sections *viz.*, flat, angular and semi-circular. More specifically, the effect of variation in cross-sectional dimensions (or slenderness) e.g. width (b_s), thickness (t_s) and length (l_s) of the stiffeners for the abovementioned stiffener patterns and cross sections have been investigated. Based on the present study, the following key conclusions are drawn:

1) For the inclined stiffeners, it is observed that the rate of increase in shear capacity (V_u/V_y) increases (in a non linear trend) with increasing stiffener length for higher thicknesses (e.g. $t_s/t_w \geq 3$), thus suggesting that the role of stiffener thickness in enhancing the shear capacity becomes more effective at longer length. It is also seen that it is possible to achieve the strength of unperforated beam, with larger stiffener length and thickness, e.g. for the

longest and thickest stiffener (l_s/d_o = 1.75 & t_s/t_w = 7) considered, the stiffened perforated beam has achieved the shear capacity of unperforated beam. It is found that, there is no significant change in the value of shear capacity for increase in stiffener width, suggesting that there is not much benefit in increasing the cross-sectional dimension (in terms of b_s and t_s) for short length stiffeners (l_s/d_o = 1.0). In the case of long stiffeners, an improved enhancement in shear capacity can be seen even for thin stiffeners e.g. an increase of ~19% in V_u/V_y as compared to non stiffened case, can be observed for b_s/h_w = 0.10 (or b_s = 60 mm). Whereas for thick stiffeners (e.g. t_s/t_w = 7), almost full strength of the unperforated beam could be achieved at lower b_s (e.g. b_s = 0.04).

2) In the case of vertical and horizontal stiffeners, there appears to have no/little significant improvement in shear capacity for both the variation in length, width and thickness, indicating that providing vertical and longitudinal stiffeners are not very beneficial (lesser than ~ 5% enhancement) in enhancing the shear capacity of the perforated beam.

3) For the ring stiffeners, it is found that, shear capacity increases with increase in both breadth and thickness of the stiffeners (i.e. when the cross section gets stockier). The rate of increase in shear capacity (with respect to the unstiffened beam) appears to be slightly higher for larger values of stiffener thickness and breadth.

4) A comparison of the effect of angular and flat inclined (also flat and semicircular) stiffeners (keeping the same cross sectional area) shows that, angular/semi-circular stiffeners predicted lesser V_u/V_y for $b_s/h_w \leq 0.08$ and 0.10 for thin and thick sections respectively, beyond which both the sections resulted in similar shear capacity values. However, comparison made between angular and semi-circular sections showed that both the sections

predicted similar behavior of shear capacity: shear capacity is found to increase with increasing stiffener width for smaller values of stiffener width (e.g. $b_s/h_w < 0.10$) and a plateauing effect is seen for larger stiffener widths.

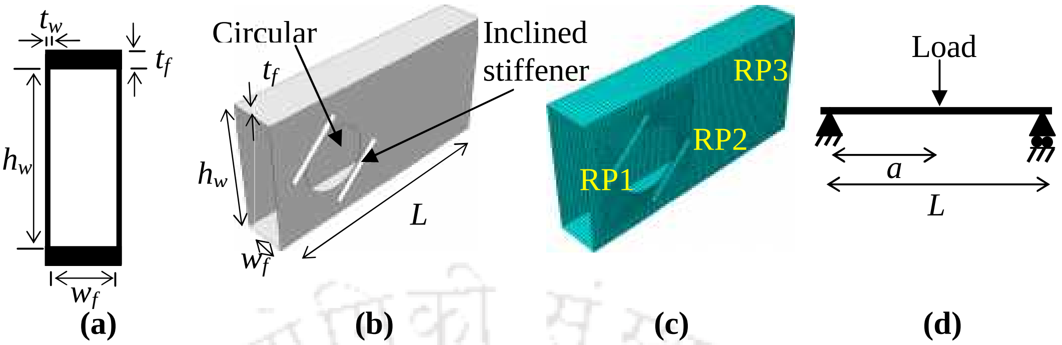

Figure 5.1: (a) Geometry (b) stiffener (c) Mesh (d) Loading and support condition.

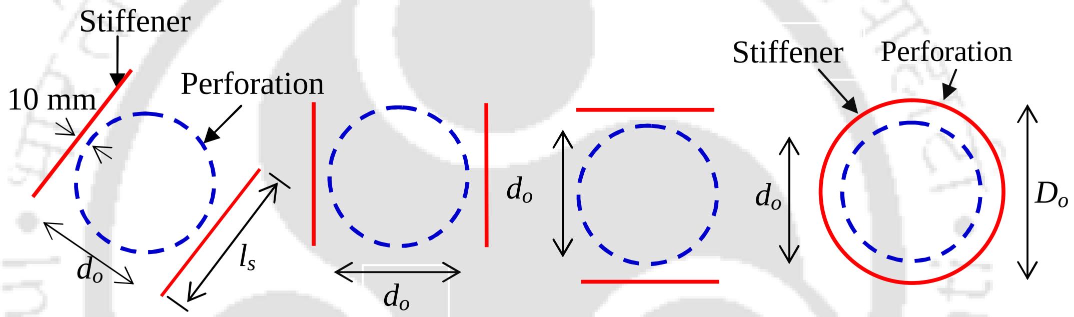

(a) Inclined (*IS*) (b) Vertical (*VS*) (c) Horizontal (*HS*) (d) Ring (*RS*)

Figure 5.2: Patterns of straight stiffeners (a-c), non straight stiffener (d)

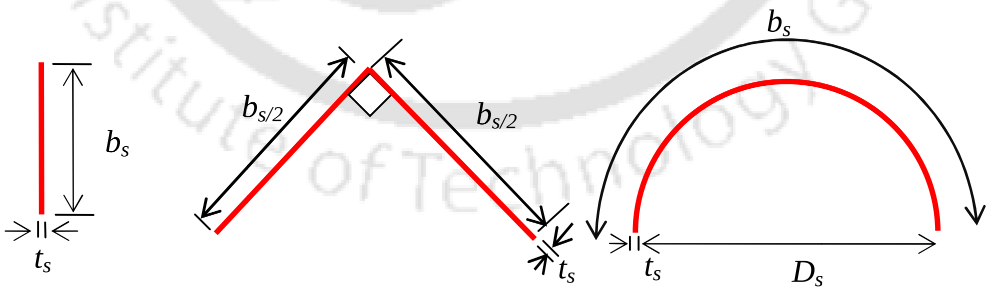

(a) Flat (*FC*) (b) Angular (*AC*) (c) Semicircular (*SC*)

Figure 5.3: Cross-section of stiffeners (a) Flat (*F*), angular stiffener (*A*), (b) semi-circular stiffener (*S*).

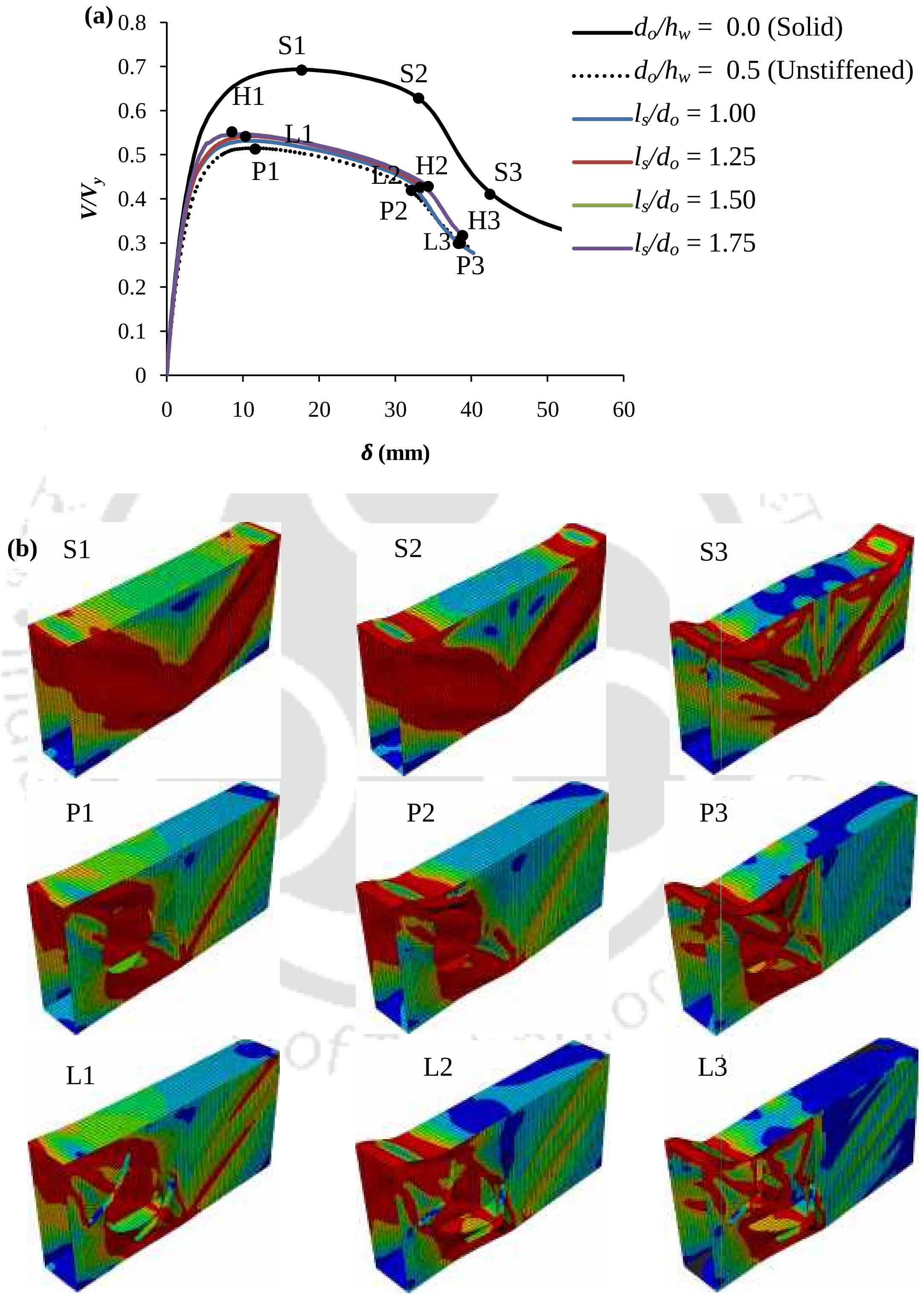
(a)
0.8
0.7
0.6
0.5
0.4
0.3
0.2
0.1
0
V/V_y
0
10
20
30
40
50
60
δ (mm)
S1
S2
S3
H1
H2
H3
L1
L2
L3
P1
P2
P3
d_o/h_w = 0.0 (Solid)
d_o/h_w = 0.5 (Unstiffened)
l_s/d_o = 1.00
l_s/d_o = 1.25
l_s/d_o = 1.50
l_s/d_o = 1.75
(b)
S1
S2
S3
P1
P2
P3
L1
L2
L3

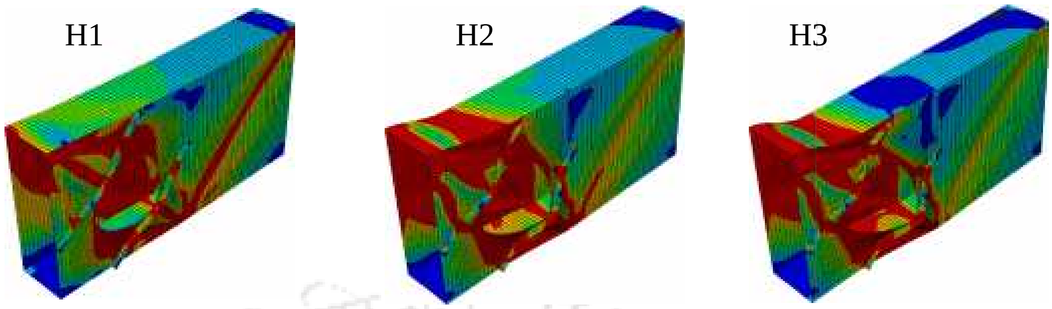

Figure 5.4: (a) Variation of V/V_y vs δ (l_s/ d_o = 1.00–1.75, b_s/h_w = 0.04, t_s/t_w = 1) for inclined stiffeners, (b) von-Mises stress contour for d_o/h_w = 0.0 (S1, S2, S3), d_o/h_w = 0.5 (P1, P2, P3) (x/h_w = 0.5, y/h_w = 0.5; a/h_w = 1.0, t_f/t_w =5), with inclined flat stiffeners l_s/d_o = 1.00 (L1, L2 & L3) & 1.75 (H1, H2 & H3) and thickness of t_s/t_w = 1.0.

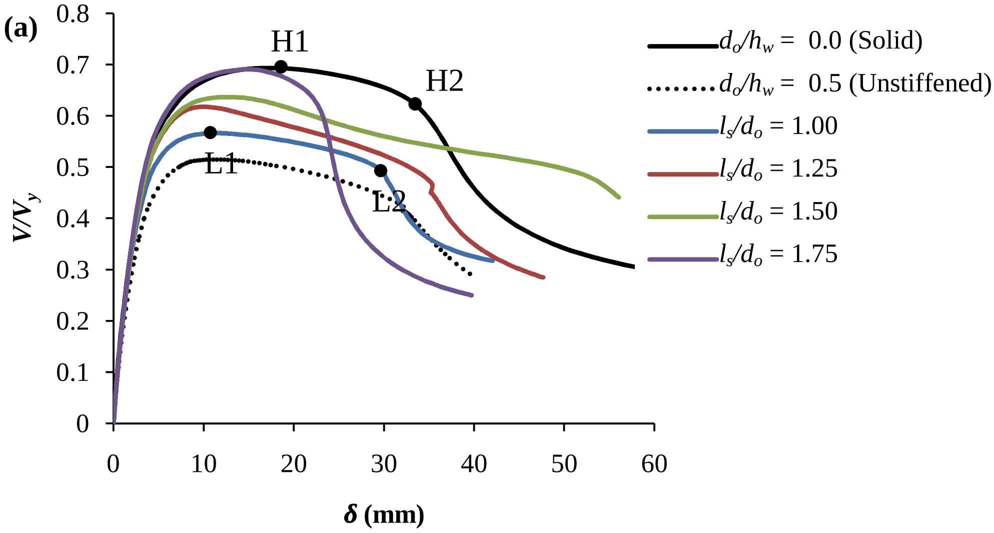

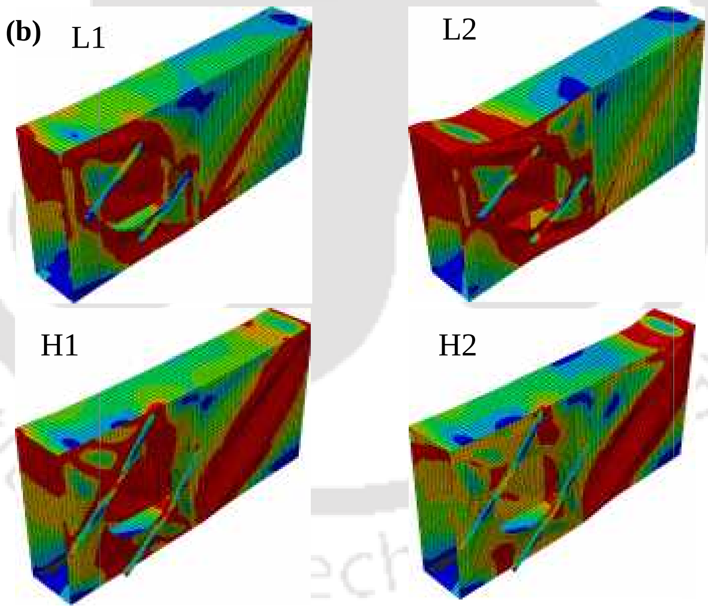

Figure 5.5: (a) Variation of V/V_y vs δ (l_s/d_o = 1.00–1.75, b_s/h_w = 0.04, t_s/t_w = 7) for inclined flat stiffeners, (b) von-Mises stress contour for length effect (l_s/d_o = 1.00 (L1 & L2) & l_s/d_o = 1.75 (H1 & H2)) of inclined flat stiffener (b_s/h_w = 0.04, t_s/t_w = 7.0).

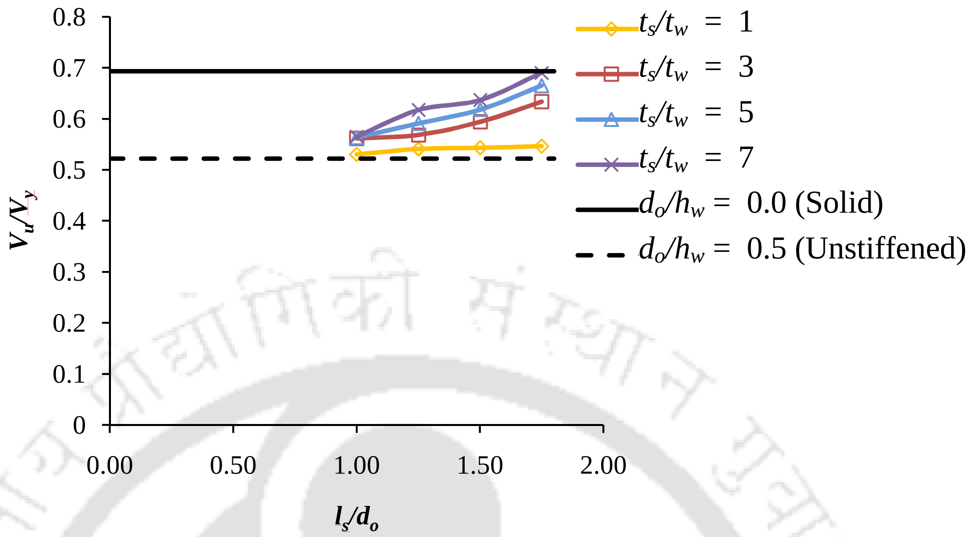

Figure 5.6: Variation of V_u/V_y with l_s/d_o (b_s/h_w = 0.04) for inclined flat stiffeners.

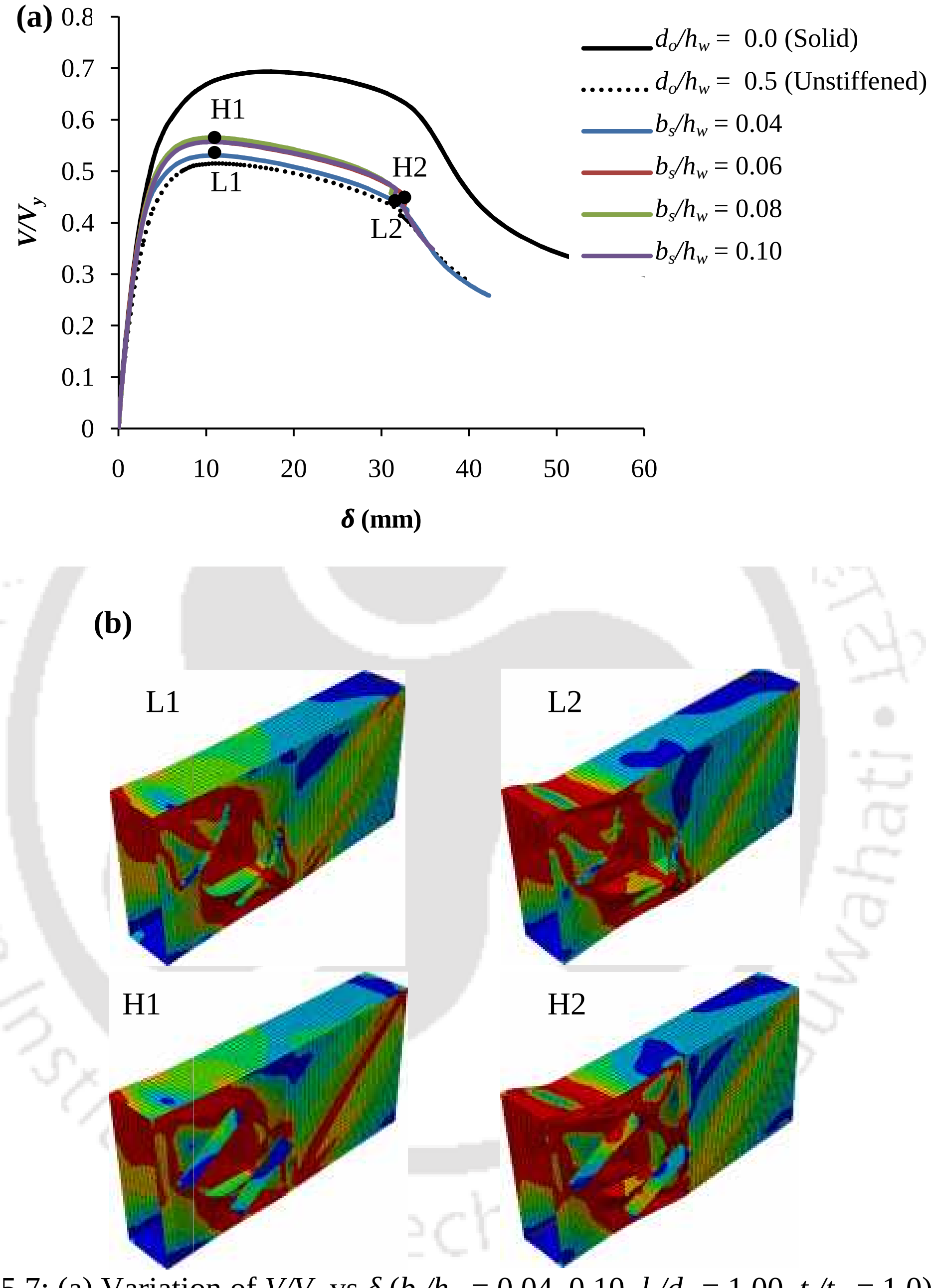

Figure 5.7: (a) Variation of V/V_y vs δ (b_s/h_w = 0.04–0.10, l_s/d_o = 1.00, t_s/t_w = 1.0) for inclined flat stiffener, (b) von-Mises stress contour for b_s/h_w = 0.04 (L1 & L2) & 0.10 (H1 & H2) with length of l_s/d_o = 1.0 (t_s/t_w = 1.0).

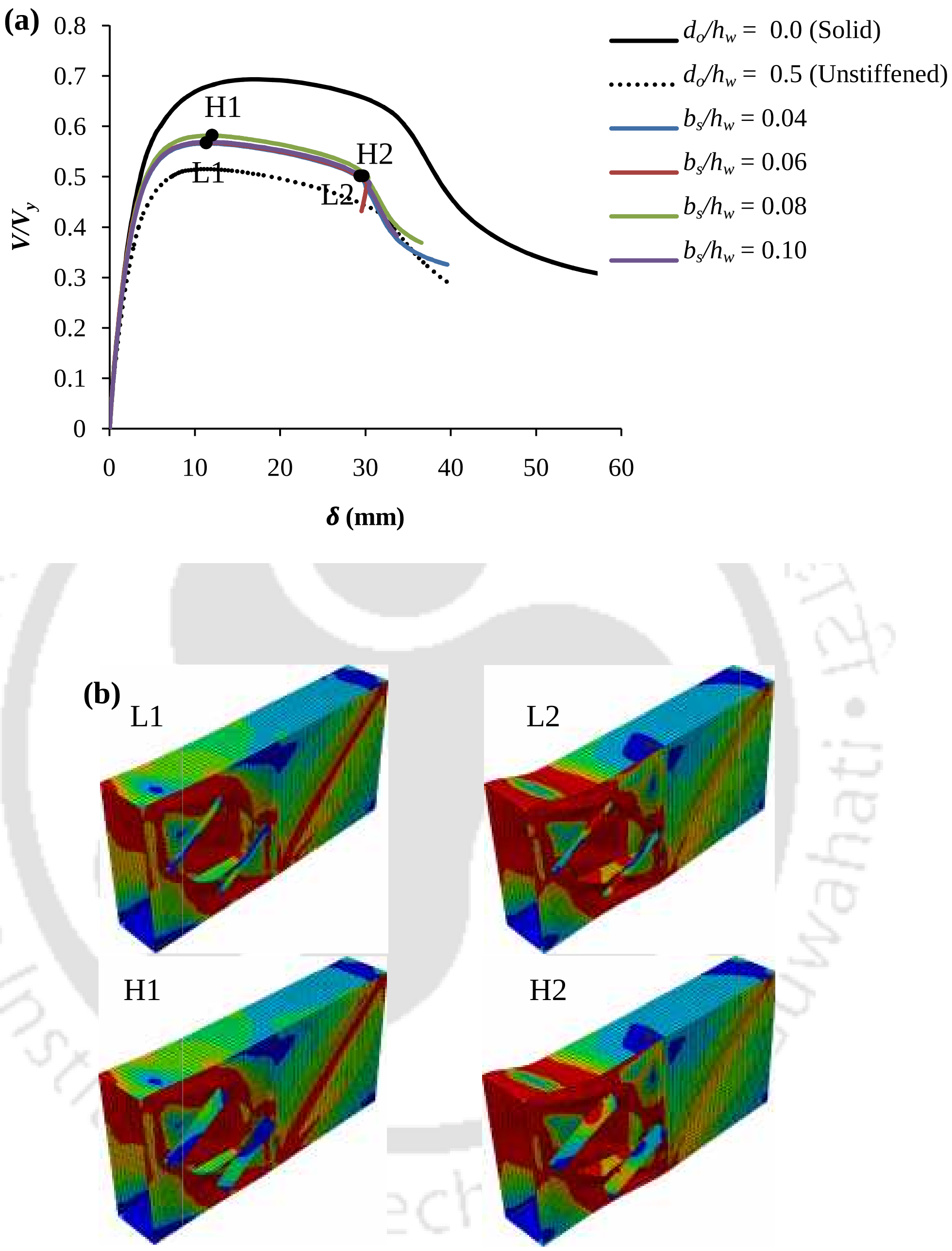

Figure 5.8: (a) Variation of V/V_y vs δ (b_s/h_w = 0.04–0.10, l_s/d_o = 1.00, t_s/t_w = 7.0) of inclined flat stiffener, (b) von-Mises stress contour for b_s/h_w = 0.04 (L1, L2 & L3) & 0.10 (H1, H2 & H3) with length of l_s/d_o = 1.0 (t_s/t_w = 7.0).

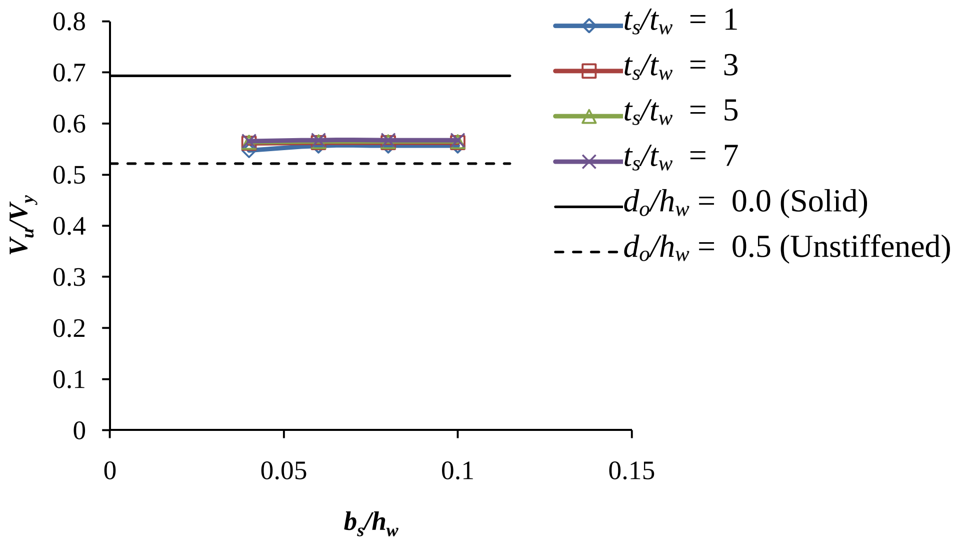

Figure 5.9: Variation of V_u/V_y with b_s/h_w (l_s/d_o = 1.0) for inclined flat stiffeners.

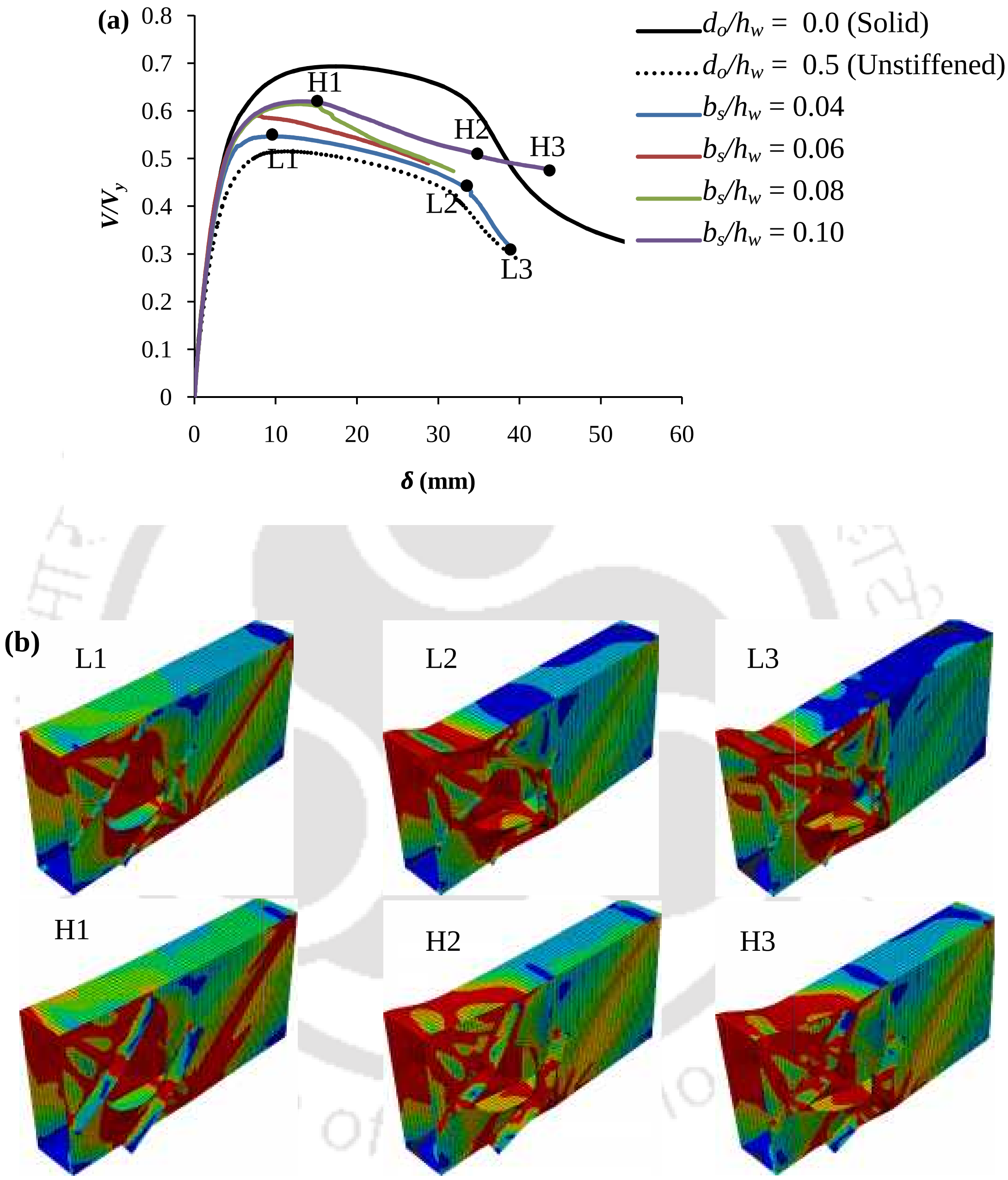

Figure 5.10: (a) Variation of V/V_y vs δ (b_s/h_w = 0.04–0.10, l_s/d_o = 1.75, t_s/t_w = 1) for inclined stiffeners, (b) von-Mises stress contour for b_s/h_w = 0.04 (L1, L2 & L3) & 0.10 (H1, H2 & H3) of inclined flat stiffener with length of l_s/d_o = 1.75 (t_s/t_w = 1.0).

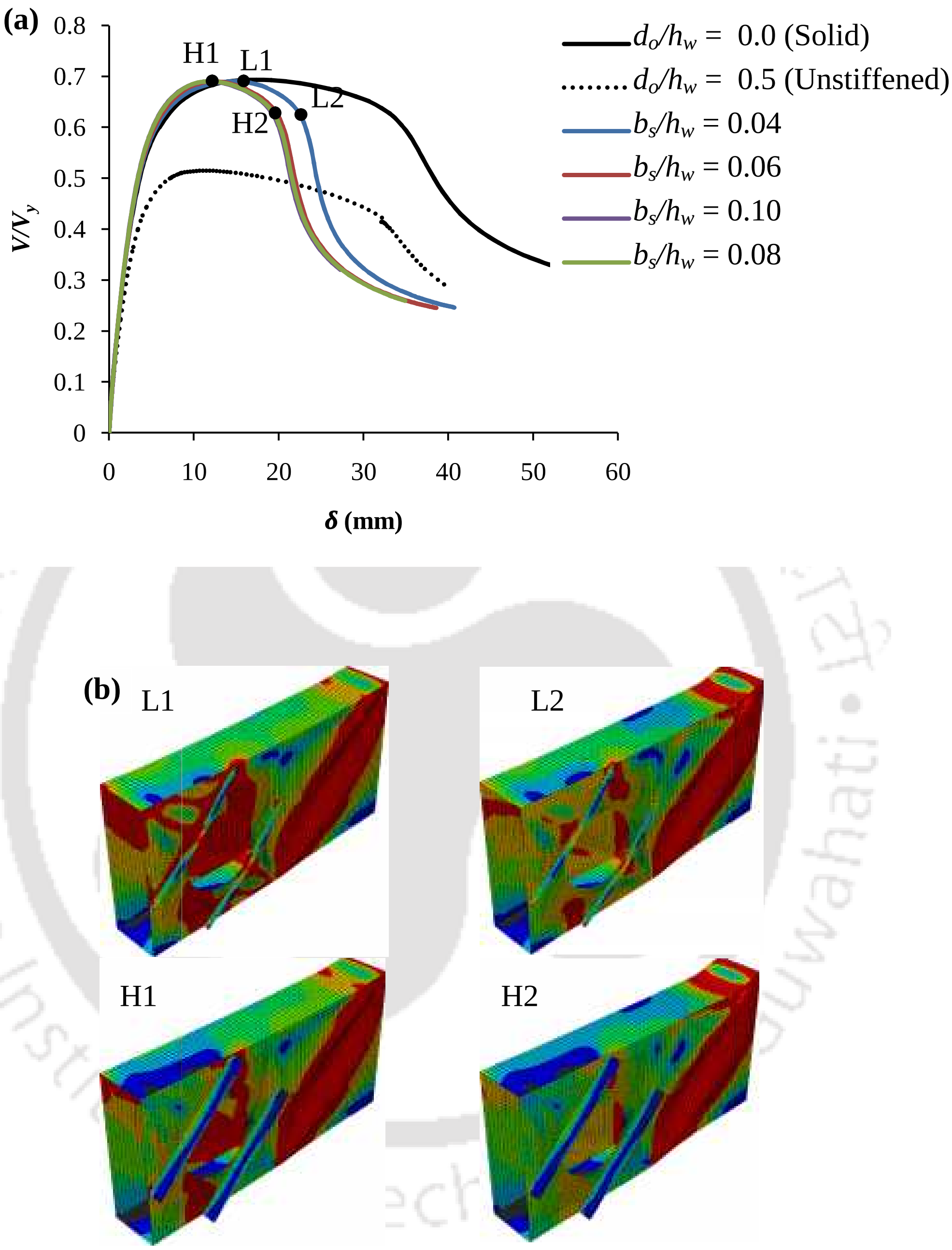

Figure 5.11: (a) Variation of V/V_y vs δ (b_s/h_w = 0.04–0.10, l_s/d_o = 1.75, t_s/t_w = 7) for inclined stiffeners, (b) von-Mises stress contour for b_s/h_w = 0.04 (L1 & L2) & 0.10 (H1 & H2) of inclined flat stiffener with length of l_s/d_o = 1.75 (t_s/t_w = 7.0).

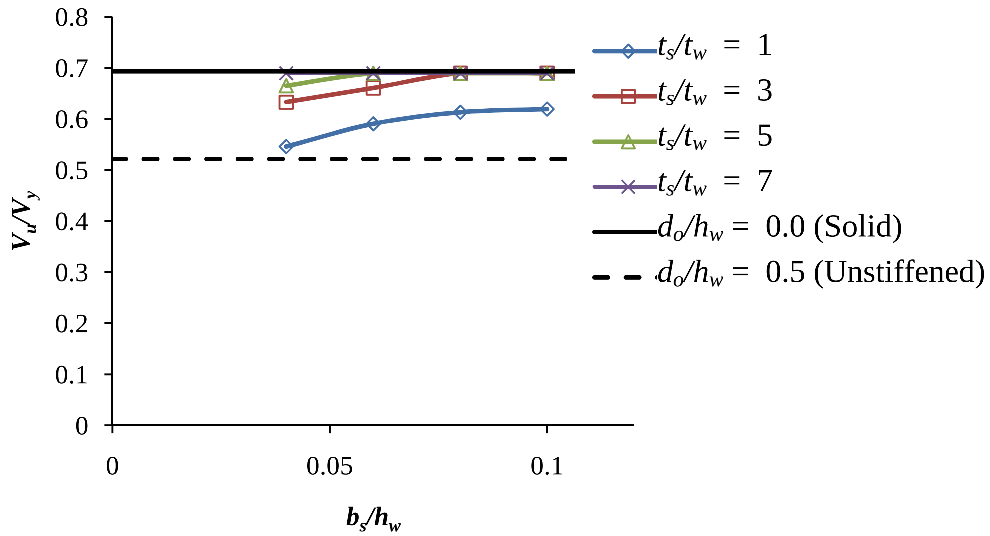

Figure 5.12: Variation of V_u/V_y with b_s/h_w (l_s/d_o = 1.75) for inclined flat stiffeners.

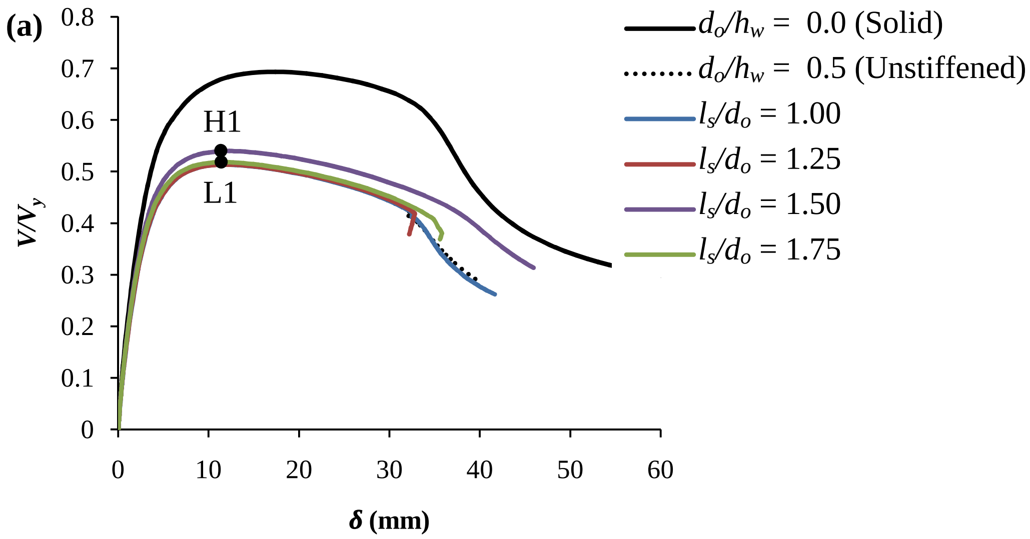

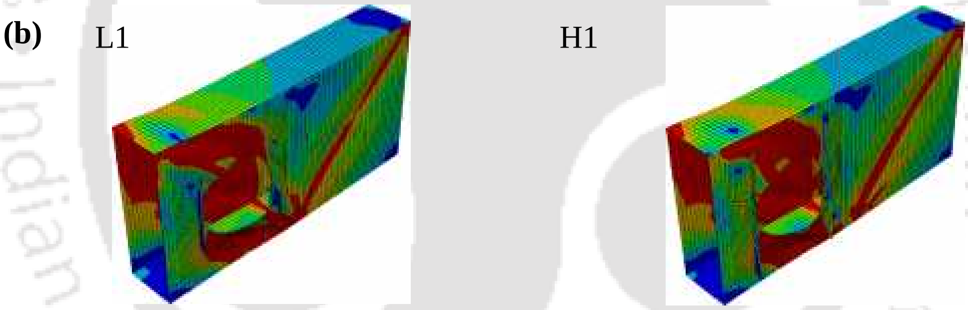

Figure 5.13: (a) Variation of V/V_y vs δ (l_s/d_o = 1.00–1.75, b_w/h_w = 0.04, t_s/t_w = 1) for vertical flat stiffeners, (b) von-Mises stress contour for l_s/d_o = 1.00 (L1) & 1.75 (H1) of vertical flat stiffener with width of b_w/h_w = 0.04 (t_s/t_w = 1.0).

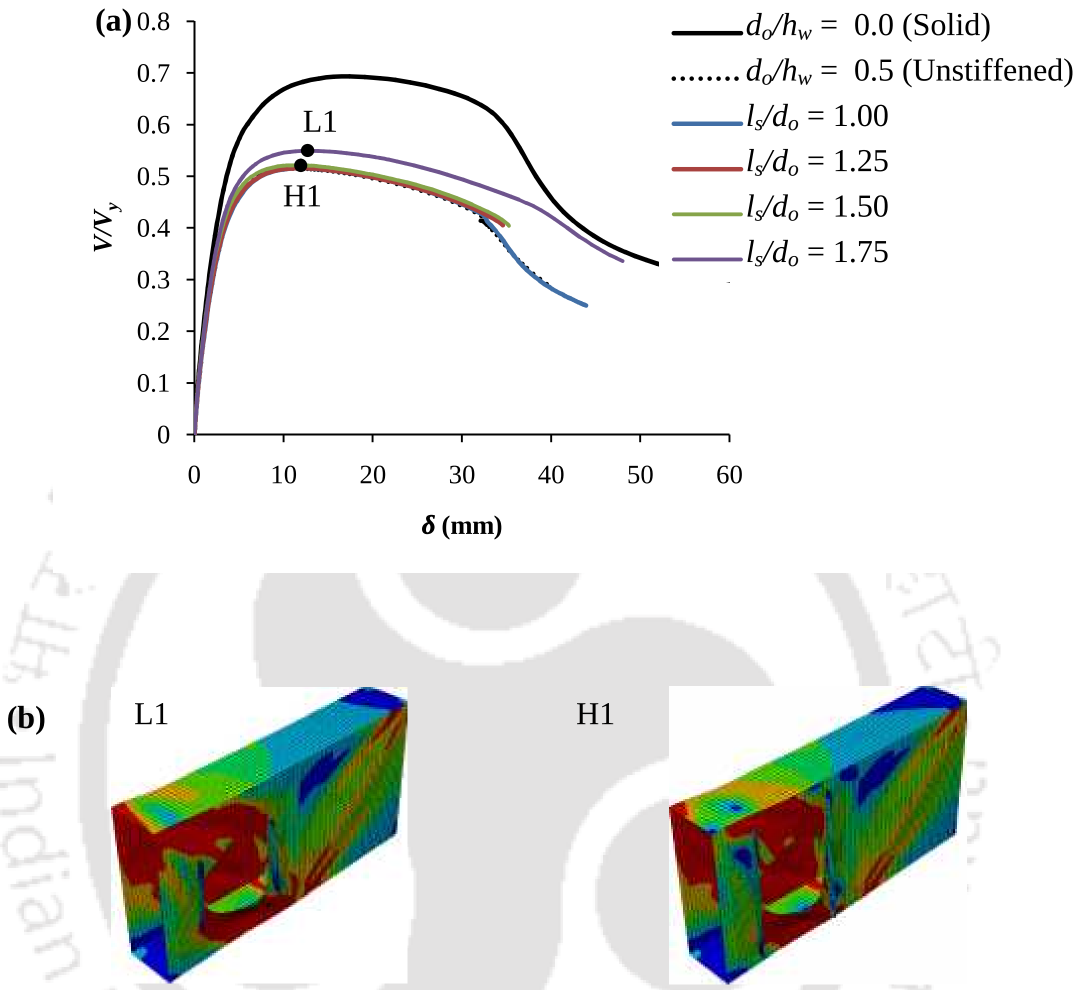

Figure 5.14: (a) Variation of V/V_y vs δ ($l_s/\ d_o$ = 1.0–1.75, b_s/h_w = 0.04, t_s/t_w = 7) for vertical flat stiffeners, (b) von-Mises stress contour for l_s/d_o = 1.00 (L1) & 1.75 (H1) of vertical flat stiffener with width of b_w/h_w = 0.04 (t_s/t_w = 1.0).

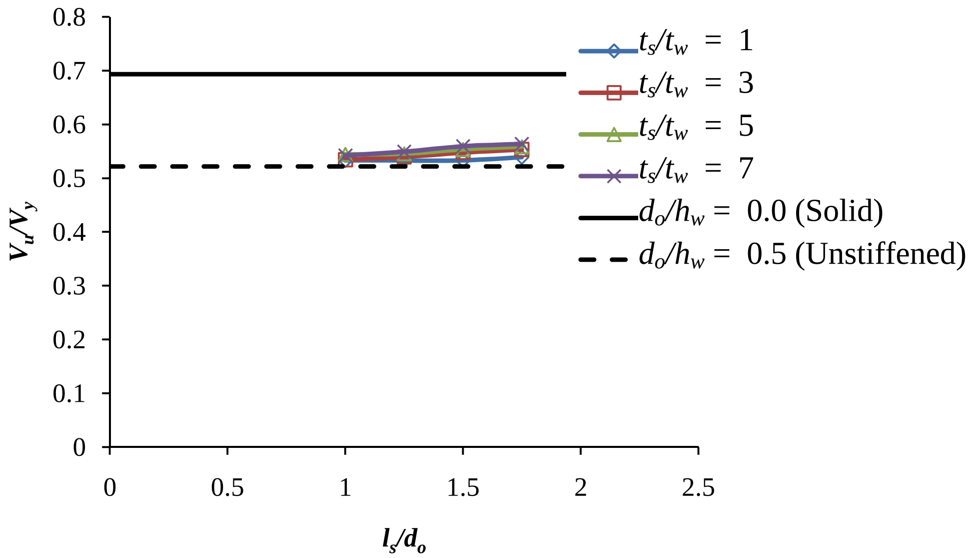

Figure 5.15: Variation of V_u/V_y with l_s/d_o (b_w/h_w = 0.04) for vertical flat stiffeners.

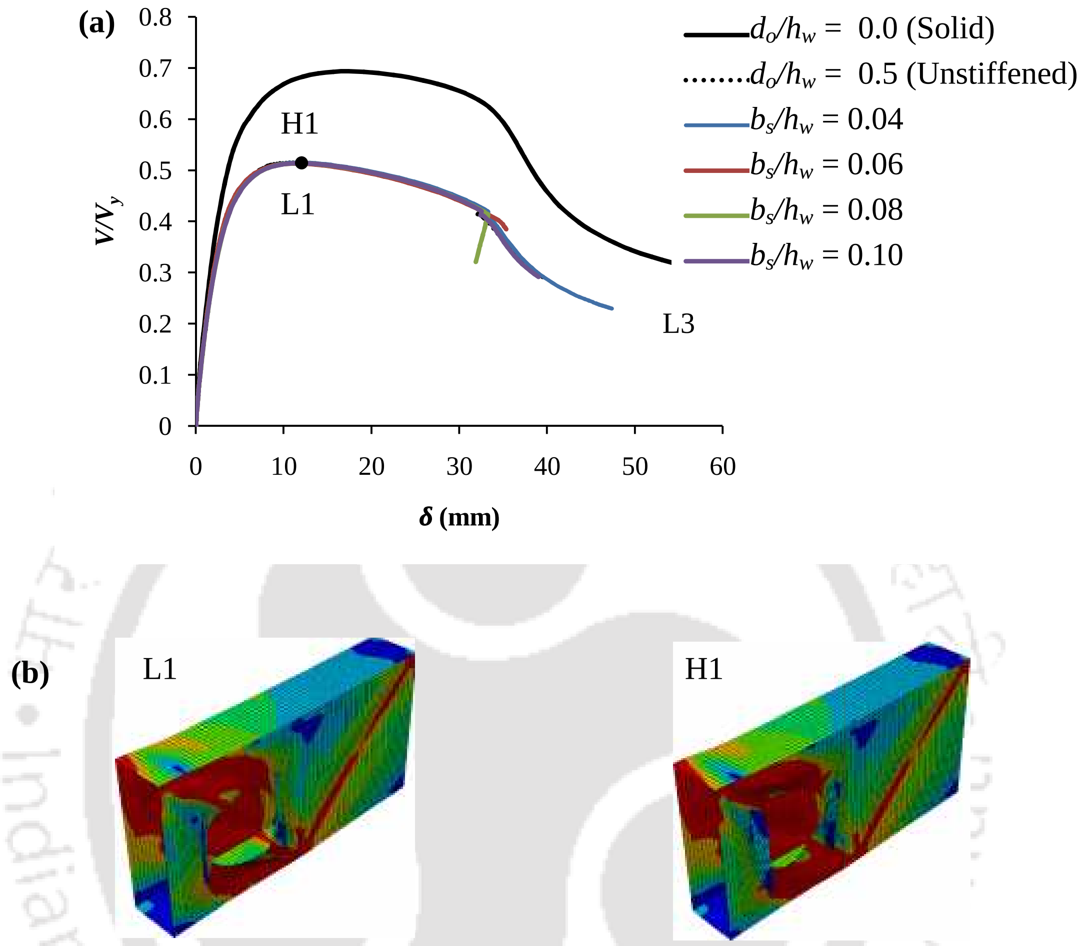

Figure 5.16: (a) Variation of V/V_y vs δ (b_s/ d_o = 0.04–0.10, l_s/d_o = 1.00, t_s/t_w = 1) for vertical flat stiffeners, (b) von-Mises stress contour for b_s/h_w = 0.04 (L1) & 0.10 (H1) of vertical flat stiffener with length of l_s/d_o = 1.0 (t_s/t_w = 1.0).

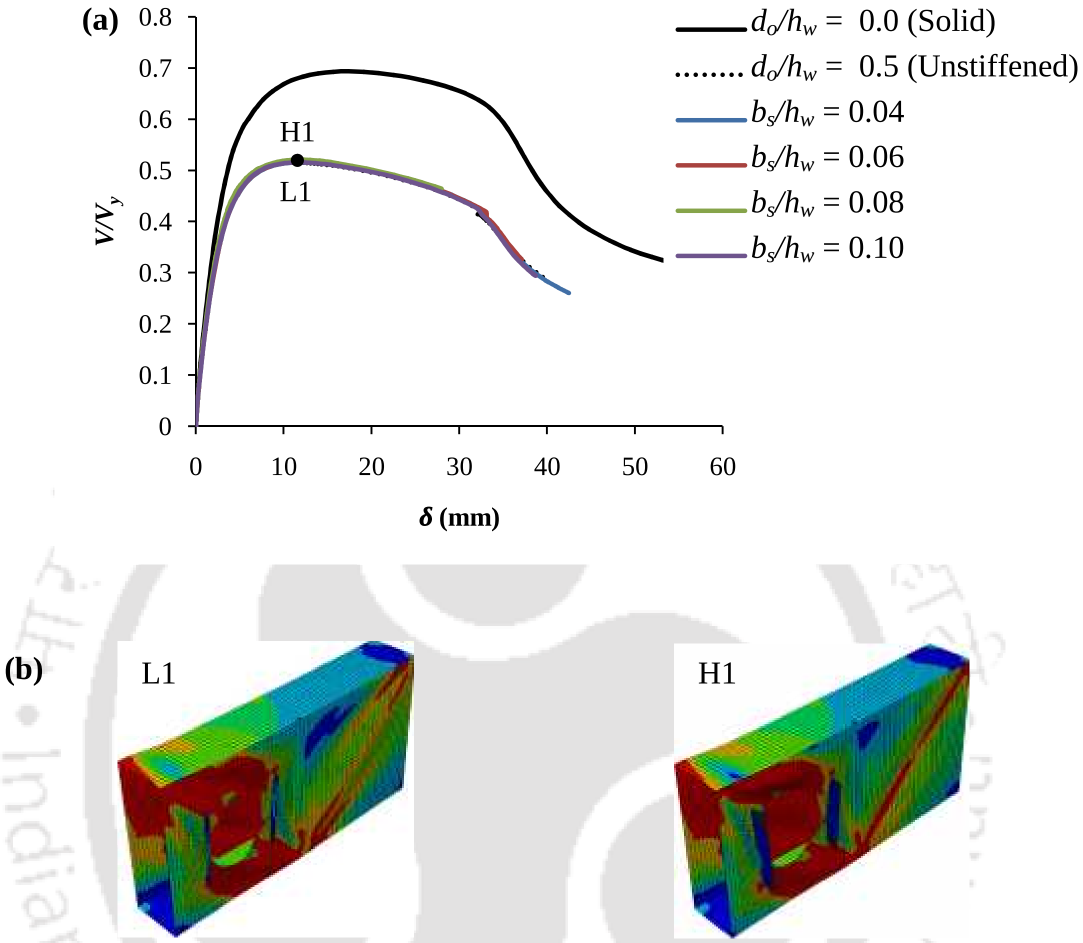

Figure 5.17: (a) Variation of V/V_y vs δ (b_s/ d_o = 0.04–0.10, l_s/d_o = 1.00, t_s/t_w = 7) for vertical flat stiffeners, (b) von-Mises stress contour for b_s/h_w = 0.04 (L1) & 0.10 (H1) of vertical flat stiffener with length of l_s/d_o = 1.0 (t_s/t_w = 7.0).

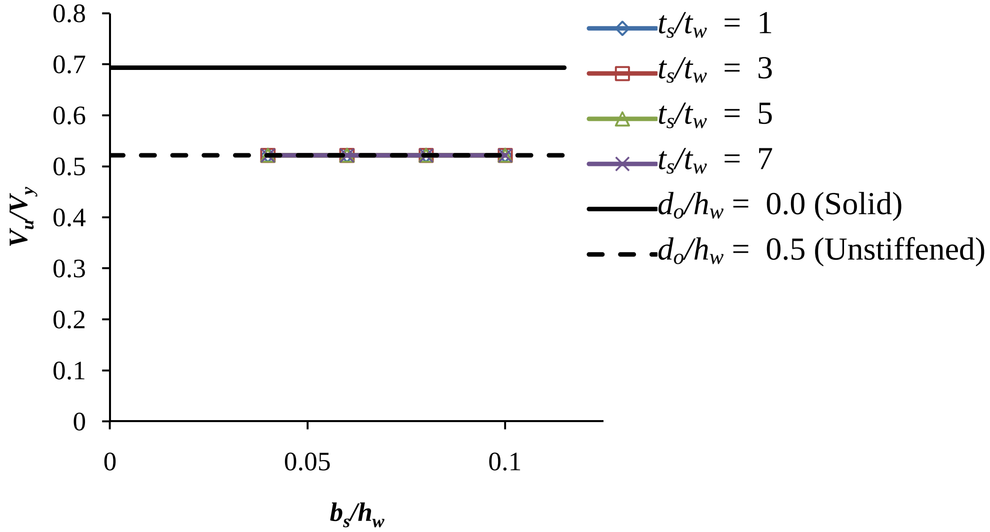

Figure 5.18: Variation of V_u/V_y with b_s/h_w (l_s/d_o = 1.00) for vertical flat stiffeners.

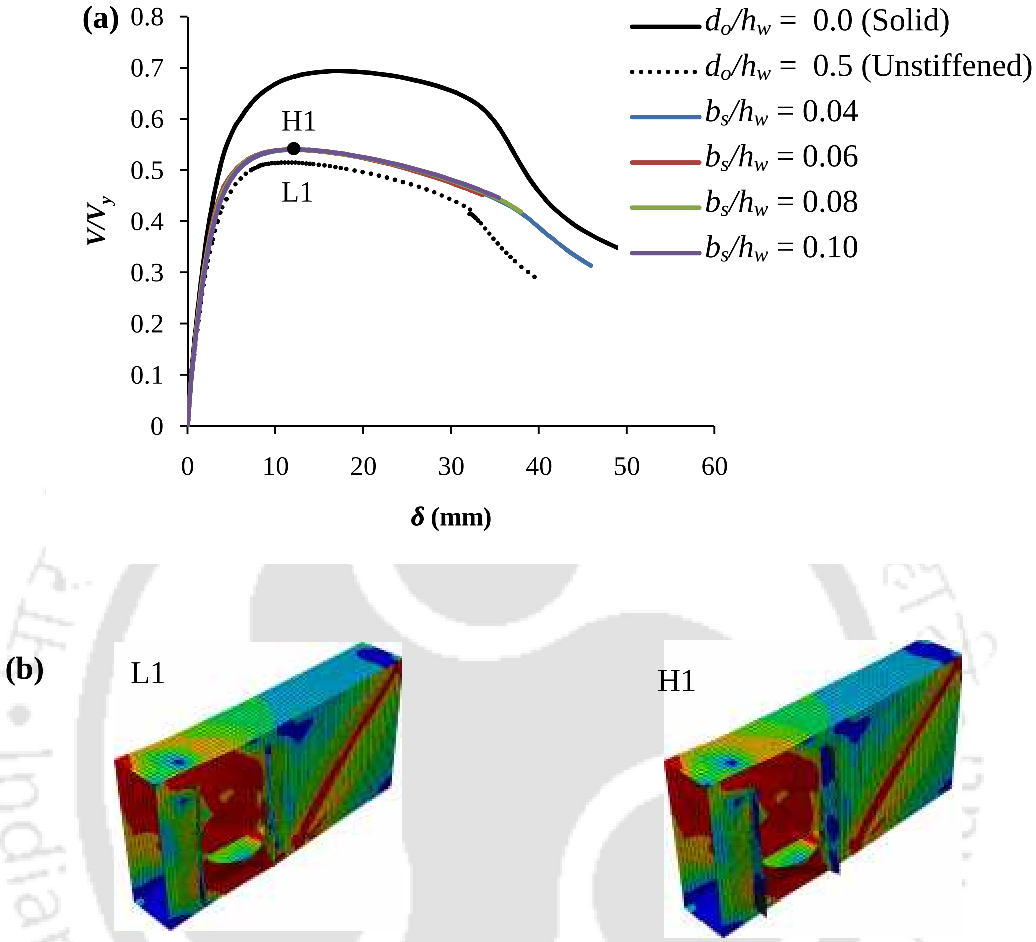

Figure 5.19: (a) Variation of V/V_y vs δ (b_s/h_w = 0.04–0.10, l_s/d_o = 1.75, t_s/t_w = 1) for vertical flat stiffeners, (b) von-Mises stress contour for b_s/h_w = 0.04 (L1) & 0.10 (H1) of vertical flat stiffener with length of l_s/d_o = 1.75 (t_s/t_w = 1.0).

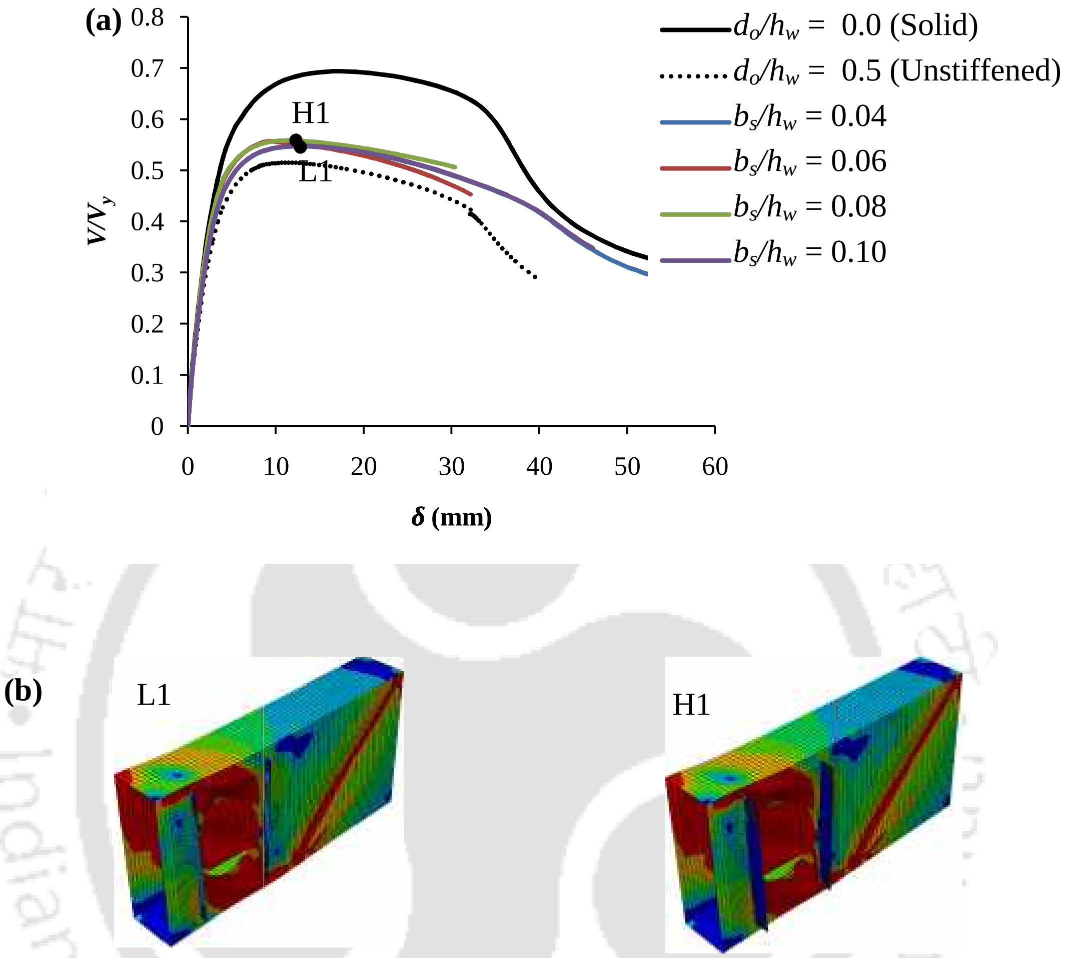

Figure 5.20: (a) Variation of V/V_y vs δ (b_s/h_w = 0.04–0.10, l_s/d_o = 1.75, t_s/t_w = 7) for vertical flat stiffener, (b) von-Mises stress contour for b_s/h_w = 0.04 (L1) & 0.10 (H1) of vertical flat stiffener with length of l_s/d_o = 1.75 (t_s/t_w = 7).

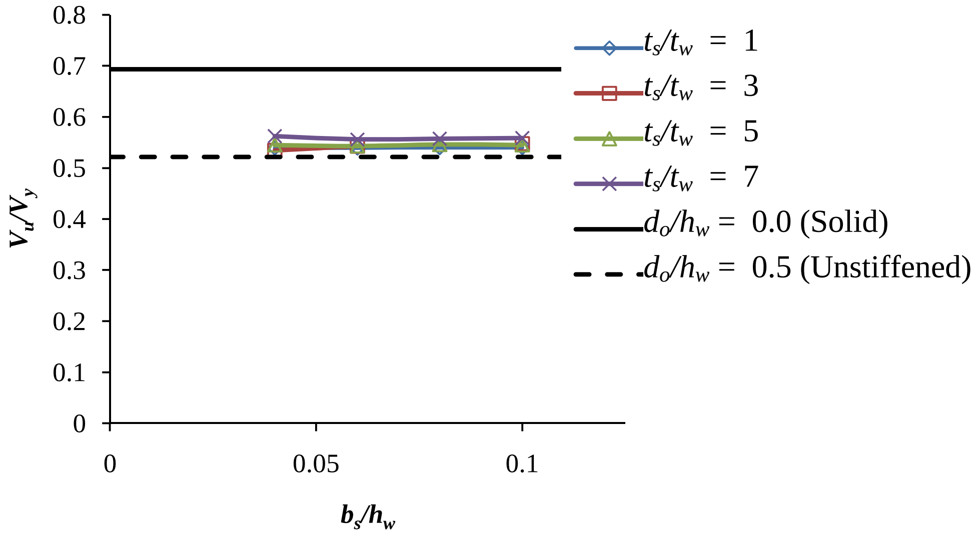

Figure 5.21: Variation of V_u/V_y with b_s/h_w (l_s/d_o = 1.75) for vertical flat stiffeners.

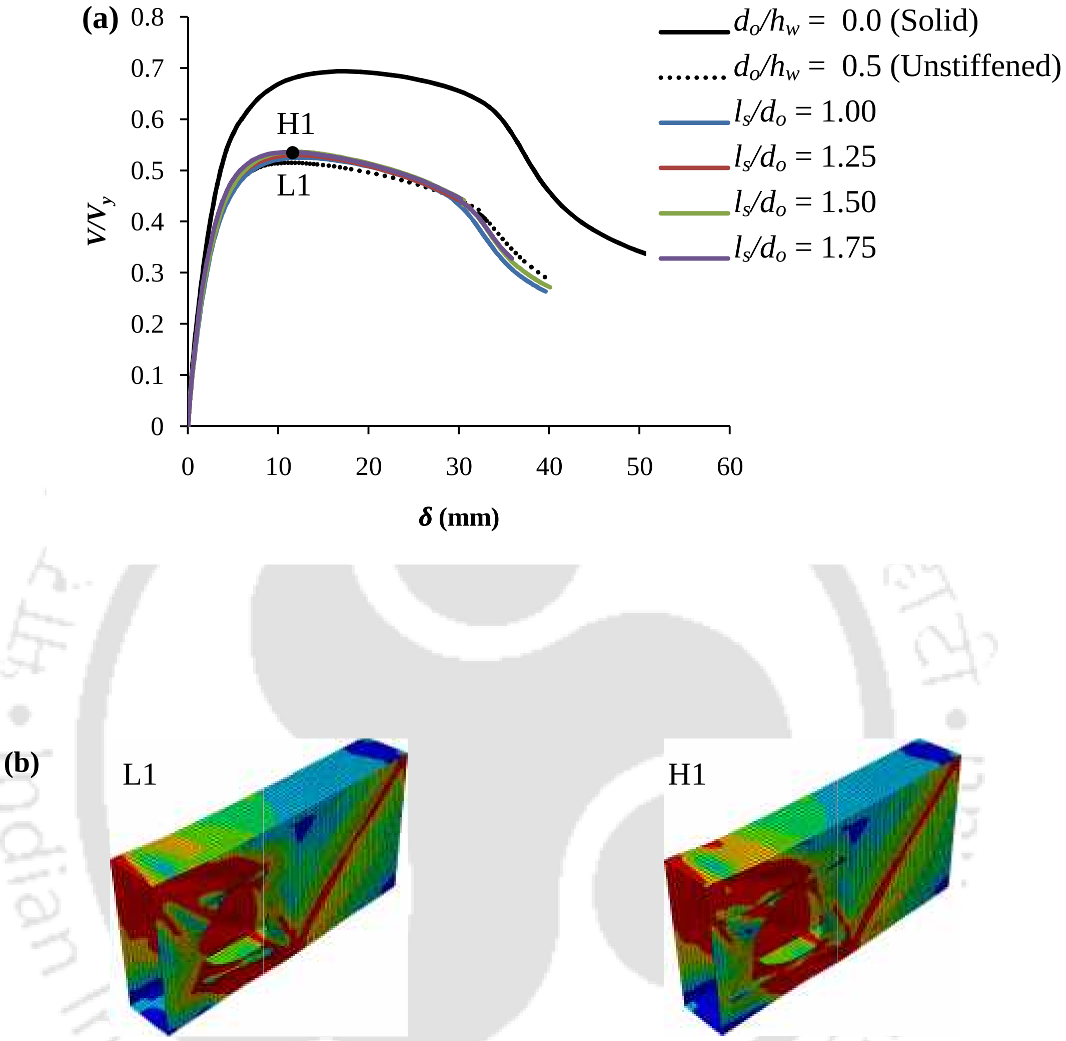

Figure 5.22: (a) Variation of V/V_y vs δ (l_s/d_o = 1.00–1.75, b_s/h_w = 0.04, t_s/t_w = 1) for horizontal flat stiffeners, (b) von-Mises stress contour for l_s/d_o = 1.00 (L1) & 1.75 (H1) of horizontal flat stiffener with width of b_s/h_w = 0.04 (t_s/t_w = 1.0).

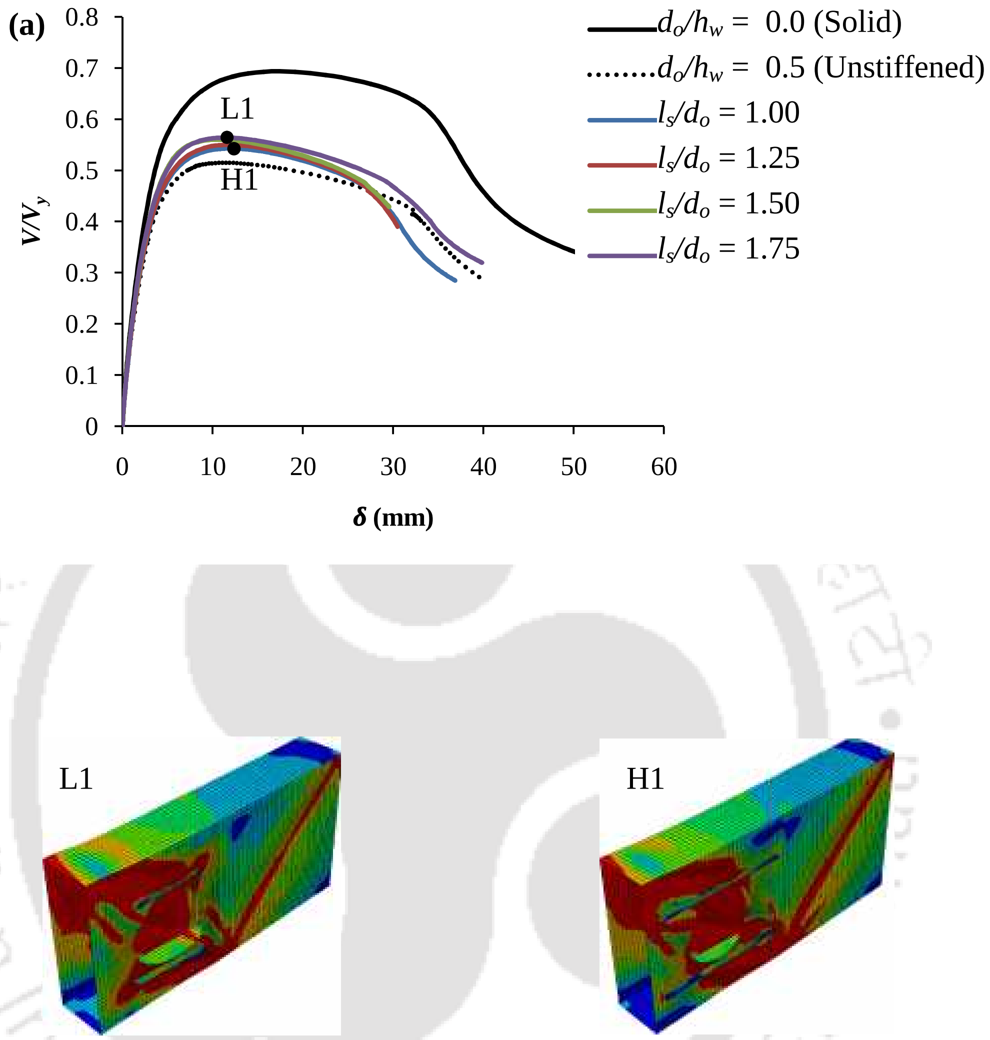

Figure 5.23: (a) Variation of V/V_y vs δ (l_s/d_o = 1.00–1.75, b_w/h_w = 0.04, t_s/t_w = 7) for horizontal flat stiffeners, (b) von-Mises stress contour for l_s/d_o = 1.00 (L1) & 1.75 (H1) of horizontal flat stiffener with width of b_s/h_w = 0.04 (t_s/t_w = 7.0).

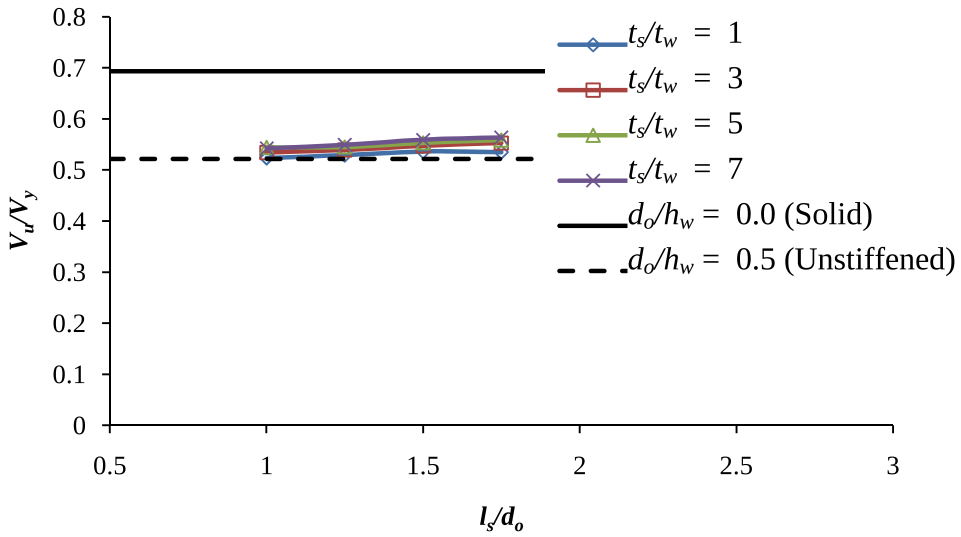

Figure 5.24: Variation of V_u/V_y with l_s/d_o (b_s/h_w = 0.04) for horizontal flat stiffeners.

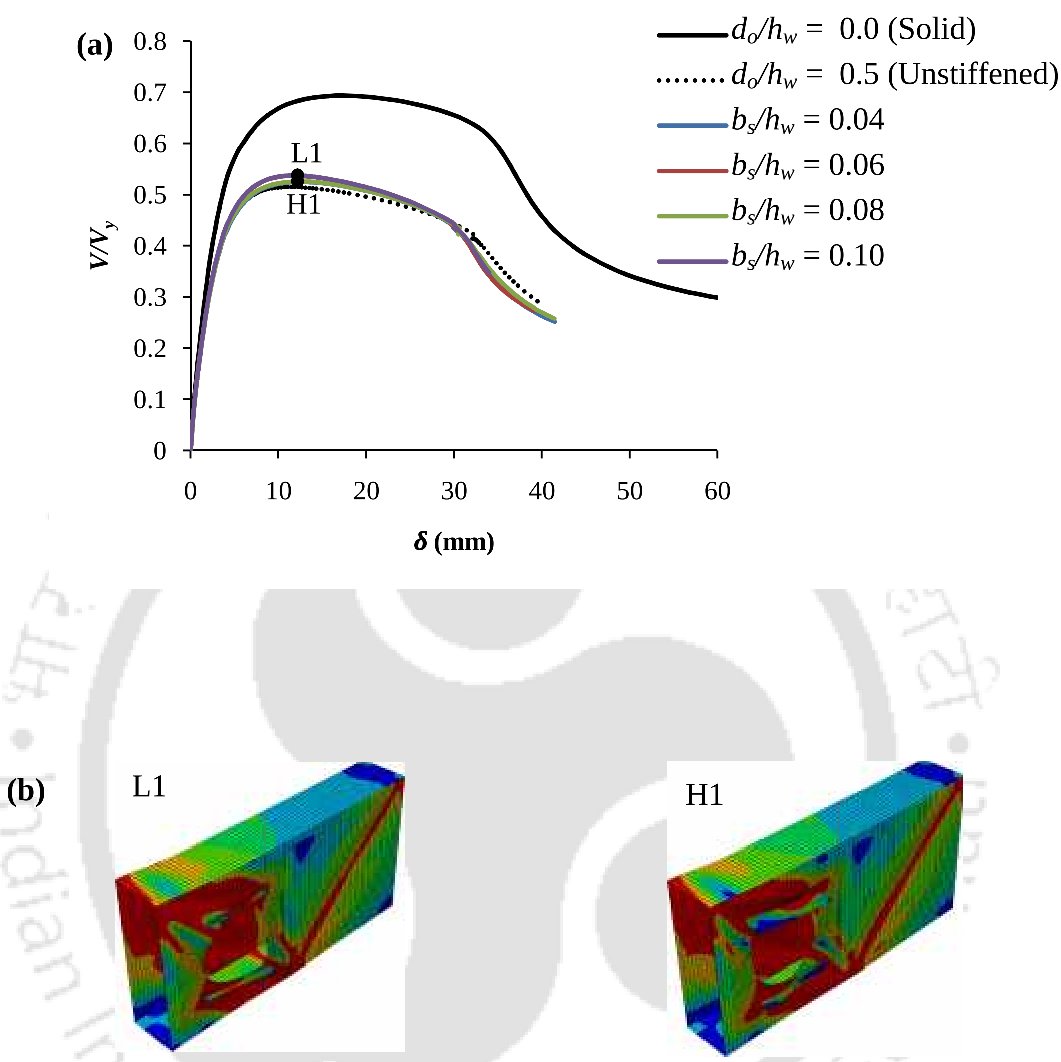

Figure 5.25: (a) Variation of V/V_y vs δ (b_s/h_w = 0.04–0.10, l_s/d_o = 1.00, t_s/t_w = 1) for horizontal flat stiffeners, (b) von-Mises stress contour for b_s/h_w = 0.04 (L1) & 0.10(H1) of horizontal flat stiffener with length of l_s/d_o = 1.0 (t_s/t_w = 1.0).

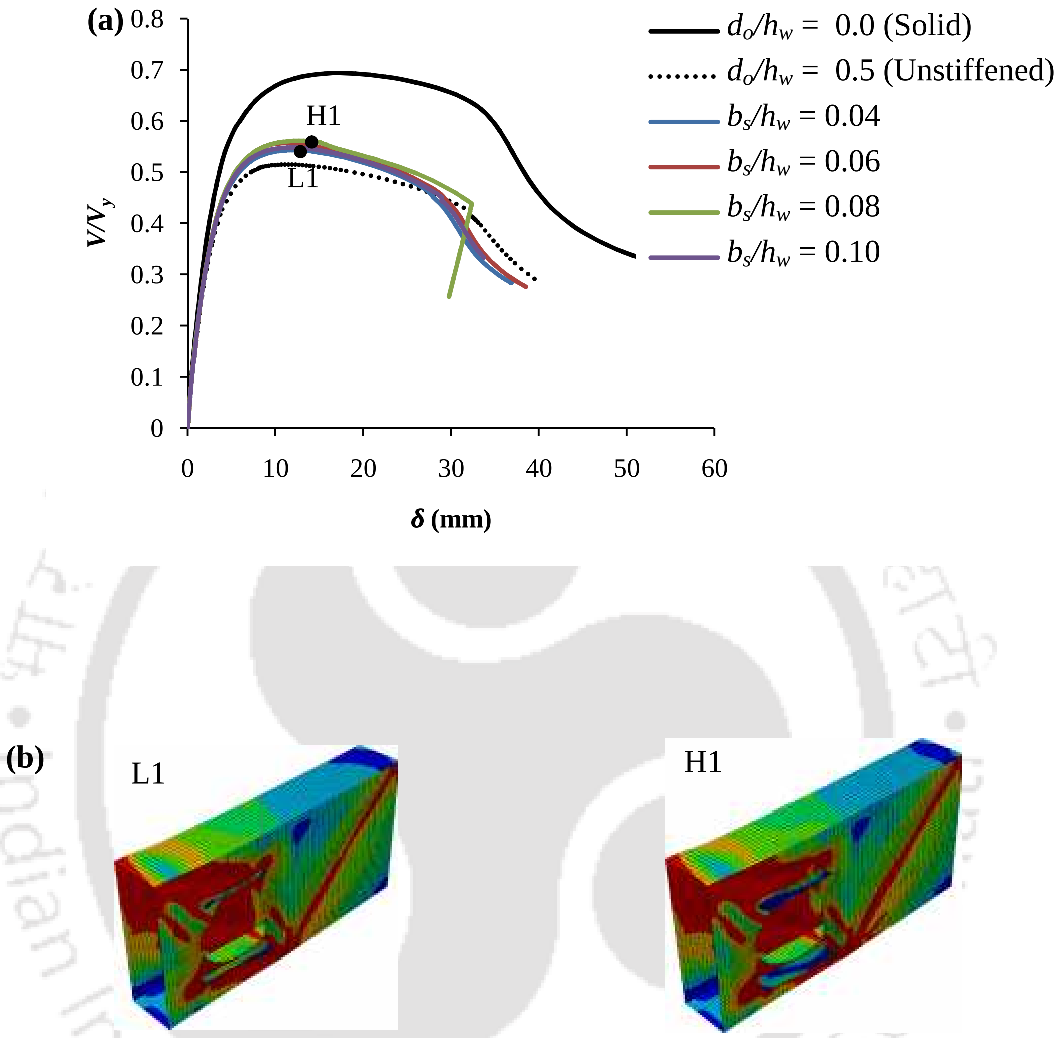

Figure 5.26: (a) Variation of V/V_y vs δ (b_s/h_w = 0.04–0.10, l_s/d_o = 1.00, t_s/t_w = 7) for horizontal flat stiffeners, (b) von-Mises stress contour for b_s/h_w = 0.04 (L1) & 0.10 (H1) of horizontal flat stiffener with length of l_s/d_o = 1.0 (t_s/t_w = 7.0).

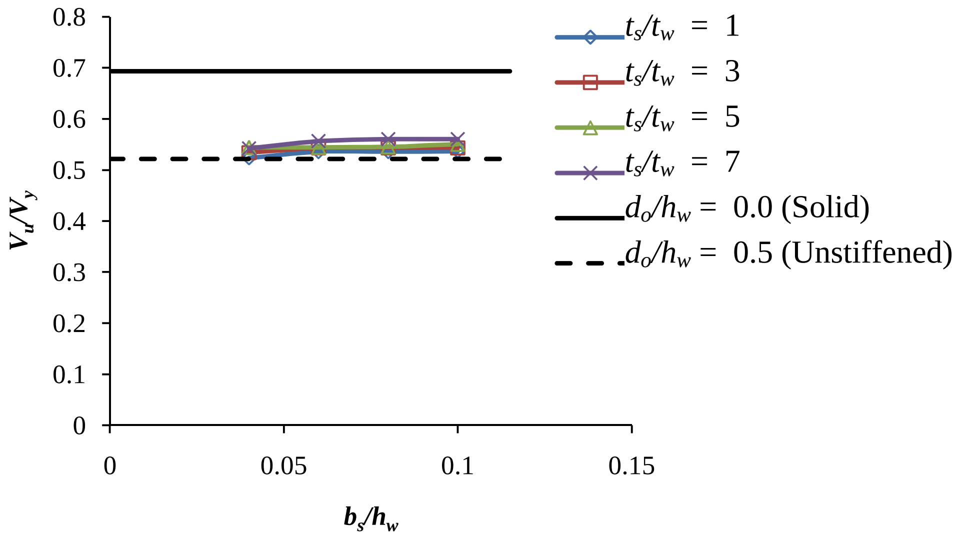

Figure 5.27: Variation of V_u/V_y with b_s/h_w (l_s/d_o = 1.00) for horizontal flat stiffeners.

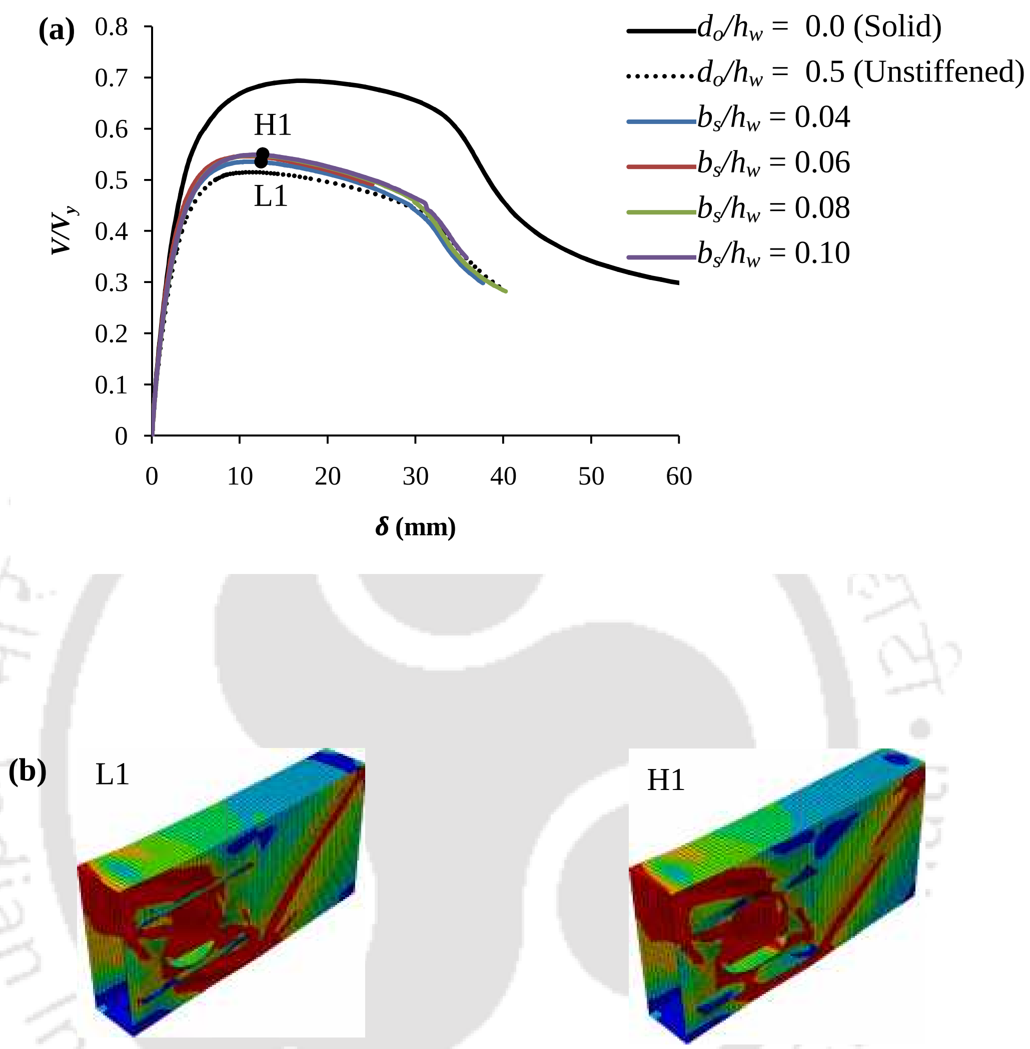

Figure 5.28: (a) Variation of V/V_y vs δ (b_s/h_w = 0.04–0.10, l_s/d_o = 1.75, t_s/t_w = 1) for horizontal flat stiffeners, (b) von-Mises stress contour for b_s/h_w = 0.04 (L1) & 0.10(H1) of horizontal flat stiffener with length of l_s/do = 1.75 (t_s/t_w = 1.0).

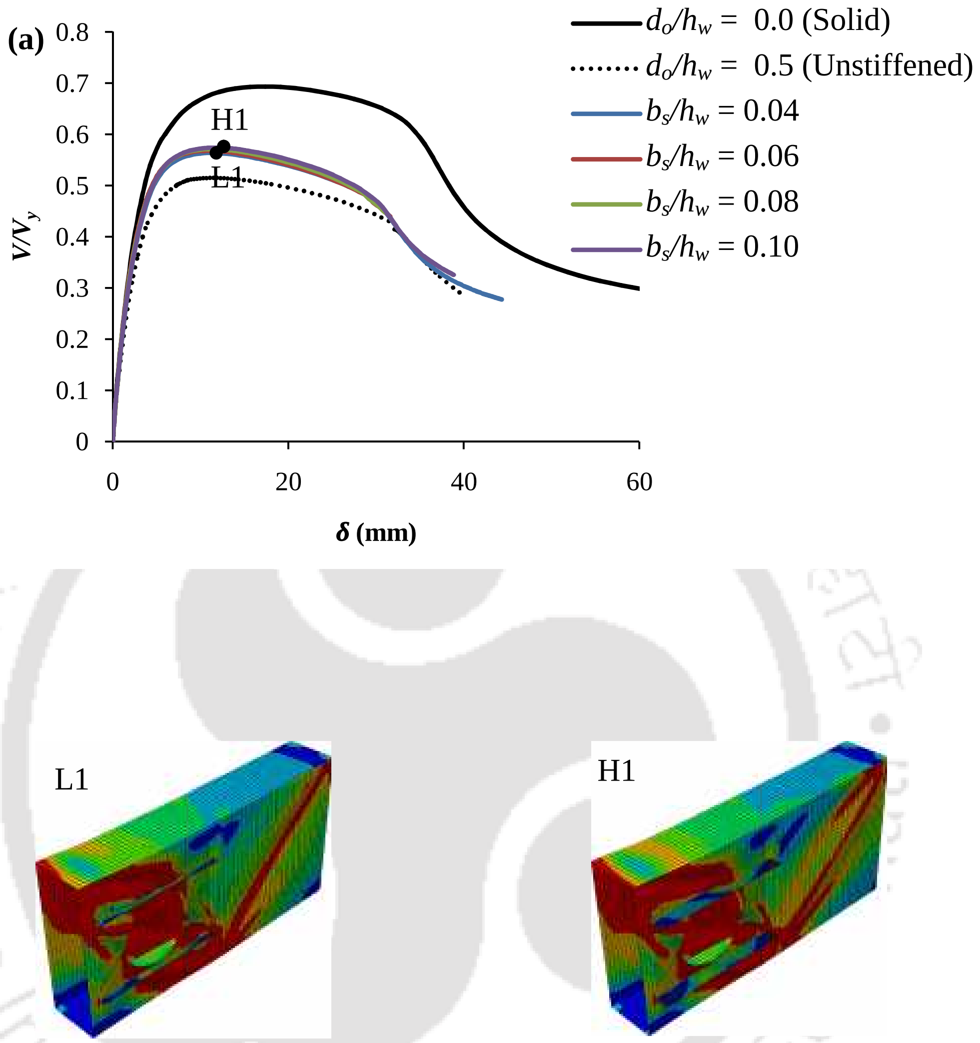

Figure 5.29: (a) Variation of V/V_y vs δ (b_s/h_w = 0.04–0.10, l_s/d_o = 1.75, t_s/t_w = 7) for horizontal flat stiffeners, (b) von-Mises stress contour for b_s/h_w = 0.04 (L1) & 0.10 (H1) of horizontal flat stiffener with length of l_s/do = 1.75 (t_s/t_w = 7.0).

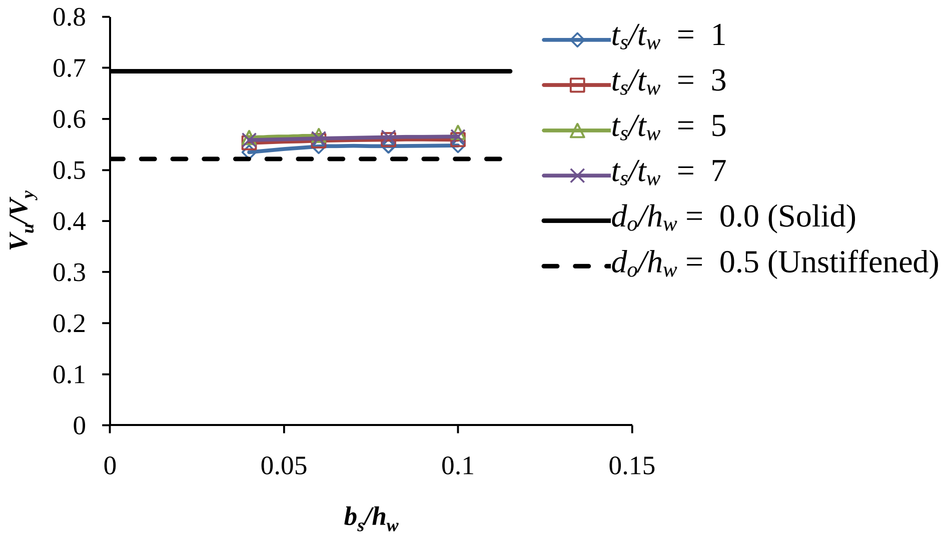

Figure 5.30: Variation of V_u/V_y with b_s/h_w (l_s/d_o = 1.75) for horizontal flat stiffeners.

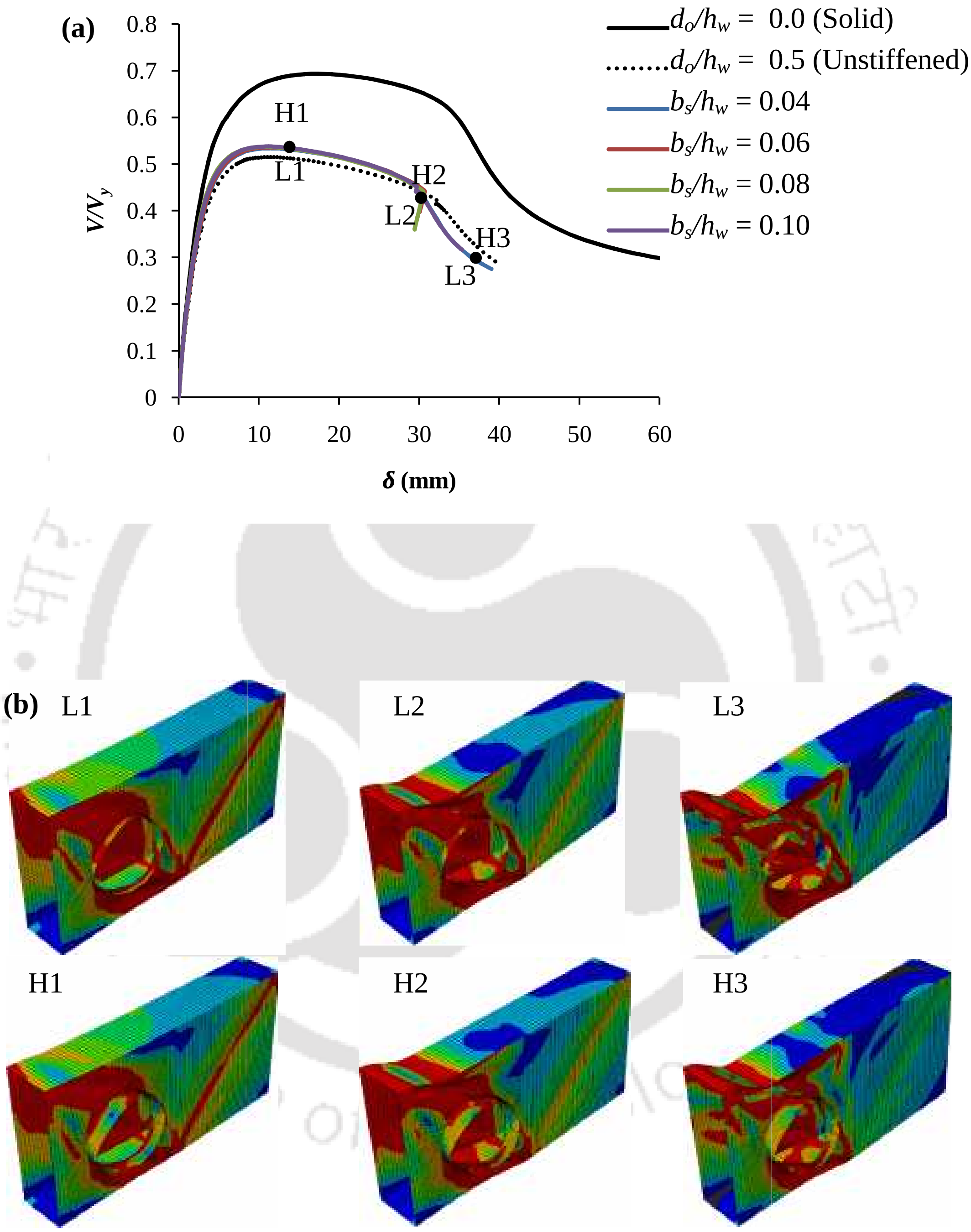

Figure 5.31: (a) Variation of V/V_y vs δ (b_s/h_w = 0.04–0.10, t_s/t_w = 1.0) for ring stiffener, (b) von-Mises stress contour for b_s/h_w = 0.04 (L1, L2 & L3) & 0.10 (H1, H2 & H3) of ring stiffener (t_s/t_w = 1.0).

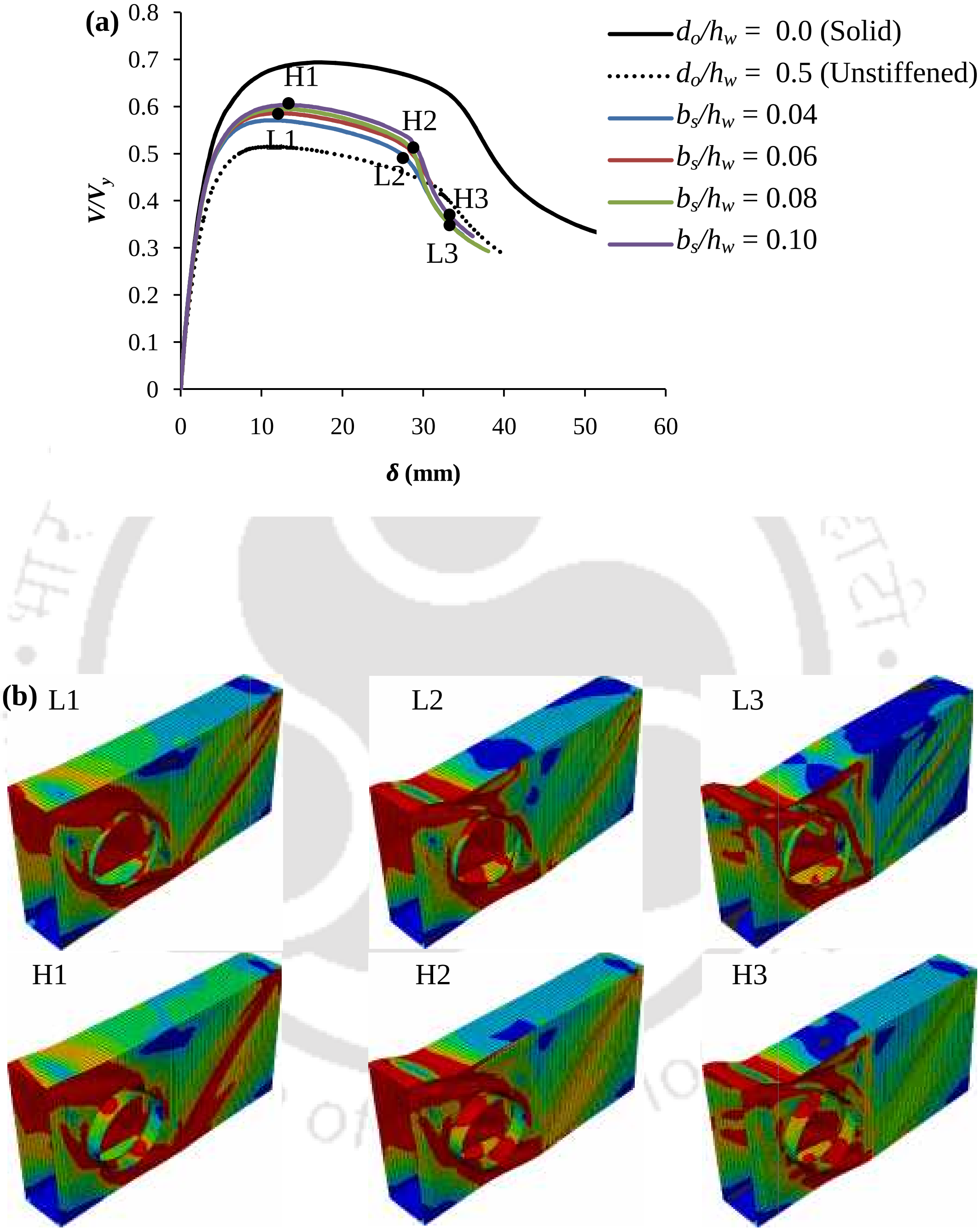

Figure 5.32: (a) Variation of V/V_y vs δ (b_s/h_w = 0.04–0.10, t_s/t_w = 7.0) for ring stiffener, (b) von-Mises stress contour for b_s/h_w = 0.04 (L1, L2 & L3) & 0.10 (H1, H2 & H3) of ring stiffener (t_s/t_w = 7.0).

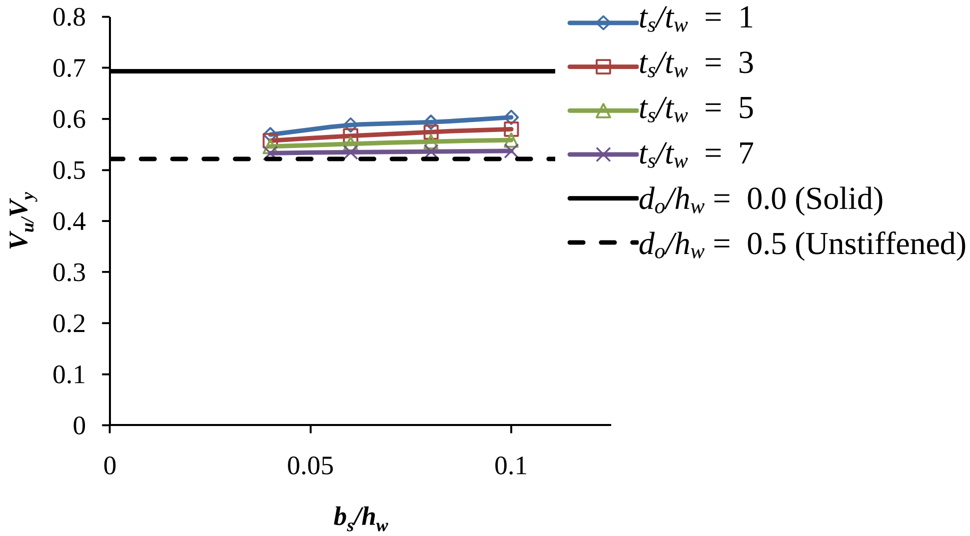

Figure 5.33: Variation of V_u/V_y with b_s/h_w of ring stiffeners.

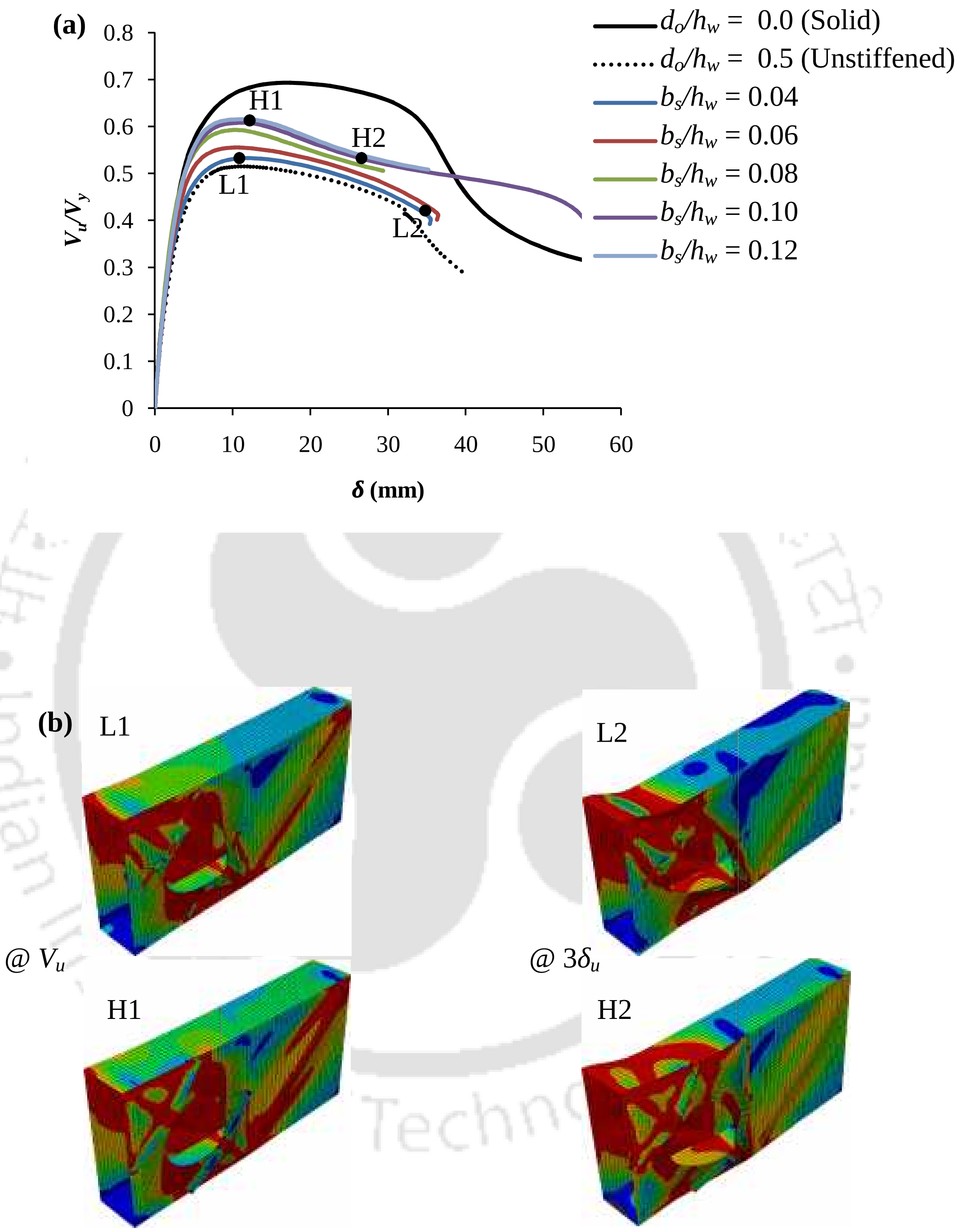

Figure 5.34: (a) Variation of V/V_y vs δ (b_s/h_w = 0.04–0.12, t_s/t_w = 1.0, l_s/d_o = 1.50) for angular stiffener, (b) von-Mises stress contour for b_s/h_w = 0.04 (L1 & L2) & 0.12 (H1 & H2).

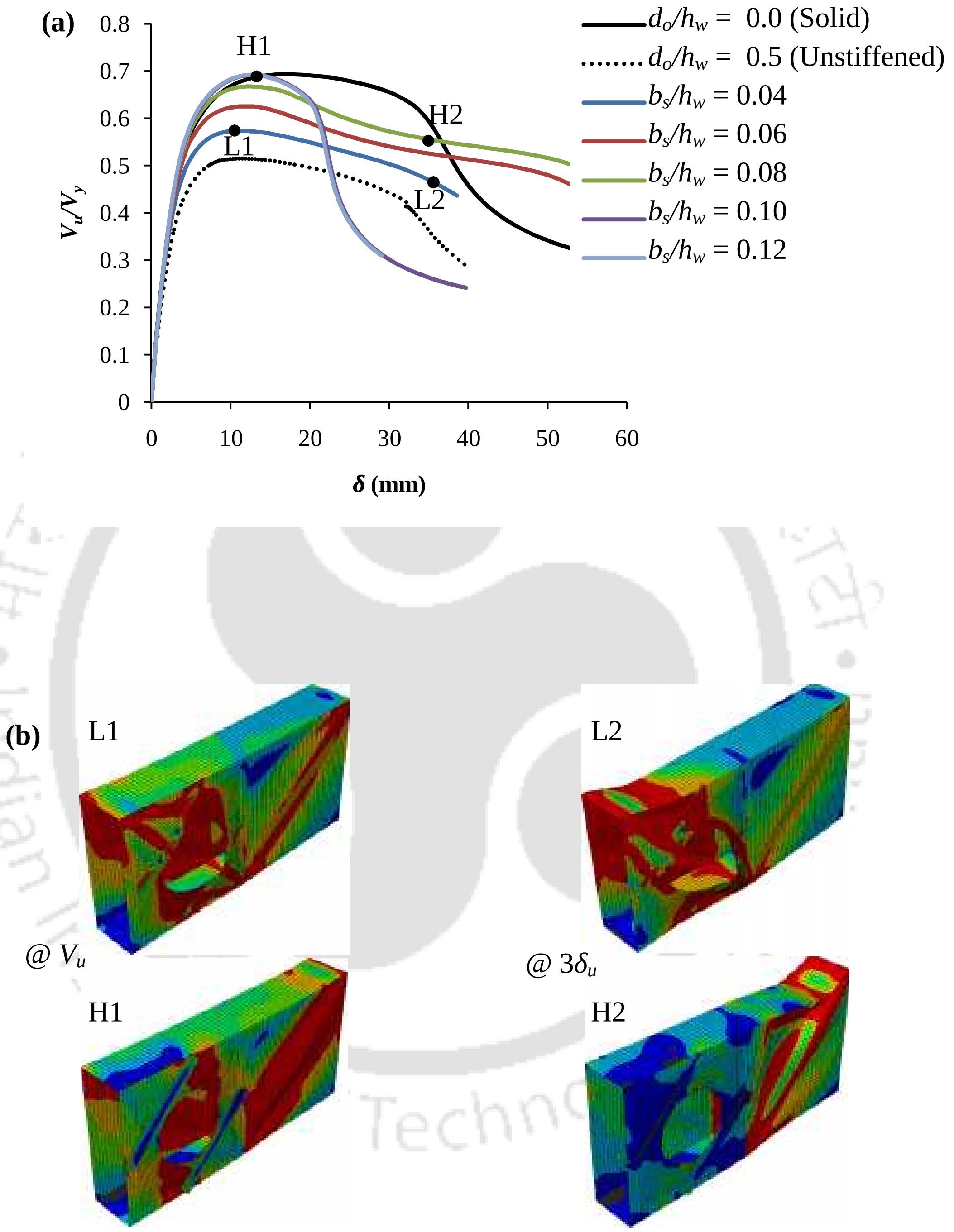

Figure 5.35: (a) Variation of V/V_y vs δ (b_s/h_w = 0.04–0.12, t_s/t_w = 5.0, l_s/d_o = 1.50) for angular stiffener, (b) von-Mises stress contour for b_s/h_w = 0.04 (L1 & L2) & 0.12 (H1 & H2).

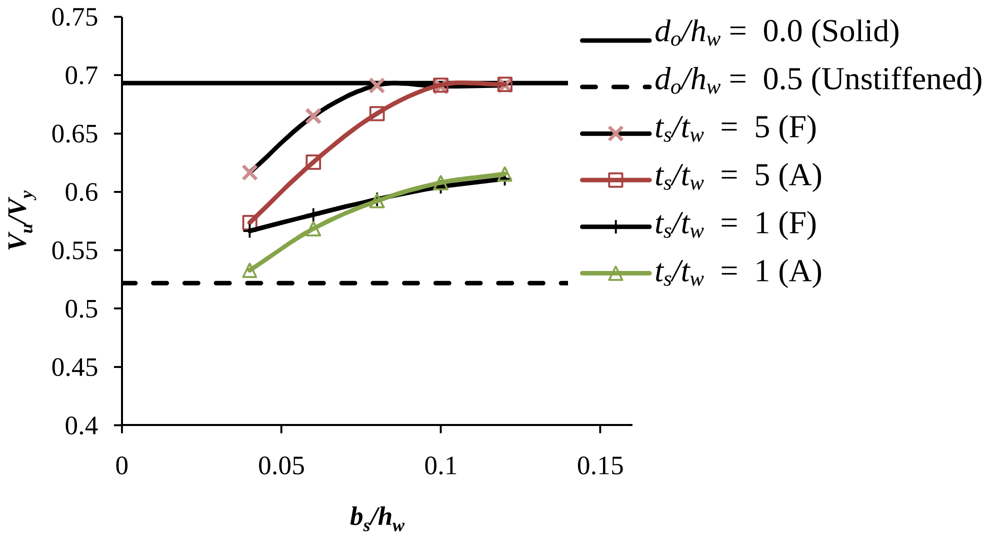

Figure 5.36: Variation of V_u/V_y vs b_s/h_w of angular stiffeners.

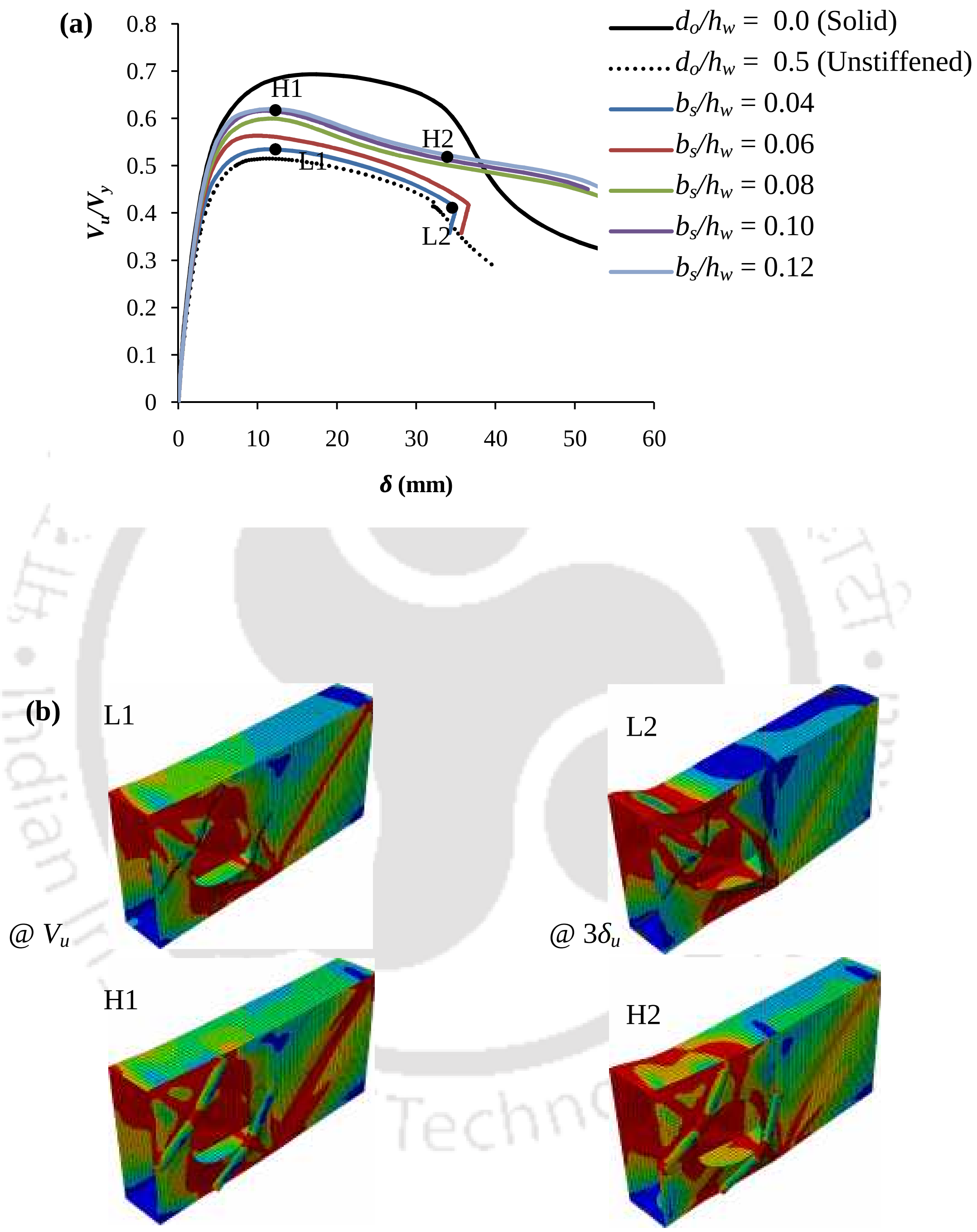

Figure 5.37: (a) Variation of V/V_y vs δ (b_s/h_w = 0.04–0.12, t_s/t_w = 1.0, l_s/d_o = 1.50) for semi-circular stiffener, (b) von-Mises stress contour for b_s/h_w = 0.04 (L1 & L2) & 0.12 (H1 & H2).

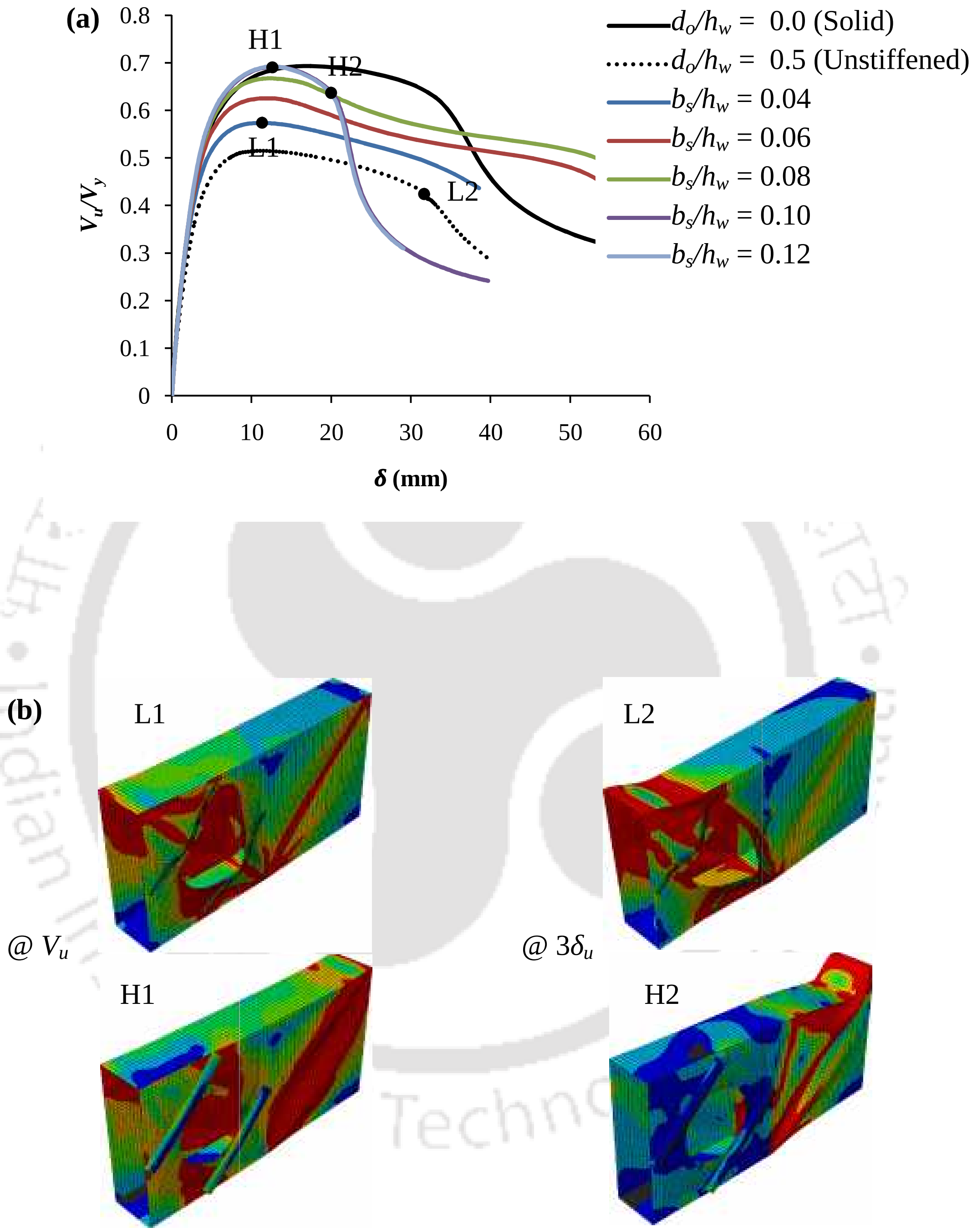

Figure 5.38: (a) Variation of V/V_y vs δ (b_s/h_w = 0.04–0.12, t_s/t_w = 5.0, l_s/d_o = 1.50) for semi-circular stiffener, (b) von-Mises stress contour for b_s/h_w = 0.04 (L1 & L2) & 0.12 (H1 & H2).

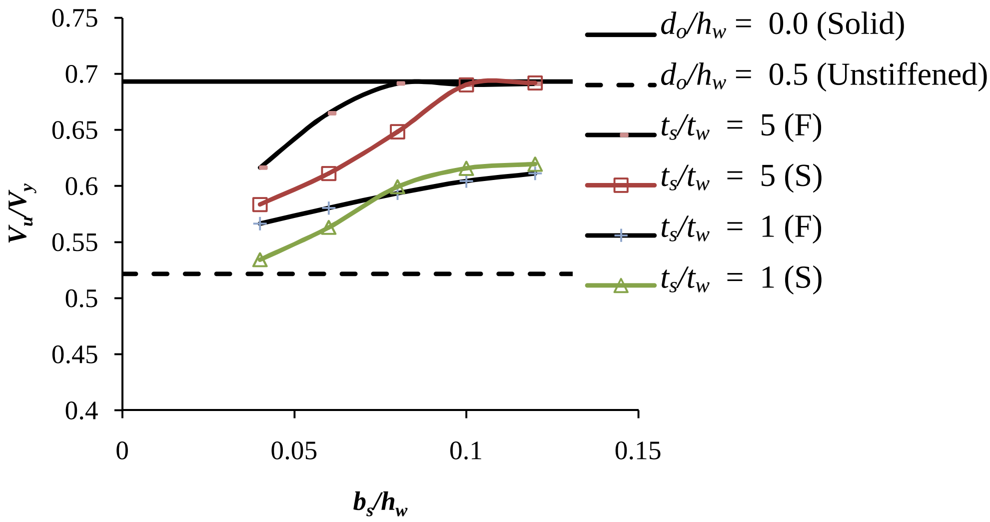

Figure 5.39: Variation of V_u/V_y vs b_s/h_w of semi-circular stiffeners.

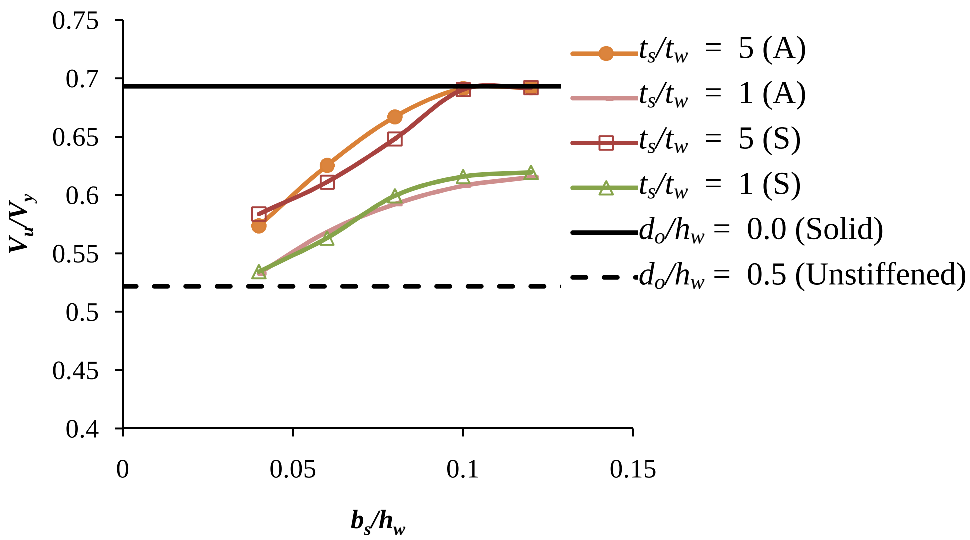

Figure 5.40: Variation of V_u/V_y vs b_s/h_w for the comparison of angular and semicircular stiffeners (made of same material quantity).

CHAPTER 6

CONCLUSIONS AND SUGGESTIONS FOR FURTHER WORK

6.1 INTRODUCTION

Lean Duplex Stainless Steel (LDSS / EN 1.4162 / UNS 32101) is relatively a new type of duplex stainless steels which offers considerable advantages such as better economy (lower nickel content = ~1.5% i.e. much lower in comparison to austenitic stainless steel), improved strength compared to commonly used austenitic grades, high temperature properties, acceptable weldability and fracture toughness properties etc (e.g. Theofanous and Gardner, 2010; Saliba and Gardner, 2013a). Recently, LDSS has been included the newly amended Eurocode (EN 1993-1-4, 2006/A1:2015) for stainless steel. In particular, new expressions on the design shear curves for stainless steel sections have been affected, based on the work of Saliba et. al., (2014). Notwithstanding, the increasing interest shown on LDSS structural members (e.g. Theofanous and Gardner, 2010, Saliba and Gardner, 2013a, Huang and Young, 2013, 2014a, 2014b), detailed investigations (both experimental and numerical studies) on LDSS is limited. In the light of expanding the understanding of the structural performance of LDSS sections or members, an investigation is initiated in this thesis, on the parametric study of hollow LDSS beam (or box girder). The effects of single circular perforation and stiffeners on the perforated rectangular hollow beams have also been studied. The present study, is believed to aid in augmenting the confidence of practising engineers and architects in using LDSS structural elements, especially for the shear design of rectangular hollow beams. Key conclusions drawn from the present work are presented in this chapter along with suggestions for future work.

6.2 CONCLUSIONS

6.2.1 Shear behavior of LDSS rectangular hollow beams

An investigation of the effect of cross sectional parameters such as flange thickness (t_f), flange width (w_f), and shear span (a) on the shear behaviour *viz*., shear capacity and failure mechanisms, of LDSS rectangular hollow beams (box girders) has been attempted in this, using finite element (FE) analysis, *via* Abaqus. On the basis of the understanding acquired from the FE analyses, presented herein, appropriateness of the design rules of EN 1993-1-4 (2006/A1:2015) and Direct Strength Method (DSM) are assessed. Based on the comparison, possible modifications to both EN 1993-1-4 (2006/A1:2015) and DSM have been proposed by bifurcating into two span ratios: 1) $a/h_w \leq 1.0$ and 2) $1 < a/h_w \leq 2.0$. Main conclusions are provided below:

1) In general, it is observed that increasing flange thickness for the same web thickness, can enhance both the ultimate shear capacity and ductility. An asymptotic drop in shear capacity (V_u) has been observed with increasing values of web slenderness (h_w/t_w), the decrease in V_u being relatively steeper till $h_w/t_w < 75$. The variation of t_f/t_w is found to have little effect on

V_u for $h_w/t_w \geq$ ~75, whereas for stockier web sections e.g. $h_w/t_w <$ ~75, an increasing rise in V_u can be seen with increasing t_f/t_w.

2) The effect of t_f is more pronounce both for lower and higher values of t_w (i.e. towards left and right extremes of h_w/t_w = ~75), whilst the effect is relatively less for intermediate values, on keeping t_f/t_w constant.

3) The shear capacity (V_u) of the beam is seen to decrease with increasing shear span for both the stocky and slender web sections.

4) The effect of increasing flange width (w_f) is found to be significant for stockier sections as compared to the slender sections.

5) Three failure mechanisms have been identified *viz*., 1) shear dominant, 2) bending dominant, and 3) combined shear and bending, in consistent to the observation made on LDSS plate girders in the literature.

6) In general, both EN 1993-1-4, 2006/A1:2015 and DSM are found to be applicable for the shear design of LDSS rectangular hollow beams (although their predictions are conservative), in comparison to the FE results presented herein. Hence, a possible modifications to both EN 1993-1-4, 2006/A1:2015 and DSM have been suggested by bifurcating two span ratios: 1) $a/h_w \leq 1.0$ and 2) $1< a/h_w \leq 2.0$.

6.2.2 Shear behavior of single perforated LDSS rectangular hollow beams

Effect of single circular web perforation in the shear characteristic of LDSS rectangular hollow beams. Primarily, the effect of single perforation size / diameter (d_o) and location (along longitudinal (x), transverse (y), and diagonals (d_1 & d_2)) are assessed with a focus on the shear load capacity (V_u/V_y), deformed shapes (or failure modes) etc. is presented, through FE analyses. Further, following the method proposed by Hagen, (2005), the proposed modification to EN 1993-1-4, 2006/A1:2015 (mentioned above) for unperforated LDSS hollow beam has been further modified to incorporate the effect of circular perforation, considering two span cases 1) $a/h_w \leq 1.0$ (short span) and 2) $1 < a/h_w \leq 2.0$ (long span). Main conclusions are provided below:

1) It has been found that perforation has relatively higher shear reducing effect for slender webs. A nearly linear decrease in the value of shear capacity (V_u/V_y) of ~ 23-25% for 500% (i.e. d_o/h_w = 0.0–0.50) increase in perforation size can be seen with slender (h_w/t_w = 300) webs. Whereas, a relatively lesser drop ~ 8-10% and ~1.7-2.7% can be observed for stockier (h_w/t_w = 20) webs, for short and long spans respectively.

2) Shear capacity is observed to increase with increasing flange thickness (or t_f/t_w) for perforated beams, consistent with the similar behaviour observed for the case unperforated beams.

3) When perforation location is changed along longitudinal and transverse directions, not very significant difference in shear capacity is seen, although maximum reduction in shear capacity appears to occur corresponding to perforations located in the highly stressed diagonal tension band.

4) It is observed that, there appears to be no significant variation on the shear capacity, when the location is changed along tension diagonal. Whereas, for the change in perforation location along compression direction, the reduction in shear capacity is seen to be relatively larger for the central diagonal region i.e. ~$0.50 \leq d_2/h_w \leq 1.0$, whereas the reduction gets smaller on either side of the central region.

5) A decrease in the shear capacity with increasing values of web slenderness (h_w/t_w) is observed for perforated beams, similar to that of unperforated beams. In general, for the case of slender webs with $h_w/t_w \geq$ ~75, there appears to be a near parallel decrease in the values of shear capacity, for 400% increase in perforation size (from d_o/h_w = 0.1). The effect of perforation in the reduction of shear capacity is felt most when the web becomes slender.

6) Based on the FE results, shear buckling factor expressions have been proposed for perforated beams considering two span regimes ($a/h_w \leq 1.0$ and $1 < a/h_w \leq 2.0$), modifying EN 1993-1-4, 2006/A1:2015.

6.2.3 Stiffening effects on the shear behavior of single perforated LDSS rectangular Hollow beams

Shear behavior of stiffened single perforated LDSS rectangular hollow beam, considering various orientations / patterns *viz.*, inclined (*IS*), vertical (*VS*), horizontal (*HS*) and ring (*RS*); and cross-sections i.e. flat, angular and semi-circular, are determined, in this work. Based on the study, it has been found that inclined stiffener (with flat cross-section) is relatively most effective in enhancing the shear capacity of perforated beams. Main conclusions are given below:

1) For the inclined stiffeners the role of stiffener thickness in enhancing the shear capacity becomes more effective at longer length, e.g. the rate of increase in shear capacity increases (in a non linear trend) with increasing stiffener length for higher thicknesses (e.g. $t_s/t_w \geq 3$). For short length stiffeners (l_s/d_o = 1.0), little benefit could be seen by increasing the cross-sectional dimension (in terms of b_s and t_s), although an improved enhancement in shear capacity can be seen even for thin stiffeners, for long stiffeners $l_s/d_o >$ ~1.0. Whereas for thick stiffeners (e.g. t_s/t_w = 7), almost full

strength of the unperforated beam could be achieved at lower b_s (e.g. b_s = 0.04).

2) In the case of vertical and horizontal stiffeners, there appears to have no/little significant improvement in shear capacity for both the variation in length, width and thickness (lesser than ~ 5% enhancement) in enhancing the shear capacity of the perforated beam.

3) For the ring stiffeners, it is found that, shear capacity increases with increase in both breadth and thickness of the stiffeners (i.e. when the cross section gets stockier), The rate of increase in shear capacity (with respect to the unstiffened beam) appears to be slightly higher for larger values of stiffener thickness and breadth.

4) A comparison of the effect of angular and flat inclined (also flat and semicircular) stiffeners (keeping the same cross sectional area) shows that, angular/semi-circular stiffeners predicted lesser V_u/V_y for $b_s/h_w \leq 0.08$ and 0.10 for thin and thick sections respectively, beyond which both the sections resulted in similar shear capacity values. However, comparison made between angular and semi-circular sections showed that both the sections predicted similar behavior of shear capacity: shear capacity is found to increase with increasing stiffener width for smaller values of stiffener width (e.g. $b_s/h_w < 0.10$) and a plateauing effect is seen for larger stiffener widths.

6.3 SUGGESTIONS FOR FUTURE WORK

In this thesis, a large number of FE models (approximately ~520 models) have been analysed systematically, considering pertinent geometrical parameters; to understand the shear behaviour of LDSS rectangular hollow beams (unperforated, perforated and stiffened perforations). In addition, proposed new design expressions have also been suggested for unperforated and perforated beams. Notwithstanding such effort, considerable work may be identified and enumerated to expand the understanding of LDSS rectangular hollow beams. Some such topics are suggested for extension, for future, in the following sections:

6.3.1 Loading conditions

The current thesis work focussed on the shear behaviour of LDSS rectangular hollow beams. Hence, it may be extended to address the effects of torsion, combined torsion and bending, combined torsion, bending and axial loadings etc, considering both static and cyclic load cases. Also, such members may also be studied for impact and blast loadings. Thermal effects / loading may also be considered, to assess its structural behaviour.

6.3.2 In-fill material

The structural behaviour of the LDSS rectangular hollow beams, may be enhanced by using suitable materials as in-fill, *viz.*, ordinary concrete of various strengths, steel fibre reinforced concrete, light weight concrete, recycled concrete etc. In addition, another hollow beam/tube can also be placed along with the concrete, to constitute a double skin type of member. The inner tube, can be of various cross-sections such as circular, elliptical, rectangular etc.; and made of another material such as carbon steel.

Different material can be filled inside the tube for increasing the load carrying capacity by restricting the local buckling and confinement of concrete by steel tube. The infill materials which may be fly ash concrete, fibre reinforced concrete, rubberised concrete, recycled material concrete, soil etc.

6.3.3 Geometrical considerations

Instead of straight beams, the effects of various loading conditions may also be considered for curved beams. Investigations on the effects of other perforation shapes like square, rectangular, elliptical etc. may be carried out. Interactions of two or more perforations (similar or different perforation sizes) can be looked into.

6.3.4 Design Considerations

In this thesis, Direct Strength Method and EN 1993-1-4 (2006/A1:2015) has been extended for the current work on unperforated beams. Such design proposals may be extended to address the structural behaviour of perforated and stiffened perforated beams. Further, Continuous Strength Method (CSM) which is a new design approach, may also be explored for possible application to the problems considered herein.

REFERENCES

Abaqus., 2009. Hibbit, Karlsson, & Sorensen, Inc. Abaqus/Standard user's manual volumes 1-III and ABAQUS CAE manual. version 6.9-EF1, Pawtucket, USA.

Ahmed, S., Ashraf, M. & Us-Saadat, M.A., 2016. The Continuous Strength Method for slender stainless steel cross-sections. Thin-Walled Structures; 107: 362–376.

Afshan, S. & Gardner, L., 2013. Experimental Study of Cold-Formed Ferritic Stainless Steel Hollow Sections. Journal of Structural Engineering; 139(5):717-728.

AISI., 2007. North American specification for the design of cold-formed steel structural members. AISI-S100-07. American Iron and Steel Institute. Washington, D.C.

AISC., 2005. American Institute of Steel Construction specification for structural steel buildings, Load and Resistance factor Design. AISC, Chicago, III.

Alinia, M.M., Gheitasi, A. & Shakiba, M., 2011. Postbuckling and ultimate state of stresses in steel plate girders. Thin-walled structures; 49 (4): 455-464.

Alinia, M.M., Shakiba, M. & Habashi, H.R., 2009. Shear characteristics of steel plate girders. Thin-Walled Structures; 47: 1498-1506.

Al-Shawi, F.A.N., 2001. On the rotation capacity of structural steel circular hollow sections in plastic analysis. Journal of Constructional Steel Research; 57(1): 29-43.

AS/NZS 4600., 2005. Standards of Australia and Standards of New Zealand. Cold-Formed Steel Structures, Sydney–Wellington.

AS/NZS 4673., 2001. Standards Australia and Standards New Zealand Australian/New Zealand Standard: Cold-formed stainless steel structures. Sydney Australia.

ASCE 8-02., 2002. Specification for the design of cold-formed stainless steel structural members. SEI/ASCE-8-02. New-York: ASCE.

Ashraf, M. & Young, B., 2011. Design formulations for non-welded and welded aluminium columns using Continuous Strength Method. Engineering Structures 2011; 33: 3197–3207.

Ashraf, M., Gardner, L. & Nethercot, D.A., 2006a. Compression strength of stainless steel cross-sections, Journal of Constructional Steel Research; 62(1-2): 105-115.

Ashraf, M., Gardner, L. & Nethercot, D.A., 2006b. Finite element modelling of structural stainless steel cross-sections. Thin-Walled Structures; 44 (10): 1048–1062.

Ayhan, A.O., Genel, K. & Eksi, S., 2012. Simulation of nonlinear bending behavior and geometric sensitivities for tubular beams with fixed supports. Thin-Walled Structures; 51: 1-9.

Becque, J., Lecce, M. & Rasmussen, K.J.R., 2008. The direct strength method for stainless steel compression members, Journal of Constructional Steel Research; 64(11): 1231-1238.

Bock, M., Gardner, L. & Real, E., 2015. Material and local buckling response of ferritic stainless steel sections. Thin-Walled Structures; 89:131–141.

Bowmick, A.K., 2014. Seismic behavior of steel plate shear walls with centrally placed circular perforations. Thin-Walled Structures; 75:30-42.

Brown, C.J. & Yettram, A.L., 1986. The elastic stability of square perforated plates under combinations of bending, shear and direct load. Thin-Walled Structures; 4 (3): 239-246.

Camotim, D., Silvestre, N., Basaglia, C. & Bebiano, R., 2008. GBT-based buckling analysis of thin-walled members with non-standard support conditions. Thin Walled Struct; 46 (7–9): 800–815.

Carvalho, E.C.G., Van den Berg, G.J. and Van der Merwe, P., 1990. Local shear buckling on cold-formed stainless steel beam webs. Proceedings of the annual technical session, stability of bridges. Structural Stability Research Council. April 10-11. St Louis, Missouri, USA.

Chan, T.M. & Gardner, L., 2008. Bending strength of hot-rolled elliptical hollow sections. Journal of Constructional Steel Research; 64(9):971–986.

Cheng, B. & Li, C., 2012. Buckling Behavior of Strengthened Perforated Plates under Shear Loading. Steel and Composite Structures; 13 (4): 367-382.

Chryssanthopoulos, M.K. & Low, Y.M., 2001. A method for predicting the flexural response of tubular members with non-linear stress–strain characteristics. Journal of Constructional Steel Research; 57(11): 1197–1216.

Corona, E. & Vaze, S.P., 1996. Buckling of elastic-plastic square tubes under bending. International journal of Mechanical Science; 38(7): 753-775.

Cruise, R.B. & Gardner, L., 2006. Measurement and prediction of geometric imperfections in structural stainless steel members. Structural Engineering and Mechanics; 24(1): 63-89.

CUFSM4.05., 2012. Finite strip buckling analysis of thin-walled members (Schafer, B.W.). Baltimore, U.S.A.: Department of Civil Engineering, Johns Hopkins University, 〈http://www.ce.jhu.edu/bschafer/cufsm/〉.

D'Aniello, M., Guneyisi, E.M., Landolfo, R. & Mermerdas, K., 2014. Analytical prediction of available rotation capacity of cold-formed rectangular and square hollow section beams. Thin-Walled Structures; 77: 141–152.

D'Aniello, M., Guneyisi, E.M., Landolfo, R. & Mermerdas, K., 2015. Predictive models of the flexural overstrength factor for steel thin-walled circular hollow section beams. Thin-Walled Structures; 94: 67–78.

Dawson, R.G. & Walker, A.C., 1972. Post-buckling of geometrically imperfect plates. Journal of the Structural Division, ASCE; 98: ST1:75-94.

Dubas, P., 1980. Reflexions sur certains problèmes de sécurité et en construction metallique. Memories CERES. 55. Liege, Belgium.

Elchalakani, M., Zhao, X.L. & Grzebieta R., 2002. Bending tests to determine slenderness limits for cold-formed circular hollow sections. Journal of Constructional Steel Research; 58(11):1407–1430.

El-Khoriby, S.R., Hassanein, M.F., Kharoob, O.F., Hadidy, A.M., Alnaggar. G.A.N., 2016. Tubular flange plate girders with corner square web openings in the panel of maximum shear: Strength and behavior. Thin-Walled Structures; 99: 142–154.

Ellobody, E. & Young, B., 2005. Structural performance of cold-formed high strength stainless steel columns. Journal of Constructional Steel Research; 61(12): 1631-1649.

Ellobody, E., Feng, R. & Young, B., 2014. Finite element analysis and Design of Metal Structures. Elsevier Inc.

EN 10088-4, 2009. Stainless steels - part 4: Technical delivery conditions for sheet/plate and strip of corrosion resisting steels for general purposes. CEN.

EN 1993-1-3, 1996. Eurocode3: Design of Steel Structures, Part 1.3: Cold Formed Thin Gauge members and Sheeting, ENV-93-1-3, European Committee for Standardisation, Brussels.

EN 1993-1-4, 2006. Eurocode 3: design of steel structures. Part 1.4: General rules – supplementary rules for stainless steels. CEN.

EN 1993-1-4, 2006/A1:2015. Eurocode 3: Design of steel structures-Part 1.4: General rules-Supplementary rules for stainless steel. CEN.

EN 1993-1-5, 1997. Eurocode 3: Design of steel structures. Part 1.5: General rules-supplementary rules for planar plated structures without transverse loading: Brussels.

EN 1993-1-5, 2003. Eurocode3: Design of Steel Structures, Part 1-5: Plated Structural Elements. CEN.

EN 1993-1-5, 2006. Eurocode3: Design of Steel Structures, Part 1-5: Plated Structural Elements. CEN.

ENV 1993-1-4, 1996. Eurocode 3: Design of steel structures. Part 1.4: General rules-supplementary rules for stainless steel. Brussels.

Estrada, I., Real, E. & Mirambell, E., 2007a. General behavior and effect of rigid and non-rigid end post in stainless steel plate girders loaded in shear. Part 1: Experimental study. Journal of Constructional Steel Research; 63 (7): 970-984.

Estrada, I., Real, E. & Mirambell, E., 2007b. General behavior and effect of rigid and non-rigid end post in stainless steel plate girders loaded in shear. Part 2: Extended numerical study and design proposal. Journal of Constructional Steel Research; 63 (7): 985-996.

Estrada, I., Real, E. & Mirambell, E., 2008. Shear resistance in stainless steel plate girders with transverse and longitudinal stiffening. Journal of Constructional Steel Research 2004; 64: 1239-1254.

Feng, R. & Young, B., 2015. Experimental investigation of aluminium alloy stub columns with circular openings. Journal of Structural Engineering; 141(11): 04015031.

Gardner, L., 2005. The use of stainless steel in structures. Progress in Structural Engineering and Materials; 7 (2): 45–55.

Gardner, L., Cruise, R.B., Sok, C.P., Krishnan, K. & Santos, J.M.D., 2007. Life-cycle costing of metallic structures. Proceedings of the Institution of Civil Engineers, Engineering Sustainability; 160: 167–177.

Gardner, L., Talja, A. & Baddoo, N.R., 2006. Structural design of high-strength austenitic stainless steel. Thin-Walled Structures; 44 (5):517–528.

Gardner, L. & Ashraf, M. 2006. Structural design for non-linear metallic materials. Engineering Structures; 28(6):926–934.

Gardner, L. & Nethercot, D.A., 2001. Numerical modelling of cold-formed stainless steel sections. In: NSCC proceedings: NSCC 2001 Ninth Nordic steel construct Conference, Helsinki, Finland, 781–790.

Gardner, L. & Nethercot, D.A., 2004a. Structural stainless steel design: a new approach. Struct Eng; 82: 21–30.

Gardner, L. & Nethercot, D.A., 2004b. Experiments on stainless steel hollow sections—Part 2: Member behaviour of columns and beams. Journal of Constructional Steel research; 60(9): 1319-1332.

Gardner, L. & Nethercot, D.A., 2004c. Numerical Modeling of Stainless Steel Structural Components-A Consistent Approach. Journal of Structural Engineering; 130(10): 1586-1601.

Gardner, L. & Theofanous, M., 2008. Discrete and continuous treatment of local buckling in stainless steel elements. Journal of Constructional Steel Research; 64(11): 1207–1216.

Gardner, L., 2008. Aesthetic, economics and design of stainless steel structures. Advanced Steel Construction; 4(2): 113-112.

Gardner, L., 2002. A new approach to structural stainless steel design. PhD Thesis. Structures Section, Dept of Civil and Environmental Engineering. Imperial College London, UK.

Gardner, L., Chan, T.M. & Wadee, M.A., 2008. Shear response of elliptical hollow sections. Proceedings of the Institution of Civil Engineers—Structures and Buildings 2008; 161 (6): 301–309.

Gardner, L., Saari, N. & Wang, F., 2010. Comparative experimental study of hot-rolled and cold-formed rectangular hollow sections. Thin-Walled Structures; 48(7): 495–507.

Gardner, L., Talja, A. & Baddoo, N.R., 2006. Structural design of high-strength austenitic stainless steel. Thin-Walled Structures; 44(5): 517-528.

Gellin, S., 1979. The plastic buckling of long cylindrical shells under pure bending. International journal of solids structures; 16:397-407.

Georgieva, I., Schueremans, L., Vandewalle, L. & Pyl, L., 2012. Design of Built-Up Cold-Formed Steel Columns According to the Direct Strength Method. Procedia Engineering; 40:119–124.

Gheitasi, A. & Alinia, M.M., 2010. Slenderness classification of unstiffened metal plates under shear loading. Thin-Walled Structures; 48:508-518.

Hagen N.R., 2005. On the shear capacity of steel plate girders with large openings. PhD Thesis. Department of Structural Engineering. Faculty of Engineering Science. Norwegian University of science and technology.

Hagen, N.C. & Larsen, P.K., 2009. Shear capacity of steel plate girders with large web openings, part 2: Design guidelines. Journal of Constructional Steel; 65(1):151-158.

Hagen, N.C., Larsen, P.K. & Alberg, A., 2009. Shear capacity of steel plate girders with large web openings, part 1: Modeling and simulations. Journal of Constructional Steel; 65(1): 142-150.

Hamoodi, M.J. & Gabar, M.S.A., 2013. Behavior of Steel Plate Girders with Web Openings Loaded in Shear. Engineering and Technical Journal; 31(15):2982-2995.

Hancock, G.J., Kwon, Y.B. & Bernard, E.S., 1994. Strength design curves for thin-walled sections undergoing distortional buckling. Journal of Constructional Steel Research; 31 (2-3): 169–186.

Hassanein, M.F. & Kharoob, O.F., 2012. An extended evaluation for the shear behavior of hollow tubular flange plate girders. Thin-Walled Structures; 56: 88–102.

Hassanein, M.F. & Kharoob, O.F., 2010. Shear strength and behavior of transversely stiffened tubular flange plate girders. Engineering Structures; 32(9): 2617-2630.

Hassanein, M.F. & Silvestre, N., 2013. Flexural behavior of lean duplex stainless steel girders with slender unstiffened webs. Journal of Constructional Steel Research; 85: 12-23.

Hassanein, M.F., 2010. Imperfection analysis of austenitic stainless steel plate girders failing by shear. Engineering Structures; 32(3): 704–713.

Hassanein, M.F., 2011. Finite element investigation of shear failure of lean duplex stainless steel plate girders. Thin-Walled Structures; 49 (8): 964–973.

Hassanein, M.F., 2014. Shear strength of tubular flange plate girders with square web openings. Engineering Structures; 58: 92–104.

Herzog, M.A.M., 1992. Web crippling with bending and shear of thin-walled plate girders. Journal of constructional steel research; 22: 87-97.

Hill, H.N., 1944. Determination of stress-strain relations from “offset” yield strength values. Washington DC, USA: national Advisory Committee for Aeronautics.

Hoglund T., 1973. Design of thin plate I girders in shear and bending with special reference to web buckling, Bulletin No. 94, Division of Building Statics and Structural Engineering, Royal Institute of Technology, Stockholm, Sweden.

Hoglund, T., 1971. Strength of thin-plate girders with circular or rectangular web holes without stiffeners. In: Proceeding of the colloquium of the international association of bridge and structural engineering, London: 353-365.

Hoglund, T., 1997. Shear buckling resistance of steel and aluminum plate girders. Thin –Walled Structures; 29(1-4):13-30.

Holmquist, J.L. & Nadai, A., 1939. A theotetical and experimental approach to the problem of collapse of deep-well casing. Drilling and Production Practice: 392-420.

Huang, Y. & Young, B., 2012. Material properties of cold-formed lean duplex stainless steel sections. Thin-Walled Structures; 54: 72-81.

Huang, Y. & Young, B., 2013. Experimental and numerical investigation of cold-formed lean duplex stainless steel flexural members. Thin-Walled Structures; 73: 216–228.

Huang, Y. & Young, B., 2014a. Structural performance of cold-formed lean duplex stainless steel columns. Thin-Walled Structures;83:59–69.

Huang, Y. & Young. B., 2014b. Experimental investigation of cold-formed lean duplex stainless steel beam-columns. Thin-Walled Structures; 76: 105-117.

Islam, S.M.Z. & Young, B., 2014. FRP strengthening of lean duplex stainless steel hollow sections subjected to web crippling. Thin-walled structures; 85: 183-200.

Jiao, H. & Zhao, X.L., 2004. Section slenderness limits of very high strength circular steel tubes in bending. Thin-Walled Structures; 42(9): 1257-1271.

Keerthan, P. & Mahendran, M., 2015a. Improved shear design rules of cold-formed steel beams. Engineering Structures; 99: 603–615.

Keerthan, P. & Mahendran, M., 2015b. Experimental investigation and design of lipped channel beams in shear. Thin-walled Structures; 86: 174-184.

Keerthan, P. & Mahendran, M., 2011. New design rules for the shear strength of LiteSteel beams. Journal of Constructional Steel Research Volume; 67 (6): 1050–1063.

Keerthan, P. & Mahendran, M., 2013. Suitable stiffening systems for LiteSteel beams with web openings subjected to shear. Journal of Constructional Steel Research; 80: 412-428.

Keerthan, P. Mahendran, M. & Narsey, A., 2015. Shear tests of hollow flange channel beams with real support conditions. Structures; 3: 109-119.

Kim, J.H., Jeon, J.H., Park, J.S., Seo, H.D., Ahn, H.J. & Lee, J.M., 2015. Effect of reinforcement on buckling and ultimate strength of perforated plates. International Journal of Mechanical Sciences; 92: 194-205.

Kiymaz, G., 2005. Strength and stability criteria for thin-walled stainless steel circular hollow section members under bending. Thin-Walled Structures; 43 (10): 1534–1549.

Korol, R.M., 1979. Critical buckling strains of round tubes in flexure. International Journal of Mechanical Sciences; 21(12): 719-730.

Kwon, Y.B. and Ryu, S.W., 2016. The shear strength of end web panels of plate girders with tension field action. Thin-walled structures; 98(B): 573-591.

Kwon, Y.B., 2014. The development of the direct strength method for welded steel members with buckling interactions. Thin-Walled Structures; 81: 121–131.

Lagaros, N.D., Psarras, L.D., Papadrakakis, M. & Panagiotou, G., 2008. Optimum design of steel structures with web opening. Engineering Structures; 30(9): 2528-2537.

Landesmann, A. & Camotim. D., 2013. On the Direct Strength Method (DSM) design of cold-formed steel columns against distortional failure. Thin-Walled Structures Volume; 67: 168–187.

Lawson, R.M., Basta, A. & Uzzaman, A., 2015. Design of stainless steel sections with circular openings in shear. Journal of Constructional steel research; 112:228-241.

Lee, S.C., Yoo, C.H. & Yoon, D.Y., 2003. New design rule for intermediate transverse stiffeners attached on web panels. Journal of Structural Engineering; 129: 1607-1614.

Lee, S.C. & Yoo, C.H., 1998. Strength of plate girder web panels under pure shear. Journal of structural Engineering; 124 (2): 184-194.

Lee, S.C. & Yoo, C.H., 1999. Experimental study on ultimate shear strength of web panels. Journal of structural Engineering; 125 (8): 838-846.

Liew, A. & Gardner, L., 2015. Ultimate capacity of structural steel cross-sections under compression, bending and combined loading. Structures; 1: 2-11.

Liu, T.C. & Chung, K.F., 2003. Steel beams with large web openings of various shapes and sizes; finite element investigation. Journal of Constructional steel research; 59(9): 1159-1176.

Luo, R. & Edlund, B., 1996. Shear Capacity of plate girders with trapezoidal corrugated webs. Thin-Walled Structures; 26 (1): 19-44.

Maiorana, E., Pellegrino, C. & Modena, C., 2009. Elastic stability of plates with circular and rectangular holes subjected axial and bending moment. Thin Walled Structures; 47(3): 241-255.

Ma, J.L, Chan, T.M. & Young, B., 2016. Experimental investigation of cold-formed high strength steel tubular beams. Engineering Structures; 126: 200–209.

Mann, A.P., 1993. The structural use of stainless steel. Structural Engineering; 71(4): 60–69.

Mirambell, E. & Real, E., 2000. On the calculation of deflections in structural stainless steel beams: an experimental and numerical investigation. Journal of Constructional Steel Research; 54(1): 109–133.

Narayanan R., Al-Amery, R.I.M. & Roberts, T.M., 1989. Shear strength of composite plate girders with rectangular web cut-outs. J of Constructional steel Research; 12; 151-166.

Narayanan, R. & Der-Avanessian, N.G.V. 1986. Analysis of plate girders with perforated webs. Thin-walled structures; 4; 363-380.

Narayanan, R. & Der-Avanessian, N.G.V., 1984a. Strength of webs with corner openings. The structural Engineer; 62 B(1): 6-11.

Narayanan, R. & Der-Avanessian, N.G.V., 1984b. Elastic buckling of perforated plates under shear. Thin-Walled Structures (1); 2:51-73.

Narayanan, R. & Rockey, K.C., 1981. Ultimate load capacity of plate girders with webs containing circular cut outs. Proc Inst Civil Eng, London; 71 (2): 845-862.

NAS., 2001. North American specification for the design of cold-formed steel structures. Washington (DC): American Iron and Steel Institute.

NAS., 2007. Commentary on North American Specification for the Design of Cold-Formed Steel Structural Members, Washington, DC: American Iron and Steel Institute.

Nilsson, J.O., Chai. G, & Kivisäkk, U., 2008. Recent development of stainless steels. In: Proceedings of the sixth European stainless steel conference: 585–590.

Olsson, A., 2001. Stainless steel plasticity-material modelling and structural applications. Doctoral Thesis. Sweden: Lulea University of Technology.

Paik, J.K., 2007. Ultimate strength of perforated plates under edge shear loading, Thin-walled structures; 45:301–306.

Patton, M.L. & Singh, K.D., 2012. Numerical modeling of lean duplex stainless steel hollow columns of square, L-, T-, and +-shaped cross sections under pure axial compression. Thin-Walled Structures; 53: 1–8.

Pavlovcic, L., Detzel, A., Kuhlmann, U. & Beg, D., 2007. Shear resistance of longitudinally stiffened panels-Part 1: Tests and numerical analysis of imperfections. Journal of Constructional Steel Research; 63(3):337-350.

Pellegrino, C., Maiorana, E. & Modena, C., 2009. Linear and non-linear behaviour of steel plates with circular and rectangular holes under shear loading. Thin-Walled Structures; 47(6-7): 607-616.

Pham, C.H. & Hancock, G.J., 2010. Experimental investigation of high strength cold formed C-sections in combined bending and shear. Journal of Structural Engineering; 136: 866-878.

Pham, C.H. & Hancock, G.J., 2015. Numerical investigation of longitudinally stiffened web channels predominantly in shear. Thin-Walled Structures; 86: 47–55.

Pham, S.H., Pham, C.H. & Hancock, G.J., 2014. Direct strength method of design for shear including sections with longitudinal web stiffeners. Thin-Walled Structures; 81: 19–28.

Pi, Y.L. and Trahair, N.S., 1995. Lateral buckling strengths of cold-formed rectangular hollow sections. Thin-Walled Structures; 22: 71-95.

Ramberg, W. & Osgood, W.R., 1943. Description of stress-strain curves by three parameters. Washington DC, USA: National Advisory Committee for Aeronautics; technical Note No. 902.

Rasmussen, K.J.R. & Hancock, G.J., 1993. Design of Cold-Formed Stainless Steel Tubular Members. II: Beams. Journal of Structural Engineering; 119(8): 2368–2386.

Rasmussen, K.J.R., 2000. Recent research on stainless steel tubular structures. Journal of Constructional Steel Research; 54: 75-88.

Rasmussen, K.J.R., 2003. Full-range stress–strain curves for stainless steel alloys. Journal of Constructional Steel Research; 59 (1): 47–61.

Real, E. & Mirambell, E., 2005. Flexural behavior of stainless steel beams. Engineering Structures; 27: 1465-1475.

Real, E., Mirambell, E. & Estrada, I., 2007. Shear response of stainless steel plate girders. Engineering Structures; 29: 1626-1640.

Reddy, B.D., 1979. An experimental study of the plastic buckling of circular cylinders in pure bending. International Journal of Structures; 15: 669-683.

Ridley-Ellis, D.J., 2000. Rectangular Hollow sections with circular web openings-Fundemental behavior in torsion, bending and shear. Ph.D. thesis, University of Nottingham.

Riks, E., 1979. An incremental approach to the solution of snapping problems. International Journal of Solids and Structures; 15:529-51.

Roberts, T.M. & Azizian, Z.G., 1984. Strength of perforated plates subjected to in-plane loading. Thin-Walled Structures; 2(2):153-164.

Rockey, K.C., Anderson, R.G. & Cheung, Y.K., 1967. The behaviour of square shear webs having a circular hole. Proceedings of the Swansea Symposium on Thin-Walled Structures: 148-169.

Ruiz-Teran, A.M. & Gardner, L., 2008. Elastic buckling of elliptical tubes. Thin-Walled Structures, 46 (11), 1304–1318.

Safar, S.S., 2013. Shear strength of end web panels. Thin-walled structures; 67: 101-109.

Saliba N, Real, E. & Gardner, L., 2014. Shear design recommendations for stainless steel plate girders. Engineering Structures; 59: 220–228.

Saliba, N. & Gardner, L., 2013a, Experimental study of the shear response of lean duplex stainless steel plate girders. Engineering Structures; 46: 375–391.

Saliba, N. & Gardner, L., 2013b. Cross-section stability of lean duplex stainless steel welded I-sections. Journal of Constructional Steel Research; 80: 1–14.

Saliba, N., 2012. Structural behavior of Lean Duplex Stainless Steel Welded I-Sections. PhD Thesis. Department of Civil and Environment Engineering, Imperial College London, UK.

Schafer, B.W. & Pekoz. T., 1998. Computational modeling of cold-formed steel: characterizing geometric imperfections and residual stresses. Journal of Constructional Steel Research; 47: 193–210.

Schafer, B.W., 2005. Direct strength method design guide, American Iron and Steel Institute (AISI) report, Washington DC.

Schafer, B.W., 2008. Review: the Direct Strength Method of cold-formed steel member design. Journal of Constructional Steel Research; 64 (7–8): 766–788.

SEI/ASCE, 2002. Specification for the Design of Cold-Formed Stainless Steel Structural Members, (SEI/ASCE 8-02), American Society of Civil Engineers (ASCE), Reston.

Shafer, B.W., 2010. User's Manual and Tutorials of CUFSM 3.12.

Shanmugam, N.E., 1997. Opening in Thin-Walled Steel Structures. Thin-Walled Structures; 28(3-4): 355-372.

Shanmugam, N.E., Lian, V.T. & Thevendram, V., 2002. Finite element modelling of plate girders with web openings. Thin-Walled structures; 40(5): 443-464.

Sharkley, T.M. & Brown, C.J., 1996. Elastic buckling of plates with eccentrically positioned rectangular perforations. International Journal of Mechanical Sciences; 38 (8-9): 825-838.

Su, M.N., Young, B. & Gardner, L., 2012. Bending tests of aluminium alloy cross-sections. Tubular structures; 509-515.

Theofanous, M. & Gardner, L., 2009. Testing and numerical modeling of lean duplex stainless steel hollow section columns. Engineering Structures; 31(12): 3047–3058.

Theofanous, M. & Gardner, L., 2010. Experimental and numerical studies of lean duplex stainless steel beams. Journal of constructional steel research; 66(6): 816-825.

Theofanous, M. & Gardner, L., 2011. Effect of element interaction and material non-linearity on the ultimate capacity of stainless steel cross-sections. Steel and Composite Structures; 12(1): 73-92.

Theofanous, M., Chan, T.M. & Gardner, L., 2009. Flexural behaviour of stainless steel oval hollow sections. Thin-Walled structures; 47(6-7): 776-787.

Theofanous, M., Saliba, N., Zhao, O. & Gardner, L., 2014. Ultimate response of stainless steel continuous beams. Thin-Walled Structures; 83: 115-127.

THIN-WALL, 2006. A computer program for cross-sectional analysis and finite strip buckling analysis and direct strength design of thin-walled structures. Version 2.1 (Computer Software). School of Civil Engineering, Centre for Advanced Structural Engineering, Univrersity Of Sydney; Sydney, Australia.

Tsavdaridis, K.D. & D'Mello, C., 2011. Web buckling study of the behaviour and strength of perforated steel beams with different novel web opening shapes. Journal of Constructional Steel Research; 67(10): 1605–1620.

Tsavdaridis, K.D. & D'Mello, C., 2012. Optimisation of novel elliptically-based web opening shapes of perforated steel beams. Journal of Constructional Steel Research; 76: 39–53.

Uenoya, M. & Redwood, R.G., 1977. Buckling of webs with openings. Computers and Structures; 9(2): 191-199.

Umbarkar, K.R., Patton, L.M. & Singh, K.D., 2013. Effect of single circular perforation in lean duplex stainless steel (LDSS) hollow circular stub columns under pure axial compression. Thin-Walled Structures; 68: 18-25.

Young, B. & Lui, W.M., 2005. Behavior of Cold-Formed High Strength Stainless Steel Sections. Journal of Structural Engineering; 131(11): 1738-1745.

Zhang B. Shu G, Xin L, Yuang R. Jiang Q, 2016. Study on the shear bending capacity of cold formed stainless steel hollow sections. Structures; 8(1): 63-74.

Zhao, O. & Rossi, B., Gardner L, Young B. 2015a. Behaviour of structural stainless steel cross-sections under combined loading – Part I: Experimental study. Engineering Structures; 89:236–246.

Zhao, O., Rossi, B., Gardner, L. & Young, B., 2015b. Behaviour of structural stainless steel cross-sections under combined loading – Part II: Numerical modelling and design approach. Engineering Structures; 89: 247–259.

Zhao, X.L. & Hancock, G.J., 1992. Square and rectangular hollow sections subject to combined actions. e Journal of Structural Engineering; 118: 3.

Zheng, B., Shu, G., Xin, L., Yang, R. and Jiang, Q., 2016. Study on the Bending Capacity of Cold-formed Stainless Steel Hollow Sections. Structures; 8(1): 63-74.

Zhou, F. & Long, G. 2016. Element interaction of cold-formed stainless steel cross-sections subjected to major axis bending. Journal of Constructional Steel Research; 118: 22–40.

Zhou, F. & Young, B., 2005. Tests of cold-formed stainless steel tubular flexural members. Thin-Walled structures; 43(9): 1325-1337.

Zhu, J.H. & Young, B., 2009. Design of aluminium alloy flexural members using the direct strength method, Journal of Structural Engineering; 135(5): 558-566.

Zhu, J.H. & Young, B., 2012. Design of cold-formed steel oval hollow section columns. Journal of Constructional Steel Research; 71: 26–37.

APPENDIX A

DESIGN SAMPLE OF LDSS RECTANGULAR HOLLOW BEAMS

Shear capacity based on class 4 from EN 1993-1-4 (2006/A1:2015) is explained below and also based on Direct strength method and Continuous Strength method. The cross section taken for explaining an example is t_w = 2 mm, t_f = 8mm, L = 1200 mm, w_f = 200 mm, h_w = 600 mm.

A1 *Classification of cross-section elements (Table 5.2 of EN 1993-1-4 (2006/A1:2015))*

Material properties

$E = 2 \times 10^5$ MPa, $\upsilon = 0.3$, $\sigma_y = 711$ MPa, $\sigma_u = 839$ MPa

a) ***Web***

For bending member

$c/t = 600/2 = 300$, $90\varepsilon = 90 \times 0.57 = 51.3$

$c/t > 51.3$ therefore class 4

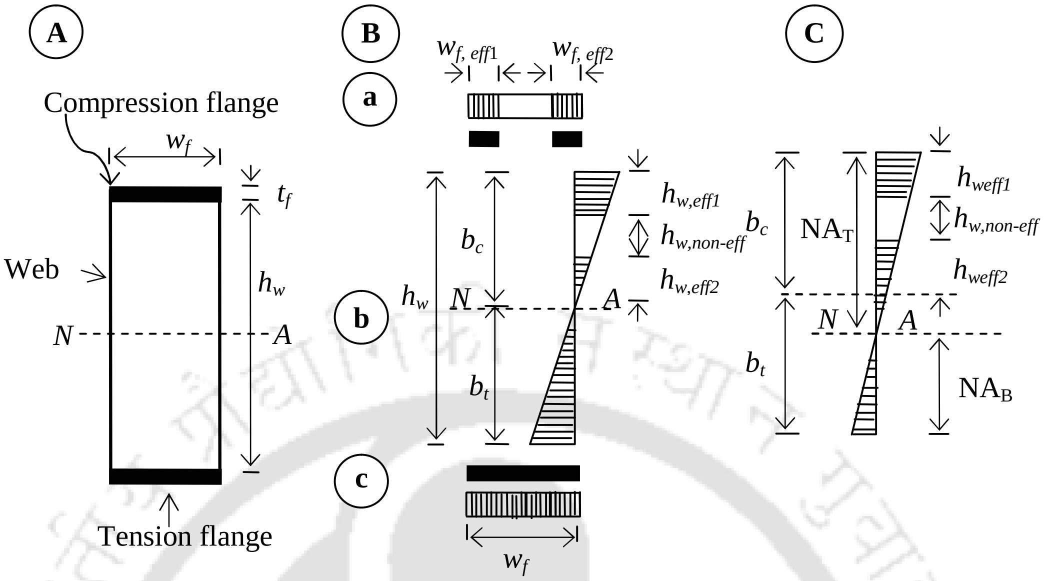

Figure A1: A) Cross-section, B) Stress-distribution of a) compression flange, b) web, c) tension flange, C) Stress distribution in web and shifted neutral axis for cross-section

b) *Compression Flange*

Similarly from Table 5.2 of EN 1993-1-4 (2006/A1:2015) for internal compression members

c = 200 – 2 × 2 = 196 mm

c/t = 196/8 = 24.5

Checking for Class 4, 37ε = 37 × 0.57 = 21.09

$c/t > 37\varepsilon$, therefore it is class 4

Flange and web are in class 4, hence it is a class 4 cross-section.

A2 *Eurocode* (EN 1993-1-4 (2006/A1:2015)) *Design Calculation*

Effective widths in Class 4 cross-sections

A2.1 *Effective widths of elements in Class 4 cross-section*

Cold formed or welded internal elements

a) *Web*

Reduction factor due to buckling of plate is

$$\rho = \frac{0.772}{\bar{\lambda}_p} - \frac{0.079}{\bar{\lambda}_p^2} \text{ but} \leq 1 \quad \frac{0.772}{3.79} - \frac{0.079}{3.79^2} = 0.19$$

According to Clause 5.2 of EN 1993-1-4 (2006/A1:2015)

$$\varepsilon = \left[\frac{235}{f_y} \times \frac{E}{210000}\right]^{0.5}$$

$$= \left[\frac{235}{711} \times \frac{210000}{210000}\right]^{0.5} = 0.57$$

Equation 5.1 from Clause 5.2.3 of EN 1993-1-4 (2006/A1:2015) or Equation 3.11,

$$\bar{\lambda}_p = \frac{\bar{b}/t}{28.4\varepsilon\sqrt{k_\sigma}}$$

$$= \frac{600/2}{28.4 \times 0.57 \times \sqrt{23.9}} = 3.79$$

t is relevant thickness

k_σ is the buckling factor corresponding to the stress ratio ψ and boundary conditions from Table 5.1 or Table 5.2 in EN 1993-1-5 as appropriate

$\bar{b}$ = clear distance

$\bar{b}$ = flat element width for webs of RHS

$\bar{b}$ = flat element width for RHS flanges, which can be taken as b - 2t

ε is the material factor defined in Table 5.2 of EN 1993-1-4 (2006/A1:2015)

f_y = 711 MPa

$\psi = -1$; $k_\sigma = 23.9$ from *Table 4.2 of EN 1993-1-4 (2006/A1:2015),*

$$h_{w,eff} = \circ b_c = \frac{\circ \bar{b}}{(1-\cdot\,)} = \frac{0.19\times 600}{(1+1)} = 58 \text{ mm}$$

$h_{w,eff1} = 0.4\, h_{w,eff}$, $h_{w,eff2} = 0.6\, h_{w,eff}$; $h_{w,eff1} = 23$ mm, $h_{w,eff2} = 35$ mm

Non-effective area in web, $h_{w,non\text{-}eff} = 300 - (23 + 35) = 241$ mm

b) *Flange*

$\cdot = 1$; $k_{\pm} = 4$ *from Table 4.1 of EN 1993-1-4 (2006/A1:2015),*

$w_f = 200 - 2 \times 2 = 196$ mm

Reduction factor due to buckling of plate *according to Clause 5.2.3 of EN 1993-1-4 (2006/A1:2015),*

$$\circ = \frac{0.772}{\bar{a}_p} - \frac{0.125}{\bar{a}_p^2} \text{ but} \leq 1 = \frac{0.772}{0.74} - \frac{0.125}{0.74^2} = 0.81$$

$$\bar{a}_p = \frac{\bar{b}/t}{28.4£\sqrt{k_{\pm}}} == \frac{196/8}{28.4\times 0.57\times\sqrt{23.9}} = 0.75$$

From Table 4.2 of EN 1993-1-4 (2006/A1:2015),

$w_{f,\,eff} = \circ b_c = 0.75 \times 196 = 172$ mm

$w_{f,\,eff1} = 0.5 w_{eff}$, $w_{f,eff2} = 0.5 w_{f,eff}$

$w_{f,\,eff1} = 86$ mm, $w_{f,eff2} = 86$ mm

A2.2 *Neutral axis depth calculation*

Take moment of area about bottom edge of the compression flange

Neutral axis depth from bottom (tension) flange (NA_B)

$$= \frac{\begin{array}{l} w_{f,eff1} \times t_f \times \left(h_w + 2\times t_f - t_f \times 0.5\right)\times 2 + h_{w,eff1} \times t_w \times \begin{pmatrix} h_w + 2\times t_f - t_f - 0.5 \\ \times h_{w,eff1} \end{pmatrix} \times 2 \\ + h_{w,eff2} \times t_w \times \left(h_w \times 0.5 + t_f + h_{w,eff2} \times 0.5\right)\times 2 + \left(h_w \times 0.5 \times t_w \times \begin{pmatrix} h_w \times 0.5 \\ \times 0.5 + t_f \end{pmatrix}\right)\times 2 \\ w_f \times t_f \times t_f \times 0.5 \end{array}}{A_{eff}}$$

$$= \frac{\begin{array}{l} 86\times 8\times(600+2\times 8-8\times 0.5)\times 2+23\times 2\times(600+2\times 8-8-0.5\times 23)\times 2+35\times 2 \\ \times(600\times 0.5+8+35\times 0.5)\times 2+(600\times 0.5\times 2\times(600\times 0.5\times 0.5+8))\times 2 \\ +196\times 8\times 8\times 0.5 \end{array}}{4156}$$

=261 mm

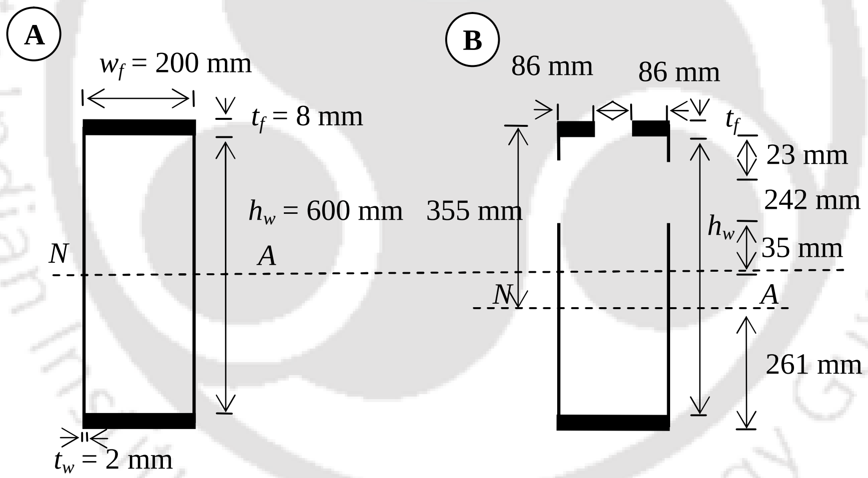

Figure A2: A) Cross-section B) dimensions of effective cross-section

Effective Area, A_{eff} = 86 × 8 × 2 + 23 × 2 × 2 + 74 × 2 × 2 + 253 × 2 × 2 + 196 × 8 = 4344 mm^2

Neutral axis depth from top (compression) flange (NA_T) = $h_w + 2t_f$ – NAB = 600 + 2 × 8 – 261 = 355 mm

A2.3 *Effective section modulus*

$$W_{\text{eff, min}} = \frac{Moment\ of\ inertia}{y_{highest}}$$

$$
= \frac{\begin{array}{l}
\left\{\left(\dfrac{w_{f,eff1} \times t_f^3}{12}\right) + w_{f,eff1} \times t_f \times \left(w_{f,eff1} \times \left(NA_T - 0.5 \times t_f\right)^2\right)\right\} \times 2 \\
+\left\{\left(\dfrac{h_{w,eff1}^3 \times t_w}{12}\right) + h_{w,eff1} \times t_w \times \left(NA_T - t_f - h_{w,eff1} \times 0.5\right)^2\right\} \times 2 \\
+\left\{\left(\dfrac{h_{w,eff2}^3 \times t_w}{12}\right) + h_{w,eff1} \times t_w \times \left(NA_T - t_f - h_{w,eff1} - h_{w,non-eff} - h_{w,eff2} \times 0.5\right)^2\right\} \times 2 \\
+\left\{\begin{array}{l}
\left(\dfrac{t_w \times \left(h_w + 2t_f - NA_B - h_{w,eff1} - h_{w,non-eff} - h_{w,eff2}\right)^3}{12}\right) + \\
\left(t_w \times \left(h_w + 2t_f - NA_B - h_{w,eff1} - h_{w,non-eff} - h_{w,eff2}\right)\right) \times \\
\left(\left(\begin{array}{l} h_w + 2t_f - NA_B - \\ h_{w,eff1} - h_{w,non-eff} - h_{w,eff2} \end{array}\right) \times 0.5\right)^2
\end{array}\right\} \times 2 \\
+\left\{\left(\dfrac{t_w \times \left(NA_B - t_f\right)^3}{12}\right) + t_w \times \left(NA_B - t_f\right) \times \left(\left(NA_B - t_f\right) \times 0.5 + t_f\right)^2\right\} \times 2 \\
+\left(\dfrac{w_f \times t_f^3}{12}\right) + \left(w_f \times t_f \times \left(NA_B - 0.5 \times t_f\right)^2\right)
\end{array}}{NA_T}
$$

$$= \frac{\begin{aligned}&\left(\left(\frac{86\times 8^3}{12}\right)+86\times 8\times(355-4)^2\right)\times 2+\left(\left(\frac{2\times 23^3}{12}\right)+23\times 2\times\begin{pmatrix}355-8\\ -23\times 0.5\end{pmatrix}^2\right)\times 2\\ &+\left(\left(\frac{74^3\times 2}{12}\right)+2\times 74\times 2\times 74\times 52^2\right)\times 2\\ &+\left\{\begin{array}{l}\left(\dfrac{2\times(600+2\times 8-261-23-242-35)^3}{12}\right)\\ +\left((600+2\times 8-261-23-242-35)\times\left(\begin{pmatrix}600+2\times 8-261-23-\\ 242-35\times 0.5\end{pmatrix}\times 0.5\right)^2\right)\end{array}\right\}\times 2\\ &+\left(\left(\frac{2\times 253^3}{12}\right)+2\times 253\times 127^2\right)\times 2+\left(\left(\frac{196\times 8^3}{12}\right)+196\times 8\times 257^2\right)\end{aligned}}{376}$$

$=8.7 \times 10^5$ mm^3

For Class 4 sections *EN 1993-1-4 (2006/A1:2015),*

Effective bending resistance,

$$M_{c,Rd} = \frac{W_{eff,\min} f_y}{\text{¥}_{MO}}$$

$$= \frac{8.7\times 10^5 \times 711}{1.0} = 618\ kNm$$

A2.4 *Plastic section modulus of cross-section*

$W_{pl,\,Rd}$ = 86 × 8 × 355 × 2 + 23 × 2 × 326.5 × 2 + 74 × 2 × 37 × 2 + 253 × 2 × 126.5 × 2 + 196 × 8 × 257

$= 1.06 \times 10^6$ mm^3

$$M_{pl,\,Rd} = \frac{1.04 \times 10^6 \times 711}{1.0} = 755 \text{ kNm}$$

Plastic section modulus for flange,

$$W_f = \frac{\left(\left(\left(\frac{86 \times 8^3}{12}\right) + \left(86 \times 8 \times 351^2\right)\right) \times 2 + \left(\frac{196 \times 8^3}{12}\right) + \left(196 \times 8 \times 257^2\right)\right)}{355}$$

$$= 0.76 \times 10^6 \text{ mm}^3$$

$$M_{f,\,Rd} = \frac{W_f \times f_y}{1.0}$$

$$= \frac{0.76 \times 10^6 \times 711}{1.0} = 540 \text{ kNm}$$

A2.5 *Web Slenderness*

Considered as webs are stiffened at support and midspan (coupled),

$$\bar{a}_w = \frac{h_w}{37.4 t_w \text{£} \sqrt{k_2}}$$

t_w = is the web thickness

k_τ = is the minimum shear buckling co-efficient for the web panel

$$= 5.34 + 4.00\left(\frac{h_w}{a}\right) \qquad \text{when } \frac{a}{h_w} \geq 1$$

$$= 4.00 + 5.34\left(\frac{h_w}{a}\right) \qquad \text{when } \frac{a}{h_w} < 1$$

a is the shear span, h_w is clear distance between the flanges.

For the present example, $\dfrac{a}{h_w} = \dfrac{600}{600} = 1$

for $\dfrac{a}{h_w} \geq 1,\; k_\tau = 5.34 + 4 \times 1 = 9.34$

$$\bar{\lambda}_w = \frac{600}{37.4 \times 2 \times 0.57 \times \sqrt{9.34}} = 4.61$$

A2.6 *Design strengths*

The design resistance is the total of shear contribution from web ($V_{bw,\,Rd}$) and flange ($V_{bf,\,Rd}$)

$$V_{b,\,Rd} = V_{bw,\,Rd} + V_{bf,\,Rd} \leq \frac{\eta f_{yw} h_w t}{\sqrt{3}\gamma_{M1}}$$, (Equation 3.7)

$$V_{bw,\,Rd} = \frac{\chi_w f_{yw} h_w t}{\sqrt{3}\gamma_{M1}}$$, is contribution from web (Equation 3.8),

χ_w is shear buckling factor, which is the contribution of the web to shear buckling resistance as shown below (*Clause 5.6 of EN 1993-1-4 (2006/A1:2015)*),

$$\chi_w = \frac{1.56}{0.91 + \bar{\lambda}_w} = \frac{1.56}{0.91 + 4.61} = 0.28 \text{ for } \bar{\lambda}_w \geq 0.65$$

$$\chi_{w,prop} = \frac{2.42}{1.53 + \bar{\lambda}_w} = \frac{2.42}{1.53 + 4.61} = 0.39$$

Contribution of shear from flange (*Clause 5.4 of EN 1993-1-4 (2006/A1:2015)*),

$$V_{wf,Rd} = \frac{w_f t_f^2 f_{yf}}{c\gamma_{M1}}\left(1-\left(\frac{M_{Ed}}{M_{f,Rd}}\right)^2\right)$$

c is the distance which the position of plastic hinge in ultimate shear capacity (Olsson, 2001).

$$c = 600 \times \left(0.17 + \frac{3.5 \times 196 \times 8^2 \times 711}{4 \times 600^2 \times 711}\right) = 136 \text{ mm}$$

$M_{ed} = V_{u,\,FE} \times 0.6 = 650 \times 0.6 = 390$ kNm

$$V_{wf,Rd} = \frac{196 \times 8^2 \times 711}{16.7 \times 1.0 \times 10^3} \times \left[1-\left[\frac{390}{540}\right]^2\right] = 65 \text{ kN}$$

$$V_{bw,Rd} = \frac{0.28 \times 711 \times 600 \times 2 \times 2}{\sqrt{3} \times 1.0} = 277 \text{ kN}$$

$$V_{bw,\,Rd,\,prop} = \frac{0.39 \times 711 \times 600 \times 2 \times 2}{\sqrt{3} \times 1.0} = 387 \text{ kN}$$

According to Clause 5.2 of EN 1993-1-4 (2006/A1:2015)

$$V_{b,\,Rd} = V_{bw,\,Rd} + V_{bf,\,Rd} \leq \frac{\eta f_{yw} h_w t}{\sqrt{3}\gamma_{M1}}$$

$V_{b,\,Rd} = 277 + 65 = 342$ kN

$V_{b,Rd,\,prop} = 387 + 65 = 452$ kN

$$\frac{\eta f_{yw} h_w t_w}{\sqrt{3}\gamma_{M1}} = \frac{1.2 \times 711 \times 600 \times 2 \times 2}{\sqrt{3} \times 1.0} = 1182 \text{ kN}$$

$$V_{b,\,Rd} \leq \frac{\eta f_{yw} h_w t}{\sqrt{3}\gamma_{M1}}$$

$V_{u,FE}$ = 650 kN

$$\frac{V_{u,FE}}{V_{b,Rd}} = \frac{650}{342} = 1.9$$

$$\frac{V_{u,FE}}{V_{b,Rd,prop}} = \frac{650}{452} = 1.43$$

A2.7 *Moment-Shear* (M-V) *Interaction calculation* (*Clause 7.1 of EN 1993-1-4 (2006/A1:2015)*)

Interaction avoids when design shear force is less than the 50% of the shear resistance of web alone, $V_{Ed} < 50\% V_{bw,Rd}$

$V_{u,FE}$ = 650 kN

$50\% V_{bw,Rd} = 0.5 \times 277 = 138.5$ kN

$V_{Ed} > 50\% V_{bw,Rd}$

Therefore, the interaction should be considered.

$$\eta_1 + \left(1 - \frac{M_{f,Rd}}{M_{pl,Rd}}\right)(2\eta_3 - 1)^2 \le 1.0$$

$$\eta_1 = \frac{M_{Ed}}{M_{pl,Rd}}$$

$$\eta_3 = \frac{V_{Ed}}{V_{bw,Rd}}$$

$$\frac{M_{f,Rd}}{M_{pl,Rd}} = \frac{540}{755} = 0.71$$

Table A1 *M-V* interaction from EN 1993-1-4 (2006/A1:2015)

M_{Ed}	$V_{bf, Rd}$	$V_{b, Rd} = V_{bf,Rd} + V_{bw, Rd}$	$M/Mc,Rd$	$V/V_{b,Rd}$
0	64.36	343.05	0.00	1.23
50	63.93	342.62	0.07	1.23
100	62.66	341.35	0.13	1.22
200	57.58	336.27	0.26	1.21
300	49.10	327.79	0.40	1.18
400	37.24	315.93	0.53	1.13
500	21.98	300.68	0.66	1.08
550	13.09	291.78	0.73	1.05
600	3.34	282.03	0.79	1.01
616	0.00	278.69	0.82	1.00
650			0.86	0.93
675			0.89	0.88
680			0.90	0.87
690			0.91	0.84
700			0.93	0.82
710			0.94	0.79
725			0.96	0.73
755			1.00	0.50
			1.00	0.00

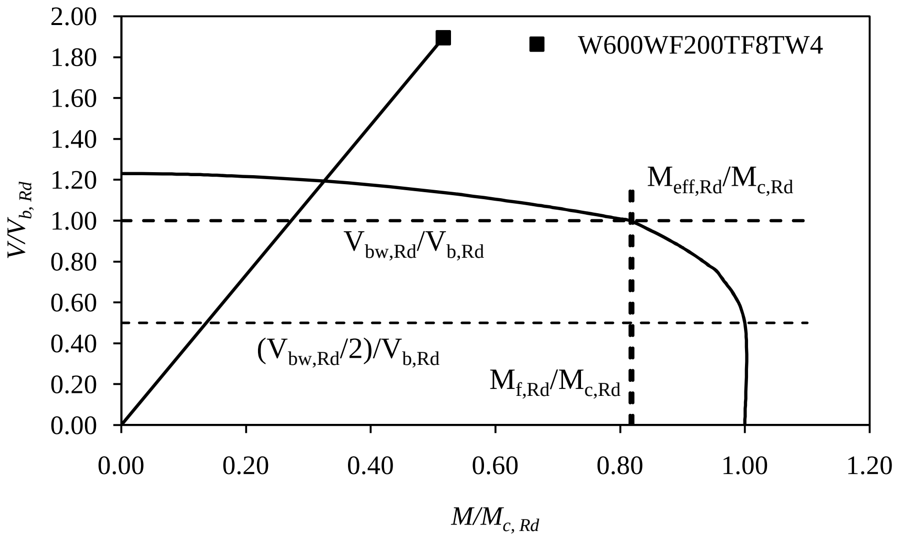

Figure A1: M-V interaction curve based on EN 1993-1-4 (2006/A1:2015) for sample, t_w = 2 mm, t_f = 8mm, L = 1200 mm, w_f = 200 mm, h_w = 600 mm.

$M_{f,Rd}$ = 616 kNm

M_{eff} = 619 kNm

$M_{c,\,Rd}$ = 755 kNm

M_{ed} = 390 kNm

c = 138 mm

$V_{bw,\,Rd}$ = 278 kN

$V_{bw,prop}$ = 551 kN

$M_{u,FE}$ = 390 kNm

$V_{u,FE}$ = 650 kN

$M_{pl,\,Rd}$ = Plastic moment resistance of a cross-section class.

$M_{eff,\,Rd}$ = Effective moment resistance for Class 4 sections

$$\frac{M_{u,FE}}{M_{pl,Rd}} = 0.63$$

$$\frac{V_{u,FE}}{V_{b,Rd}} = 1.95$$

$$\frac{V_{u,FE}}{V_{b,Rd,prop}} = 1.17$$

A2.8 Comparison of $V_{u,\,FE}$ with EN 1993-1-4

$$i_{w,prop} = \frac{V_{u,FE} - V_{flange}}{V_y}$$

$$= \frac{650 - 66}{985} = 0.59$$

$$V_y = \frac{f_y \times h_w \times t_w}{\sqrt{3}}$$

$$= \frac{711 \times 600 \times 2 \times 2}{\sqrt{3}}$$

= 985 kN

A3 Shear capacity based on Direct Strength Method (DSM)

For example, t_w = 2 mm, t_f = 8mm, L = 1200 mm, w_f = 200 mm, h_w = 600 mm

$a/h_w \leq 1.0$

V_{cr} is determined from FE

$$a = \sqrt{\frac{V_y}{V_{cr}}}$$

$$= \sqrt{\frac{1023}{68}} = 3.88$$

Shear capacity with post buckling

DSM design rules proposed by Keerthan and Mahendran (2015)

$$\frac{V_v}{V_y} = 1 \qquad a \leq 0.815$$

$$\frac{V_v}{V_y} = \frac{0.815}{a} + P_n\left[1 - \frac{0.815}{a}\right] \qquad 0.815 < a \le 1.23$$

$$\frac{V_v}{V_y} = \frac{1}{a^2} + P_n\left[1 - \frac{1}{a^2}\right] \qquad a > 1.23$$

A3.1 Post buckling coefficient (P_n) *for LCBs (Keerthan and Mahendran, 2015)*

	Keerthan and Mahendran (2015) for open sections	Proposed	
		$a/h_w \le 1.0$	$1.0 < a/h_w \le 2.0$
P_n	0.25	0.52	0.33

where V_{yw} = yield shear capacity of web based on an average shear yield stress of 0.6 f_y ; V_{cr} = elastic shear buckling capacity of web, for more unique cross-sections it is determined by finite element analysis (Schafer, 2008).

For $a > 1.23$, $\frac{Vv}{Vy} = \frac{1}{3.88^2} + 0.52\left(1 - \frac{1}{3.88^2}\right)$

$= 0.55$

$V_{prop,\ DSM} = 562$ kN

$V_{u,FE} = 650$ kN

Hence, $\frac{V_{u,FE}}{V_{prop,DSM}} = \frac{650}{562} = 1.15$

APPENDIX B

DESIGN SAMPLE FOR CIRCULAR WEB OPENING IN LDSS RECTANGULAR HOLLOW BEAMS

Shear capacity of circular perforated LDSS beam

<u>Circular opening</u>

e.g. h_w = 600 mm, t_w = 2 mm, t_f = 10 mm, L = 1200 mm (a/h_w = 1.0), d_o/h_w = 0.5, vertical side of opening = 300 mm, longitudinal side = 450 mm, $V_{u,FE}$ = 514 kN.

Shear resistance of web with regularly shaped opening, $\text{¡}_{w,mod}$ is the modified shear buckling factor is a function of reduction factor c.

$$\text{¡}_{w,mod} = c\ \text{¡}_{w,prop}$$

$\text{¡}_{w,prop}$ is the proposed shear buckling factor for solid webs is shown in Table 3.3.

$$\text{¡}_{w,prop} = \frac{2.42}{1.53 + \bar{\text{a}}_w} = \frac{2.42}{1.53 + 4.61} = 0.39$$

$$\chi_{u,FE} = \left(\frac{494 - 80}{985}\right) = 0.44$$

c is reduction factor, depends upon the factors web slenderness (h_w/t_w), opening size $\left(\frac{d_o}{h_w}\right)$, yield stress ($f_y$) and $\sqrt{\frac{f_y}{E}}$

$$c = \left(1 - \frac{1}{2}\frac{d_o}{h_w}\right)$$

Reduction factor for $\dfrac{d_o}{h_w}$ = 0.5, (opening sizes is 50% of web height)

$$c = 1 - 0.5 \times (0.5) = 0.75$$

Expressions to calculate web slenderness parameter ($\bar{\lambda}_w$) (Equations 3.11-3.13)

$$k_\tau = 5.34 + 4 \times \left(\frac{600}{0.5 \times 1200}\right)^2 = 9.34$$

$$\lambda_w = \frac{600}{\left(37.4 \times 2 \times 0.57 \times \sqrt{9.34}\right)} = 4.60$$

Modified shear capacity web,

$$V_{bw,\,Rd,\,mod} = \chi_{w,mod} \frac{f_{yw}}{\gamma_{M1}\sqrt{3}} h_w t_w$$

$$= \frac{\left(c \times \chi_{w,prop} \times f_y \times h_w \times t_w\right)}{\left(\gamma_{Mo} \times \sqrt{3} \times 1000\right)}$$

$$= \frac{\left(0.75 \times 0.39 \times 711 \times 600 \times 2\right)}{\left(1.0 \times \sqrt{3} \times 1000\right)}$$

= 288 kN

Shear capacity of flange is,

$$V_{bf,\,Rd} = \frac{b_f t_f^2 f_{yf}}{c \gamma_{M1}} \left(1 - \left(\frac{M_{Ed}}{M_{f,Rd}}\right)^2\right)$$

$$c = a\left(0.25 + \frac{1.6 b_f t_f^2 f_{yf}}{t_w h_w^2 f_{yw}}\right) = 176 \text{ mm}$$

Moment due to flange to calculate the shear capacity of flange is given below.

$M_{f,\,Rd} = A_f h_w f_{yf}$

$M_{f,\,Rd}$ = 867 kNm

A_f is area of flange considered by effective width ($w_{f,eff}$)

$V_{bf,Rd}$ = 80 kN

Shear capacity of perforated beam,

Total shear capacity, $V_{u,\,pp} = V_{bw,\,Rd} + V_{bf,\,Rd}$ = 288 + 80 = 368 kN

$V_{u,FE}$ = 514 kN

$$\frac{V_{u,FE}}{V_{u,pp}} = \frac{514}{368} = 1.39$$

APPENDIX C

ADDITIONAL VALIDATION

In this appendix, additional validations of the present FE procedure using shell FE elements are provided by comparison with the available experimental data on LDSS hollow beam (Theofanous and Gardner, 2010) and plated I girder (Saliba and Gardner, 2013a). Beam dimensions as well as the material properties are shown in Tables C1-C2 and Tables C3-C4 respectively. Comparison of the present FE and experimental responses are given in Figures C1-C3. It can be seen from Figures 1-3, that the present FE modelling approach is able to capture accurately both the Moment-Rotation (and Load-deformation) profiles and deformed shapes.

Table C1: Beam dimensions (Theofanous and Gardner, 2010) of LDSS hollow beam

Specimen	L (mm)	B (mm)	D (mm)	t (mm)	r_i (mm)	w_o
SHS 100 x 100 x 4-B1	1100	100	100	3.92	3.8	Eq. 2.8

L = Length, B = Width, D = Depth, t = thickness, r_i = internal corner radius, w_0 = local geometric imperfection

Table C2: LDSS material properties of 100 x 100 x 4 – B1 (Theofanous and Gardner, 2010)

SHS 100 × 100 × 4 – B1 specimen						
Cross-section regions	E_o (MPa)	$\sigma_{0.2}$ (MPa)	$\sigma_{1.0}$ (MPa)	σ_u (MPa)	Compound R-O coefficients	
					n	$n'_{0.2,0.1}$
a) Tension flat	198771	586	632	761	9	2.8
b) Compression flat	198238	560	642		8.3	2.6
c) Tensile corner	206000	811	912	917	6.3	4.1

Table C3: Beam dimensions (Saliba and Gardner, 2013a) of LDSS plated I-girder

Specimen	L (mm)	a (mm)	t_w (mm)	t_f (mm)	w_f (mm)	t_s (mm)	b_s (mm)	e (mm)
I – 600 x 200 x 12 x 4 -1	1360	600	4	12	200	20.9	98	80

L = Length, a = shear span, t_w = web thickness, t_f = flange thickness, w_f = flange width, e = centre to centre distance between the stiffeners in support

Table C4: Average of material properties of LDSS plated I-girder (Saliba and Gardner, 2013a)

a) **Tensile material property**

I – 600 x 200 x 12 x 4 -1						
Cross-section regions/parts	E_o (MPa)	$\sigma_{0.2}$ (MPa)	$\sigma_{1.0}$ (MPa)	σ_u (MPa)	Compound R - O coefficients	
					n	$n'_{0.2,0.1}$
a) Web	199500	513	583	755	10	3.7
b) Flange	210000	489.5	538.5	709	9.9	2.05

b) **Compressive material property**

Cross-section regions/parts	E_o (MPa)	$\sigma_{0.2}$ (MPa)	$\sigma_{1.0}$ (MPa)	Compound R - O coefficients	
				n	$n'_{0.2,0.1}$
a) Web	207000	522	599.5	6.1	1.8
b) Flange	204000	467.5	545	5.65	1.7
c) Stiffeners	202000	464	543	5.9	1.6

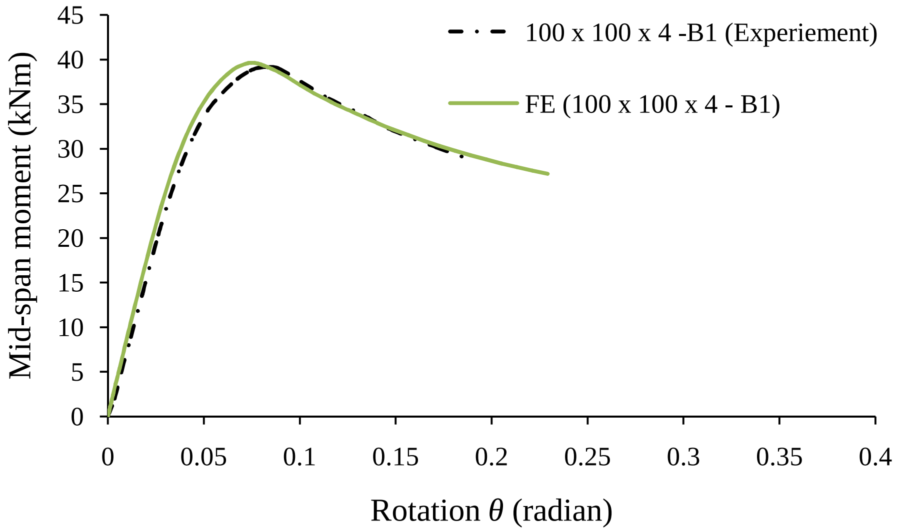

Figure C1: Comparison of FE and experimental (Theofanous and Gardner, 2010). mid-span moment *vs* rotation, for hollow LDSS beams.

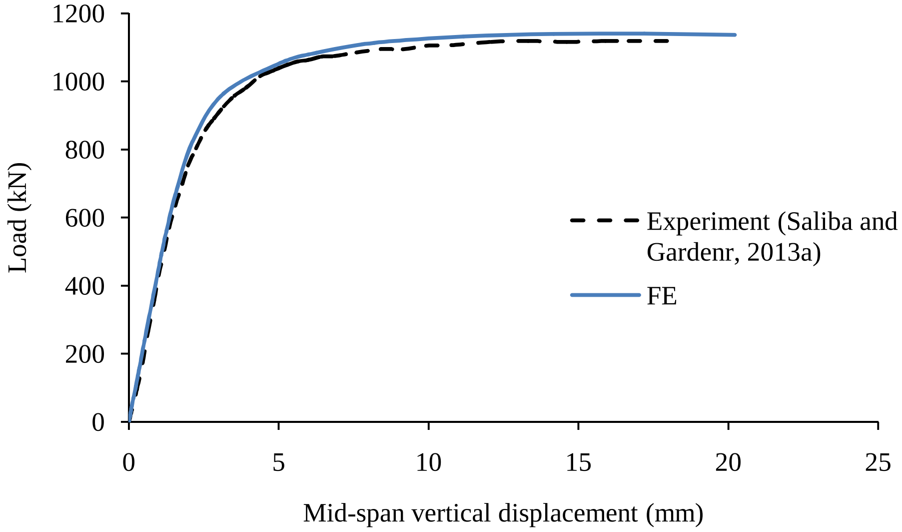

Figure C2: Comparison of FE and experimental (Saliba and Gardner, 2013a) load *vs* mid-span vertical displacement, for LDSS plated I-girder.

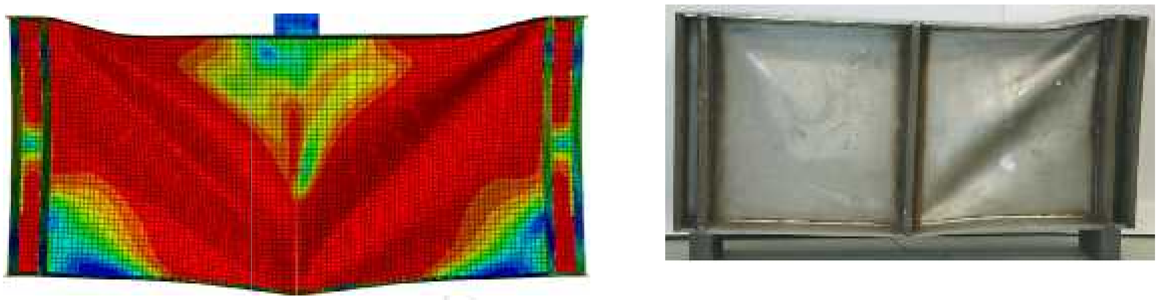

FE Experiemntal (Saliba and Gardner, 2013a)

Figure C3: Comparison of FE and experimental (Saliba and Gardner, 2013a) deformation modes, for LDSS plated I-girder.

LIST OF PUBLICATIONS

A) Journals

Sonu, J.K. & Singh, K.D., 2017. Shear characteristics of Lean Duplex Stainless Steel (LDSS) rectangular hollow beams. Structures; 10: 13-29.

Sonu, J.K. & Singh, K.D., 2016. Shear characteristics of single perforated LDSS rectangular hollow beams (**submitted for review**).

Sonu, J.K. & Singh, K.D., 2016. Stiffening effects on the shear behaviour of single perforated lean duplex stainless steel (ldss) rectangular hollow beams (**manuscript prepared**).

B) Conferences

1. **Sonu, J.K.** & Singh, K.D., 2013. Shear characteristics of rectangular Lean Duplex Stainless Steel (LDSS) Tubular Beams − A Finite Element Study. In *National Conference on Recent Advances in Civil Engineering*, Itanagar, India.
2. **Sonu, J.K.** & Singh, K.D., 2014. Shear Behaviour of Rectangular Lean Duplex Stainless Steel (LDSS) Tubular Beams with Asymmetric Flanges − A Finite Element Study. Advances in Structural Engineering, In *9th Biennial Event Structural Engineering Convention*, Delhi, India.
3. **Sonu, J.K.** & Singh, K.D., 2016. Effect of Circular Web Perforation in Rectangular Lean Duplex Stainless Steel (LDSS) Tubular Beams − A Finite Element Study. In *Sixth International Congress on Computational Mechanics and Simulation*, Mumbai, India.